Thermal Management of Concentrator Photovoltaics

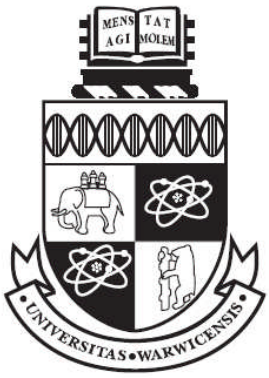

by

Yupeng Wu

BEng MSc

A Thesis submitted to the University of Warwick

for the degree of

Doctor of Philosophy

Department of Engineering

University of Warwick

September 2009

Abstract

Photovoltaic Concentrator systems, which increase the solar radiation intensity on the photovoltaic cells, may reduce the system cost, if the cost of the concentrator is less than the photovoltaic material displaced. An Asymmetric Compound Parabolic Photovoltaic Concentrator (ACPPVC) for building façade integration with a solar concentration ratio of 2.0 has been designed, fabricated and experimentally characterised. The truncated ACPPVC has acceptance half angles of 0° and 55° and an absorber width of 125mm. Phase Change Materials (PCM) have been integrated to the rear of the PV panel to moderate the temperature rise of the PV and maintain good solar-electrical conversion efficiency. The thermal behaviour of a Fresnel lens PV Concentrator (FPVC) has also been studied in this work.

A two-dimensional ray trace technique has been used to predict the optical performance and the angular acceptance of the ACPPVC system. The predicted highest optical efficiency was 88.67% for the ACPPVC-55 system. Extensive indoor experimental characterisation of a number of PV systems was undertaken for a range of incident solar radiation intensities using a highly collimated solar simulator developed specifically for this project. Experimental results showed that the electrical output from the ACPPVC-55 was approximately 1.8 of that of a non-concentrating PV system with similar solar cells area. The electrical conversion efficiency for the ACPPVC-55 system was further increased, when RT27 PCM was incorporated to its rear.

Table of contents

List of figures

List of tables

Nomenclature

Term	Details	Units
A	Area	m^2
a	Radius of an aperture	m
a'	Radius of an absorber	m
C	Geometric concentration ratio	
c_p	Specific heat capacity	$J\,kg^{-1}K^{-1}$
c	Specific heat capacity	$J\,kg^{-1}K^{-1}$
D	Hydraulic depth of a duct coupled at the rear of the PV	m
E	Energy of the photon	J
f	Focal length of a parabola	m
ff	Fill factor	
G	Irradiation	$W\,m^{-2}$
g	Gravitational constant	$m\,s^{-2}$
H	Height of a solar chimney	m
H	Enthalpy	J
h	Heat transfer coefficient	$W\,m^{-2}\,K^{-1}$
I	Current	A
I_t	Incident energy	$W\,m^{-2}$
i	Current	A
K	Extinction coefficient of the glazing material	m^{-1}
k	Thermal conductivity	$W\,m^{-1}\,K^{-1}$
L	Length	m

l	Length	m
$\dot{m}$	Mass flow rate	kg/s^{-1}
n	Refractive index	
P	Power	W
Q	Energy	W
q	Heat flux	$W\,m^{-2}$
r	Radius	
r	Reflectance	
r	Resistance	Ω
S	General source term	J
s	Shadow length	m
T	Temperature	$°C$
t	Time	s
Δt	Time step	s
u	x-direction velocity	$m\,s^{-1}$
V	Voltage	V
v	y-direction velocity	$m\,s^{-1}$
W	Width of a solar chimney	m
X	X-Component in a Cartesian coordinate system	
x	x-Component in a Cartesian coordinate system	
Δx	Depth of the PCM system	m
Y	Y-Component in a Cartesian coordinate system	
y	y-Component in a Cartesian coordinate system	
z	z-Component in a Cartesian coordinate system	

Symbols	Details	Units
α	Absorptance	
β	Thermal expansion coefficient	
h	Planck's constant (6.6256×10^{-34})	J/s
v	Photon's frequency	Hz
η	Efficiency	
θ	Angle	°
θ_a	Maximum acceptance-half angle	°
δ	Mirror error	
ϕ	Angle	°
ω	Angle	°
ρ	Density	$kg\ m^{-3}$
ρ	Reflectance	
τ	Transmittance	
μ	Viscosity	s^{-1}

Subscripts and superscripts

abs	Absorber
abr	Absorbed
amb	Ambient
ape	Aperture
C	Convection

Cond	Conduction
Cell	Solar cell
el	Electrical
f	Fin effectiveness
fin	Fin
front	Front
in	Inflow
in	Incident
L	Liquid
l	Left
m	Melt
max	Maximum
MPP	Maximum Power Point
optimum	Optimum
opt	Optical
out	Outflow
oc	Open circuit
PCM	Phase Changer Material
PV	Photovoltaics
R	Radiation
r	Reflected
r	Right
r	Reflectance
rear	Rear

*ref*1	Reflector 1
*ref*2	Reflector 2
s	Solid
sc	Short circuit
T	Truncation
th	Thermal
tr	Transmitted
wall	Wall
withoutfin	Without fin
α	Absorptance
$\amalg$	Parallel
$\perp$	Perpendicular
$\rightarrow$	to
0	Reference

Abbreviations

Term	Details
ACPPVC	Asymmetric Compound Parabolic Photovoltaic Concentrator
AR	Anti-reflection
Al	Aluminium
Al_2O_3	Aluminium Oxide
a-Si	Amorphous Silicon
BIPV	Building Integrated Photovoltaics
CFD	Computational Fluid Dynamics
CHAPS	Combined Heat And Power Solar
CIGS	CIS compounds alloyed with gallium and sulphur
CIS	Copper Indium Diselenide
CNC	Computer Numerical Control
CPC	Compound Parabolic Concentrator
CdS	Cadmium Sulphide
CdTe	Cadmium Telluride
CO_2	Carbon Dioxide
DSC	Ruthenium-dye-sensitized Solar Cell
ERHs	Electrical Resistance Heats
FPVC	Fresnel Lens PV Concentrator
IMS	Insulated Metal Substrate
ITO	Indium Tin Oxide
LDA	Laser Doppler Anemometry
LED	Light Emitting Diodes

MJ	Multijucation
MPP	Maximum Power Point
PCM	Phase Change Material
PV	Photovoltaics
PV/PCM	PV and Phase Change Material
PV-T	PV and Thermal collector
Ta_2O_5	Tantalum Pentoxide
TiO_2	Titanium Dioxide

Acknowledgment

First and foremost, I would like to express my sincere gratitude to my supervisor Professor Philip Charles Eames for his immeasurable guidance, encouragement and support provided throughout the duration of this research. I am also grateful to my advisor Dr Mervyn Smyth of Centre of Sustainable Technologies, University of Ulster for his valuable advice and discussion.

Many thanks and appreciations are extended to all the technical staffs in the School of Engineering, University of Warwick for their assistance.

Special thanks go to Dr Tapas Mallick and Dr Mohamed Sabry for helping me to design and fabricate my experimental systems, Mr Peter Kimber and Mr Richard Kasler for helping design the solar simulator. I am also thankful to Dr David Allinson for reading through my work, Dr Ing-Liang Wong, Dr Francis Agyenim, Dr Mingjun Huang and Dr Harjit Singh for their encouragement and support throughout my whole research period.

This research was supported and funded by the School of Engineering, University of Warwick through a Departmental Scholarship to the author. I would like to thank BP Solar, Madrid, Spain for supply the Photovoltaic cells, and Alanod Limited, Milton Keynes, UK for supply the reflective material and Ulbrich Precision Metals Ltd, Galway, Republic of Ireland for supply PV ribbon in this work.

Finally, to my parents Xiaoguang Wu and Rong Li and my wife Fangyuan Zhou, the author says, thank you all.

Declaration

The author declares that, to the best of his knowledge, the data contained within this thesis is original and his own work under the supervision of his supervisor, Professor Philip Eames. The material in this thesis is submitted for the degree of PhD to the University of Warwick only and has not been submitted to any other university. All sources of information have been specifically acknowledged in the form of references.

Yupeng Wu

September 2009

Chapter 1 Introduction and literature review

1.1 Background

During the twentieth century, the world total annual consumption of all forms of primary energy increased more than ten-fold (Boyle, 2004). In year 2007, it reached an estimated amount of 11099.3 million tonnes oil equivalent of which approximately three quarters was from fossil fuels (BP, 2008). There has been a growing concern about the amount of fossil fuels remaining, its ability to meet the world's continuously increasing energy requirements and the environmental problems that are caused by conventional energy production systems. At the current consumption rates, proven world coal reserves should last for about 200 years, oil for approximately 40 years and natural gas for around 60 years (Boyle, 2004). At the same time, Carbon dioxide (CO_2) produced by the use of fossil fuels is one of the main causes of global warming. More than 95% of carbon dioxide, sulphur dioxide, nitrogen oxides and black smoke emitted can be attributed to global fossil fuel combustion (Boyle, 2004).

To reduce dependence on fossil fuel energy resources and environmental degradation resulting from their combustion, renewable energy sources, must play an increasingly significant role. One renewable energy source, solar energy is both clean and has the potential to meet all of the world's energy needs. The average extraterrestrial solar radiant energy is 1367 W/m^2 (Duffie and Beckman, 2006). Due to absorption and reflection in the earth's atmosphere (where filtration of x-ray and ultraviolet takes place), the final solar radiation intensity at the earth's surface is less than 1050W/m^2 (Duffie and Beckman, 2006). This flux is comparatively low, but a significant amount of energy can be captured if a large collecting area is utilized. The total incident solar energy on the earth's surface is

approximately 1.5×10^{18} kWh/year which exceeds approximately 9,000 times the current annual world energy demand (Andreev et al., 1997; Peuser et al, 2002; BP, 2008).

Solar energy can be converted into both thermal and electrical energy. Solar thermal energy can be collected using different types of collectors. The solar thermal collector type selected for use is mainly dependent on the temperature requirement of the application for which the collection is to be employed. Different solar thermal collector types and their approximate working temperature ranges are presented in table 1.1 (Norton, 1992).

Name	**Indicative temperature obtained (K)**
Flat-plate absorber	300<T<350
Evacuated envelope	320<T<460
Compound parabolic concentrator	340<T<510 340<T<560
Parabolic reflector	340<T<560
Fresnel refractor	340<T<540
Parabolic dish refractor	340<T<1200
Heliostat field	400<T<3000

Table 1.1 Common types of solar collectors and their approximate working temperature ranges (Norton, 1992)

Photovoltaic cells can transform solar energy into useful electrical energy by the interaction of photons and electrons within a semiconductor material. Silicon is an ideal material for photovoltaic cells. It is non-toxic and the Earth's second most abundant element resource in the crust of Earth (only after oxygen). Silicon solar cells are fabricated in three forms, monocrystalline, multicrystalline (polycrystalline) and amorphous. As shown in figure 1.1, monocrystalline silicon has a well-ordered structure whereas multicrystalline silicon consists of abutting grains, in which the atoms have a periodic arrangement of the

crystalline material in each grain. Atoms are arranged randomly in amorphous silicon (Gordon, 2001).

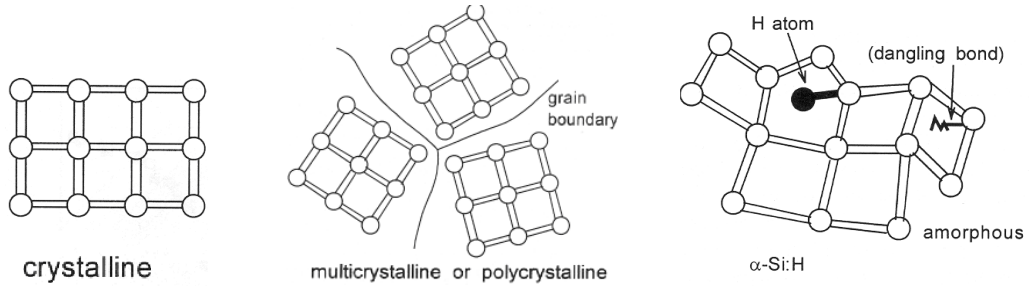

Figure 1.1 The structure of Monocrystalline, Multicrystalline and Amorphous Silicon (Gordon, 2001)

The first solar cell was constructed in 1883 by Charles Fritts, who used junctions formed by coating selenium with an extremely thin layer of gold, which, however, had a solar to electrical conversion efficiency of less than 1%. Russell Ohl described the first silicon solar cell in 1941. Following the work of Russell Ohl, Gerald Pearson, Calvin Fuller and Daryl Chapin reported the first crystalline silicon solar cell in 1954 with a 6% energy-conversion efficiency when used in direct sunlight (Luque and Hegedus, 2003). A large improvement in the silicon cell conversion efficiency was achieved in subsequent years, the crystalline silicon cell reached approximately 25% in 1996 (Green et al, 2008). However, there has been no significant improvement beyond this value since then (Green et al, 2008). The evolution of the solar cells' efficiencies for several key technologies over the last 15 years is shown in figure 1.2 (Green et al, 2008). The monolithic III-V stacked concentrator cells have demonstrated the largest improvement in the last 15 years with efficiency increasing from below 30% up to 42.8%.

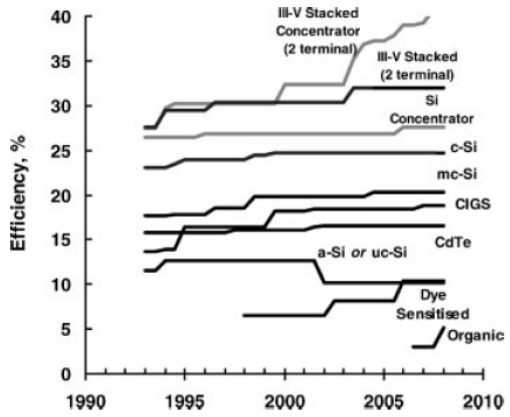

Figure 1.2 Evolution of solar cell efficiency from 1993 to 2006 for several major cell categories (Green et al, 2008)

Although significant advances in PV efficiency have been made in the past twenty years, high costs and low efficiencies remain barriers to wide scale adoption of PVs. The installation prices for single crystal and polycrystalline silicon modules are in the range of $2.90-$3.50 per Watt peak (Maycock, 2005). The main options to increase the adoption of crystalline silicon PV systems include:

- Reduction in the photovoltaic system cost, by development of low cost production methods for the PV modules and their materials.
- Improving the operational PV solar to electrical conversion efficiency. PV cooling can be achieved using systems, such as solar chimneys, low temperature solar thermal collectors and phase change materials with appropriate phase transition temperatures.
- Employing solar concentration. A smaller area of high efficiency solar cells combined with a low cost concentrator can reduce the cost of the PV system required to produce a given power output.

1.2 Solar to electric conversion

1.2.1 Progress in the development of crystalline silicon cells

The most common forms of photovoltaic cells are made of crystalline silicon. These consists of a p-type silicon base, an n-type silicon layer, front and back electrical contacts and a thin cover layer. A schematic of a silicon cell structure is shown in figure 1.3 (a) (Duffie and Beckman, 1991). When a photon of incident solar radiation is absorbed by an atom of n-silicon in the crystal lattice, if the energy of the photon is high enough, an electron from the outer shell of the n-silicon is released. When these layers are connected by an external circuit, electrons (i.e., a current) will flow through that circuit. Figure 1.3 (b) illustrates a silicon cell in a circuit (Duffie and Beckman, 1991).

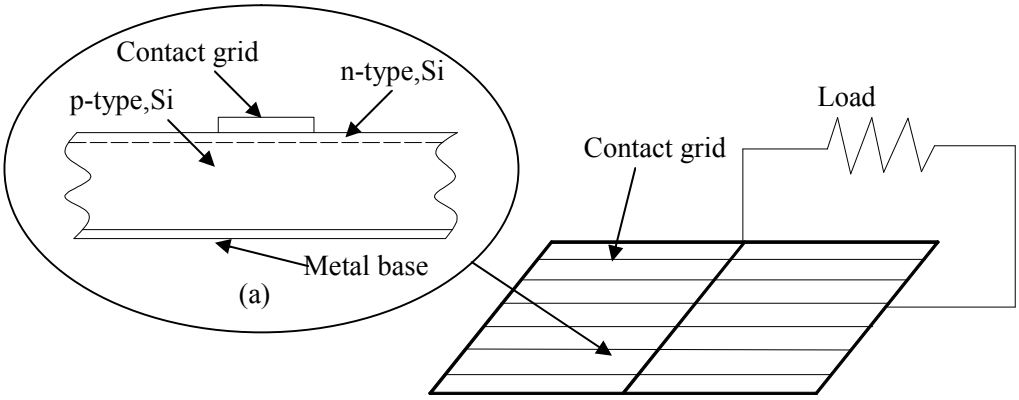

Figure 1.3 (a) Section of a silicon solar cell, (b) A schematic detail of a silicon solar cell, showing top contacts (Duffie and Beckman, 1991)

The energy of a photon is a function of the frequency of radiation (and thus also of the wavelength)

$$E = hv \tag{1.1}$$

Where h is Planck's constant $6.6256\times10^{-34}Js^{-1}$, v is the photon's frequency (Duffie and Beckman, 1991). There is a minimum energy level (at maximum wave length) of photons that can cause the creation of a electron-hole pair. For silicon, the maximum wavelength is 1.15μm, and the radiation incident at higher wavelengths that is absorbed is dissipated as heat.

The first commercial silicon cell structure was developed in the early 1970s and is shown in figure 1.4. The ingots are doped with boron to give a p-type material then phosphorus is lightly diffused on the top of the cell to form the p-n junction. The depth of phosphorus diffusion is quite small (~0.25 μm), it allows the photogenerated carriers, between the junction and the surface to have a better chance of being collected by the junction than recombining at the surface. A single anti-reflection layer (AR) of Titanium dioxide (TiO_2) or Tantalum pentoxide (Ta_2O_5) or a double layer anti-reflection coating of TiO_2 followed by Aluminium oxide (Al_2O_3) is deposited on the surface to reduce reflection losses (Gordon, 2001).

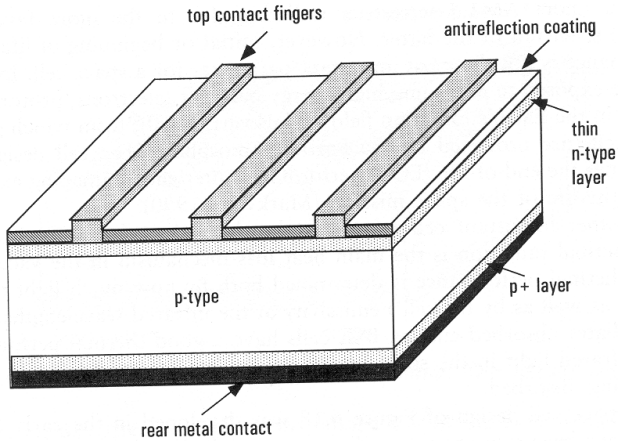

Figure 1.4 Sketch of the first commercial silicon cell (Gordon, 2001)

The Passivated Emitter Rear Locally-diffused (PERL) cell was subsequently developed as illustrated in figure 1.5. A pattern of inverted pyramids, the base of which are about 10μm wide, are used on the cell surface to minimize reflection of the incident light from the cells top surface (Gordon, 2001). When solar radiation is incident on the solar cell surface, most of the incident light is refracted obliquely onto the cell, and the remaining light is reflected downwards giving more chance of if being absorbed into the cell. The specific cell surface design also increases the proportion of incident light that is absorbed close to the active top surface (Green et al, 1999).

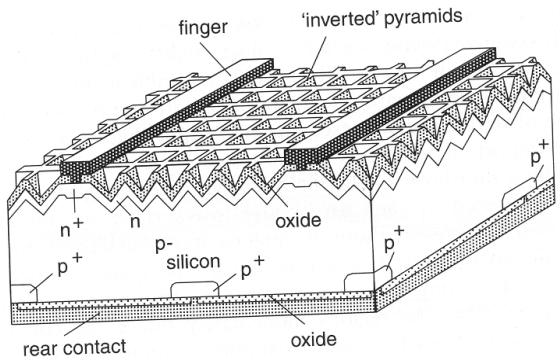

Figure 1.5 Sketch of the Passivated Emitter Rear Locally-diffused Cell (PERL cell) (Green et al, 1999).

The screen-printing approach to crystalline cell manufacture was first introduced to the market in the 1970s, and became the standard commercial production method in the early 1980s (Gordon, 2001). A sketch of a screen-printed crystalline cell is shown in figure 1.6 (Green, 2000). Chemical etching is used to give the random layout of upright pyramids which reduce the incident light reflection losses at the cells surface (Green, 2000). The screen-printing silver pastes are applied at the top and rear contacts. Phosphorus is often added to reduce contact resistance in the top surface pastes (Gordon, 2001.)

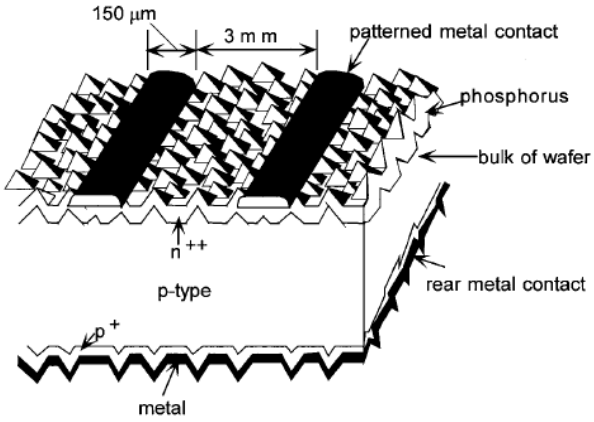

Figure 1.6 Sketch view of the screen-printed crystalline cell (Green, 2000)

Special technologies have been developed for high-efficiency solar cells that improve contact features and minimise reflection losses at the cell surface. The laser grooved buried contact solar cell was invented by Wenham and Green at the University of New South Wales, Australia in 1985 (Mason et al, 2004). Following the early development of the technology in Australia (1986-1989), the project moved to BP solar in Madrid, Spain in 1990 (Mason et al, 2004), and then BP solar developed and marketed this technology for commercial production. A sketch of a laser grooved buried contact solar cell is shown in figure 1.7. The cells have a textured front surface to reduce light reflective loss. The incident light is reflected and refracted several times at the surface of the upright pyramids. Laser grooving narrow buried contacts which reduce line width shading are applied to the front surface. The specifically selected n-type emitter optimizes the maximum current collection from blue light absorption in the surface n^+ layer. There are lower resistance losses between the silicon (n^{++} layer) and the buried conductor.

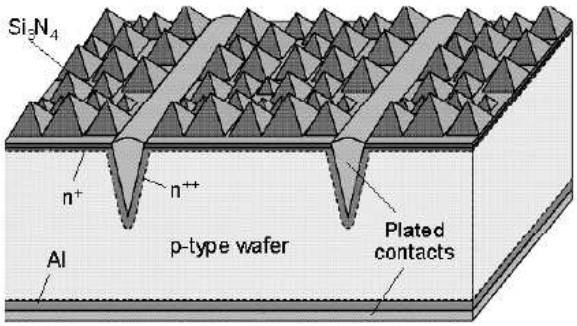

Figure 1.7 Sketch view of the laser grooved buried contact solar cell (Mason et al, 2004)

1.2.2 Thin film solar cells

The application of photoactive semiconductors in thin layers to a substrate is called thin film processing. Since the 1990s, this method of manufacturing solar cells has become increasingly important, because it can lead to reduced processing costs compared to that using bulk materials (Anon, 2005a). There are three main semiconductor materials: amorphous silicon, Copper Indium Diselenide (CIS) and Cadmium Telluride (CdTe) that are used due to their high light absorption properties, achieving a sufficient electrical conversion efficiency even in a layer having a thickness of less than 0.001mm.

1.2.2.1 Amorphous silicon cells (a-Si)

Amorphous silicon (a-Si) differs from crystalline silicon in that the silicon atoms are located at various distances from each other, and the angles between the Si-Si bonds do not have a unique value (Markvart, 1994). Pure amorphous silicon has poor electronic properties. It was found in 1969 that by the incorporation of hydrogen in amorphous silicon significant photoconductivity was exhibited and this material could be doped n-type or p-type (Gordon, 2001).

When p-n junctions have been made in a-Si, it was found that both p and n material had poor transport properties, and simple p-n junction cells had low efficiencies. The p-i-n junction cells shown in figure 1.8 was subsequently developed to improve the poor transport properties. Instead of the grid contacts used in crystalline silicon cells, a transparent conducting contact is deposited as a thin film at the surface of the p+ layer and a metal contact is located at the rear of the cell. Tin oxide is usually used for the transparent conducting material (Markvart, 1994).

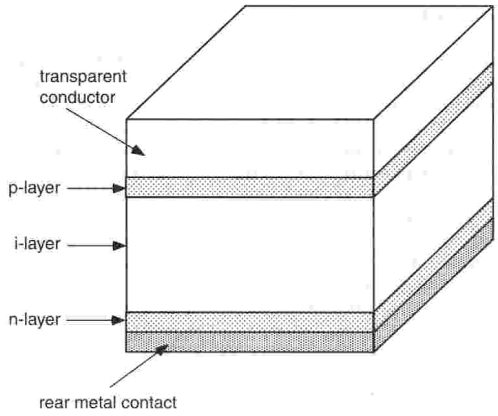

Figure 1.8 Amorphous silicon p-i-n solar cell structure (Markvart, 1994)

1.2.2.2 Copper Indium Selenide cells (CIS)

Elements from group I, III, VI in the periodic table are of interest for photovoltaic applications, and are especially attractive for thin film solar cell application. CIS is an abbreviation for general copper iron sulfates mineral films of copper indium selenide ($CuInSe_2$) which can achieve an electrical conversion efficiency greater than 14% (CIS films, no gallium) (Anon, 2005a). The CIS compounds alloyed with gallium and sulphur are called CIGS and have demonstrated solar to electrical conversion efficiencies of 19.9% (Green et al, 2008). However, manufacturing costs of CIS and CIGS solar cells are at present high when compared with amorphous silicon solar cells (Anon, 2005a).

1.2.2.3 Cadmium telluride cells (CdTe)

CdTe solar cells are often manufactured on a glass substrate with a transparent conduction layer and an indium tin oxide (ITO) coated front contact cover. That is usually sandwiched with Cadmium Sulphide (CdS) to form a p-n junction photovoltaic solar cell. Typically, CdTe cells use a n-i-p structure. Simple manufacturing processes such as screen-printing, galvanic disposition or spray pyrolysis can be used to produce the CdTe cells. Large-scale modules can be achieved through a vapour deposition process. CdTe can achieve an electrical conversion efficiency of approximately 14% (Green et al, 2008).

1.2.3 III-V semiconductor solar cells

III-V semiconductors such as GaAs, GaAlAs, InSb and InP have received increasing attention as photovoltaic materials. The III-V cells have a solar-electrical conversion efficiency higher than 30%, which is higher than that of Si cells (Green et al, 2008). The disadvantage of using the III-V compounds in photovoltaics devices is that they use rare materials and have high production costs (Miles et al, 2005).

Unlike the single junction cells, when the photon energy exceeds the bandgap of the solar cells, the photon energy is lost as heat. The multi-junction III-V solar cells have a number of junctions with a range of different bandgap values suitable for utilising a range of photon energies available in the solar spectrum. They have the potential to significantly increase the cell solar to electrical conversion efficiency. Multi-junction (MJ) III-V solar cells were first reported in the 1950s (Miles et al, 2005). Herry (1980) indicated that a predicted theoretical efficiency of 72% could be achieved for a MJ cell with 32 bandgaps. Green et al

(2008) reported that a multi-junction cell GaInP/GaAs/Ga tested at NREL had an efficiency of 42.7% under a concentration at 325 suns.

1.2.4 Dye sensitised and organic cells

The basic material of a dye sensitised cell is the semiconductor titanium dioxide (TiO_2). Dye-sensitised cells have a different mode of function compared to p-n junction cells. Absorption occurs at a very specific location in the dye molecules which are attached to a porous titania medium (Green, 2002), This is similar to the way plants use chlorophyll to capture energy from sunlight through photosynthesis (Anon, 2005a). The materials used are non-toxic and inexpensive to produce. Dye sensitised cells are tolerant to poor incidence angles and shading with solar to electrical conversion efficiency increasing at higher temperatures in contrast to crystalline silicon cells. The highest reported dye sensitised cell efficiency achieved to date was 10.4% by the AIST test centre (Green et al, 2008).

Because of the compatibility of solution-processible organic semiconductors with printing-based manufacturing and low cost flexible substrates, organic cells offer a significant potential for solar-electric systems in the future. Molecular and polymeric semiconductors and fullerene (C60) and its derivatives are interesting materials for the development of organic cells (Miles et al, 2005). Significant progress has been made in improving the performance of organic solar cells in recent years, however, they still do not meet the requirements for practical applications. The highest achieved efficiency reported for organic cells to date by NREL is around 5.15% (Green et al, 2008).

1.3 Building Integrated Photovoltaics (BIPV)

In Building Integrated Photovoltaics (BIPV) systems, instead of mounting PV modules on separate supporting structures, they are directly mounted onto the building or integrated into the building structure (Oliver and Jackson 2001). They can be installed in retrofit or new buildings and have become a popular way to use solar energy to generate electricity. Examples of BIPV systems are as follows (Bloem, 2008),

- PV modules used to replace roofing tiles.
- PV modules used to replace rainscreen cladding and curtain walling.
- PV cells or modules mounted onto building to form external shading devices.

1.3.1 Building rooftop mounted or integrated PV systems

Roofing PV systems account for more than 70% of the total BIPV installation as shown in figure 1.9 (Yang and Li, 2007). They perform the same function as a standard roof by providing water tightness, drainage, and insulation. They can either be mounted onto a flat roof or can replace the roof tiles as shown in figure 1.10(a) (Cooperative Community Energy, 2009). Some of the roofing PV systems are retrofitted and do not replace the roof tiles but are mounted onto existing roofs as shown in figure 1.10(b) (Cooperative Community Energy, 2009).

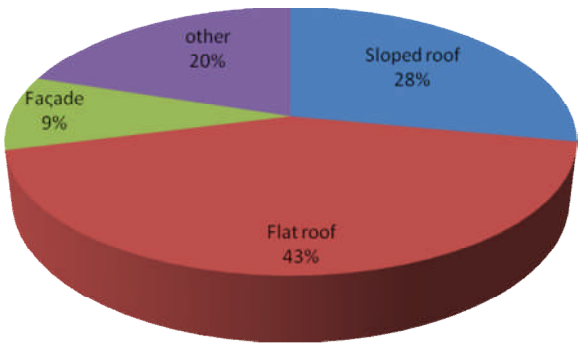

Figure 1.9 The BIPV system by integrating or mounting building structure (Yang and Li, 2007).

(a)

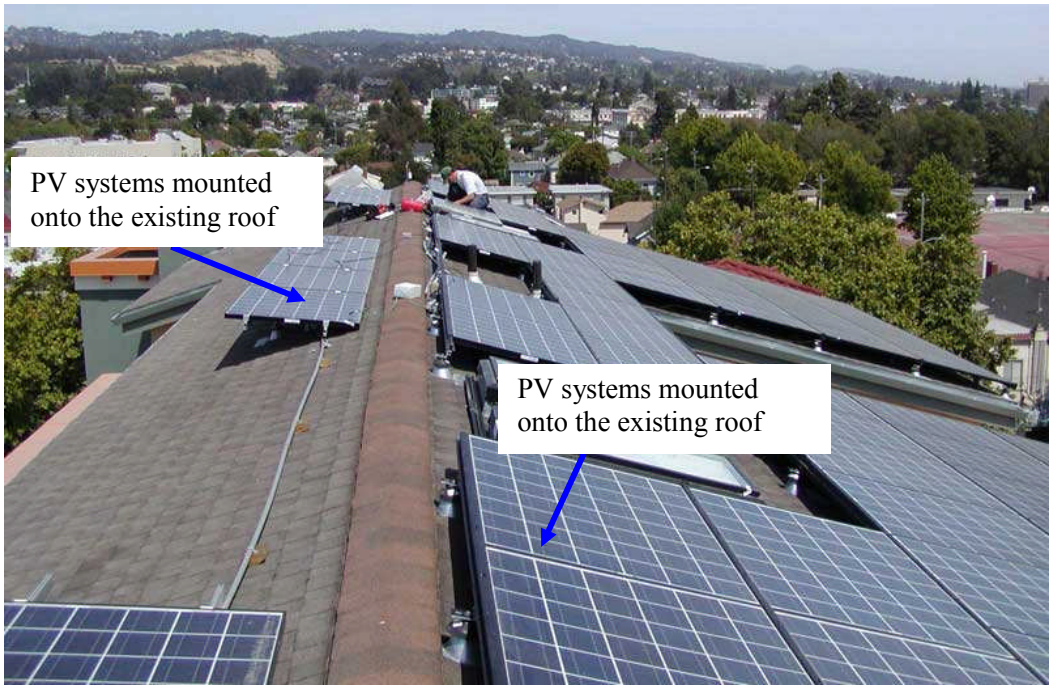

(b)

Figure 1.10 (a) Building roofing PV systems, (b) PV system mounted on existing sloped roof (Cooperative Community Energy, 2009).

For roofing PV systems, semi-transparent PV modules can be used as glazing to replace skylights as shown in figure 1.11. Building roofs with semi-transparent PV modules may benefit from the advantage of increased indoor illumination and natural space heating during winter. However, problems such as summer overheating and glare could occur if inappropriately designed (Wong et al, 2008).

Figure 1.11 Semi-transparent PV module installed in a building roof as skylights (Cooperative Community Energy, 2009).

1.3.2 Building façade integrated PV systems

Photovoltaic systems can be integrated into the building façade as structural curtain walling systems as shown in figure 1.12(a). Building windows need some methods for solar or daylight gain control which is often achieved with interior curtains or blinds, however, the solar gain still reaches the indoor space and the view to outdoors is restricted or eliminated. PV systems integrated into the building façade as a structural glazing curtain walling systems provides both solar radiation collection and filtered light to the building interior

space as a viable alternative (Ayoub et al, 2001). Figure 1.12(b) illustrates the PV systems mounted onto a vertical building façade creating a BIPV system which provides protection for the building from the weather.

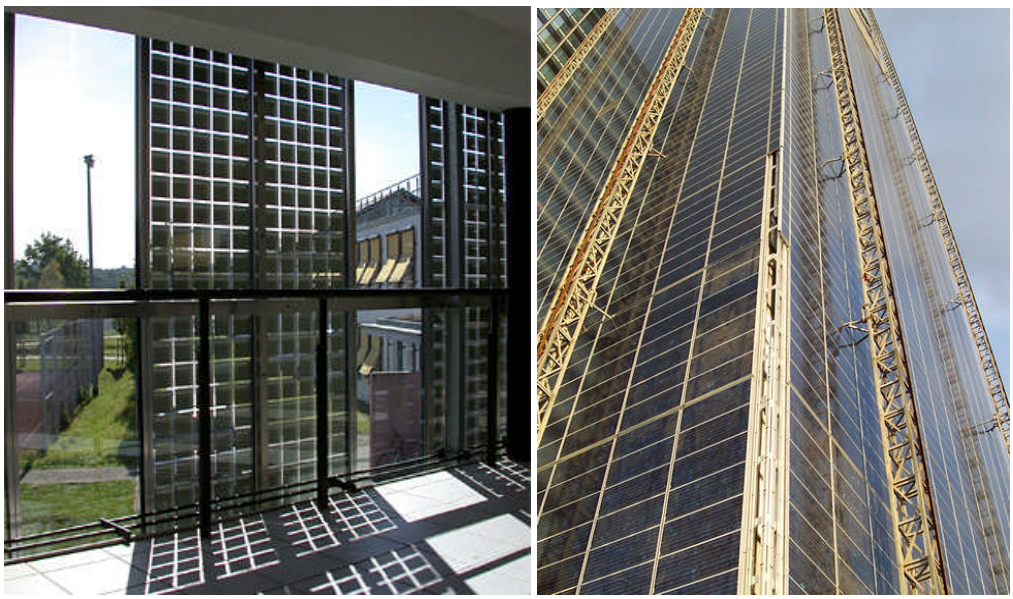

(a) (b)

Figure 1.12 (a) PV system integrated into the vertical wall replacing the glazing curtain walling, (b) PV system mounted onto the vertical wall providing weather protection (Cooperative Community Energy, 2009).

BIPV systems have lots of advantages which are summarised as follows (Oliver and Jackson 2001):

- PV systems integrated into or mounted onto buildings avoid the cost of land acquisition, fencing, and reduce the cost of the major support structures generally required for PV modules.
- Cabling costs can be reduced, because buildings are normally connected to the grid.
- The cost and the loss associated with transmission and distribution of electricity are avoided, because the electricity is produced at or near the point of use.
- PVs integrated into the building structure protect the building from the weather and displace the use of other building materials.

1.4 Improving PV performance by heat removed

The effect of temperature on silicon PV module efficiency is indicated in figure 1.13, where typical current/voltage curves are plotted for various module temperatures. The standard characterising temperature for PV cells is 25°C. As the module surface temperature rises above 25°C, the maximum voltage output decreases, and the subsequent output power also decreases (Anon, 2005a). In bright conditions with incident solar radiation of approximately 800W/m^2, photovoltaic module operating temperatures can exceed 75°C (Brinkworth et al, 1997). PV cooling reduces the reduction in performance caused by increased temperature. A range of cooling methods are available to reduce PV module temperatures and thus increase solar to electrical conversion efficiency.

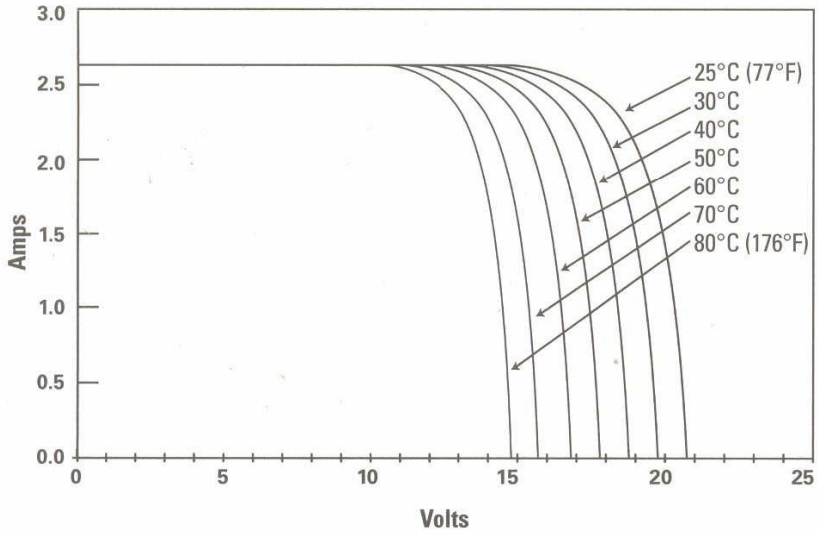

Figure 1.13 Effect of cell temperature on crystalline PV module performance (Anon, 2005a)

1.4.1 Passive air cooling of PV system

A solar chimney (duct) which can be constructed into the façade of a building is able to enhance the natural ventilation of that building. It usually consists of positioned glazing in front of a cavity and a massive wall which absorbs solar radiation (Miyazaki et al, 2006).

The transparent glazing can be replaced by a glass laminate PV panel which allows solar radiation incident on the wall to heat the wall and to induce buoyancy driven convection, leading to a solar chimney effect which cools the PV. As the temperature of the air in the chimney increases, an air density gradient forms between the air inside and outside the chimney, which causes a natural upwards movement of the air (Bansal, 2005).

Cross (1994) undertook the design, characterisation and commercialisation of a roof mounted PV system cooled by a rear air duct. It was first tested indoors using a solar simulator prior to installation on a building in Oxford. During the indoor experimental characterisation, it was found that the temperature difference was approximately 43°C between the top and the bottom edge of the 5m long roof mounted PV systems at a solar radiation intensity of 800W/m^2. Yang et al (1996) built an indoor PV wall test rig with a ventilation structure at the rear of the wall. With ventilation at the rear surface of the PV cell, its temperature was reduced by 15°C and power output was increased by 8% compared to a PV wall with no ventilation structure. Brinkworth et al (1997) conducted a comparison between Computational Fluid Dynamics (CFD) predictions and Laser Doppler anemometry (LDA) measurements for the air flow rate in a duct mounted behind a PV panel. A schematic sketch of the PV wall and roof system is shown in figure 1.14. In the proof-of-concept study, it was indicated that although the air velocities induced in the duct were very low around 0.2m/s, the rear duct effectively reduced the temperature rise experienced by the PV. When the solar radiation was 800W/m^2 and ambient temperature was 25°C, the top-most PV cells had a temperature of 80°C with the rear duct open and a temperature of 106°C with the rear duct closed. The predicted airflow rate flow was well validated by the experimental LDA measurements. Brinkworth et al (2000a) carried out a simplified method

using one-dimensional 'loop analysis' where the buoyancy forces were balanced by the pressure drops due to friction to estimate the mass flow rate and temperature rise in naturally ventilated BIPV. Brinkworth (2000b) also set out a mathematical calculation procedure for determining the air flow and convective heat transfer in inclined cooling ducts used in PV installations. It included local wind effects or buoyancy condition domination, or both conditions occurring together. Brinkworth and Sandberg (2006a) and Brinkworth (2006b) reported an optimum value of PV duct design, such that when the L/D (L was the length of PV array at the front surface of the duct, D was the hydraulic depth of the duct) ratio was about 20, the minimum PV temperature was obtained. They also indicated this value was not significantly affected by the slope of the PV array.

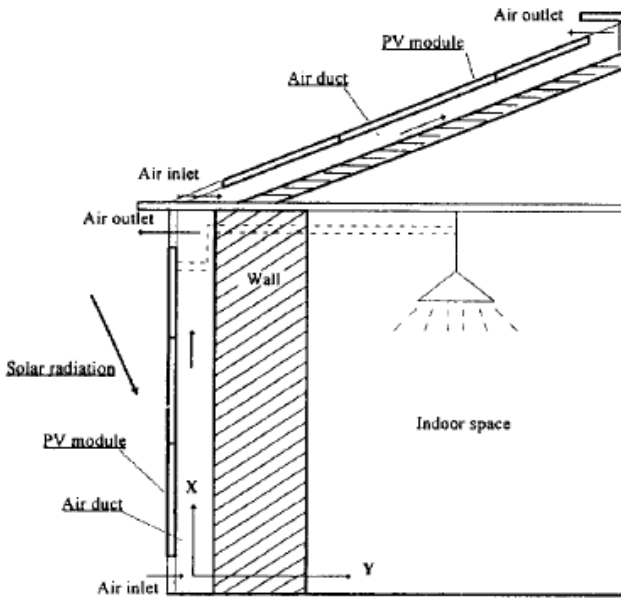

Figure 1.14 Schematic diagram of a generic PV wall and roof (Brinkworth et al, 1997)

Bouchair (1994) built a 2m high solar chimney together with a cubic room (Dimension 3m×3m×3m). He suggested that if the height of the solar chimney was less than 2m, the relationship between the optimum width and the height of the solar chimney is that given in equation 1.2. In this way, the maximum inlet air flow rate can be obtained. With a higher

chimney, the optimum width would be wider. Gan and Riffat (1998) confirmed Bouchair's optimum relationship of width and height of a solar chimney through experimental measurements and CFD predictions.

$$W_{optimum} = H/10 \tag{1.2}$$

Where the $W_{optimum}$ is the optimum width of a solar chimney, and H is the chimney height.

Moshfegh and Sandberg (1998) used both CFD predictions and experimental measurements as complementary techniques to analyse the performance of air flow and heat transfer in an air gap behind PV panels. A 7m high solar chimney was built, and heat fluxes at values of 20W/m^2, 300Wm^2 and 500W/m^2 were investigated on the surface walls. The results showed that the air's velocity and temperature increased with increase in the heat flux from the heated wall. The PV panel surface temperature increased rapidly along the height of the channel. The separation effect close to the lower edge of the heated wall caused instability in temperature values at the lower part of the heated wall. When the heat flux was 500W/m^2 on the wall, the surface temperature at the top edge of the heated wall was about 63°C. The temperature difference between the top and the bottom edges of the heated wall was around 40°C. Jensen (2001) undertook research into PV combined with a solar chimney system. The chimney was 3m high, and had an air gap of 0.16m behind the PV panel. The measured temperature of the PV panel was often higher than 50°C due to the low air velocity.

Gan and Riffat (2004) investigated the use of natural ventilation to cool roof-integrated photovoltaics in an atrium by experimental measurements and CFD predictions of thermal behaviour. After validating the CFD model, it was used to predict the air flow and

temperature distribution in the atrium. Two openable glass screens functioned as air vents in the south and north walls. A schematic sketch of the atrium is shown in figure 1.15. The fresh air flowed into the atrium from the inlet opening in the south façade. The measured inlet temperature was 14.8°C, the mean temperature of the atrium was 21.6°C and the average PV temperature was 24.6°C for 153.1W/m^2 incident solar radiation. The same boundary conditions were used in the CFD modelling, the predicted average PV temperature was 29.1°C which was significantly higher than the measured result, this was determined to be due to an overestimation of the solar radiation absorbed by the PV. After using the average absorptivity of the roof glazing and the PV arrays, the predicted average PV temperature was reduced to 26.8°C which is much closer to the measured results. This indicated that for validation of CFD models, accurate PV cell solar radiation absorption data and other boundary conditions are required. They also used the CFD model to predict the effects of modifying the opening glazing position, size and inlet air velocity to optimize the PV cooling effect. Their predictions indicated that PV arrays installed in this glazing could not be cooled effectively due to the negative buoyancy effect consequent of the original opening position. Moving the air inlet closer to the roof increased the effectiveness of cooling of the PV arrays while not compromising the thermal comfort in the occupied zone of the atrium space.

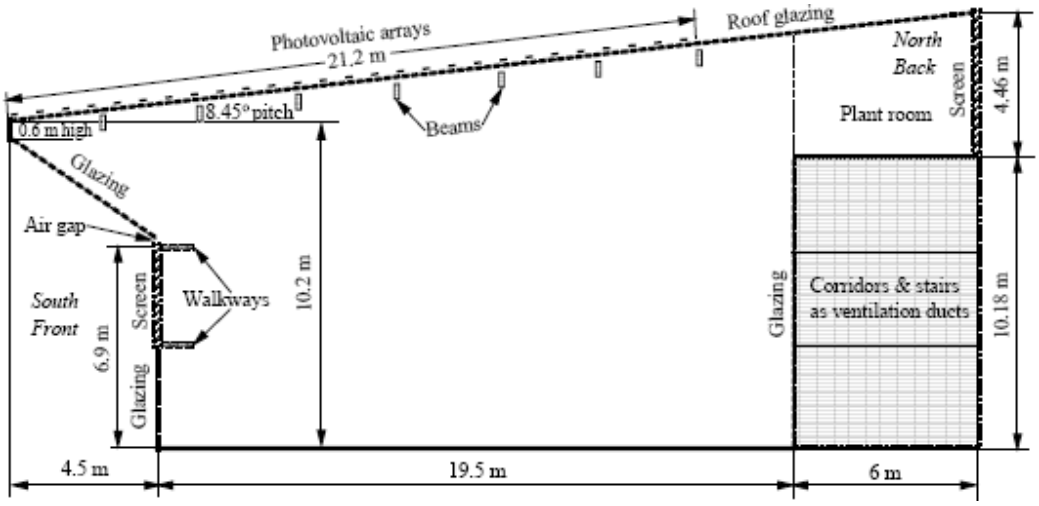

Figure 1.15 Schematic diagram of the atrium cross-section (Gan and Riffat, 2001)

1.4.2 Cooling by coupling to a solar thermal collector

PV and solar thermal collector systems can be combined into one system with the solar thermal collector used to absorb heat from the PV thereby reducing its temperature, and increasing the electrical conversion efficiency. In this way, both thermal energy and electricity are obtained from a PV-Thermal collector (PV-T).

There are two main types of combined PV-T system,

a) The air PV-T system is shown in figure 1.16(a) (Sørensen and Munro, 2000), where the photovoltaic panel is combined with a solar air heating collector which is typically used to preheat the air used for building ventilation.

b) The liquid PV-T system shown in figure 1.16(b) (Tripanagnostopoulos et al, 2002), where the photovoltaic panel is combined with a solar water heating collector. The liquid PV-T systems always have a higher efficiency than the air PV-T collector system, due to the liquid having a much higher heat capacity than the air, however,

an additional cost is incurred in the inclusion of the fluid flow system and thus protection from leaking and freezing (Zondag and van Helden, 2003).

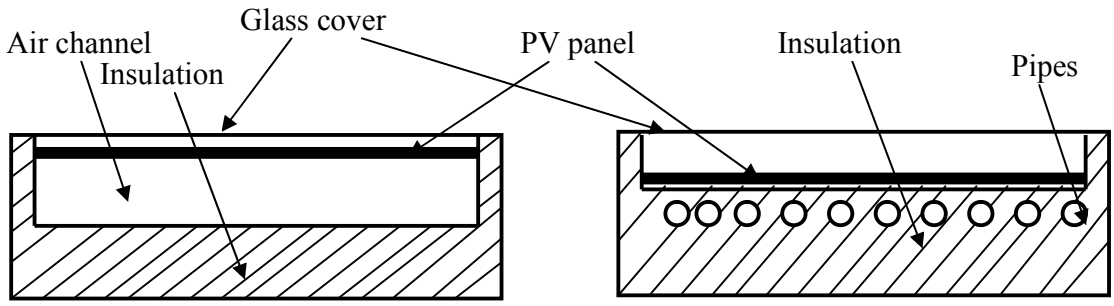

(a) Air PV-T system (b) Water PV-T system,

Figure 1.16 Cross-section view of air and water PV-T systems (Tripanagnostopoulos et al, 2002)

The thermal, electrical and overall system efficiencies of the PV-T system are defined as follows (Agarwal and Garg, 1994, Zondag et al, 2003, Tonui and Tripanagnostopoulos, 2007).

Thermal efficiency:

$$\eta_{th} = \dot{m} c_p \frac{(T_{out} - T_{in})}{GA} \tag{1.3}$$

Electrical efficiency:

$$\eta_{el} = \frac{V_{MPP} I_{MPP}}{GA} \tag{1.4}$$

Overall system efficiency:

$$\eta = \eta_{th} + \eta_{el} \tag{1.5}$$

V_{MPP} and I_{MPP} represent the voltage and the current at the maximum power point, A is the PV panel working area, c_p is the heat capacity of the collector medium, $\dot{m}$ is the mass flow rate, G is the irradiation, T_{in} and T_{out} are the inflow and outflow temperatures.

Hendrie (1980) predicted the thermal and electric performance of an air and a liquid PV-T system with maximum predicted thermal efficiencies of 32.9% and 40.4%, respectively. Bhargava et al (1991) studied the thermal and electrical performance of a combined air thermal collector and photovoltaic system in India. Agarwal and Garg (1994) conducted both experimental tests and numerical simulations for a PV-T system with a cylindrical water storage tank (Dimension 1.5m long by 0.36m diameter). The PV-T and water tank were installed at New Delhi, India, and the experiments were carried out on the 31st March, 14th May and 30th August 1988. The maximum obtained storage temperature was 69.2°C on the 14th of May 1988. They also indicated that there was little difference in the maximum storage temperature, when the PV/T system surface was fully covered with solar cells compared to the surface with no solar cells, and Garg and Agarwal (1995) also undertook a finite difference based simulation to find the thermal and electrical performance of a liquid PV-T system with a water storage tank for different areas covered by solar cell, different system inlet mass flow rates and different storage water masses. They used meteorological data recorded on the 11th May 1988 and 22nd January 1989, in New Delhi, India. Sopian et al (1995) presented a steady state model to predict the thermal performance of single-pass and double pass Photovoltaic systems combined with air thermal collectors shown in figure 1.17. Their results indicated that the double pass PV-T system had a higher thermal and electrical conversion efficiency than the single pass PV- T system for the same simulation conditions.

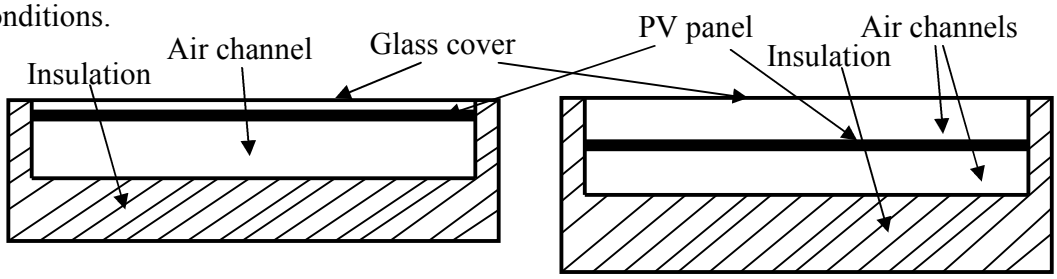

(a) Single pass air PV-T system (b) Double pass air PV-T system

Figure 1.17 Cross-section view of single and double pass PV-T systems (Sopian et al, 1995)

Garg and Adhikari (1997) undertook a performance analysis of a conventional hybrid photovoltaic thermal air heating collector using numerical modelling. They found that the double-glass configuration had a better thermal performance than the single-glass system, due to the reduction in convective and radiative losses from the absorber to the ambient environment. The single-glass configuration however had higher PV electrical conversion efficiency than the double glass configuration at the same incident solar radiation and ambient temperature, this was due to the addition of an extra cover increasing the transmission losses. Garg and Adhikari (1998a, 1999a) developed a computational model for predicting the transient performance of a conventional PV-T air heating collector using typical climate data for New Delhi, India. Tripanagnostopoulos et al (2002) indicated that for a hybrid polycrystalline silicon PV module and water thermal collector system, the total cost increase was about 8% compared to a plain polycrystalline silicon PV module used as the base element. When the cost of external pipes and other components required for water circulation were included, the total cost increase was about 10%. In hybrid systems with heat extraction by air, the estimated total cost increase was about 5% in comparison with a plain polycrystalline silicon PV module, and about 8% if the system included a forced air circulation system. The measured experimental solar cell temperatures and electrical conversion efficiencies for different PV-T and PV stand alone systems are presented in Table 1.2. It can be seen there are no significant PV module temperature differences for the water PV-T, air PV-T and the PV stand alone (both surfaces free to ambient) systems. The electrical efficiency of the air PV-T system increased by 1.6% compared with that of the PV stand alone-1 system. An increase of 3.1% was measured for the water PV-T system compared with the PV stand alone system-1. The obtained gain in electrical efficiency for

the water and air PV-T systems was lower than the additional systems cost. The main advantage of using a PV-T system was the achieved thermal output.

System type	Ambient temperature	Inlet medium temperature	PV module temperature	Electrical efficiency
Water PV-T system	29°C	21°C (Water)	38°C	12.8%
Air PV-T system	29°C	29°C (Air)	41°C	12.6%
PV stand alone module -1 (With both surface free to ambient)	29°C	N/A	43°C	12.4%
PV stand alone module -2 (With rear insulation)	29°C	N/A	55°C	11.3%

Table 1.2 Measured inlet air/water temperature, PV module temperature and electrical conversion efficiency for different PV-T and PV stand alone systems (Tripanagnostopoulos et al, 2002).

Aste et al (2002) designed a prototype PV-T air heating collector shown in figure 1.18. The prototype PV system consisted of two BP SX 60 photovoltaic modules and one BP 120 photovoltaic module. A 75mm deep and 1065mm wide air duct was installed behind the photovoltaic modules. During outdoor experimental tests on the 17th of May 2002 in Milan, Italy, a PV electrical conversion efficiency of approximately 10% was measured with incident solar radiation of 850W/m^2 at around 13:00 o'clock, with a measured PV module temperature of 52°C. They also obtained overall system efficiencies (thermal + PV) varying from 20 to 40% during May 2002. The PV efficiency for the crystalline silicon was about 10-12%, with the remaining contribution from the thermal system.

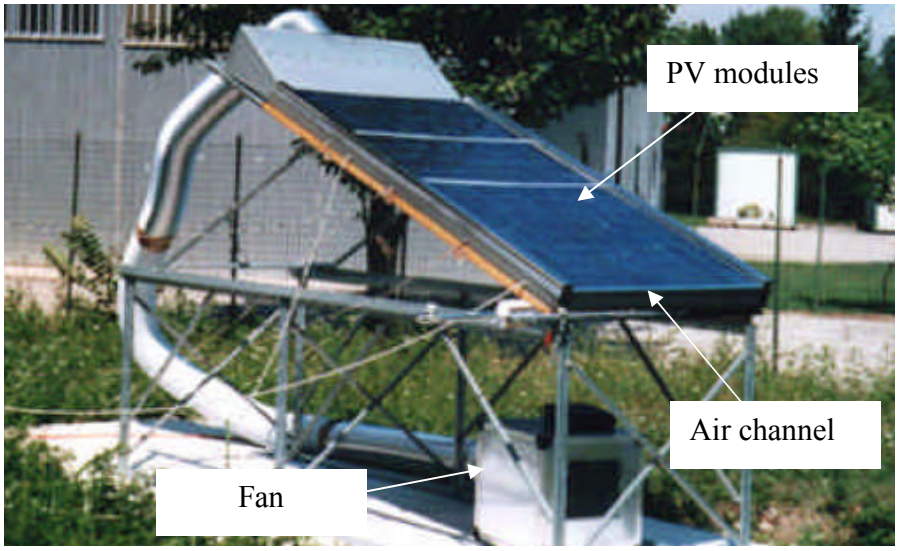

Figure 1.18 A prototype of an air PV-T system (Aste et al, 2002)

Bakker et al (2004) indicated that the thermal efficiency of a PV-T system can be increased by increasing the number of glazing aperture covers on the PV-thermal collector system. However this sacrifices the solar to electrical conversion efficiency. Uncovered PV/ Thermal Collector systems are cheaper and have a higher electrical yield, but a relatively low thermal performance. Tonui and Tripanagnostoploulos (2007) studied two designs to improve the overall performance of a typical single-pass air PV-T system. One improvement was to insert a suspended thin flat metallic sheet at the middle of the air duct (called TMS system); another design installed fins at the back wall of the PV-T system (called FIN system). They found that the thermal efficiency of the TMS and FIN system were increased by 12% and 20% respectively, compared with that of a PV-T system with no fins for the same experimental conditions.

1.4.3 Temperature control by integrating Phase Change Materials (PCM) in the PV module

A Phase change material (PCM) is a material that on undergoing phase change absorbs or releases latent heat at a relatively constant temperature. Phase change materials can be broadly grouped into two categories: organics and inorganics. Organic phase change materials can be further divided into paraffin and non-paraffin organics (Pal and Joshi, 1999). Paraffins and waxes are obtained from refining crude oil. The general chemical formula for them is C_nH_{2n+2}. Non-paraffin organics include a wide range of materials such as fatty acids, esters, alcohols etc. Inorganic PCMs are components of hydrate salts (M_nH_2O), such as sulphate pentahydrate (Glauber's salt), and mixtures of eutectic-hydrate salts (Ure, 1998). When a PCM undergoes a solid to liquid phase change, the energy absorbed by the PCM can be determined from equation 1.6 (Duffie and Beckman, 1991).

$$Q_s = m[C_{so}(T_m - T_i) + \lambda + C_{li}(T_e - T_m)] \quad (1.6)$$

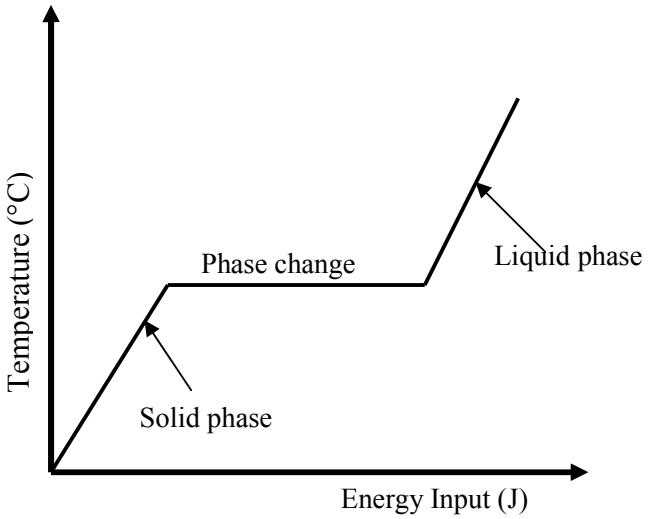

Figure 1.19 Energy and temperature relationship for a PCM heating or cooling process (Huang, 2002)

Phase change materials can provide temperature stabilisation when undergoing phase transition as shown in figure 1.19. They can be used in two main ways; temperature control or thermal energy storage (Pal and Joshi, 1999), however, the direct use of phase change materials for temperature control and energy storage is limited due to the low thermal conductivity of the material, and also the effect of solidification at the heat transfer surface which can lead to a drastic reduction in heat transfer when energy is extracted from the liquid phase (Griffiths and Eames, 2007).

Siegel (1976) undertook a simplified analysis to determine the heat transfer enhancement provided by the addition of high conductivity particles into a low conductivity salt, which neglected subcooling energy and assumed that particles inside the container retained a uniform distribution during both freezing and melting cycles. It was determined that the embedded particles increased the thermal conductivity in both the melting and solidifying processes. Particles occupying 20% of the storage by volume increased the heat extraction rate by 10% to 20% depending on the ratio of particle to matrix conductivity. Pal and Joshi (1999) conducted a study of organic phase change materials (n-Triacontane) contained in a porous aluminium matrix enclosed inside a shallow container, with a volume of 76.2mm × 76.2mm × 25.4mm as illustrated in figure 1.20. Thermocouples were connected at the top and bottom of the cavity. A constant power input was provided by a heater element mounted underneath the container. The experimental results for the container without PCM, with n-Triacontane and with n-Triacontane incorporated in an aluminium foam are shown in table 1.3. It can be seen that the phase change material provides viable thermal management particularly if the thermal conductivity of the PCMs is enhanced by using aluminium/ metal foams or other techniques.

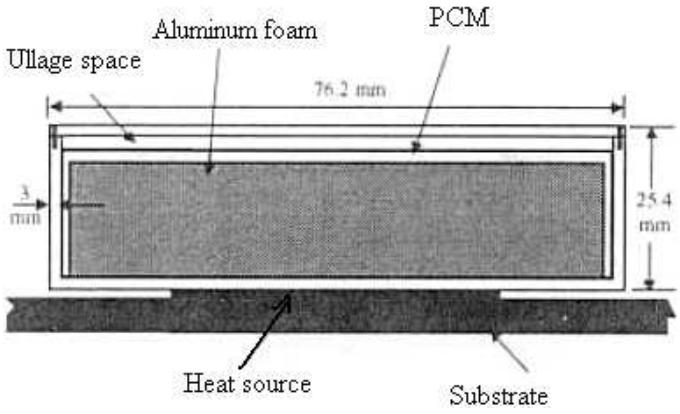

Figure 1.20 Cross sectional view of the heat sink (Pal and Joshi, 1999)

System type	Input power	Results
Container	10W	Heater surface temperature reached 100°C after 25 minutes
Container with n-Triacontane	10W	Heater surface temperature <100°C for 110 minutes
Container with n-Triacontane incorporated aluminium foams	10W	Heater surface temperature <90°C for 250 minutes

Table 1.3 Measured experimental results for selected container(Pal and Joshi, 1999)

Cabeza et al (2002) undertook experimental tests to study heat transfer enhancement into PCM for a small thermal energy storage device using stainless steel fins, copper fins, or a graphite composite material. It was concluded that the addition of stainless steel fins in the PCM did not increase the heat flux significantly, the addition of copper pieces enhanced heat transfer especially during the melting process. The utilisition of a graphite composite obtained the highest heat transfer flux of the three methods, and increased the heat transfer by a factor of four times compared with that of pure PCM. Stritih (2004) applied experimental studies to heat transfer in a rectangular PCM thermal storage system. The thermal storage system had dimensions of 650mm × 500mm × 120mm. RUBITHERM RT 30 paraffin having a melting point of 30°C was used in the investigation. Comparisons of

PCM melting and solidification with fins and without fins were made. The heat transfer during solidification was greater if fins were included, and a 40% reduction in the solidification time was obtained.

Huang et al (2004) undertook both experimental tests and numerical simulations to study the thermal behaviour of PV/PCM systems. The numerical simulations were well validated by the experimental measurements. The PCM RT25, having a melting temperature of 26.6°C was used in their experimental work. Comparisons were made for three different systems, a single flat aluminium plate system, a PV/PCM system without internal fins and a PV/PCM system with internal fins. All configurations had the same size of front aluminium plate, 0.3m long by 0.132m high. The applied solar intensity was 750W/m^2 at the front surface for all systems. After 60 minutes, the front surface temperature of the single plate system was steady at 63°C. The front surface of the PV/PCM system without fins maintained a temperature of around 36°C for the elapsed time between 50 and 100 minutes, and then slowly increased to 44°C at 280 minutes. The front surface of the PV/PCM system with two fins maintained a temperature of around 32 to 33°C for the elapsed time from 50 to 100 minutes, and sharply increased to 38°C at 170 minutes. It was concluded that the fins enabled a more uniform temperature distribution within the PV/ PCM system to be maintained. Simulations indicated that for a south east orientated PV/PCM system with a 30mm depth and no fins in the PCM container, the front surface temperature could be maintained at less than 35°C for UK weather data for the 21st of June repeated for three consecutive days. Huang et al (2006a) conducted an experimental evaluation of PCMs for PV cooling. It was found that RT25 had a better thermal control potential than GR40 for the PV panel. They also conducted experimental tests on embedding different numbers and

types of fins in the PCM to improve the effect of thermal management of PVs. Huang et al (2006b) investigated and analysed numerical simulations of encapsulated PCM materials incorporated into the gypsum wallboards of buildings for indoor comfort application. Huang et al (2006c) reported the development of a three-dimensional numerical model which they used to simulate a phase change material container linked to a PV system used to control the temperature rise of the PV cells.

1.5 Improving PV performance and reducing cost by optical concentration

PV concentrator systems increase the solar radiation intensity on photovoltaic cells and may reduce the total system cost, if the cost of the assembly material of the concentrator system is less than the photovoltaic cells displaced (Rabl, 1976a, Winston et al, 2005). PV concentrators can be either reflective, refractive or a combination of both. They are generally classified into two types: those that use a mirror such as parabolic trough, parabolic dish or compound parabolic reflector, and those that use such as Fresnel lenses.

1.5.1 Fresnel lens PV concentrator

A schematic sketch of a Fresnel lens PV concentrator shown in figure 1.21 illustrates how a Fresnel lens concentrator can focus sunlight onto a small area. Salim and Eugenio (1990) reported the performance of a 350kW Fresnel lens PV concentrator system located about 45km northwest of Riyadh, the capital city of Saudi Arabia. They concluded that this large PV system was a reliable source of power with minimum operation and maintenance requirements.

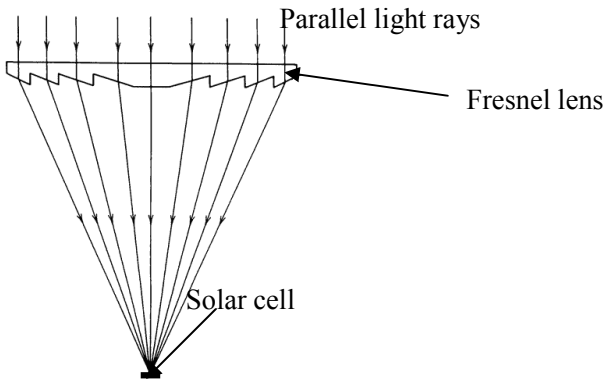

Figure 1.21 A schematic diagram of a Fresnel lens PV concentrator (Ryu et al, 2006)

Nabelek et al (1991) analysed the optical performance of a linear Fresnel lens manufactured from glass. It was found that the glass Fresnel lens had a concentration ratio of less than 10, and an effective transmissivity of less than 0.75, due to the physical properties of the glass and the rough edges of the grooves in the Fresnel lens that scattered the incident light. They also discussed the light distribution at different distances behind the lens to aid in the decision of where to locate the photovoltaic cells. Whitfield et al (1999) undertook experimental tests for a point-focus Fresnel lenses in a two-axis tracking PV concentrator with a concentration ratio of 32 with a system aperture area of approximately $2m^2$. During a single 12h outdoor test at Reading UK on the 8th August 1998, the Fresnel lens PV concentrator system generated 505Wh of energy. It was also shown that a two-axis tracking concentrator system had the advantage of maximum beam insolation collection. Andreev et al (2004) inserted a secondary lens between the primary Fresnel lens and the solar cells to increase the system concentration ratio to more than 1000X, the secondary lens was also used to protect the solar cells from the environment. With a secondary lens, the optical efficiency of the system was decreased by 6.25%, compared to the primary Fresnel lens system only which had a system optical efficiency of 85%. The secondary lens however

increased the off-normal angular acceptance, compared with the one without the secondary lens. Ryu et al (2006) proposed to use modularly faceted Fresnel lenses to achieve uniform intensity on the absorber plane. In their design, a modular Fresnel lens composed of a number of lens blocks, which had the same or slightly larger area than that of the solar cell, bends the normally incident solar radiation onto the solar cell surface shown in figure 1.22. The predicted uniformity of irradiance at the absorber plane was reported to be within 20%, with an optical efficiency of greater than 70% at a concentration ratio of less than 50.

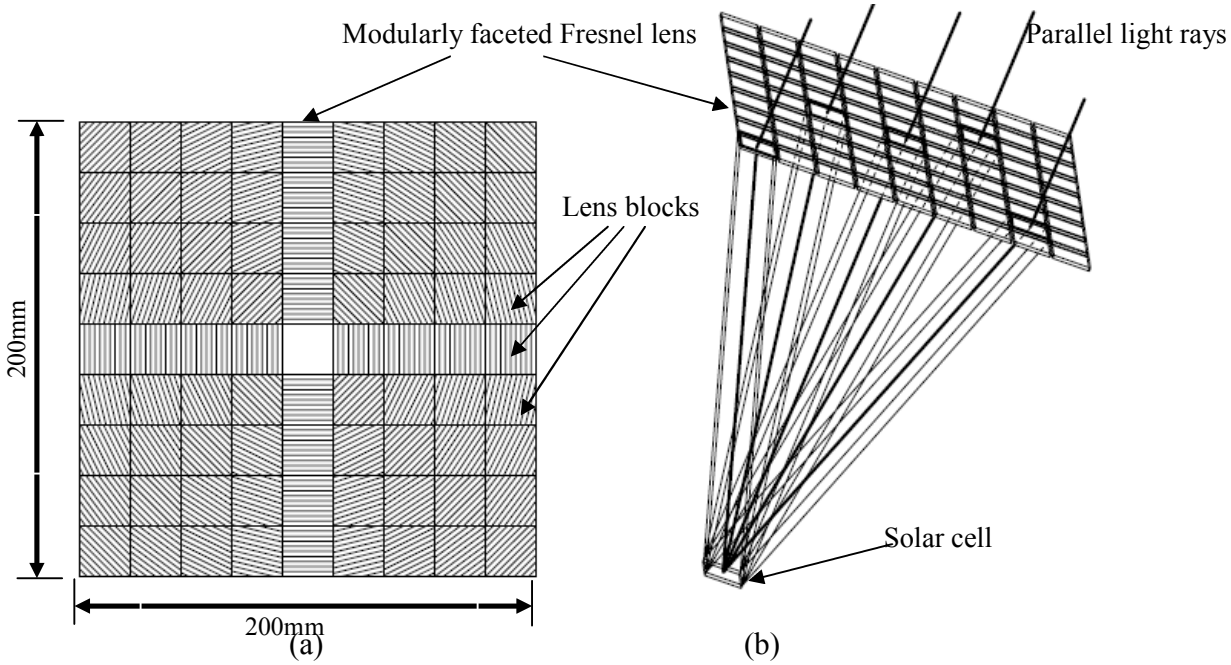

Figure 1.22 (a) Schematic of the modularly faceted Fresnel lens (b) a 3D sketch view of the Fresnel lenses and solar cell (Ryu et al, 2006)

Mallick and Eames (2007c) conducted an optical performance prediction for the self shading between adjacent high concentration point focus Fresnel lens based photovoltaic concentrators as shown in figure 1.23 The predicted self shading loss was reduced from

23% to 12% by increasing the pivot spacing between adjacent concentrator troughs from 160mm to 360mm for concentrator systems located at Sevilla, Spain.

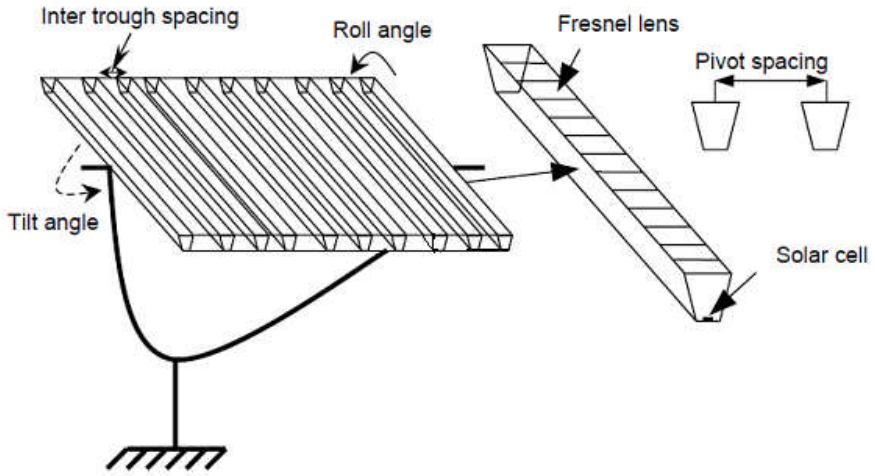

Figure 1.23 A schematic sketch of a Fresnel lens PV concentrator. (Mallick and Eames, 2007c)

Mallick and Eames (2007d) investigated the optical and thermal behaviour of high concentration point focus Fresnel lens photovoltaic concentrators. The predicted solar cell temperature was reduced from 58.23°C to 48.86°C when the cooling fin (Shown in figure 1.24) thickness was increased from 0.2mm to 0.5mm. Little effect in reducing the cell temperature was observed when increasing the fin depth from 50mm to 100mm.

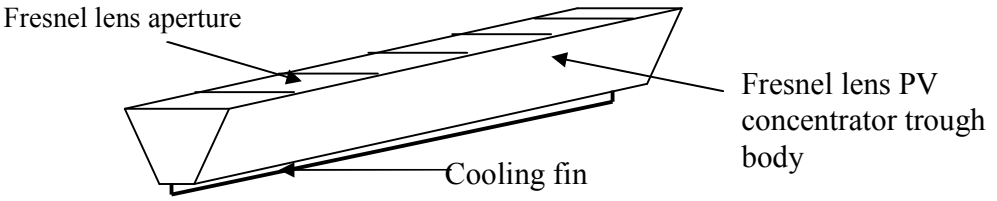

Figure 1.24 A schematic sketch of a Fresnel lens PV concentrator with cooling fin (Mallick and Eames, 2007d)

1.5.2 Parabolic trough and parabolic dish concentrators

A basic sketch of a parabolic trough PV concentrator and a parabolic dish PV reflector is shown in figures 1.25 and 1.26, respectively, illustrating how a parabolic trough and a parabolic dish concentrator focus sunlight onto the receiver. Parabolic trough technology uses reflectors curved around one axis into a linear parabolic shape to collect parallel rays along a single line focus. A parabolic dish reflector uses a parabolic dish shaped mirror to focus the incoming solar radiation onto a receiver positioned at the dish focal point.

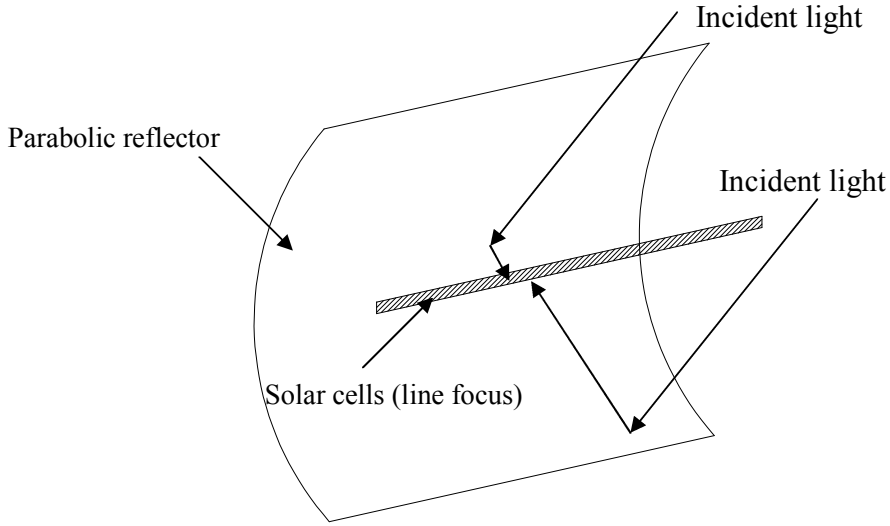

Figure 1.25 A sketch of a parabolic trough PV concentrator (Luque and Hegedus, 2003)

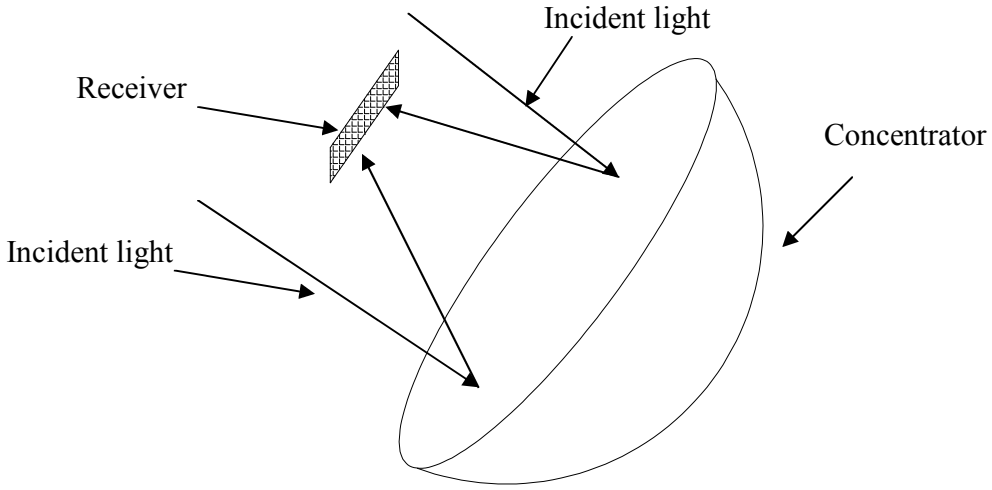

Figure 1.26 A sketch of a parabolic dish concentrator (Luque and Hegedus, 2003)

Parabolic trough and parabolic dish concentrators are usually used for solar thermal electricity generation in which directly collected solar energy is converted to electricity through a heat to electricity conversion device typically a Stirling Engine (Trieb et al 1997, Mills, 2004). However, they can also be used as a PV concentrator converting solar energy directly to electricity.

The first single-axis parabolic trough solar electric generating system with a north-south axis of rotation was installed in southern California by LUZ International, Inc in 1984. The first generation and second generation systems had optical concentrations of 19 and 26, respectively. However, these systems had a low acceptance of diffuse solar radiation (Frier and Cable, 1999). Coventry et al (2002a) developed the first domestic style parabolic trough PV concentrator system with a concentration ratio of 25. Subsequently, a single-axis tracking parabolic trough PV concentrator system with a concentration ratio of 35 was investigated for installation on the roof of a commercial building. Coventry (2002b) conducted both experimental tests and numerical predictions for a parabolic trough PV/thermal collector with a concentration ratio of 30, and the predicted thermal energy output agreed well with the measured values. Feuermann and Gordon (2001) have demonstrated a miniature parabolic dish with a dish diameter of 10cm for photovoltaic applications with a concentration ratio of 1000. The GaAs and Ga-As-In-P solar cells installed in the concentrating system had a peak efficiency of 24-30%. Johnston et al (2003) improved the flux distribution obtained from a parabolic dish concentrator by using identical equilateral triangular mirror panels having spherical profiles to form a paraboloidal reflector.

1.5.3 Compound Parabolic Concentrator (CPC)

The Compound Parabolic Concentrator (CPC) has the theoretical maximum geometric concentration ratio within its angular acceptance. A CPC can reflect both direct and a fraction of the diffuse incident radiation at the entrance aperture onto the absorber as well as the direct solar radiation absorbed directly by the absorber. A 2D flat absorber CPC composed of two parabolic reflector segments with different focal points is shown in figure 1.27. The axis of the parabola makes an maximum acceptance-half angle θ_a or $-\theta_a$ with the collector mid plane and its focus is at P (or Q) (Welford and Winston, 1978). Hinterberger and Winston (1966) described the first example of a CPC as a light collector for Čerenkov radiation counters. Winston (1974) pointed out the potential use of a CPC as a solar energy concentrator. Rabl (1976a) tested a Compound Parabolic Concentrator at Argonne National Laboratory, his study indicated that the ideal concentrator CPC, was different from conventional systems such as focussing parabolas and acted as radiation funnel with no focus. For a given acceptance angle, a CPC has a concentration ratio of two to four times that of other solar concentrators, but requires larger reflector areas.

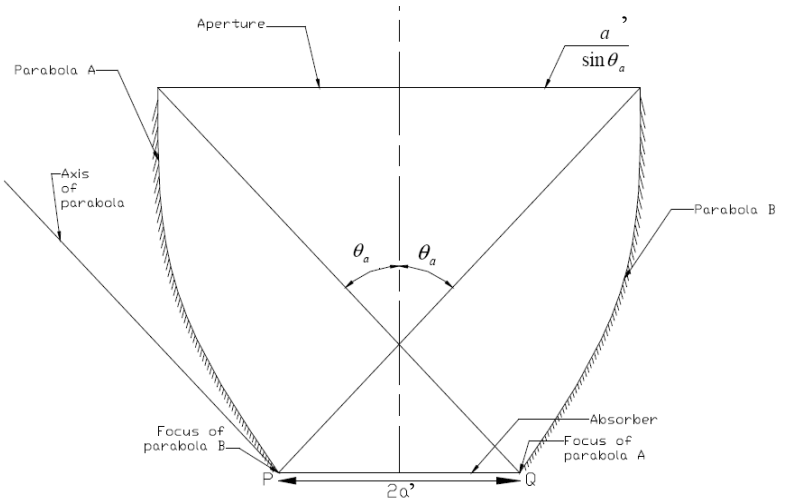

Figure 1.27 Sectional view of the compound parabolic concentrator (CPC) (Welford and Winston, 1978)

1.5.3.1 Concentration ratio of the CPC

The area concentration ratio is defined as the ratio of the area of aperture to the area of the receiver (Duffie and Beckman, 1991), and the geometric concentration ratio of a CPC can be given by equation 1.7.

$$C = \frac{A}{A_{abs}} = \frac{\text{Aperature area}}{\text{Absorber area}} = \frac{1}{\sin\theta_a} \tag{1.7}$$

The focal length of the parabola is calculated as shown in equation 1.8.

$$f = a'(1+\sin\theta_a) \tag{1.8}$$

The overall length can be calculated by equations1.9 and 1.10.

$$L = a'(1+\sin\theta_a)\cos\theta_a / \sin^2\theta_a \tag{1.9}$$

$$\text{or} \quad L = (a+a')\cot\theta_a \tag{1.10}$$

Where C is the geometric concentration ratio, a is the radius of the entry aperture, a' is the radius of the absorber and θ_a is the maximum acceptance-half angle.

1.5.3.2 Equation of a CPC with a flat absorber

For the coordinates presented in figure 1.28, by rotation of the CPC axis and translation of the origin (point O), in terms of the diameter ($2a'$) of the exit aperture and the maximum acceptance-half angle θ_a , the equation for the meridian section of a CPC is given by equation 1.11 (Welford and Winston, 1978).

$$(r\cos\theta_a + z\sin\theta_a)^2 + 2a'(1+\sin\theta_a)^2 r - 2a'\cos\theta_a(2+\sin\theta_a)z - a'^2(1+\sin\theta_a)(3+\sin\theta_a) = 0 \tag{1.11}$$

After using polar coordinates, the compact parametric equation becomes equations 1.12 and 1.13 (Welford and Winston, 1978).

$$r = \frac{2f\sin(\phi - \theta_a)}{1-\cos\phi} - a' \tag{1.12}$$

$$z = \frac{2f\cos(\phi - \theta_a)}{1-\cos\phi} \tag{1.13}$$

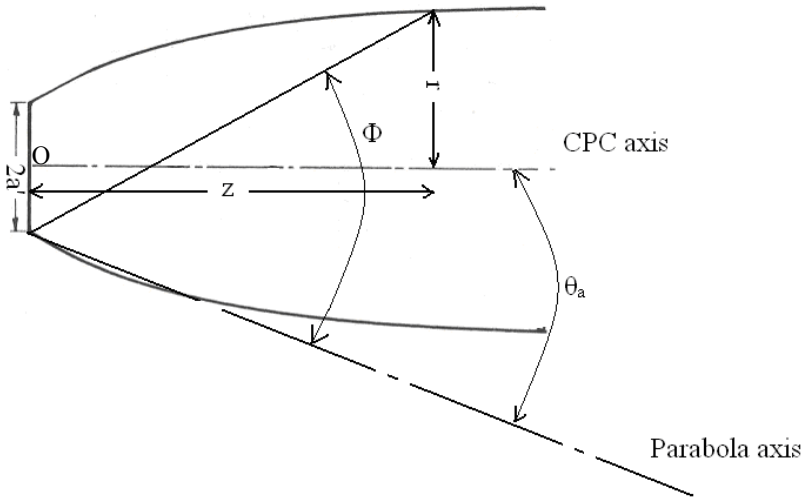

Figure 1.28 The CPC reflector geometry showing the angle Φ used in the parametric equations (Welford and Winston, 1978)

For a CPC with $(\pi/2)+\theta_a \le \theta \le (3\pi/2)-\theta_a$, the x and y coordinates of the reflectors are calculated as follows (Baum and Gordon, 1984)

$$x = a'(\sin\theta - l(\theta)\cos\theta) \tag{1.14}$$

$$y = -a'(\cos\theta + l(\theta)\sin\theta) \tag{1.15}$$

Where

$$l(\theta) = \frac{(\pi/2)+\theta_a+\theta-\cos(\theta-\theta_a)}{1+\sin(\theta-\theta_a)} \tag{1.16}$$

1.5.3.3 The optical performance of the CPC and the effect of truncation

Theoretically, all rays incident at the aperture within the maximum acceptance-half angle ($|\theta| < \theta_a$) of a CPC system strike the absorber, whilst rays with $|\theta| > \theta_a$ are bounced back and forth between the reflector sides and finally exit through the aperture (Rabl, 1976a). Figure 1.29 illustrates the proportion of light collected at different angles (angular acceptance) up to the theoretical maximum, θ_a. An ideal collector would behave according to the full line (Winston et al, 2005).

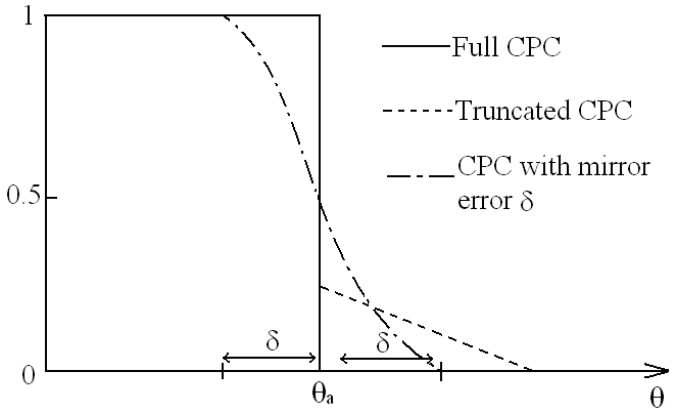

Figure 1.29 The angular acceptance function of a full, truncated CPC and a CPC with edge error δ (Winston et al, 2005)

The CPC is very long compared to the diameter of the collecting aperture or width for 2D systems (Welford and Winston, 1989). For economic reasons, part of the reflector at the entrance aperture end can be truncated, the reduction in length can be achieved with very little reduction in concentration. Figure 1.30 illustrate the truncation of a 2D flat CPC system. With truncation, some rays outside the maximum acceptance-half angle (θ_a) can reach the absorber (Rabl, 1985). Figure 1.29 also illustrates the increase of angular acceptance due to truncation of a CPC system.

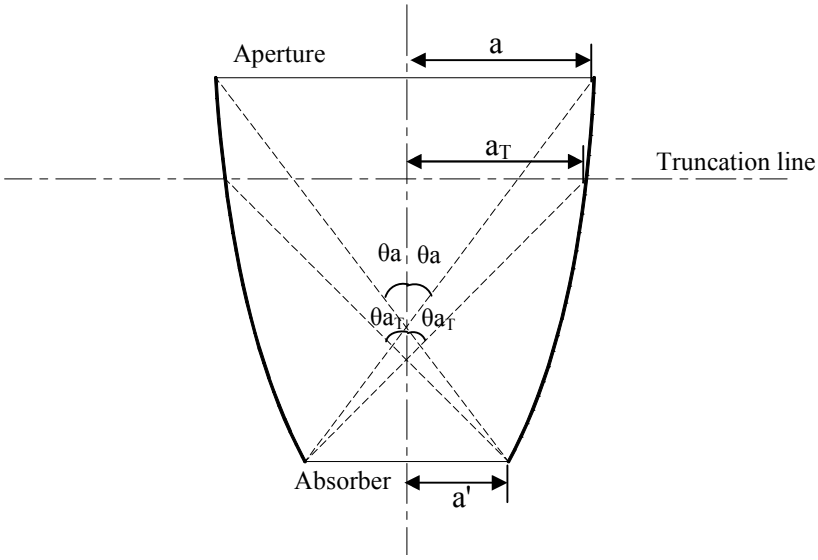

Figure 1.30 Full CPC and its truncation (Winston et al, 2005)

1.5.3.4 Asymmetric Compound Parabolic Concentrator (ACPC)

The focus and end points of the two parabolas of an asymmetric compound parabolic concentrator make different maximum acceptance-half angles with the absorber surface as shown in figure 1.31 (Mills and Giutronich, 1978). The axes of the left and right parabola subtend an angle Φl and Φr with the absorber normal. Fl and Fr are the focus of the left and right parabola, respectively. Rabl (1976a) suggested that this type of concentrator had a maximum geometrical concentration ratio $C = 1/\sin\theta_a$, where $2\theta_a = \phi_l + \phi_r$. However, Mills and Giutronich (1978) suggested that a maximum concentration ratio considerably in excess of $C = 1/\sin\theta_a$ was possible within the angle of acceptance. From the figure 1.31, the maximum concentration equals d_1/d_4, when ABH>90°, and d_2/d_4 given by equation 1.17, when ABH≤ 90°.

$$d_2 / d_4 = \frac{1+\sin\phi_l}{\tan\theta_a} - \cos\phi_l \qquad (1.17)$$

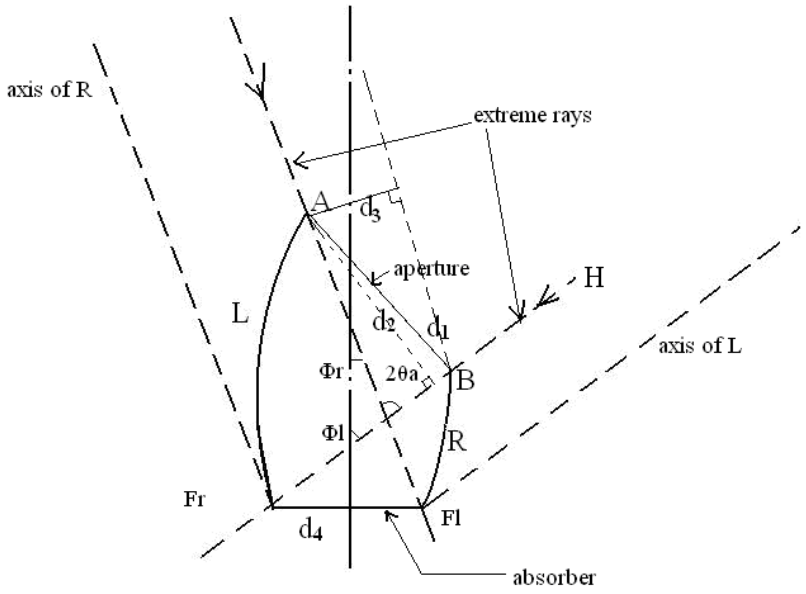

Figure 1.31. A schematic diagram of an ACPC with acceptance angle $2\theta_a = \Phi_l + \Phi_r$ (Rabl, 1976a. Mills and Giutronich, 1978)

The maximum concentration ratio of a general parabolic asymmetric concentrator may be expressed as (Mills and Giutronich, 1978)

$$C = \left[\frac{1+\sin\phi_l}{\tan\theta_a} - \cos\phi_l \right] \cdot \left[\cos(\phi_l - \omega)^{-1} \right] \tag{1.18}$$

$$\text{Where } \cos\omega = \frac{(\sin 2\theta_a - \cos\phi_l + \cos\phi_r)}{2(1-\cos\phi\cos\phi_r)^{1/2}} \tag{1.19}$$

The 'lesser' maximum concentration (for radiation perpendicular to d_3) expressed as (Mills and Giutronich, 1978)

$$C = \frac{1+\sin\phi_r}{\tan\theta_a} - \cos\phi_r \tag{1.20}$$

Zacharopoulos et al (2000) undertook optical analysis of three dimensional dielectric-field symmetric and asymmetric compound parabolic PV concentrators for building façade

integration. The results showed that both systems achieved optical efficiencies of over 90%, the asymmetric system maintained an optical efficiency of over 40% even for incidence angles outside its two-dimensional angular acceptance range, the asymmetric CPC was more suitable for building façade integration than a symmetric one. They also predicted that with an aperture tilt of 70° and the same PV absorber areas, the symmetric and the asymmetric systems collected 2.7 and 2.3 times more solar energy than the same area of PV in a flat plate system. Mallick et al. (2002) used ray trace techniques to predict the optical characteristics of non-imaging asymmetric compound parabolic photovoltaic concentrators (ACPPVC) suitable for south facing façades in the UK (52° N). The truncated air filled ACPPVC had a geometric concentration ratio of 2.0 with acceptance angles of 0° and 50° as shown in figure 1.32. A 91% optical efficiency of the ACPPVC system was achieved for a wide range of solar incidence angles.

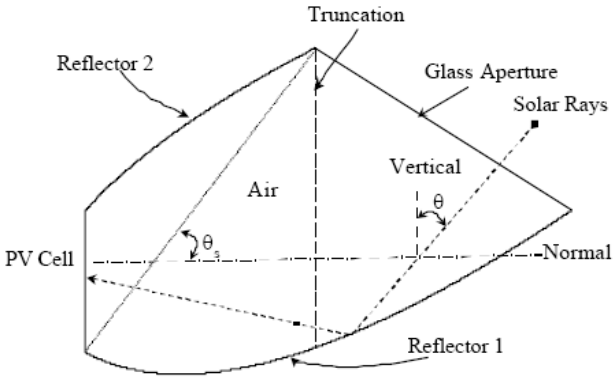

Figure 1.32 Modelled photovoltaic concentrator for building façade integration in the UK (Mallick et al, 2002)

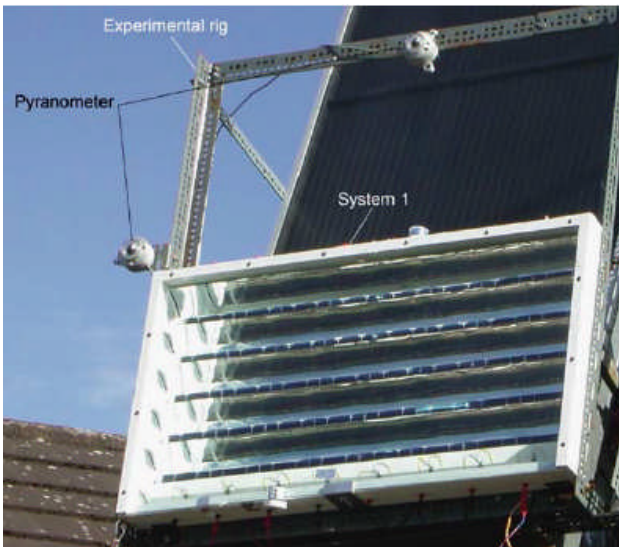

Figure 1.33 ACPPVC system under outdoor experimental characterizations at the University of Ulster (Mallick et al, 2004)

Mallick et al (2004) designed a novel non-imaging asymmetric compound parabolic photovoltaic concentrator (ACPPVC), which had acceptance-half angles of 0° and 50°. The ACPPVC system had a geometric concentration ratio of 2.0 with 54% truncation. The ACPPVC system was comprised of forty BP Saturn solar cells (50mm × 125mm) connected in eight strings of five cells. The ACPPVC system was mounted 18° to the vertical on a south facing platform as shown in figure 1.33. After a one day outdoor experimental tests at the University of Ulster, Northern Ireland, on the 21st of August 2003, a maximum system efficiency of 7.8% was obtained at a solar radiation level of 800W/m^2, and the maximum power generated by the system was 26W. Mallick et al (2006) undertook a detailed experimental characterisation of a non-imaging Asymmetric Compound Parabolic PV Concentrator with acceptance-half angles of 0° and 50° (ACPPVC-50) with its non-concentrating counterpart PV system shown in figure 1.34. It was found that the maximum power output of the ACPPVC-50 system increased by 62%, compared to its non-concentrating counterpart. The obtained solar to electrical conversion efficiency of the

ACPPVC-50 and its non-concentrating counterpart system were 6.8% and 8.8%, respectively.

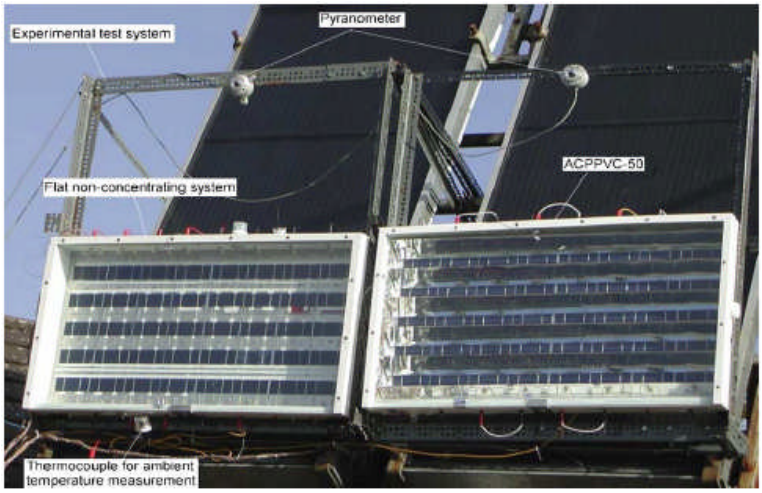

Figure 1.34 Non-concentrating and asymmetric compound parabolic photovoltaic concentrators (Mallick et al, 2006).

Mallick et al (2007a) studied air filled asymmetric compound parabolic photovoltaic concentrators (ACPPVC) using a comprehensive validated unified model for optics and heat transfer in line-axis solar energy systems. An average PV surface temperature of 71.8°C was predicted at 1000W/m^2 incident solar radiation. It was also found that by installing additional air channels at the front and rear of the system, the PV surface temperature was significantly reduced. Mallick et al (2007b) analysed the power loss in an Asymmetric Compound Parabolic Photovoltaic Concentrator with a geometric concentration ratio of 2.0. Due to a combination of optical and electrical resistance losses, the maximum output power achieved was only 1.62 times that of its non-concentrating counterpart. The optical loss of the ACPPVC system was 15%, due to the reflection loss that occurred at the aperture and reflectors. A power loss of 0.6% occurred, due to the increased temperature of the PV cells in the ACPPVC system. The long PV ribbons within

the ACPPVC system between the PV cells caused a resistive power loss of approximately 3.4%.

1.6 Combined optical enhancement and cooling techniques for PV systems

The combination of a PV and thermal collector system can improve the solar to electrical conversion efficiency and yield potential cost benefits compared to a conventional stand alone PV or a thermal collector system. The combination of an optical concentrator and PV/T system could further improve the solar to electrical conversion efficiency and is a promising cost reduction technique for solar cells (Garg et al, 1991, Garg and Adhikari, 1998b 1999b, Tripanagnostopoulos et al, 2002).

Al-Baali (1986) conducted experimental measurements of a stand alone PV system and a PV system integrated with reflecting mirrors and water circulation cooling system. It was found that the reflecting mirrors increased the solar radiation intensity by 400W/m^2 on the PV surface giving a 0.7A increase in current output compared to that of a stand alone system. At the same time, the PV panel temperature was maintained around 37°C by the water circulation system. Garg et al (1991) indicated that booster reflectors could increase both thermal and electrical conversion efficiency of a PV-T system. Garg and Adhikari (1998b) fabricated a PV-T system coupled with a CPC having a geometric concentration ratio of 3. Garg and Adhikari (1999b) undertook predictions for both thermal and electrical performances of a PV-T coupled CPC system. They found that the CPC increased thermal and electrical performance of the PV-T system compared to that of the PV-T system with no concentrator. Brogren et al (2001) conducted both experimental tests and predictions of

the optical performance of a water PV-T combined with a CPC system in Älvkarleby, Sweden (60.58 N, 17.48 E). The CPC coupled PV-T system is illustrated in figure 1.35. The geometric concentration ratio of the truncated symmetric CPC was 4, and the total solar cell area was 1.5 m^2. The measured optical efficiency agreed well with the numerical prediction, both at approximately 71%. They indicated that this system could deliver 270kWh electricity and 800kWh of low temperature heat per m^2 cell area per year.

Figure 1.35 Water cooled PV-thermal hybrid system with a low concentrating aluminium Compound Parabolic Concentrator (Brogren et al, 2001)

Tripanagnostopoulos et al (2002) investigated the combination of a PV-T system with diffuse booster reflectors. Diffuse booster reflectors were placed between the parallel PV rows as shown in figure 1.36 (a). Figure 1.36(b) illustrates the ray tracing of the booster reflector PV-T systems. They found that the system had a mean concentration ratio of 1.35 for summer and 1.15 for winter. The solar to electrical conversion efficiency of a PV-T system was increased by 16% when using diffuse booster reflectors, compared to that of a PV-T having no reflectors.

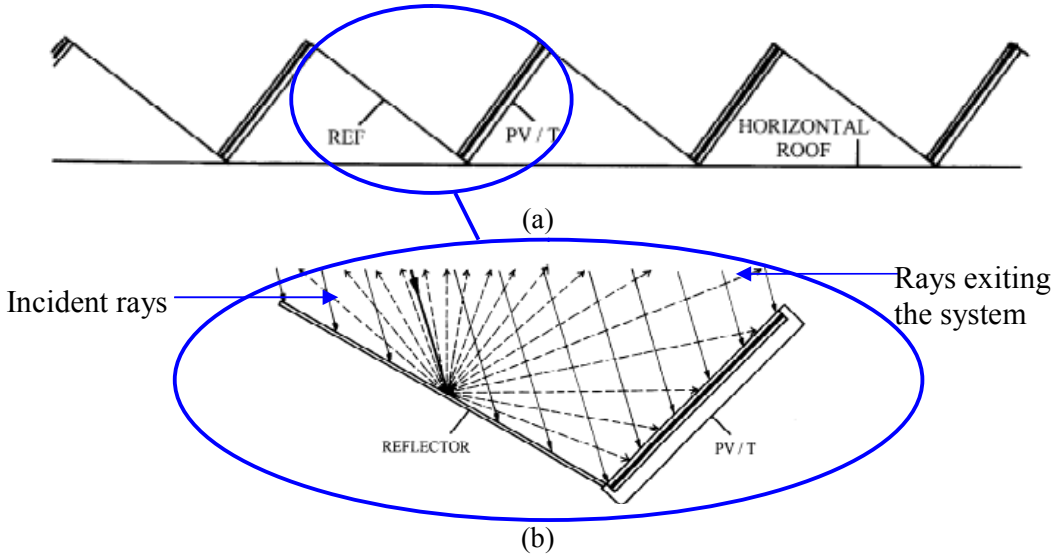

Figure 1.36 (a) Horizontal building roof system installation (b)Ray trace diagram for PV/ T systems with diffuse booster reflectors (Tripanagnostopoulos et al, 2002)

Coventry et al (2002a) fabricated a Combined Heat and Power Solar system (CHAPS) at the Australian National University as shown in figure 1.37. The CHAPS comprised of a concentrating parabolic trough having a concentration ratio of 25 to 35, a 40mm wide strip of monocrystalline silicon solar cells and a copper pipe. During outdoor experimental characterisation on the 16th Aug 2001, thermal efficiencies of up to 50% and electrical efficiencies of 10% were achieved. Coventry (2002b) conducted numerical predictions to compare the thermal and electrical performance of the CHAPS system with a stand alone PV array and hot water system. It was found that the CHAPS system had a thermal efficiency of 57.6% and a electrical efficiency of 9.9%. They were similar to a stand alone PV system having an electrical efficiency of 11.7% and a stand alone solar thermal system having an efficiency of 58.9% for the same conditions. If the cost of the CHAPS system was lower than the sum of the cost of the separate systems, savings could be achieved. Coventry (2005) analysed the performance of a parabolic trough photovoltaic-thermal collector with a geometric concentration ratio of 37. The total system efficiency was 69% at

25°C ambient temperature and 1000W/m^2 solar radiation. The drop in cell efficiency with increasing temperature was of the order of 3.5% per 10°C.

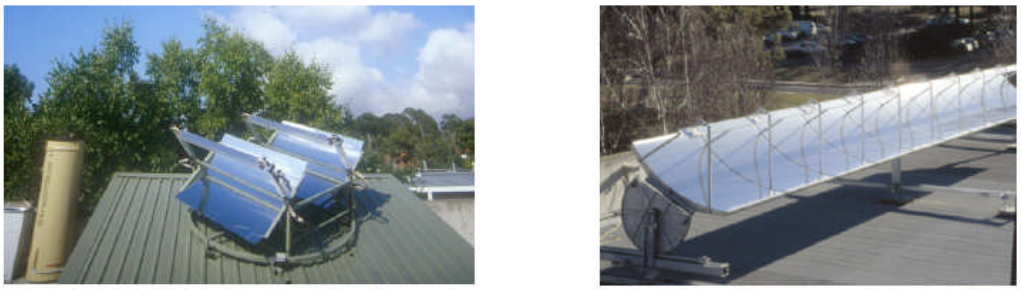

(a)

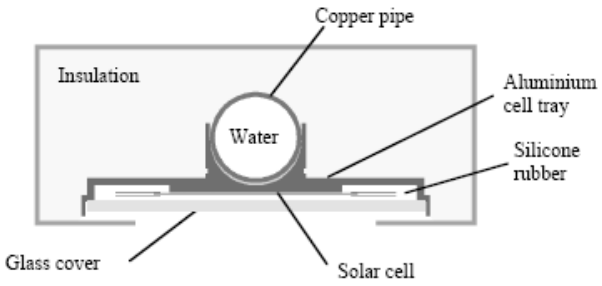

(b)

Figure 1.37 (a) CHAPS domestic system and Long CHAPS system (b) Cross-section view of a CHAPS receiver (Coventry et al, 2002a)

Othman et al (2005) conducted mathematical predictions and experimental studies for a double-pass photovoltaic-thermal solar air collector combined with a CPC and fins. A sketch of the system is shown in figure 1.38. For the indoor experimental characterisation, with the incident radiation intensity at 500W/m^2, the air flow rate was varied from 0.015 to 0.16kg/s and the obtained system electrical conversion efficiency was constant at around 3%. The system thermal efficiency increased from 39% to 65%, when the air flow rate increased from 0.015 to 0.069 kg/s. With further increasing it to 0.16kg/, there was no significant increase of the system thermal efficiency which was 70%. The predicted electrical conversion efficiency was 5%, which is slightly higher than the measured one at

the same conditions. This difference may have been caused by using a tungsten halogen lamp as the light source instead of solar radiation.

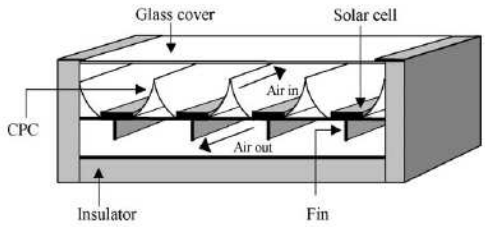

Figure 1.38 A sketch of a double-pass PV- T solar air collector combined with CPC and fins (Othman et al, 2005)

1.7 Solar simulators

For the experimental characterisation of solar systems in the outdoor environment, the issue of repeatability is problematic as the parameters, such as solar radiation intensity, ambient temperature, wind velocity vary with time. This can be avoided under indoor laboratory conditions. This is known as indoor testing which includes solar radiation intensity and climate simulations (Garg, 1985). It allows the applied indoor environmental conditions to be controllable. All of the experimental work can be achieved in a shorter time period and can be easily repeated, compared to tests in the outdoor environment.

Artificial light sources, to replace the sun, have been used to characterise solar cells performance in controlled indoor condition. Bickler (1967) used more than one light source to simulate solar radiation and obtained a spectral output similar to that of the sun in space. Bohm et al (1985) used a commercial Oriel solar simulator equipped with a 1000W high-pressure Xenon arc lamp for solar cell indoor experimental characterisations. Figure 1.39 shows a cross-section of the lamp house and of the output ray trace of the solar simulator system. The output beam uniformity showed a less than 5% deviation within a 20cm diameter circular area.

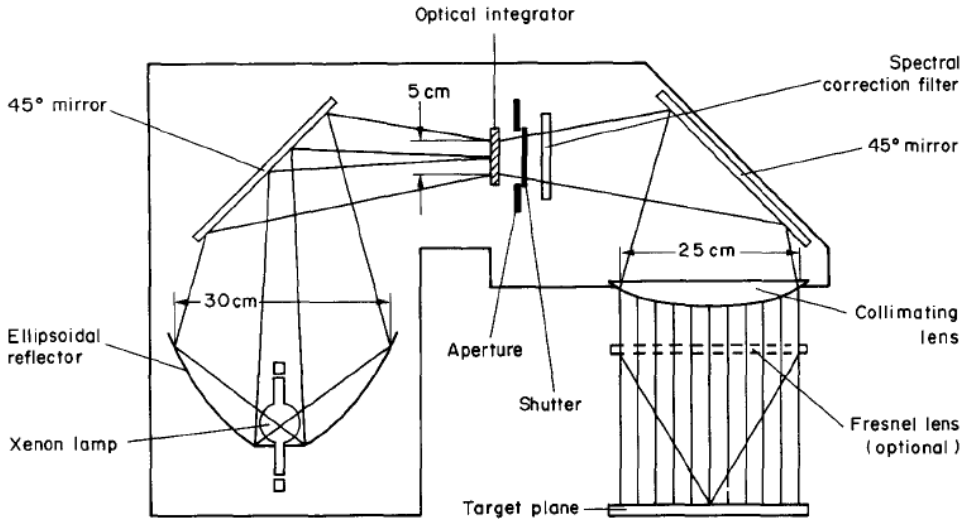

Figure 1.39 A cross-section of lamp housing and output beams of the solar simulator (Bohm et al, 1985)

Tabatabaie-Raissi and Antal (1986) fabricated a bench scale solar simulator which included a 30,000W xenon arc lamp, two 1.52 diameter parabolic dish reflectors and a 0.38m long by 0.06m diameter reflective cavity. An average flux density of 350,000W/m^2 was obtained on the test plane at 15,900W power input to the lamp. Kuhn and Hunt (1991) established a solar simulator comprised of a 30,000W Xenon arc lamp and an ellipsoidal concentrator with a maximum diameter of 80cm to produce highly concentrated radiation. Peak fluxes of up to 16,000W/m^2 were achieved. Reber et al (2005) tested the spectral output of a xenon arc lamp solar simulator with filters. Figure 1.40 illustrates the spectral output between the solar simulator and measured natural solar radiation. It can be seen that the spectral output of the xenon arc lamp was close to that of the solar radiation. Ito et al (2004) measured electrical conversion efficiencies of ruthenium-dye-sensitized solar cells (DSC) using a xenon-lamp solar simulator. Kohraku and Kurokawa (2006) used Light-Emitting Diodes (LED) instead of the expensive Xenon and Halogen lamps as a solar simulator light source

for measuring Si solar cells. Four colours (blue, red, infrared and white) of LEDs were used as the simulator light source.

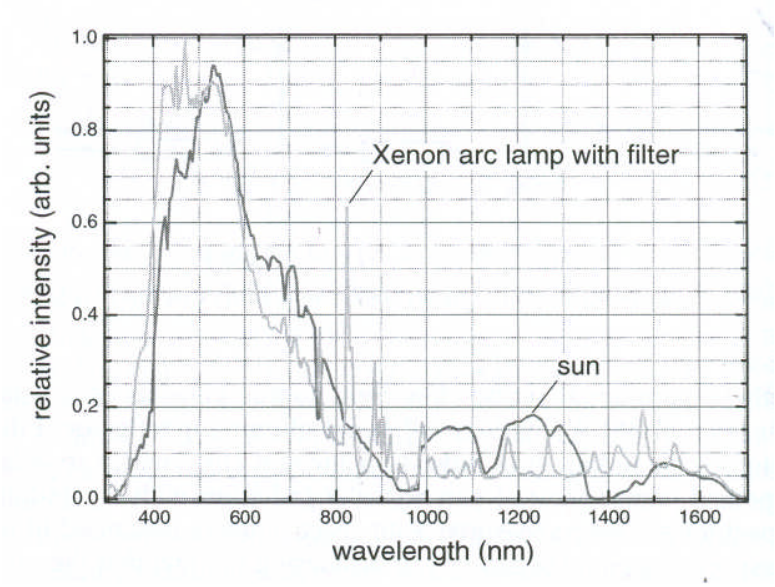

Figure 1.40 Spectral output of a Xenon lamp and natural solar radiation (Reber et al, 2005)

1.8 Conclusions

Several techniques can be employed at the rear of PV systems to moderate the temperature rise experienced by the PV and maintain good solar to electrical conversion efficiency. Optical concentrator systems that increase the solar radiation intensity on the PV system may reduce the system cost, however temperature control becomes more important. There are several options available to improve PV system performance and also reduce the system cost. Table 1.4 highlights different options that use a range of various mechanisms to improve PV system performance.

Recent work indicates that in a solar chimney (duct) the surface temperature increases rapidly along the height of the channel (Moshfegh and Sandberg, 1998). Therefore, the PV systems integrated to the solar chimney will have a non-uniform temperature distribution which may reduce the electrical conversion efficiency of the PV system. Integrating PV and thermal systems moderates the PV system temperature rise. However, the additional system cost of a PV-T system can be higher than the value of the obtained additional electricity. The main advantage of the PV/ T system was the achieved thermal energy output (Tripanagnostopoulos et al, 2002).

Different methodologies	Main advantages	Main disadvantages
PV and passive air cooling system	1. Comfortable indoor environment and electricity can be obtained at the same time 2. Passive systems, no additional energy consumption 3. Systems integrated into buildings save land area	1. Passive natural ventilation limited by the ambient environment 2. Lower inlet air flow rate causes high temperatures and low PV electrical conversion efficiency. Can be improved by addition of fans in the solar chimney, but additional electrical energy consumed by the fan. 3. Non-uniform surface temperatures influence PV performance
PV / Thermal Collector system	1.Both electrical energy and thermal energy can be obtained 2.PV efficiency increased 3. Systems integrated into buildings save land area	1. Net electricity gain reduced, because energy consumed by a fan or pump 2. The increased electrical efficiency is lower than additional system cost. 3. Non-uniform surface temperatures influence PV performance
PV / PCM system	1. Systems integrated into buildings save land area 2. PV efficiency increased 3. PCM keeps the PV panel temperature uniform 4.Passive storage system can store daytime thermal energy for night use	1. Organic PCM has lower thermal conductivity (can be overcome through container design). 2. Inorganic PCMs has higher thermal conductivity than that of organic PCM, but can be toxic and have complex melt behaviour
Concentrator PV	1. Reduced PV cost 2. PV efficiency increased	1. Non-uniform surface temperature caused by concentrator may influence PV performance
Concentrator, PV and its air or water cooling system	1.Reduced PV cost 2.Both electrical energy and thermal energy can be obtained 3.PV efficiency increased 4. Systems integrated into buildings save land area	1. Passive natural ventilation limited by the ambient environment 2. Net electrical gain reduced, when using an active method for PV cooling, due to the energy consumed by the fan or pump 3. High additional cooling system cost 4. Non-uniform surface temperature influences PV performance

Table 1.4 A summary of the key characteristices of PV thermal and PV concentrator systems

1.9 Scope of the research

The thesis describes work undertaken to increase PV efficiency whilst decreasing capital costs. To achieve this, the following low and high concentration ratio PV systems were analysed,

- A combination of building integrated low concentration ratio photovoltaic concentrator integrated with a PCM system
- A high concentration ratio Fresnel PV concentrator system.

Extensive indoor experimental characterisations were undertaken to identify the electrical and thermal performance of the selected PV systems for a range of incident solar radiation intensities using a highly collimated solar simulator built specifically for this project.

The objectives of the research were to:

- Develop and undertake the design of an Asymmetric Compound Parabolic Photovoltaic Concentrator (ACPPVC) coupled PCM system to reduce the system's initial cost and moderate the temperature rise of the PV
    - Undertake 2D ray tracing to predict the optical performance of ACPPVC systems and chose an ACPPVC system being suitable for the solar inclination angles in the UK
    - Design and manufacture the ACPPVC system
    - Identify the PCM, design and manufacture the PCM container
    - Combine an ACPPVC and PCM systems together
- Design and fabricate a highly collimated solar simulator to assistant indoor experimental characterisations

- Investigate the thermal characteristics and electrical performance of the ACPPVC-PCM at varying levels of insolation and controlled indoor environmental conditions
- Identify the ACPPVC-PCM system performance by comparing with counterpart ACPPVC system with no PCM and non-concentrating stand alone PV system at similar conditions
- Design and fabricate a test chamber suitable for indoor experimental characterisations for high concentration ratio Fresnel lens PV concentrators
- Investigate the thermal behaviour of the selected Fresnel lens PV Concentrator system (FPVC) and provide suggestions to improve the design of the FPVC systems in the future

Chapter 2 Optical performance analysis and predictions of Asymmetric Compound Parabolic Photovoltaic Concentrators (ACPPVC)

2.1 Introduction

Ray tracing can be used to design optical systems, to predict the optical performance of solar energy systems for which rays are assumed to be specular, and the vector forms of reflection and refraction laws can be applied (Welford and Winston, 1989; Winston et al, 2005). Zacharopoulos et al (2000), Mallick et al (2002, 2007a) and Wu et al (2007a, 2007b) undertook ray trace analysis to predict the optical performance of Asymmetric Compound Parabolic Concentrators for Photovoltaic applications. When a ray enters an Asymmetric Compound Parabolic Photovoltaic Concentrator, it may strike the PV absorber directly, strike the PV absorber after a finite number of reflections, or not strike the PV absorber and be reflected back out through the aperture of the ACPPVC system after a finite number of reflections as shown in figure 2.1 (Mallick, 2003).

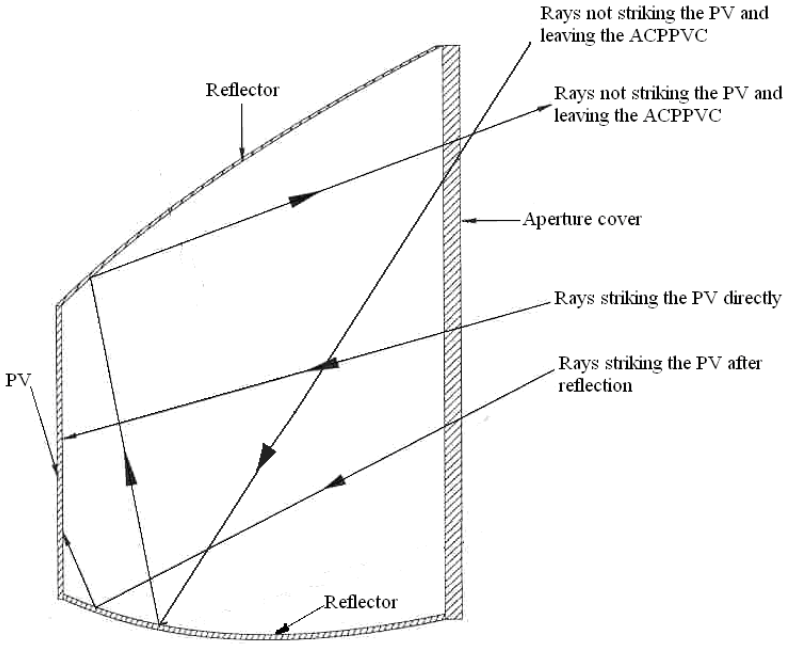

Figure 2.1 The possible behaviour of the incident rays in an ACPPVC system (Mallick, 2003)

2.2 The optical analysis of selected Asymmetric Compound Parabolic Photovoltaic Concentrator (ACPPVC) systems

2.2.1 The geometrical characteristics of ACPPVC systems

Rabl (1976b) used equation $y = 1/4f \cdot x^2$ to obtain a two dimensional Parabolic Concentrator (CPC) in the coordinate system shown in figure 2.2. Following Rabl's method, a PASCAL computer program was developed to design ACPPVC systems. An illustration of an asymmetric compound parabolic photovoltaic concentrator system generated by the program is shown in figure 2.3. The ACPPVC system had an absorber width of 0.125m and acceptance half angles of 0° and 50°.

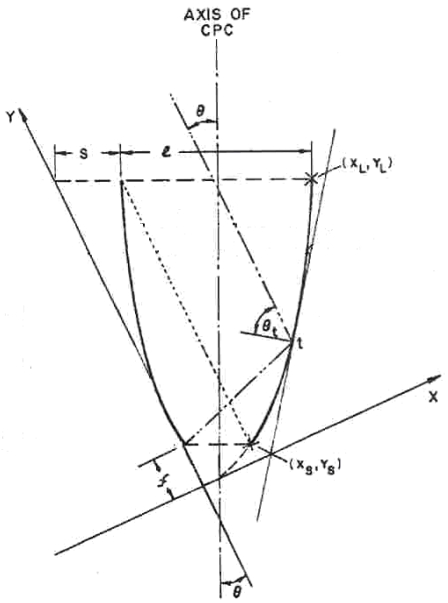

Figure 2.2 Coordinate system used for describing a 2-D compound parabolic concentrator (Rabl, 1976b)

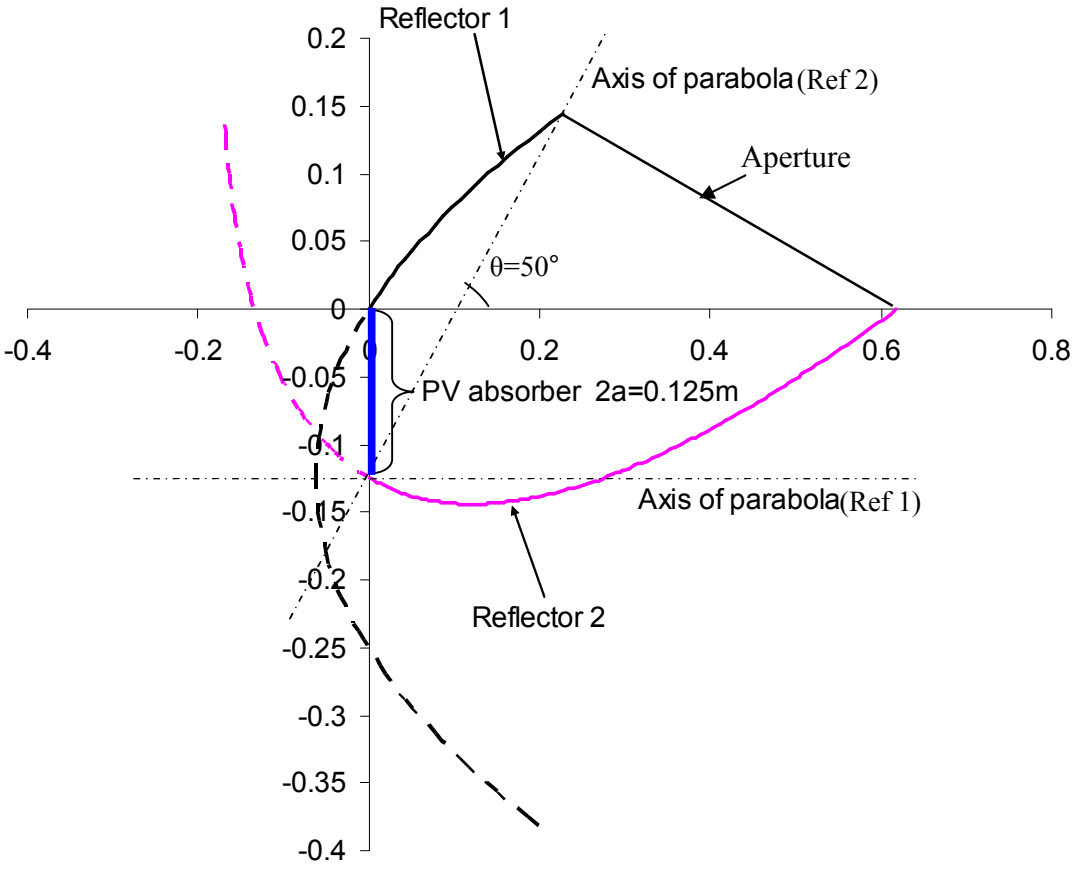

Figure 2.3 The cross-sectional profile of the parabolas that form an ACPPVC system with acceptance half angles of 0° and 50°, all dimensions in 'm'.

2.2.2 Ray intersection at the glass aperture cover

When a ray is incident at the glass aperture cover, it may be reflected back from the aperture surface, transmitted through the aperture cover, or be absorbed by the aperture glass. Figure 2.4 illustrates the reflections for a ray incident on a glass aperture cover, this neglects absorption in the cover (Duffie and Beckman, 1991).

Reflection of radiation

The reflective coefficient of a glass aperture cover can be calculated using equations 2.1 to 2.3 (Duffie and Beckman, 1991)

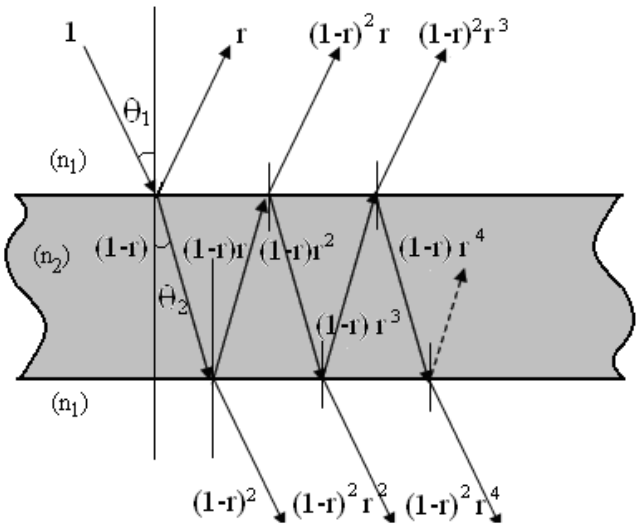

Figure 2.4 Transmission through an aperture cover neglecting absorption. (Duffie and Beckman, 1991)

$$r_{\perp} = \frac{\sin^2(\theta_2 - \theta_1)}{\sin^2(\theta_2 + \theta_1)} \tag{2.1}$$

$$r_{\mathrm{II}} = \frac{\tan^2(\theta_2 - \theta_1)}{\tan^2(\theta_2 + \theta_1)} \tag{2.2}$$

and

$$r = \frac{1}{2}(r_{\perp} + r_{\mathrm{II}}) \tag{2.3}$$

For normal incidence, the reflective coefficient becomes equation 2.4 (Duffie and Beckman, 1991)

$$r(0) = \left(\frac{n_1 - n_2}{n_1 + n_2}\right)^2 \tag{2.4}$$

From figure 2.4, it can be seen that when a ray is incident on a glass aperture, for the perpendicular component of polarization of the incoming flux, $(1 - r_{\perp})$ of the incident ray reaches the second interface. Of this, $r_{\perp}(1 - r_{\perp})$ is reflected back to the first interface and $(1 - r_{\perp})^2$ passes through the second interface and so on (Duffie and Beckman, 1991).

The transmittance for the perpendicular component of polarization can be calculated using equation 2.5 (Duffie and Beckman, 1991)

$$\tau_{\perp} = (1-r_{\perp})^2 \sum_{n=0}^{\infty} r_{\perp}^{2n} = \frac{(1-r_{\perp})^2}{1-r_{\perp}^2} = \frac{1-r_{\perp}}{1+r_{\perp}} \tag{2.5}$$

Using the same principle as for the perpendicular component, the parallel component of polarization can be calculated using equations 2.6 (Duffie and Beckman, 1991)

$$\tau_{\text{II}} = \frac{1-r_{\text{II}}}{1+r_{\text{II}}} \tag{2.6}$$

And

$$\tau_r = \frac{1}{2}(\tau_{\perp} + \tau_{\text{II}}) \tag{2.7}$$

Absorption in the glass aperture cover

When a ray passes through glass, energy is absorbed by the glass and can be determined by equation 2.8 (Duffie and Beckman, 1991)

$$dI = -IKdx \tag{2.8}$$

Integrating along the ray path length in the medium (i.e., from zero to $L/\cos\theta_2$) yields equation 2.9 (Duffie and Beckman, 1991)

$$\tau_a = \frac{I_{transmitted}}{I_{incident}} = \exp(-\frac{KL}{\cos\theta_2}) \tag{2.9}$$

Where I is the insolation, K is the extinction coefficient of the glazing material, x is the path length of the ray through the glazing material and L is the glazing thickness.

Optical properties of glass cover

From the above equations, the transmittance of the glass aperture cover can be calculated using equation 2.10

$$\tau \cong \tau_a \tau_r \tag{2.10}$$

The absorption of the glass aperture cover is given by equation 2.11

$$\alpha \cong 1 - \tau_{\alpha} \tag{2.11}$$

The reflectance of the glass aperture cover found from $\rho = 1 - \alpha - \tau$ can be approximated by equation 2.12

$$\rho \cong \tau_{\alpha}(1 - \tau_{r}) = \tau_{\alpha} - \tau \tag{2.12}$$

2.2.3 Ray intersection at the reflector surface

When a ray intersects with the reflector, most of its energy is reflected whilst the rest is absorbed by the reflector and converted into heat which is subsequently transferred away by conductive, convective and radiative heat transfer as shown in figure 2.5 (Eames et al, 1993).

Where:

$$\theta_{in} = \theta_{ref} \tag{2.13}$$

The energy absorbed by the reflector is given by equation 2.14 (Eames et al, 1993),

$$E_{abr} = (1 - \rho)E_{in} \tag{2.14}$$

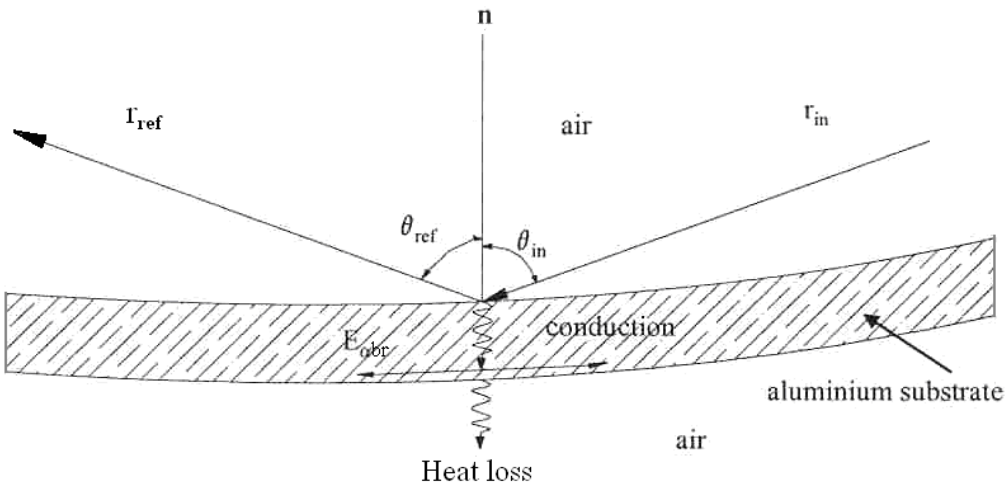

Figure 2.5 Schematic sketch of rays intersecting with the reflector (Eames et al, 1993)

2.2.4 Ray intersecting with the PV absorber

PV cells are designed to transform solar radiation into electricity. It is assumed that the PV cells are a perfect black body (Mallick et al, 2007a). Therefore, all incident energy will be absorbed by the PV cell and either converted in to electrical or thermal energy.

2.2.5 Ray trace analysis and optical performance for the selected ACPPVC systems

The annual maximum and minimum altitude of the sun at noon at Coventry, UK (latitude: 52.42°N) are 60.8° and 13.8°, respectively. Annual daylight hours per day vary from about 18 to 8 hours in this location, and there is a large variation in daily available solar energy between summer and winter, due to the winter having shorter daytimes and lower solar altitudes compared to those in the summer. The designed ACPPVC system should have a wide range of angular acceptance to collect most of the annual incident solar radiation and a suitable concentration ratio to reduce the system's initial cost.

A ray trace analysis to predict the optical performance for three ACPPVC systems was undertaken. The selected ACPPVC systems were suitable for UK building façade integration with acceptance half angles close to the annual maximum altitude of the sun at noon at Coventry. The systems were an ACPPVC-50 system with acceptance-half angles of 0° and 50°, an ACPPVC-55 system with acceptance-half angles of 0° and 55°, and an ACPPVC-60 system with acceptance-half angles of 0° and 60°. The PV absorber widths in all cases were 0.125m. Detailed prediction of angular acceptance and optical efficiencies were made by tracing 10,000 rays incident on the glass aperture cover for each incidence angle between -90° and 90° at 1° intervals. For the ray trace all rays were assumed specular. The parameters used in calculating the optical efficiency are shown in table 2.1.

Thickness of the aperture glass(m)	0.004
Low iron aperture glass extinction coefficient (m^{-1})	4
Refractive index of glass	1.526
Refractive index of air	1
Reflectance of mirror reflector	0.95
Absorptance of PV cells	1

Table 2.1 System optical properties

2.2.5.1 Ray trace and optical analysis of a ACPPVC-50 system

To identify the optical performance of the ACPPVC-50 system and the ACPPVC-50 system at different truncation levels. Four variations of the ACPPVC-50 were investigated as shown in figure 2.6, they were untruncated and truncated at levels 1, 2 and 3. The untruncated ACPPVC-50 had a geometric concentration ratio of 3.33 with acceptance half angles of 0° and 50°. Truncation level 1 (T-1) of the ACPPVC-50 gave a geometric concentration ratio of 2.22 with 0% truncation for reflector 1 and 65% truncation for reflector 2. The truncation of level 2 (T-2) of the ACPPVC-50 gave a geometric concentration ratio of 2.11 with 17% truncation for reflector 1 and 72% truncation for reflector 2. The truncation of level 3 (T-3) of the ACPPVC-50 gave a geometric concentration ratio of 2.0 with 30% truncation for reflector 1 and 77% truncation for reflector 2.

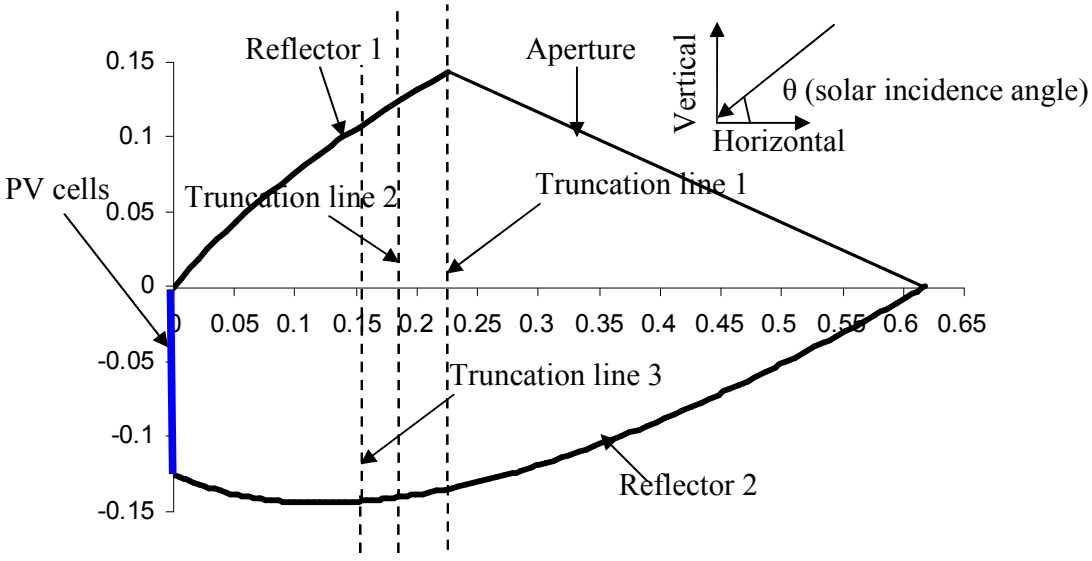

Figure 2.6 An ACPPVC-50 with acceptance-half angle of 0° and 50°, all dimensions in 'm'.

2.2.5.1.1 Ray trace and optical analysis of an untruncated ACPPVC-50

The geometrical characteristics for the untruncated ACPPVC-50 are shown in table 2.2. In all undertaken simulations, the solar incidence angle (θ) was measured from the horizontal as illustrated in figure 2.6.

Parameters		Values
Acceptance-half angles		0°& 50°
Absorber width(mm)		125
Aperture width(mm)		417.2
Length of reflector1(R1)(mm)		269.5
Length of reflector2(R2)(mm)		664.3
Concentration ratio		3.34
Truncation (%)	Ref1	0
	Ref2	0

Table 2.2 Geometrical characteristics of the untruncated ACPPVC-50

Ray trace diagrams for the untruncated ACPPVC-50 for a selection of solar incidence angles are shown in figure 2.7. To illustrate the ray trace paths for an ACPPVC-50 system, the total incident solar radiation was divided into 50 rays and the paths drawn. From figure 2.7 it can be observed that at incidence angles of 1°, 15°, 30° and 45°(from the horizontal), all the rays incident at the aperture are incident on the PV cell. When the solar incidence angle is 45°, a local high intensity flux can be seen in the middle part of the PV cell. This may lead to an increase in the local temperature of the PV cell, and potentially result in a decrease in the electrical conversion efficiency. Decreasing the solar incidence angle towards the horizontal leads to more rays being reflected onto the absorber by reflector 1, compared to reflector 2.

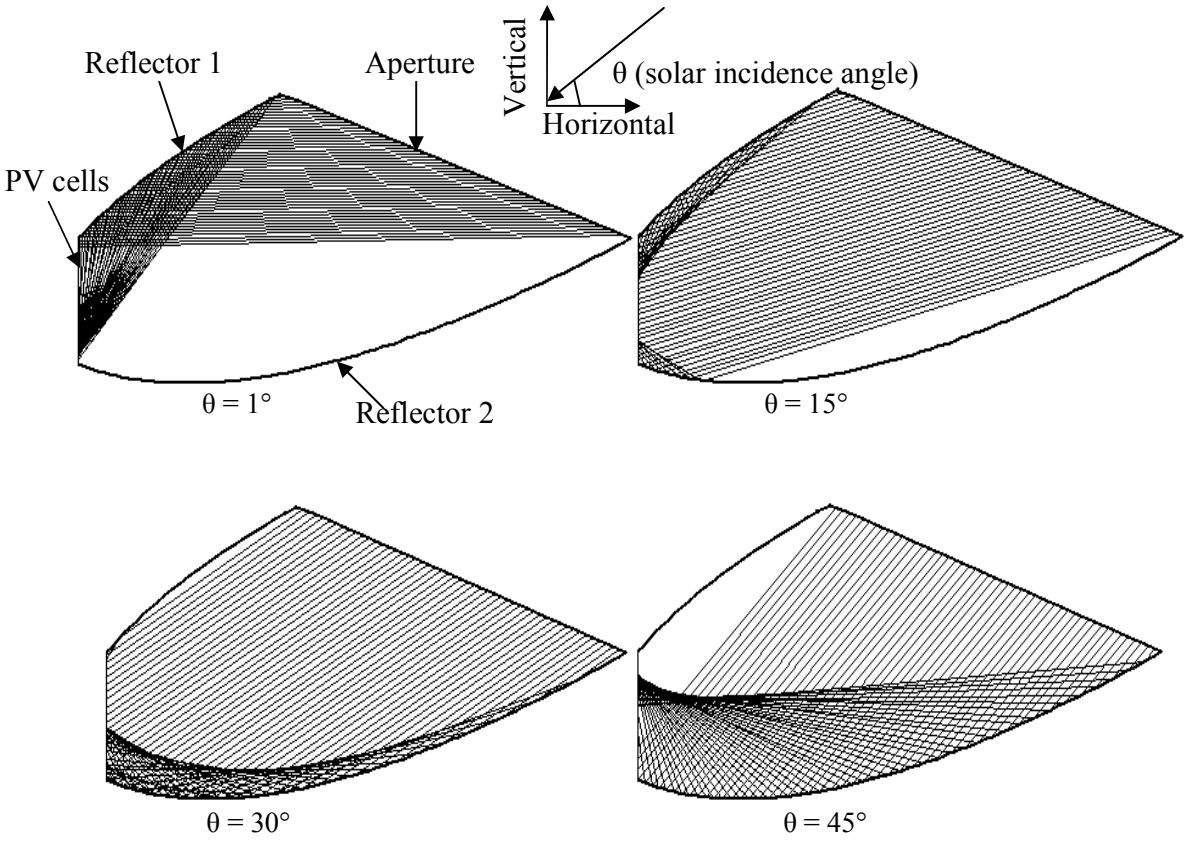

Figure 2.7 Ray trace diagrams for the untruncated ACPPVC-50, 50 rays are shown for incidence angle.

The predicted angular acceptance and optical efficiency of the untruncated ACPPVC-50 are shown in figure 2.8. For the solar incidence angles between 0° and 50°, the angular acceptance is 1. Thus, all the rays incident at the aperture are incident on the PV cell. When the solar incidence angle is above 50°, the percentage of angular acceptance instantaneously drops to 0. The highest predicted optical efficiency is 88.67% for the untruncated ACPPVC-50.

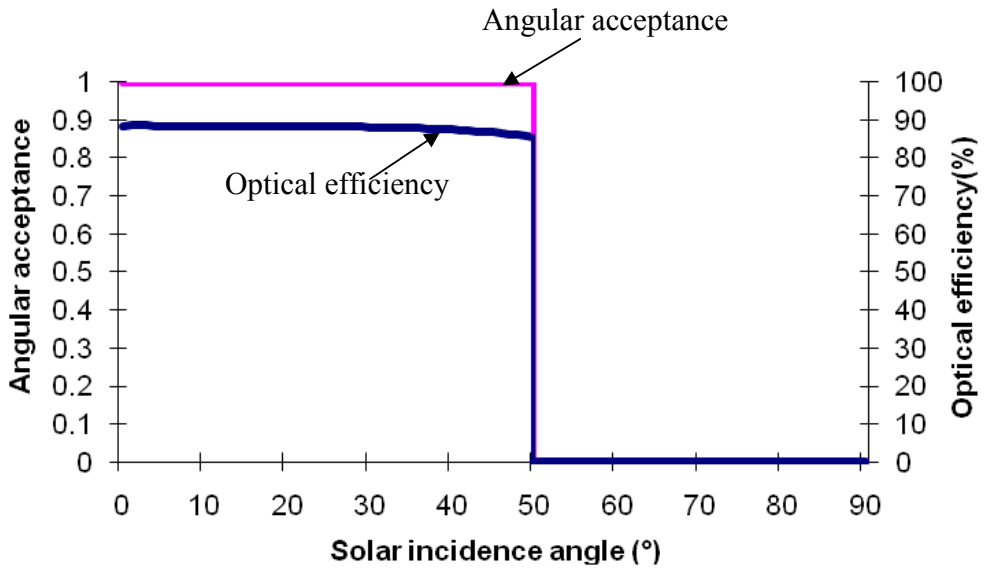

Figure 2.8 Predicted angular acceptance and optical efficiency for the untrucated ACPPVC-50

2.2.5.1.2 Ray trace and optical analysis for truncation level 1 (T-1) of the ACPPVC-50

The T-1 ACPPVC-50 had a geometric concentration ratio of 2.22 with 0% truncation of reflector 1 and 65% truncation of reflector 2. The geometrical characteristics of the T-1 ACPPVC-50 are shown in table 2.3.

Parameters		**Values**
Acceptance-half angles		30 °& 50°
Absorber width(mm)		125
Aperture width(mm)		277.9
Length of reflector1(R1)(mm)		269.5
Length of reflector2(R2)(mm)		229.2
Concentration ratio		2.22
Truncation (%)	Ref1	0
	Ref2	65

Table 2.3 Geometrical characteristics of the T-1 ACPPVC-50

Ray trace diagrams for the T-1 ACPPVC-50 for a selection of solar incidence angles are shown in figure 2.9. From figure 2.9 it can be observed that the ray trace digrams of the T-1

ACPPVC-50 have similar characteristics to those of the untruncated ACPPVC-50 system at the same solar incidence angles. At incidence angles of 1°, 15°, 30° and 45° (from the horizontal), all the rays incident at the aperture are incident on the PV cells. A local high intensity flux can be seen in the middle part of the PV cell at the solar incidence angle of 45°.

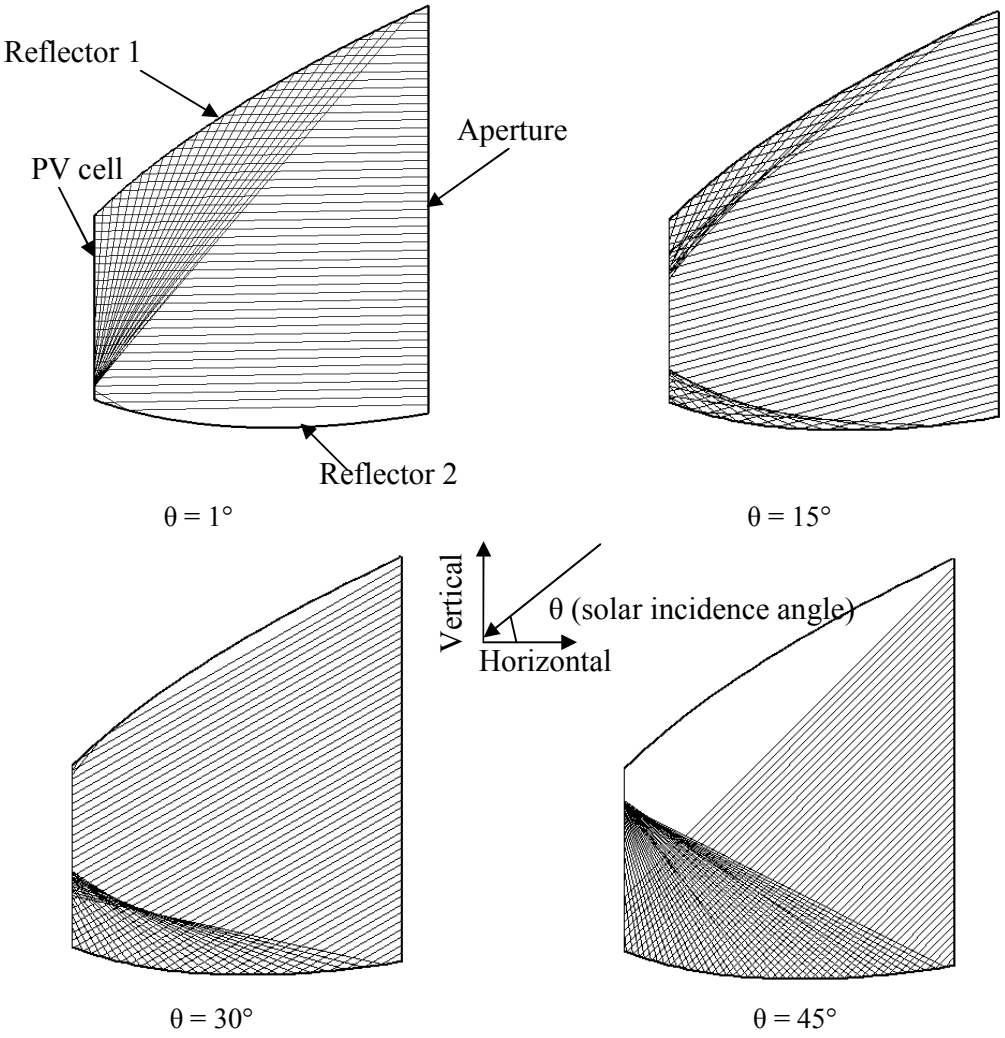

Figure 2.9 Ray trace diagrams for T-1 ACPPVC-50, 50 rays are shown for each incidence angle.

The predicted angular acceptance and optical efficiency of the T-1 ACPPVC-50 are shown in figure 2.10. From figure 2.10, it can be seen that the angular acceptance is 1 for incidence angles between 0° and 50°. When the solar incidence angle is above 50°, the

angular acceptance instantaneously drops to 0. With decreasing solar incidence angle from 0° to -90°, the percentage of angular acceptance decreases dropping to 0 at a solar incidence angle below -30°. Compared to the untruncated case, T-1 has a greater range of angular acceptance, resulting from the truncation of the reflector 2. The highest optical efficiency for the T-1 ACPPVC-50 system is 88.67%.

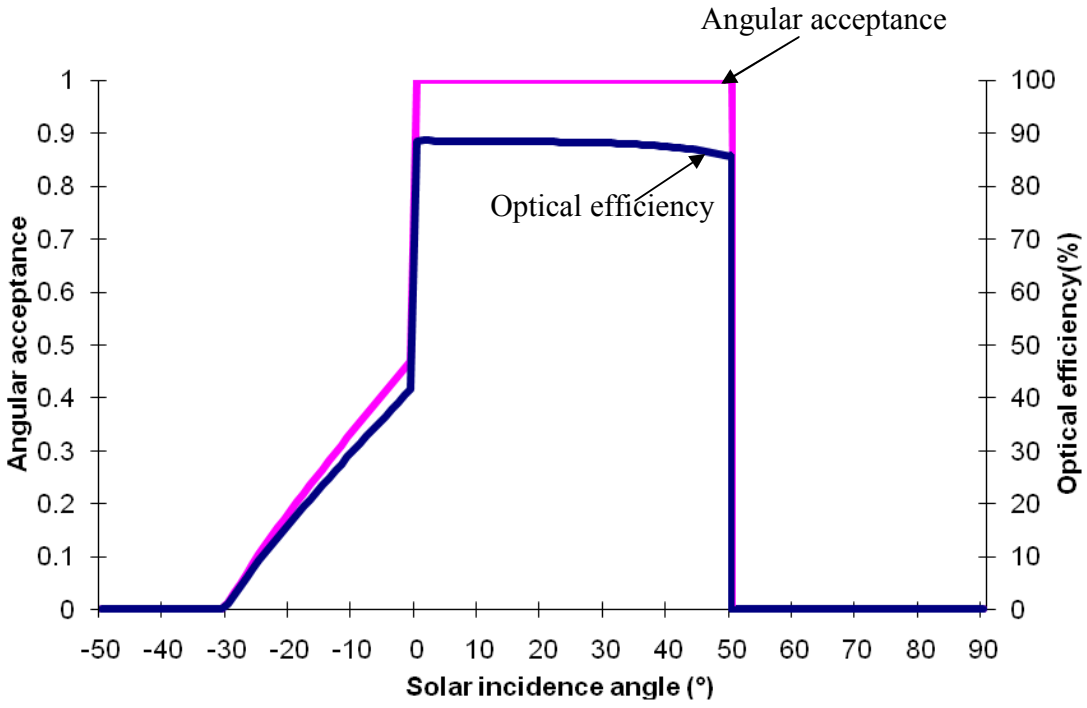

Figure 2.10 Predicted angular acceptance and optical efficiency for T-1 ACPPVC-50 system

2.2.5.1.3 Ray trace and optical analysis for truncation level 2 (T-2) of the ACPPVC-50

The T-2 ACPPVC-50 had a geometric concentration ratio of 2.11 with 17% truncation of reflector 1 and 72% truncation of reflector 2. The geometrical characteristics of the T-2 ACPPVC-50 are shown in table 2.4.

Parameters		Values
Acceptance-half angles		37°& 53°
Absorber width(mm)		125
Aperture width(mm)		264
Length of reflector1(R1)(mm)		223.5
Length of reflector2(R2)(mm)		187.3
Concentration ratio		2.11
Truncation (%)	Ref1	17
	Ref2	72

Table 2.4 Geometrical characteristics of the T-2 ACPPVC-50

The ray trace diagrams for the T-2 ACPPVC-50 for a selection of solar incidence angles are shown in figure 2.11. The ray trace diagrams of the T-2 ACPPVC-50 have similar characteristics to those of the T-1 ACPPVC-50 at the same solar incidence angle.

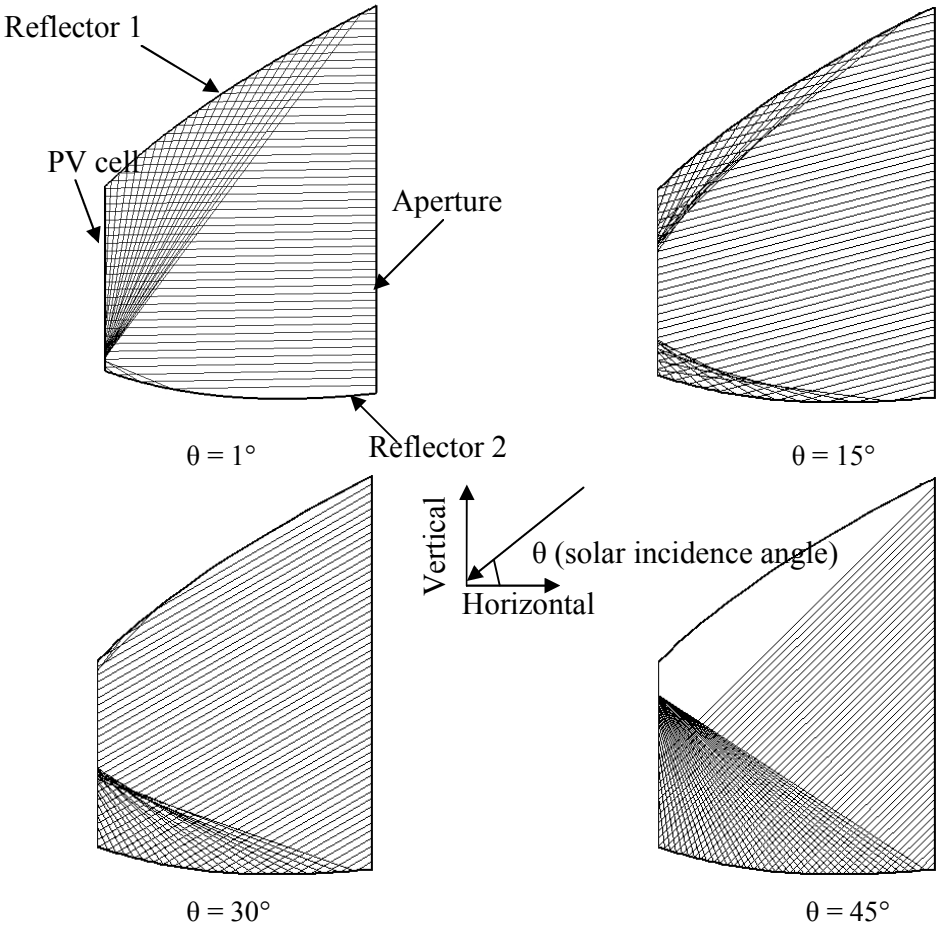

Figure 2.11 Ray trace diagrams for T-2 ACPPVC-50 system, 50 rays are shown for each incidence angle.

The predicted angular acceptance and optical efficiency of the T-2 ACPPVC-50 are shown in figure 2.12. From figure 2.12 is can be seen that the angular acceptance of T-2 ACPPVC-50 is greater than 50°, which is wider than that for the untruncated and T-1 ACPPVC-50 system, this is due to the further truncation of reflector 1 and 2 in this system. With decreasing solar incidence angle from 0° to -90°, the percentage of angular acceptance decreases dropping to 0 at a solar incidence angle below -37°. The highest optical efficiency for the T-2 ACPPVC-50 system is 88.67%.

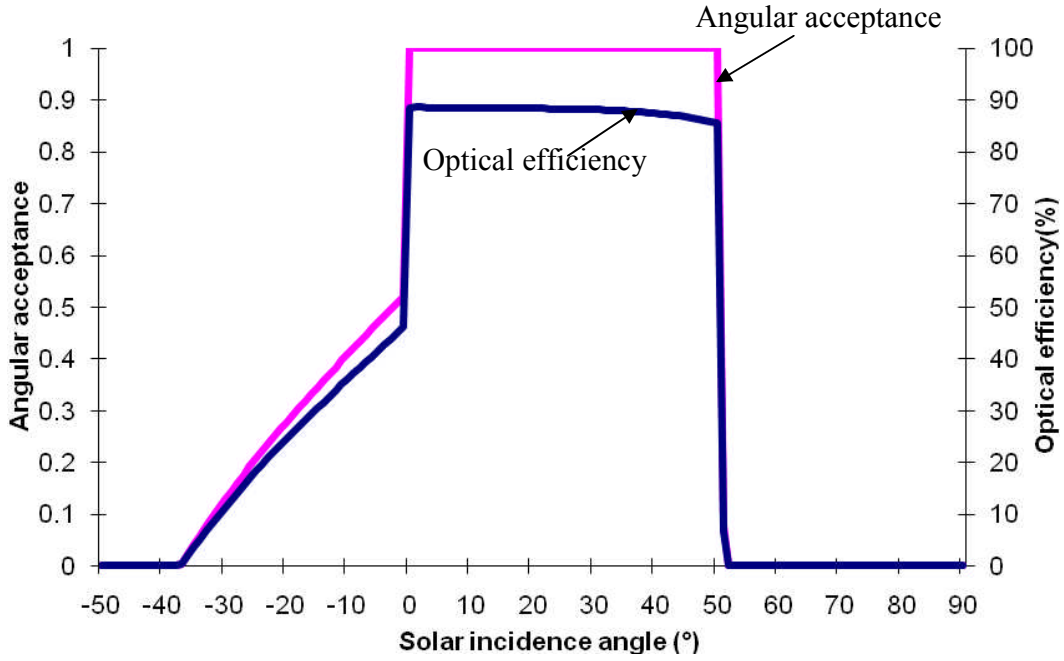

Figure 2.12 Predicted angular acceptance and optical efficiency for the T-2 ACPPVC-50

2.2.5.1.4 Ray trace and optical analysis for truncation level 3 (T-3) of the ACPPVC-50

The T-3 ACPPVC-50 had a geometric concentration ratio of 2.0 with 30% truncation for reflector 1 and 77% truncation for reflector 2. The geometrical characteristics of the T-3 ACPPVC-50 are shown in table 2.5.

Parameters		Values
Acceptance-half angles		43°& 57°
Absorber width(mm)		125
Aperture width(mm)		250
Length of reflector1(R1)(mm)		188.2
Length of reflector2(R2)(mm)		155.9
Concentration ratio		2.0
Truncation (%)	Ref1	30
	Ref2	77

Table 2.5 Geometrical characteristics of the T-3 ACPPVC-50

Ray trace diagrams for the T3 ACPPVC-50 for a range of solar incidence angles are shown in figure 2.13. The ray trace diagrams of the T-3 ACPPVC-50 have similar characteristics to those of the T-1 and T-2 ACPPVC-50 for the same solar incidence angles.

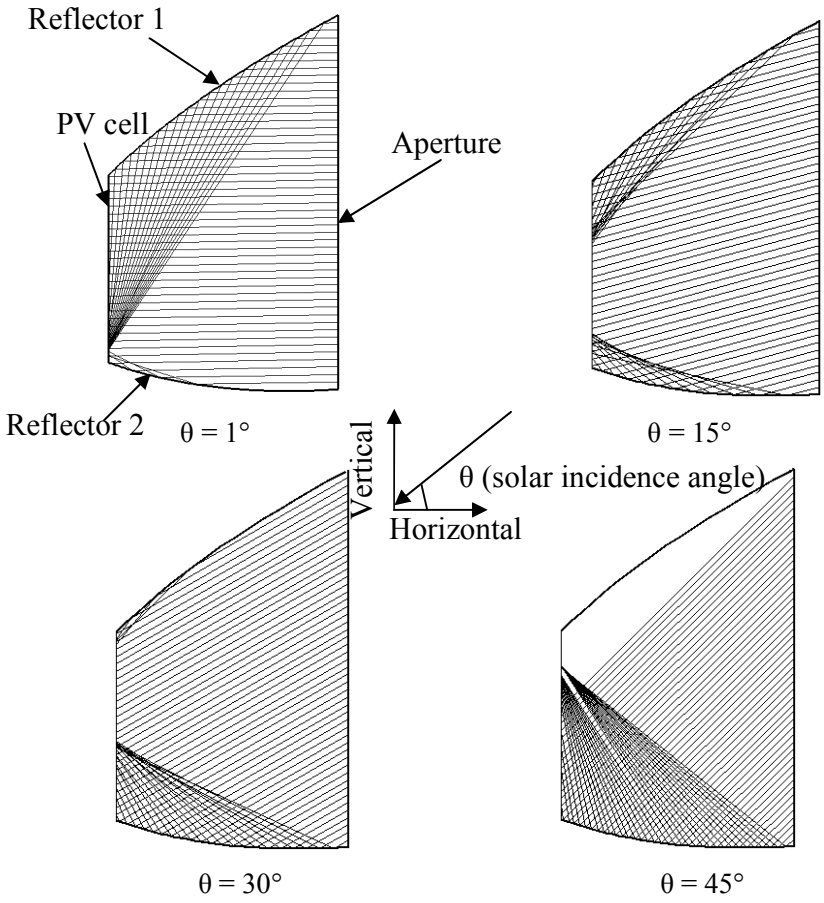

Figure 2.13 Ray trace diagrams for T-3 ACPPVC-50, 50 rays are included for each incidence angle.

The predicted angular acceptance and optical efficiency of the T-3 ACPPVC-50 are shown in figure 2.14. The T-3 ACPPVC-50 has the widest range of angular acceptance of the untruncated and truncated ACPPVC-50 systems, this is due to it having the greatest degree of truncation in reflectors 1 and 2. The highest optical efficiency for the T-3 ACPPVC-50 system is 88.67%.

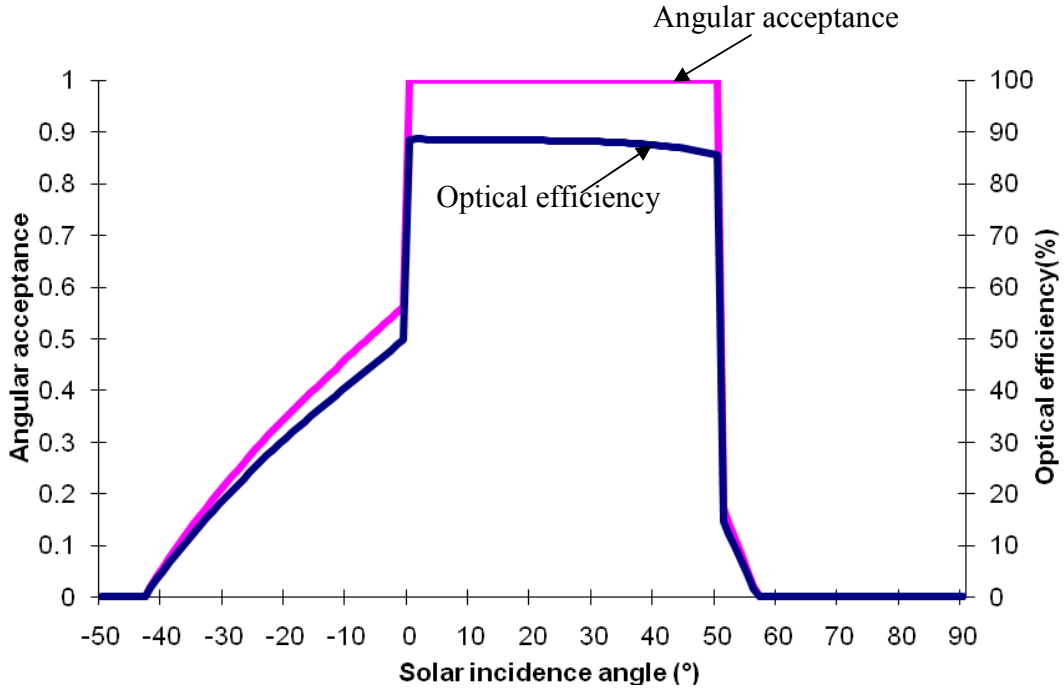

Figure 2.14 Predicted angular acceptance and optical efficiency for the T3 ACPPVC-50

2.2.5.2 Ray trace and optical analysis of an ACPPVC-55 system

Untruncated and truncated ACPPVC-55 system designs as shown in figure 2.15 were investigated. The untruncated ACPPVC-55 had a geometric concentration ratio of 3.06 with acceptance half angles of 0° and 55°, respectively. The truncated ACPPVC-55 shown in figure 2.15 had a geometric concentration ratio of 1.99 with 0% truncation for reflector 1 and 69.7% truncation for reflector 2. Further truncation of the ACPPVC-55 reduced the

concentration ratio below 2.0, therefore only one level of truncation for the ACPPVC-55 system was analysed.

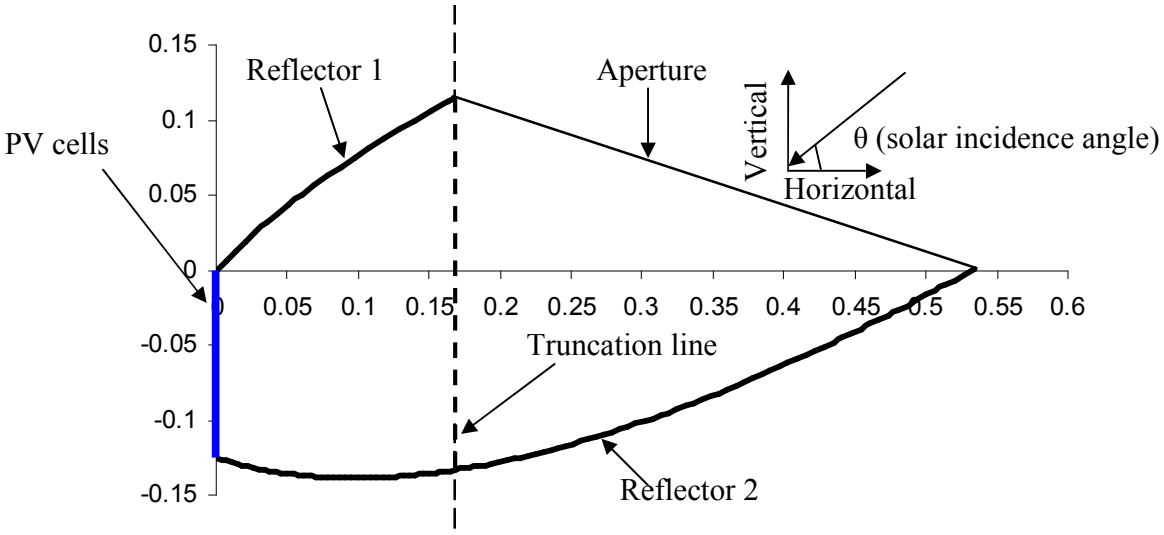

Figure 2.15 ACPPVC-55 system with acceptance-half angle of 0° and 55°, all dimensions in 'm'.

2.2.5.2.1 Ray trace and optical analysis of an untruncated ACPPVC-55

The geometrical characteristics of the untruncated ACPPVC-55 are given in table 2.6. In all simulations undertaken, the solar incidence angle (θ) was considered from the horizontal as illustrated in figure 2.16.

Parameters		Values
Acceptance-half angles		0° & 55°
Absorber width(mm)		125
Aperture width(mm)		383.0
Length of reflector1(R1)(mm)		204.5
Length of reflector2(R2)(mm)		560.4
Concentration ratio		3.06
Truncation (%)	Ref1	0
	Ref2	0

Table 2.6 Geometrical characteristics of the untruncated ACPPVC-55

Ray trace diagrams for the untruncated ACPPVC-55 for a selection of solar incidence angles are shown in figure 2.16. From figure 2.16, it can be seen that at incidence angles of 1°, 15°, 30°, 45° and 50°(from the horizontal), all rays incident at the aperture are incident on the PV cells. When the solar incidence angle is 45° and 50°, the reflected rays start concentrate on the middle and lower part of the PV cell surface. This may lead to an increase in the local temperature of the PV cell, and potentially result in a decrease in the electrical conversion efficiency. Decreasing the solar incidence angle towards the horizontal, more rays are reflected onto the absorber by reflector 1, when compared to reflector 2.

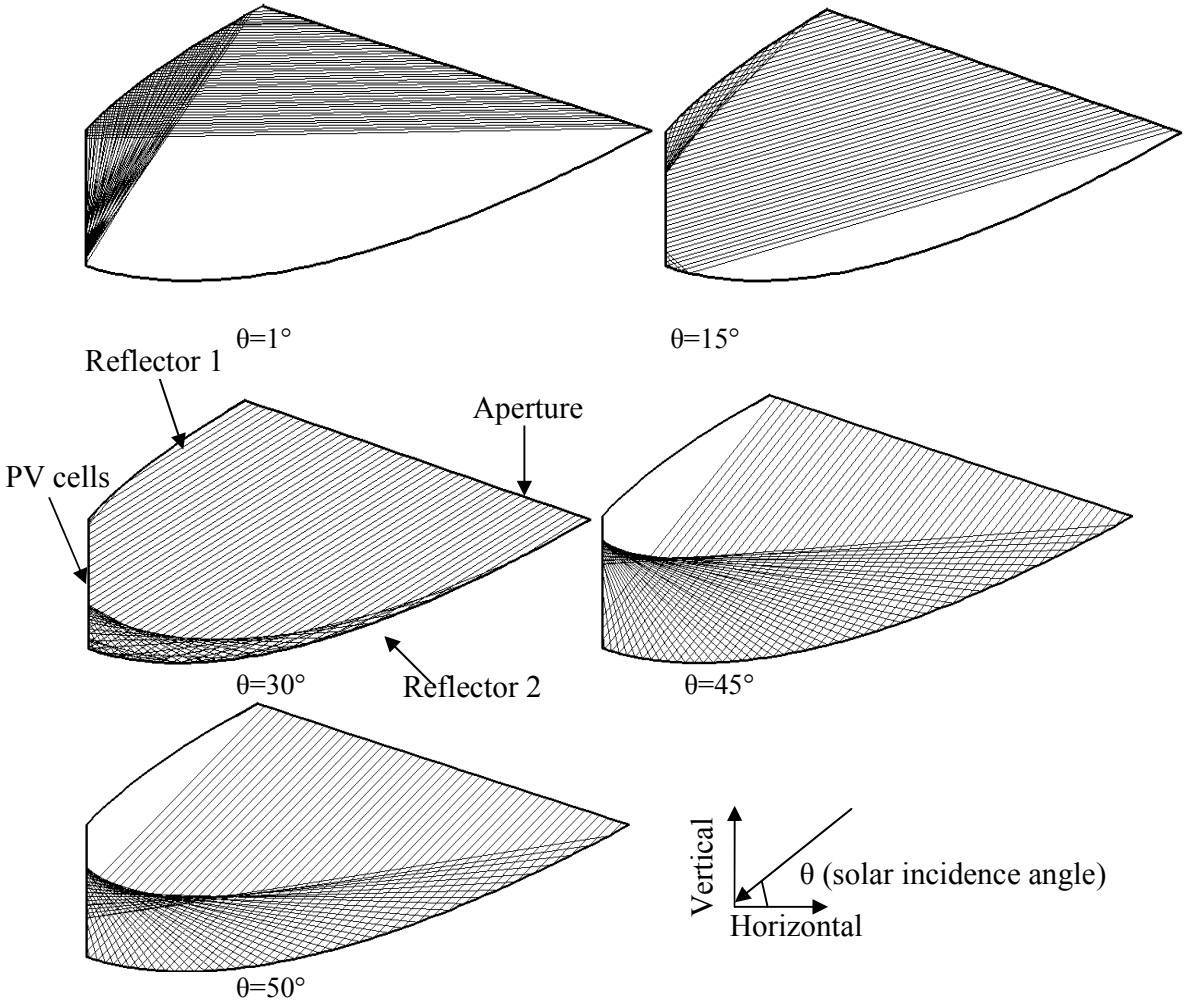

Figure 2.16 Ray trace diagrams for the untruncated ACPPVC-55, 50 rays are shown for each incidence angle

The predicted angular acceptance and optical efficiency of the untruncated ACPPVC-55 are shown in figure 2.17. The angular acceptance is 1 for incidence angles between 0° and 55°. When the solar incidence angle is above 55°, the percentage of angular acceptance instantaneously drops to 0. The highest predicted optical efficiency for the untruncated ACPPVC-55 is 88.67%.

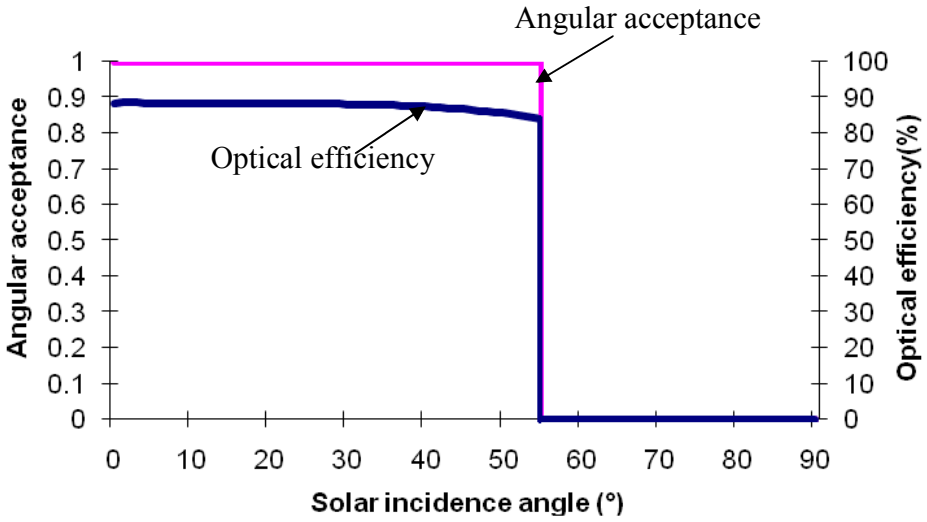

Figure 2.17 Predicted angular acceptance and optical efficiency for the untruncated ACPPVC-55 system

2.2.5.2.2 Ray trace and optical analysis for a truncated ACPPVC-55

The truncated ACPPVC-55 had a geometric concentration ratio of 1.99 with 0% truncation for reflector 1 and 69.7% truncation for reflector 2. The geometrical characteristics for the truncated ACPPVC-55 are shown in table 2.7.

Parameters		Values
Acceptance-half angles		38° & 55°
Absorber width(mm)		125
Aperture width(mm)		248.5
Length of reflector1(R1)(mm)		204.5
Length of reflector2(R2)(mm)		169.8
Concentration ratio		1.99
Truncation (%)	Ref1	0
	Ref2	69.7

Table 2.7 Geometrical characteristics of the truncated ACPPVC-55

Ray trace diagrams for the truncated ACPPVC-55 over a range of solar incidence angles are shown in figure 2.18. From figure 2.18 it can be observed that at incidence angles of 1°, 15°, 30°, 45° and 50° (from the horizontal), all the rays incident at the aperture are incident on the PV cell. When the solar incidence angles are 45° and 50°, similar behaviour is found compared to those of the untrunacted ACPPVC-55 system at the same solar incidence angles, a local high intensity flux can be seen in the middle and lower part of the PV cell. When the solar incidence angle decreases towards the horizontal, more rays are reflected onto the absorber by reflector 1, compared to reflector 2.

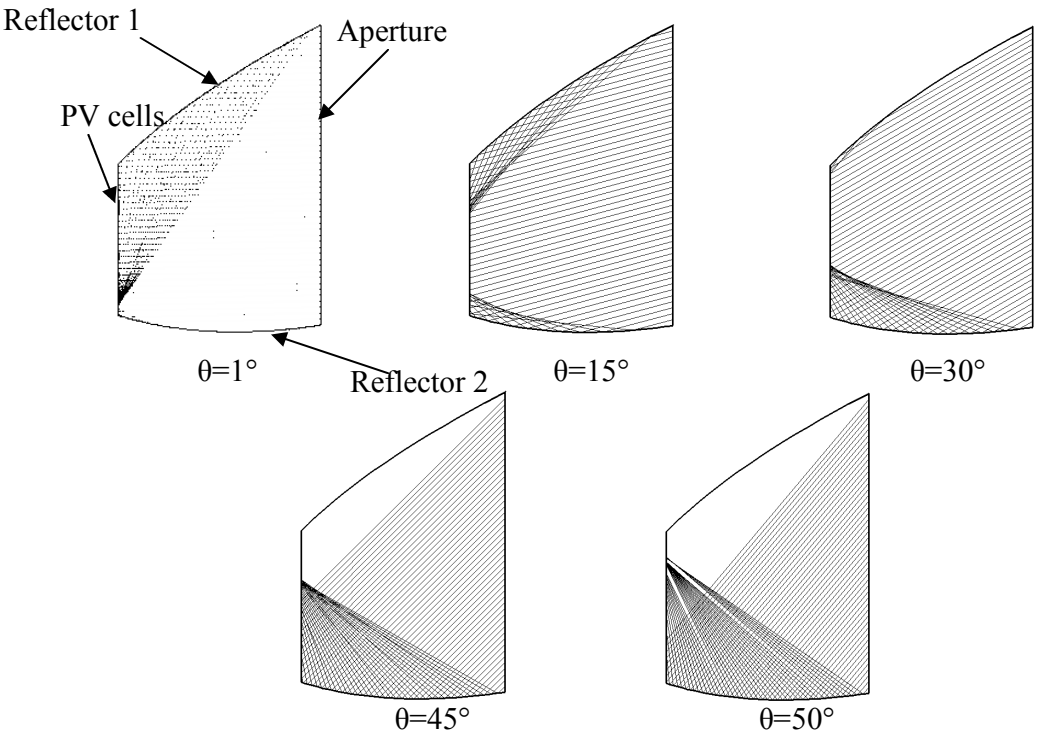

Figure 2.18 Ray trace diagrams for truncated ACPPVC-55 system, 50 rays are shown for each incidence angle

The predicted angular acceptance and optical efficiency of the truncated ACPPVC-55 are shown in figure 2.19. From figure 2.19 it can be seen that the truncated ACPPVC-55 has a wide range of angular acceptance in the range from -38° to 55°. The angular acceptance is

100% at incidence angles within the range from 0° to 55°. When the solar incidence angle is above 55°, the percentage of angular acceptance instantaneously drops to 0. The highest predicted optical efficiency of the truncated ACPPVC-55 is 88.67%.

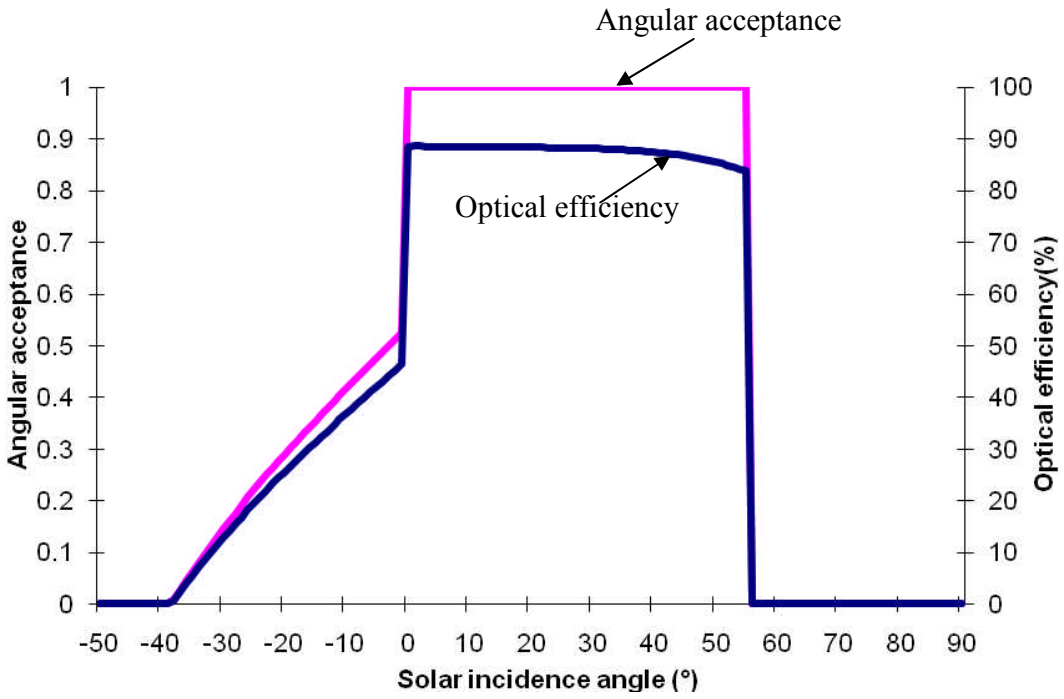

Figure 2.19 Predicted angular acceptance and optical efficiency for the truncated ACPPVC-55

2.2.5.3 Ray trace and optical analysis of an ACPPVC-60 system

Untruncated and truncated ACPPVC-60 systems were investigated, as shown in figure 2.20. The untruncated ACPPVC-60 had a geometric concentration ratio of 2.83 with acceptance half angles of 0° and 60°. The truncated ACPPVC-60 shown in figure 2.20 had a geometric concentration ratio of 1.79 with 0% truncation for reflector 1 and 74.5% truncation for reflector 2.

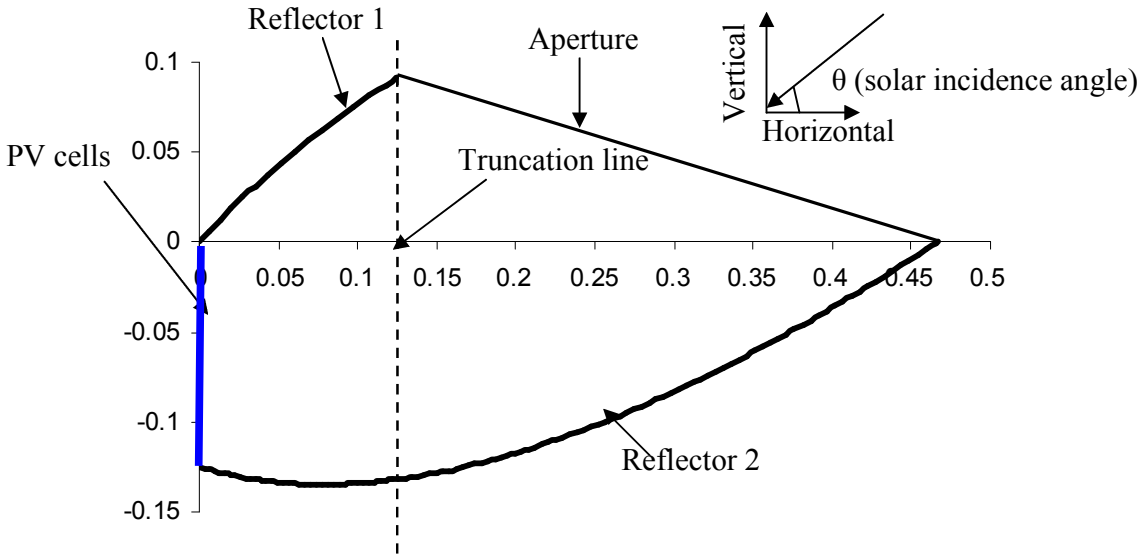

Figure 2.20 ACPPVC-60 systems with acceptance-half angle of 0° and 60°, all dimensions in 'm'.

2.2.5.3.1 Ray trace and optical analysis of an untruncated ACPPVC-60

The geometrical characteristics for the untruncated ACPPVC-60 are shown in table 2.8. In all undertaken simulations, the solar incidence angle (θ) was considered from the horizontal as illustrated in figure 2.21.

Parameters		Values
Acceptance-half angles		0°& 60°
Absorber width(mm)		125
Aperture width(mm)		353.7
Length of reflector1(R1)(mm)		155.3
Length of reflector2(R2)(mm)		494.6
Concentration ratio		2.83
Truncation (%)	Ref1	0
	Ref2	0

Table 2.8 Geometrical characteristics of the untruncated ACPPVC-60

Ray trace diagrams for the untruncated ACPPVC-60 over a range of solar incidence angles are shown in figure 2.21. From figure 2.21 it can be seen that at incidence angles of 1°, 15°, 30°, 45° and 55°(from the horizontal), all the rays incident at the aperture are incident on the PV cell. When the solar incidence angles are 45° and 55°, the reflected rays start to

concentrate on the middle and lower part of the PV cell surface. Decreasing the solar incidence angle towards the horizontal, more rays are reflected onto the PV by reflector 1, compared to the reflector 2.

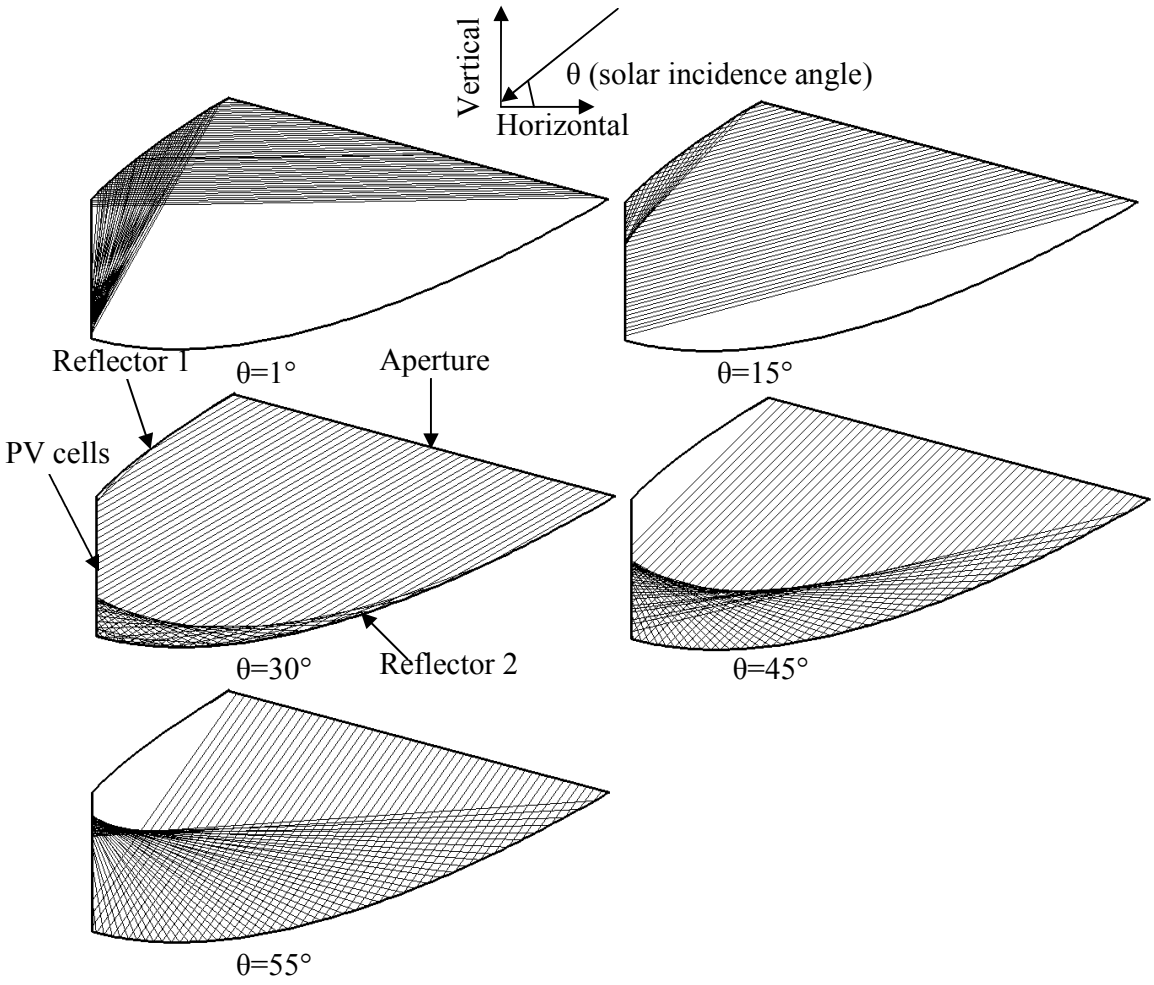

Figure 2.21 Ray trace diagrams for the untruncated ACPPVC-60 system, 50 rays are shown for each incidence angles.

The predicted angular acceptance and optical efficiency of the untruncated ACPPVC-60 are shown in figure 2.22. From figure 2.22 it can be seen that the angular acceptance is 100% at the incidence angles within the range between 0° to 60°. When the solar incidence angle is above 60°, the angular acceptance instantansouely drops to 0%. The predicted highest optical efficiency of the untruncated ACPPVC-60 is 88.67%.

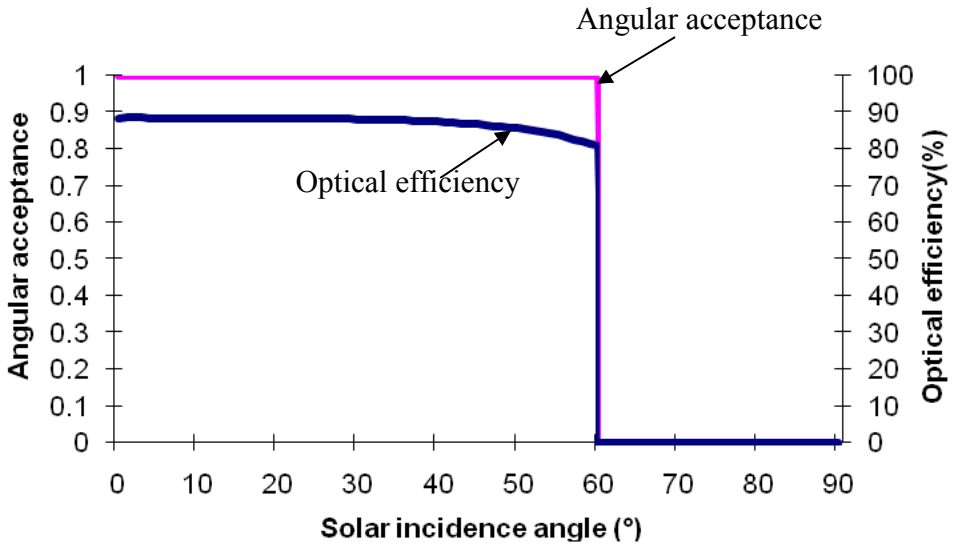

Figure 2.22 Predicted angular acceptance and optical efficiency for the untruncated ACPPVC-60

2.2.5.3.2 Ray trace and optical analysis of a truncated ACPPVC-60

The truncated ACPPVC-60 had a geometric concentration ratio of 1.79 with 0% truncation for reflector 1 and 74.5% truncation for reflector 2. The geometrical characteristics for the truncated ACPPVC-60 are shown in table 2.9.

Parameters		Values
Acceptance-half angles		46 °& 60°
Absorber width(mm)		125
Aperture width(mm)		223.3
Length of reflector1(R1)(mm)		155.3
Length of reflector2(R2)(mm)		125.9
Concentration ratio		1.79
Truncation (%)	Ref1	0
	Ref2	74.5

Table 2.9 Geometrical characteristics of the truncated ACPPVC-60

Ray trace diagrams for the truncated ACPPVC-60 over a selection of solar incidence angles are shown in figure 2.23. The truncated ACPPVC-60 system has similar optical behaviour as those of the untruncated system at the same solar incidence angles.

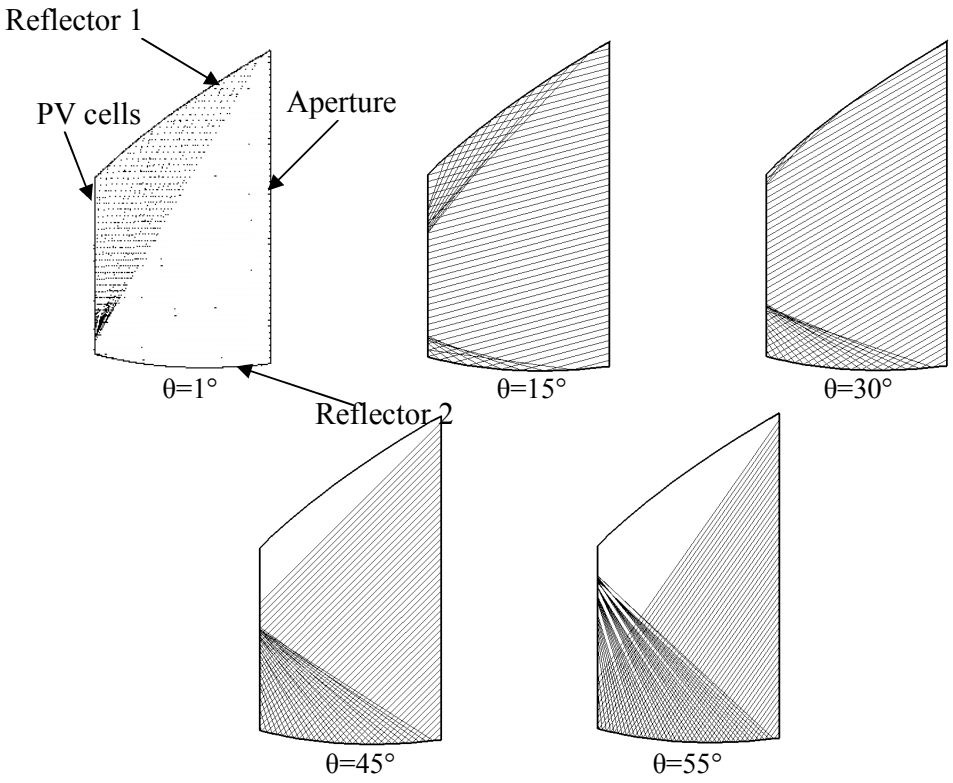

Figure 2.23 Ray trace diagrams for truncated ACPPVC-60, 50 rays are shown for each diagram

The predicted angular acceptance and optical efficiency of the truncated ACPPVC-60 are shown in figure 2.24. From figure 2.24 it can be seen that the truncated ACPPVC-60 has a wide range of angular acceptance covering the range from -46° to 60°. The angular acceptance is 1 at incidence angles between 0° and 60°. When the solar incidence angle is above 60°, the angular acceptance instantaneously drops to 0. The highest optical efficiency for the truncated ACPPVC-60 is 88.67%.

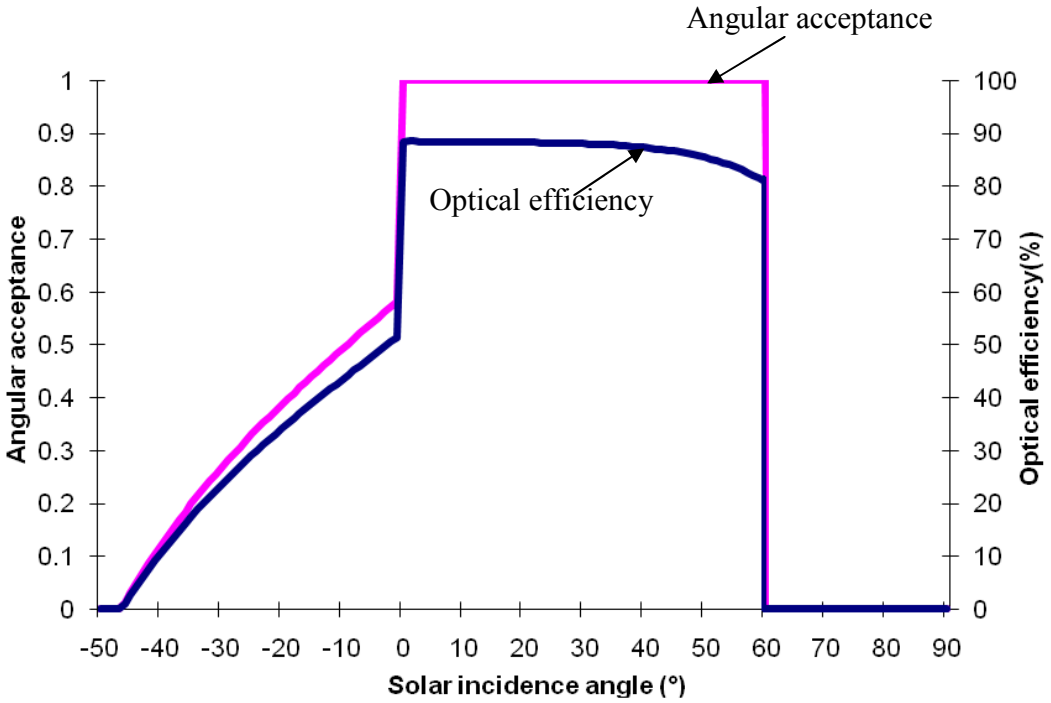

Figure 2.24 Predicted angular acceptance and optical efficiency for the truncated ACPPVC-60

2.2.5.4 Ray trace and optical analysis for the truncated ACPPVC-50 inclined by 10° to vertical

Installing the truncated ACPPVC-50 system at a 10° inclination to the vertical would increase the range of angular acceptance to include higher solar incidence angles for the ACPPVC-50 systems. The results of the simulations undertaken for the T-1, T-2, and T-3 ACPPVC-50 systems are presented in the following figures 2.25 to 2.28. Ray trace diagrams and the predicted optical performance function for the 10° tilted T-1 ACPPVC-50 are shown in figures 2.25 and 2.26. From figures 2.25 and 2.26, it can be found that the tilted T-1 ACPPVC-50 where the PV cells are inclined by 10° to the vertical shifts the angular acceptance and optical efficiency by 10°. The maximum solar incidence angle is translated from 50° to 60°. The angular acceptance of the tiled T-1 ACPPVC-50 system is 1 for the solar incidence angle between 10° and 60°, and is in the range from 0.34 to 0.47, when the solar incidence angle is between 0° and 10°.

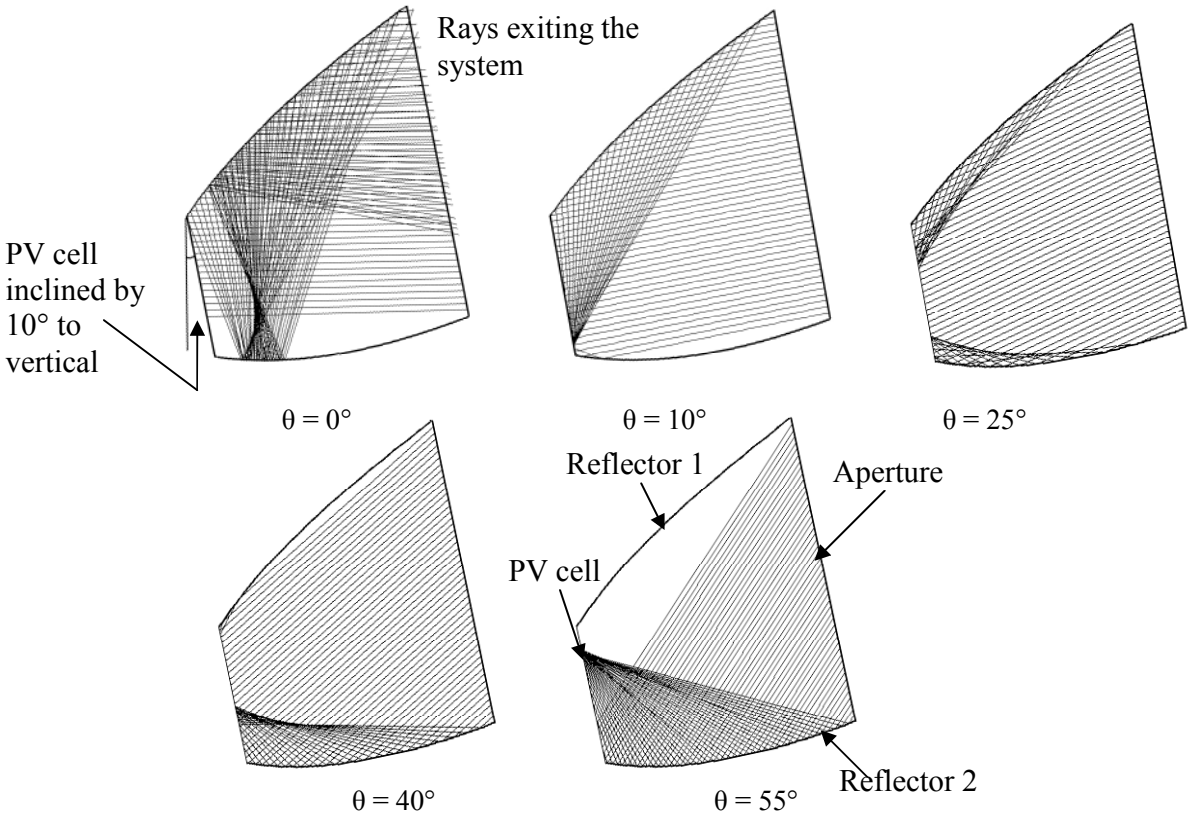

Figure 2.25 Ray trace diagrams of the T-1 ACPPVC-50 inclined by 10° to vertical, 50 rays are shown for each solar incidence angles.

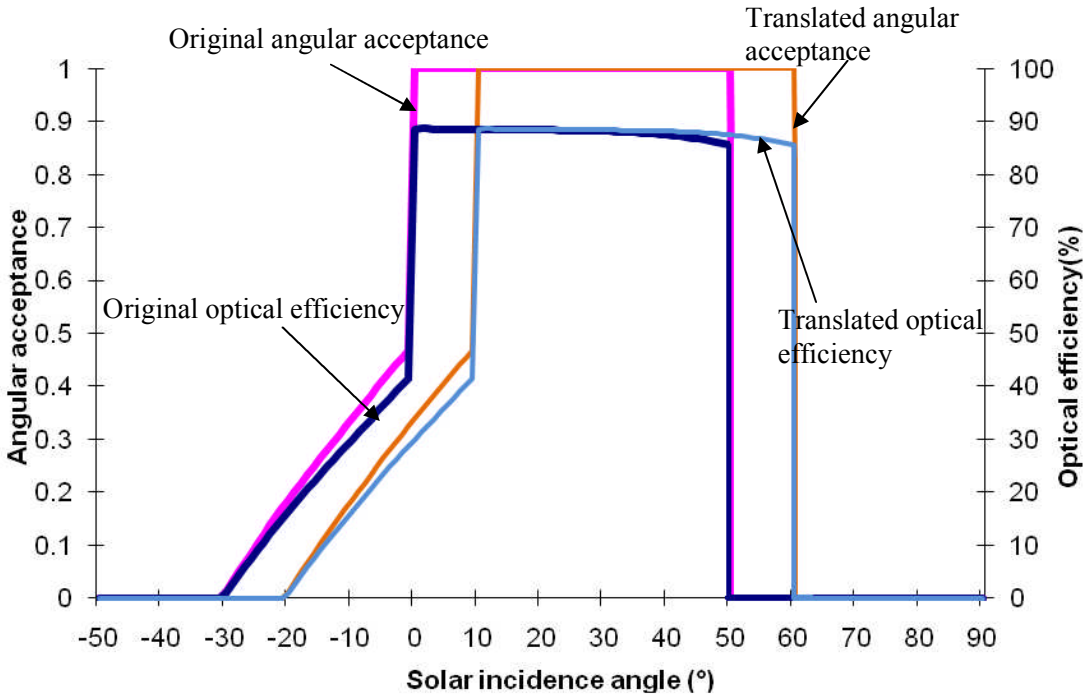

Figure 2.26 Original and translated angular acceptance and optical efficiency for the T-1 ACPPVC-50

The predicted optical performance function of the 10° tilted T-2 and T-3 ACPPVC system are illustrated in figure 2.27 and 2.28. The 10° tilted T-2 and T-3 ACPPVC-50 system have similar angular acceptance and optical efficiency to those of the T-1 ACPPVC-50. They all translate the angular acceptance and optical efficiency function by 10°. However, the angular acceptance of the T-2 and T-3 ACPPVC-50 system are higher than that of the T-1 in the range from 0° to 10°, this is due to the further truncation in reflector 1 and 2.

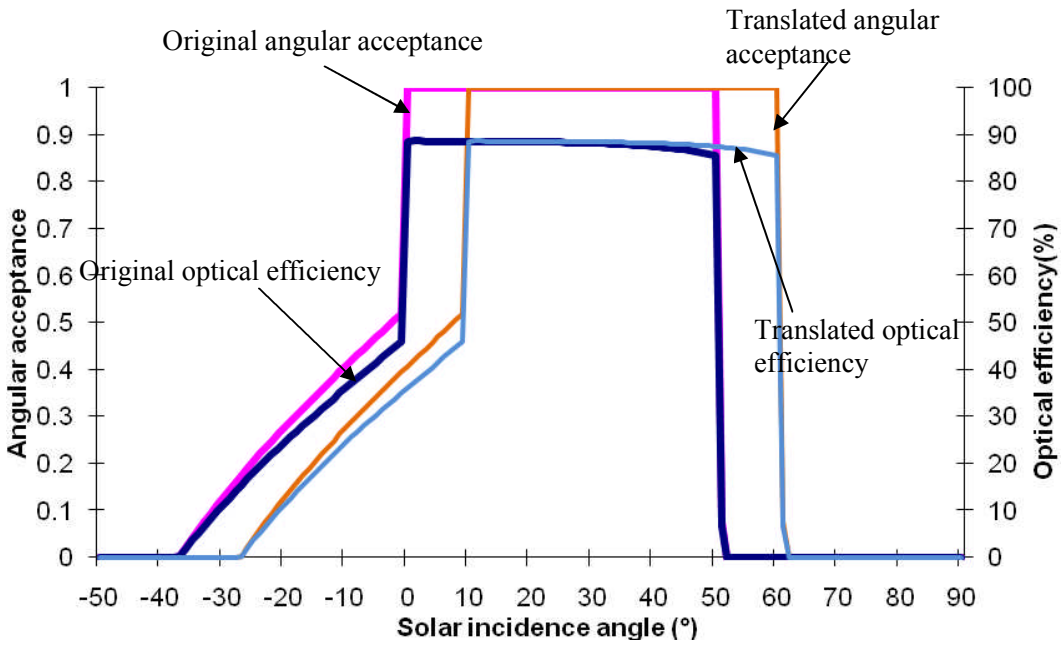

Figure 2.27 Original and translated angular acceptance and optical efficiency for the T-2 ACPPVC-50

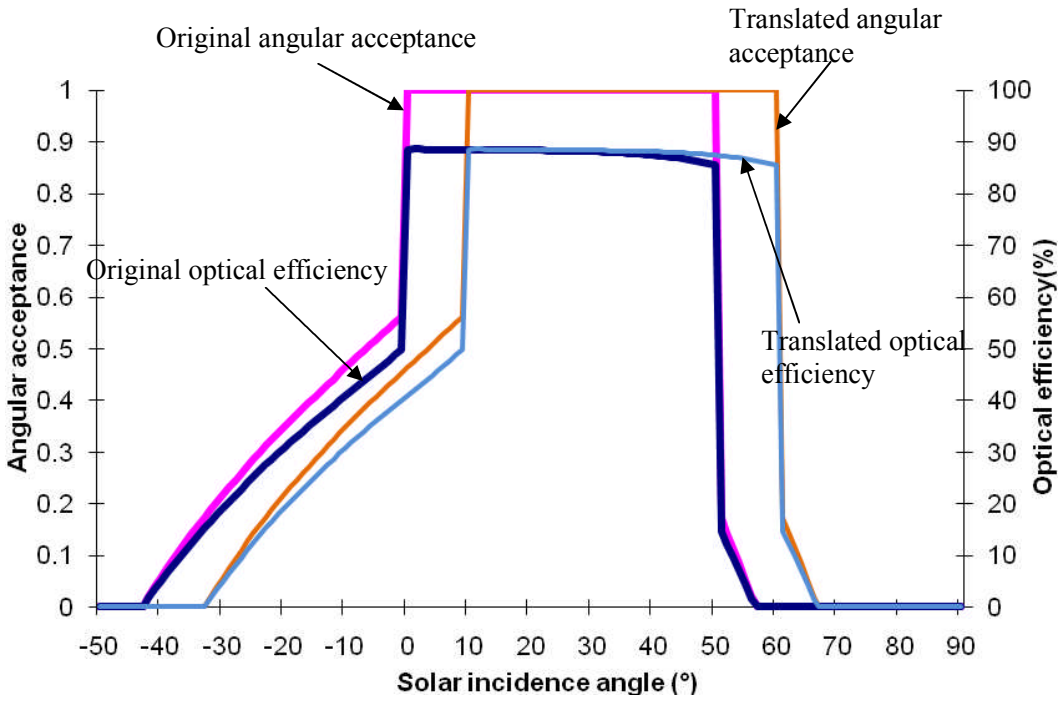

Figure 2.28 Original and translated angular acceptance and optical efficiency for the T-3 ACPPVC-50

2.2.5.5 Optical analysis for the truncated ACPPVC-55 inclined by 5° to vertical

Installing the truncated ACPPVC-55 system at a 5° inclination to the vertical would increase the range of angular acceptance to include higher solar incidence angles for the ACPPVC-55 systems. The predicted angular acceptance and optical efficiency for the tilted truncated ACPPVC-55 are shown in figures 2.29. From figures 2.29, it can be seen when the truncated ACPPVC-55 tilts to the vertical at an angle of 5°, the system angular acceptance and optical efficiency are shifted by 5°. The maximum solar incidence angle at which radiation is captured is translated from 55° to 60°. The angular acceptance of the tilted truncated ACPPVC-55 system is 1 for the solar incidence angle between 5° and 60°, and is in the range from 0.48 to 0.52, when the solar incidence angle is between 0° and 5°.

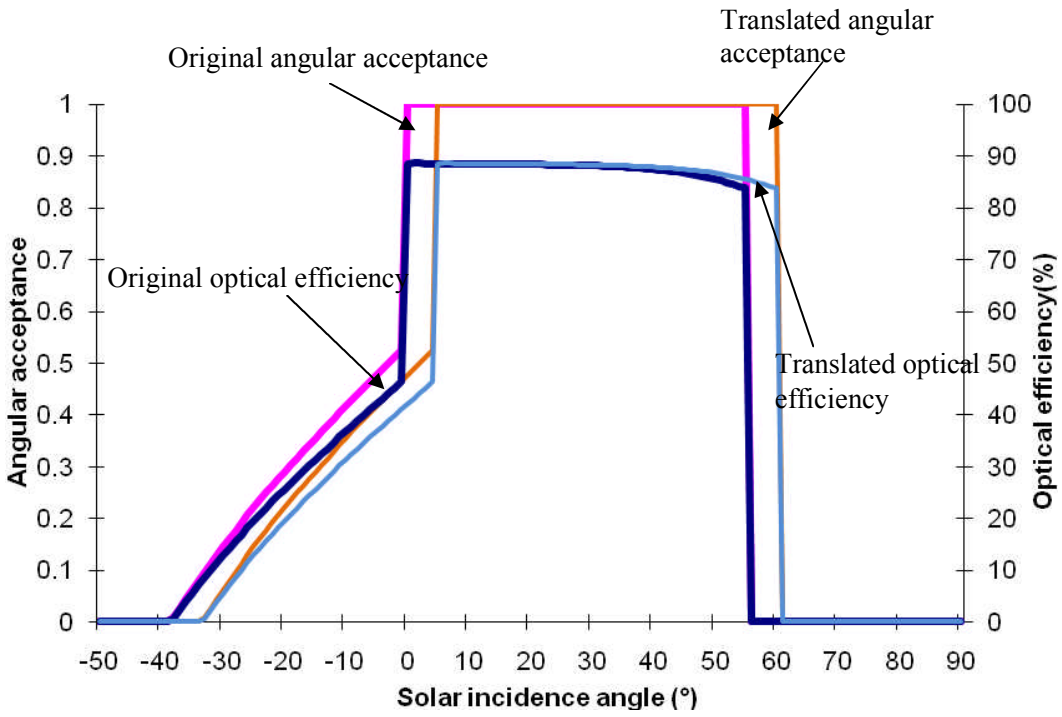

Figure 2.29 Original and translated angular acceptance and optical efficiency for the truncated ACPPVC-55

2.3 Solar concentration distribution across the PV cells

A two dimensional ray trace technique was employed to predict the solar concentration on the PV cells. The prediction of solar concentration distribution across the PV cells for the untruncated and truncated ACPPVC-50, ACPPVC-55 and ACPPVC-60 at selected solar incidence angles are shown in figures 2.30 to 2.37.

Figures 2.30 to 2.33 present the solar concentration distributions across the PV cells in the untruncated and truncated ACPPVC-50 systems. From figures 2.30 to 2.33, it can be seen that when the solar incidence angle is 15°, two peaks occur in the solar flux on the PV cells at a distance around 0.05m and 0.1m from the upper reflector of all ACPPVC-50 systems.

They are a combination of the direct radiation from the sun and reflected radiation from the upper and lower reflectors. For the 30° solar incidence angle, the solar concentration has similar characteristics to that for the 15° solar incidence angle, two peaks in solar flux are found on the PV cells at a distance around 0.01m and 0.07m from the upper reflector, respectively. For the 5° solar incidence angle, a single peak solar flux occurs on the PV cells at a distance around 0.11m from the upper reflector, due to solar radiation being reflected from the upper reflector only. For the 45° solar incidence angle, the solar concentration distribution has similar characteristics to that for the 5° solar incidence angle, a single peak in solar flux is found on the PV cell at a distance around 0.015 meter from the upper reflector, since it is reflected from the lower reflector only.

For the 15° solar incidence angle, the peak solar concentrations of the untruncated ACPPVC-50 system are around 8 and 5.5 respectively. They are higher than those of the truncated ACPPVC-50. Similar characteristics are also found at other solar incidence angles, this is due to the untruncated ACPPVC-50 system having the highest geometric concentration ratio. It also can be observed that the peak solar concentration occurring on the PV cells decreases with the decreasing system geometric concentration ratio.

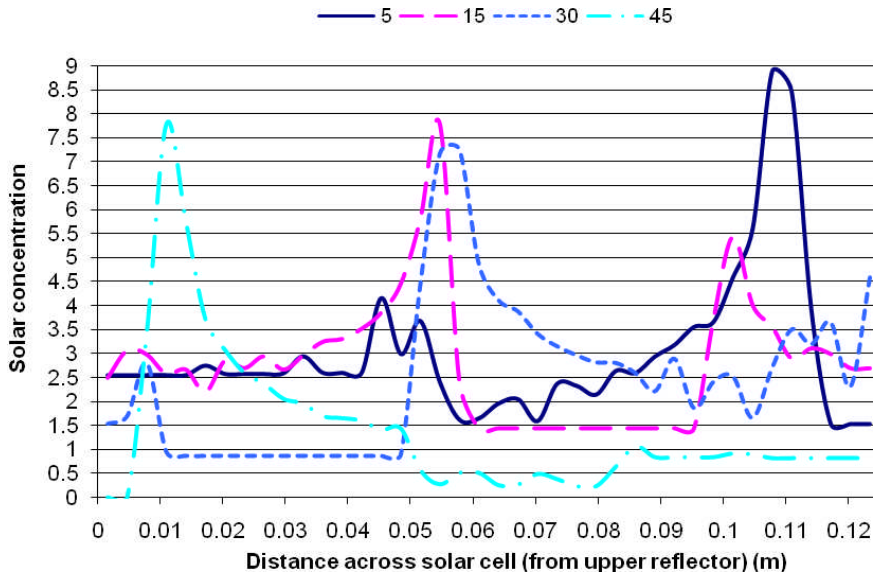

Figure 2.30 Solar concentration distributions across the photovoltaic cell of the un-truncated ACPPVC-50 system for selected solar incidence angles of 5°, 15°, 30° and 45°

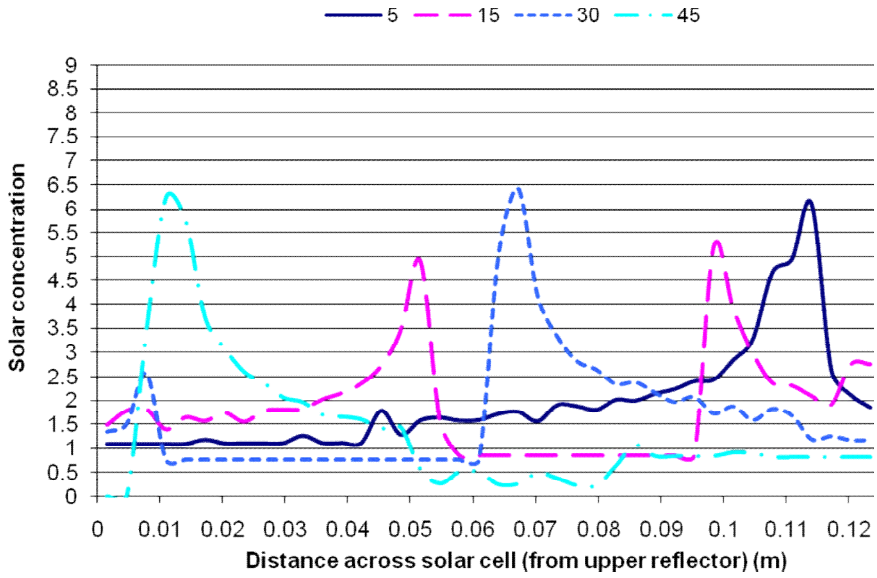

Figure 2.31 Solar concentration distributions across the photovoltaic cell of the T-1 ACPPVC-50 system for selected solar incidence angles of 5°, 15°, 30° and 45°

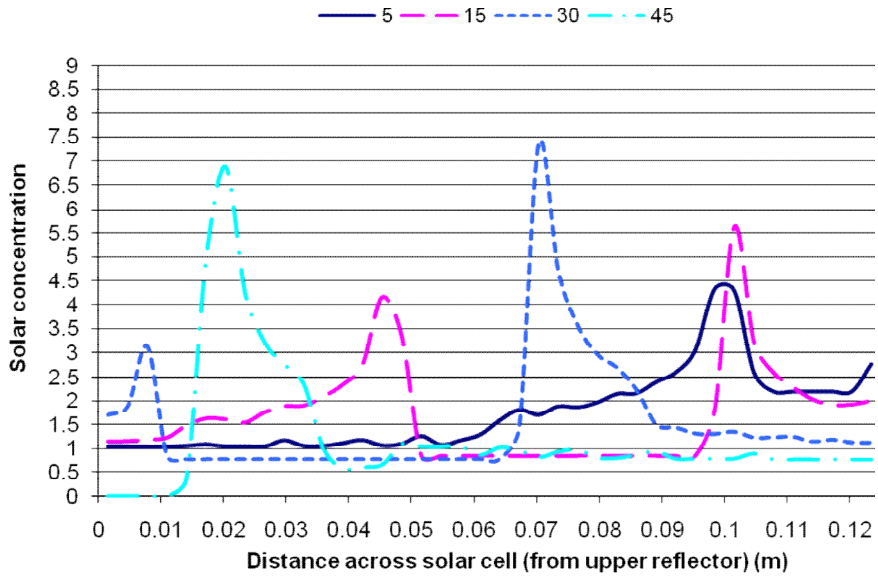

Figure 2.32 Solar concentration distributions across the photovoltaic cell of the T-2 ACPPVC-50 system for selected solar incidence angles of 5°, 15°, 30° and 45°

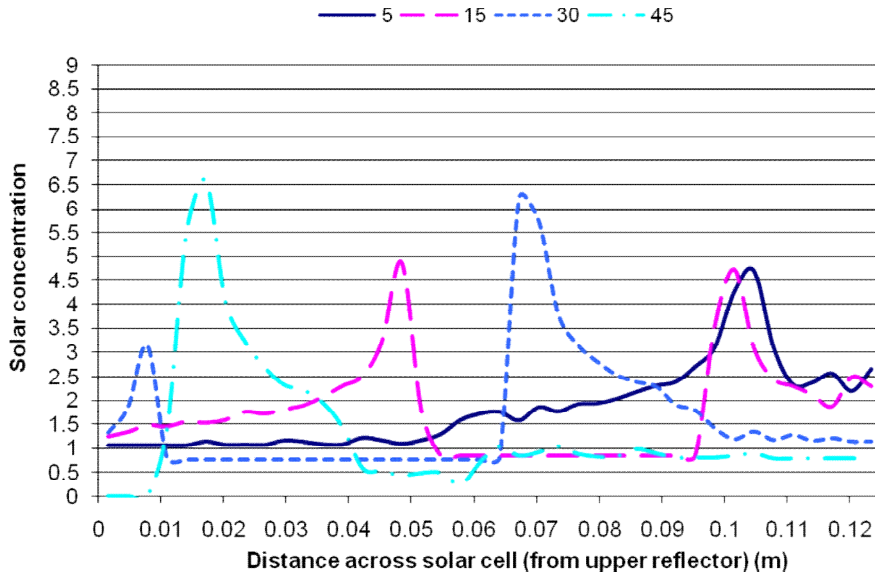

Figure 2.33 Solar concentration distributions across the photovoltaic cell of the T-3 ACPPVC-50 system for selected solar incidence angles of 5°, 15°, 30° and 45°

Figures 2.34 and 2.35 show the solar concentration distribution across the PV cells of the untruncated and truncated ACPPVC-55 systems. From figure 2.34 and 2.35, it can be seen that when the solar incidence angle is 15°, two peaks occur in the solar flux on the PV cells at a distance around 0.05m and 0.11m from the upper reflector. For the 30° solar incidence angle, the predicted solar concentration distribution has similar characteristics to that for the 15° solar incidence angle, two peaks in solar flux are found on the PV cells at a distance around 0.01m and 0.08m from the upper reflector, respectively. For the 40°, 45° and 50° solar incidence angles, a single peak solar flux occurs on the PV cell, due to solar radiation being reflected from the lower reflector only.

When the solar incidence angle is 15°, the peak solar concentrations of the untruncated ACPPVC-55 system are around 8.5 and 4, respectively. which are higher than those of approximately 4.7 for the truncated ACPPVC-55 system. Similar characteristics are found for other solar incidence angles. The peak solar concentration occurring on the PV cells of the untruncated ACPPVC-55 system is higher than that for the truncated ACPPVC-55 system, this is due to the untruncated ACPPVC-55 having a higher geometric concentration ratio of 3.06 compared to that of 1.99 for the truncated ACPPVC-55.

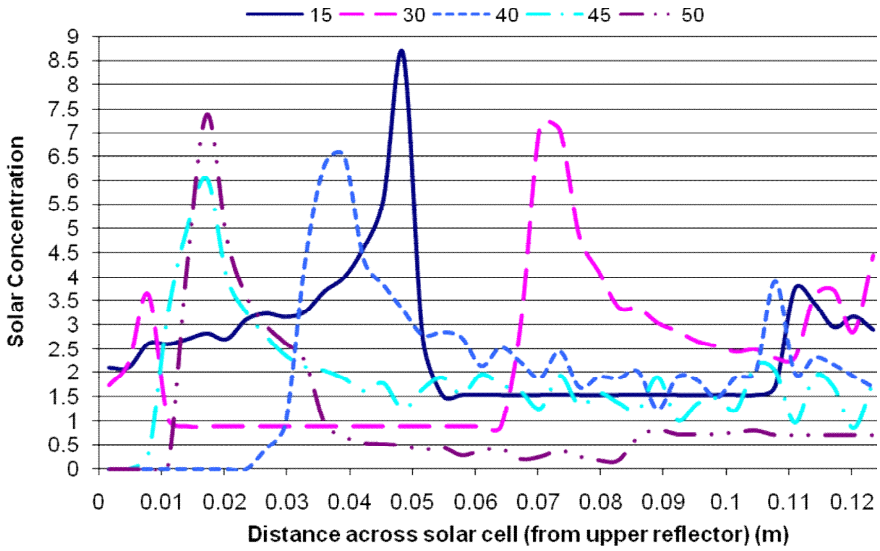

Figure 2.34 Solar concentration distributions across the photovoltaic cell of the untruncated ACPPVC-55 system for selected solar incidence angles of 15°, 30°, 40°. 45° and 50°

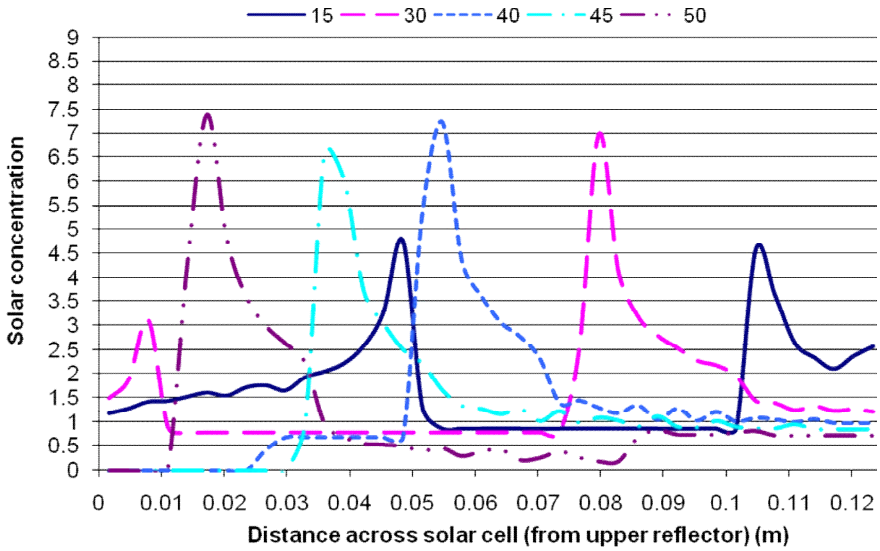

Figure 2.35 Solar concentration distributions across the photovoltaic cell of the truncated ACPPVC-55 system for selected solar incidence angles of 15°, 30°, 40°. 45° and 50°

Figures 2.36 and 2.37 illustrate the solar concentration distribution across the PV cells of the untruncated and truncated ACPPVC-60 systems. From figures 2.36 and 2.37, it can be observed that the solar concentration distribution along the ACPPVC-60 system has similar

characteristics to that for the ACPPVC-55 system. For solar incidence angles of 15° and 30°, two peaks in solar concentration are found on the PV cells. For the 40°, 45° and 50° solar incidence angles, a single peak solar flux occurs on the PV cell, due to solar radiation being reflected from the lower reflector only. The peak solar concentration occurring on the PV cells of untruncated system is higher than that for the truncated system.

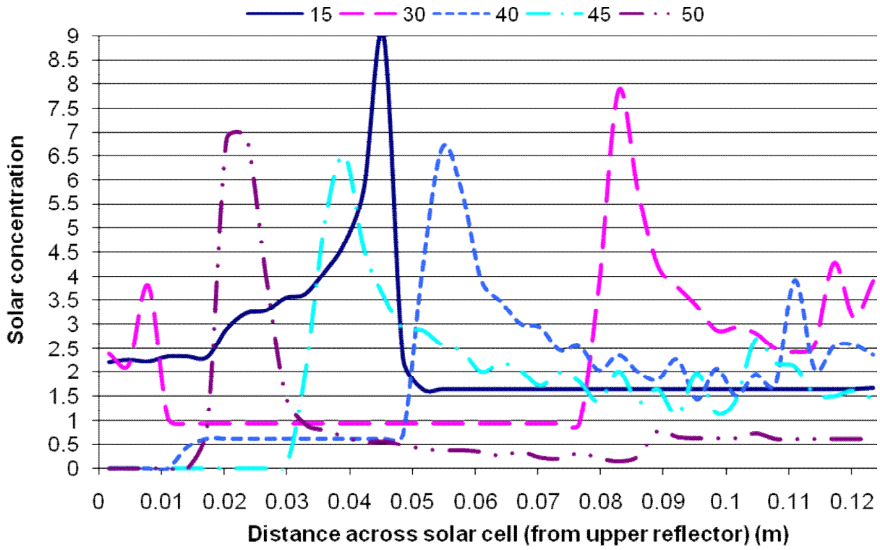

Figure 2.36 Solar concentration distributions across the photovoltaic cell of the untruncated ACPPVC-60 system for selected solar incidence angles of 15°, 30°, 40°. 45° and 50°

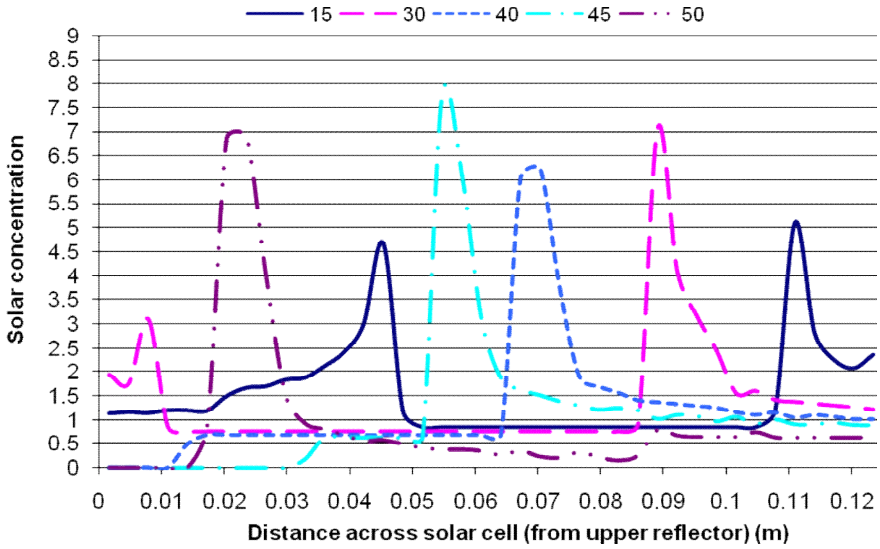

Figure 2.37 Solar concentration distributions across the photovoltaic cell of the truncated ACPPVC-60 system for selected solar incidence angles of 15°, 30°, 40°. 45° and 50°

2.4 Conclusion

A detailed analysis of the optical performance and angular acceptance of untruncated and truncated ACPPVC systems was undertaken. The following conclusions were drawn.

- The angular acceptance was 1 within the range of incidence angles between the original acceptance-half angles for the untruncated and truncated systems.
- Increased truncation leads to increased angular acceptance with reduced maximum geometric concentration. The highest optical efficiency predicted was 88.67% for all ACPPVC systems.
- The ACPPVC-60 had the greatest range of angular acceptance for solar incidence angles between 0° and 90°, due to the designed highest acceptance-half angle of 60° in the three types of ACPPVC systems.
- The solar concentrations were non-uniformly distributed on the PV cell.
- Predicted peak solar concentrations of higher than 5 were found on the PV for the untruncated and truncated ACPPVC systems at selected solar incidence angles.
- The peak solar concentration occurring on the PV cells decreased with the decreasing system geometric concentration ratio.

The truncated ACPPVC-55 system with a geometric concentration ratio of 2.0, which was more suitable for the UK climate compared to the other ACPPVC systems simulated, due to the range of angular acceptance, was chosen for the further work.

Chapter 3 Description of experimental programme

3.1 Introduction

Following the optical analysis of the untruncated and truncated ACPPVC-50, ACPPVC-55 and ACPPVC-60 systems, it was proposed to design, fabricate and experimentally investigate a prototype of the truncated ACPPVC-55 system coupled with a PCM cooling system. The annual maximum and minimum altitude of the sun at noon at the University of Warwick, Coventry, U.K are 60.8°and 13.8°, respectively, and these were used in determining the operating parameters for this investigation. The dimensions of the truncated ACPPVC-55 system were discussed in Chapter 2. The components of the ACPPVC-55/PCM included the PV absorber, reflectors, reflector supports, PCM material, PCM container, aperture cover and support frame. The materials selection for the different components, and the individual component design and fabrication of the ACPPVC-55/PCM system are described in the following sections.

3.2 Prototype ACPPVC-55/PCM system design

3.2.1 Reflective material employed for the ACPPVC-55 system (Reflectors)

The reflectors require a high reflectivity to minimise optical losses, with good durability to minimise environmental degradation. Reflectors can be classified into two main types, front surface mirrors and back surface mirrors (second surface mirrors). In a front surface reflector, the reflective material is often the structural material as well, for example a metal sheet reflector. For the back surface mirrors, the structural part of the reflector is the transmissive front surface, and the reflective layer consists of a sputtered, evaporated, sprayed or otherwise deposited highly reflective material, usually silver or aluminium (Brogren, 2004b). Brogren et al (2001) chose a bright anodised aluminium reflector with a

reflectivity of 0.81 for the reflectors in a CPC concentrator. In their later work, another sample of fresh anodised aluminium with a reflectivity of 0.87 was used for a PV concentrator (Brogren et al, 2004a). Mallick et al (2004) chose a self adhesive 'Radiant Mirror VM2000' supplied by the 3M Company as the reflector material for a PV concentrator, and its reflectivity was greater than 0.98. Unfortunately, VM 2000 reflective material is no longer manufactured. Acrosolar Company produces a laser silver mirror film, which is self-adhesive and has reflectivity of 0.94 (Anon, 2006a). A second surface silver mirror produced by Erie Electroverre Company has a reflectivity of 0.945 (Brogren, 2004b). Miro-Sun produced by Alanod Company is a weatherproof high reflective alumininum sheet and has been used for making CPC mirrors in vacuum tube collectors and for Concentrator PV. The Miro 4270 KKSP form of Miro-Sun is an aluminum-based material with the first layer under a SiO_2 low index and TiO_2 high index coating. It has a solar weighted reflectivity of 0.89-0.90 and a total reflectivity in the visible range of 0.95. It gives a high reflectivity for wavelengths in the range of 850-900nm and is suitable for PV utilisation (Anon, 2006b). The spectral reflectance of Miro 4270 KKSP at solar incidence angles of 10° and 70° in the range between 300nm and 1100nm, and the spectral response of a silicon solar cell are shown in figure 3.1. Another Alanod Company product Miro-Silver 4270 AG with a silver on aluminium sputtered first layer has a total light reflectivity of greater than 0.98, but Miro-Silver 4270 AG is not weather proof (Anon, 2006b). After comparing the above reflective materials, 0.4 mm thick Alanod Miro 4270 KKSP reflective aluminium sheets were chosen as the reflector for the experimental prototype system. The reflector dimensions are shown in table 3.1. For the prototype system, the total area of the reflectors was $0.375m^2$.

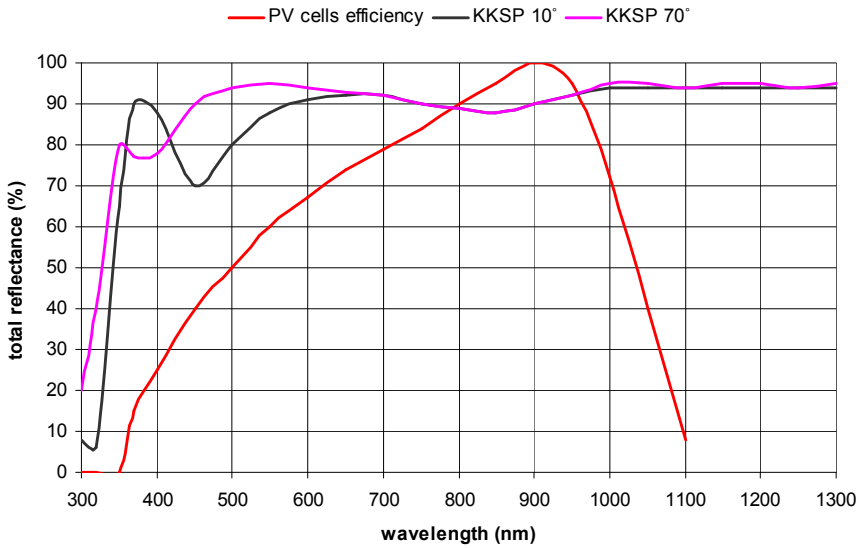

Figure 3.1 Total spectral reflectance of Miro 4270 KKSP along the wavelength (Anon, 2006a)

Truncated ACPPVC-55	Reflector 1	Reflector 2
Dimension	1000(mm)×205(mm)	1000(mm)×170(mm)

Table 3.1 Truncated ACPPVC-55 system reflector dimensions.

3.2.2 Material selection and design for reflector supports and back plate

The reflector supports and the back plate were required to construct the prototype structure, form the mirror profile and provide heat dissipation to reduce the solar cell temperature. The desired material characteristics for these components were low weight with good thermal conductivity. The physical properties of copper, aluminium and Al/Mg alloys are shown in table 3.2. After comparing the materials shown in table 3.2, aluminium which has lower density and good thermal conductivity, and is also cheap and easy to find, was selected for fabrication of the reflector supports and back plate.

Material	**Properties at 20 °C**		**Thermal conductivity** ($W\ m^{-1}K^{-1}$)	
	Density ($kg\ m^{-3}$)	**Specific heat capacity** ($kJ/kg \cdot °C$)	**0 °C**	**100 °C**
Copper	8954	0.3831	386	379
Aluminium	2707	0.896	202	206
Al/Magnesium alloys	2707	0.892	175	189

Table 3.2 Thermophysical properties of copper, aluminium and Al/Magnesium alloys (Holman, 1997)

3.2.2.1 Reflector support design

Two profiles of reflector support were designed and manufactured from 8mm thick aluminium, which had enough thickness, stiffness and strength to bond to and support the reflectors. Detailed 2D profiles for the reflector supports 1 and 2 are shown in figure 3.2 and 3.3, respectively. A 3D schematic sketch of the reflector supports are shown in figure 3.4. Steps 2mm wide and deep were machined at the base of the reflector supports to allow positive location of the reflector supports into the back plate. A further 1 mm high gap was left at the base of each reflector support to accommodate the solar cells and their coating as shown in figure 3.2(a) and 3.3(a). All the profile data points were transferred to 'AUTOCAD', and then machined using a 'CNC' machine in the workshops at the School of Engineering, the University of Warwick.

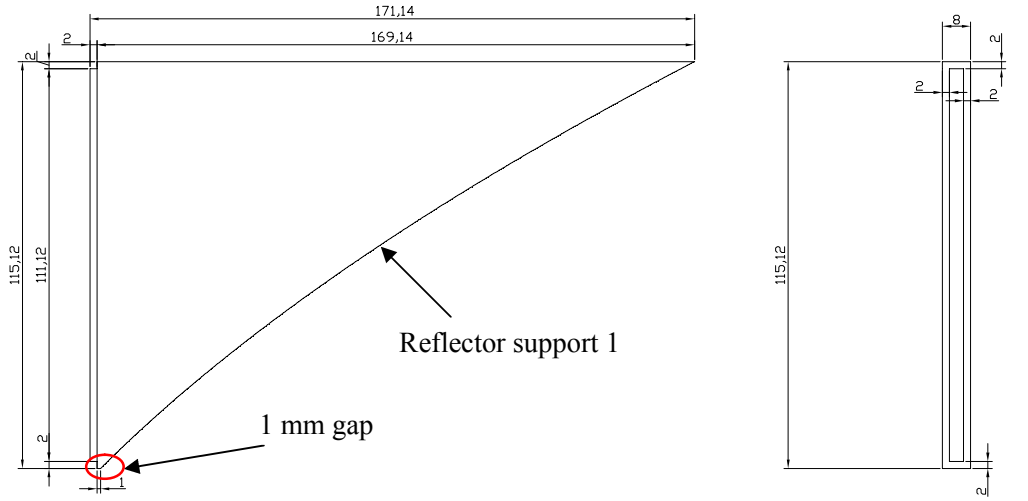

(a) (b)

Figure 3.2 (a) Detailed illustration of reflector support 1 (b) Detailed illustration of base of reflector support 1, all dimensions in 'mm'

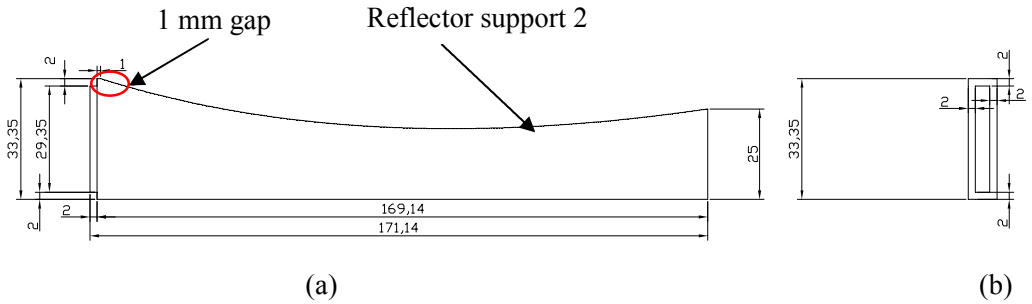

Figure 3.3 (a) Detailed illustration of reflector support 2 (b) Detailed illustration of base of reflector support 2, all dimensions in 'mm'

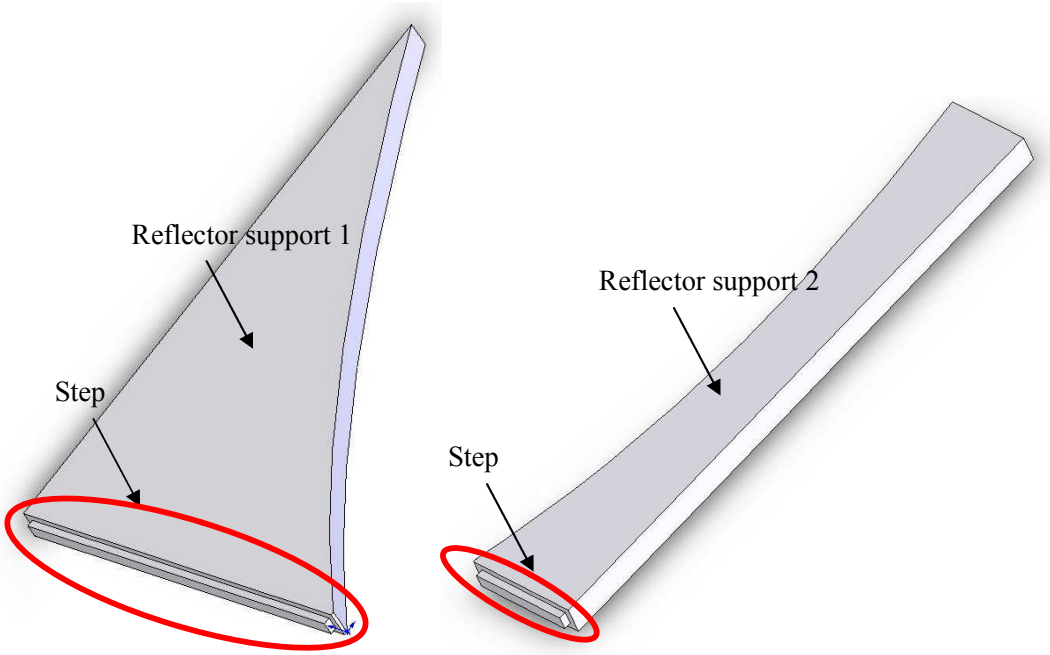

Figure 3.4 3D schematic sketch of the reflector support 1 and 2

3.2.2.2 The back plate

An 8 mm thick aluminium plate was chosen to provide the base for the PV cells and reflector supports. A plan view of the back plate that was designed for the prototype system is shown in figure 3.5. The dimensions of the aluminium back plate were 1040mm long by 334.5mm wide. Twenty-two slits, 2mm deep and 4 mm wide were machined into the aluminium back plate to accommodate the reflector supports. The relative positions of the

machined slits are illustrated in figure 3.5. The distance between the central line of each slit was 100mm along the length of the back plate with spaces 32mm wide on the upper and lower edges of the aluminium back plate to install Styrofoam insulation to prevent the heat loss of the system and a weather proof system cover. Gaps 20mm wide on both the left and right side edges of the back plate were left for the weather proof cover.

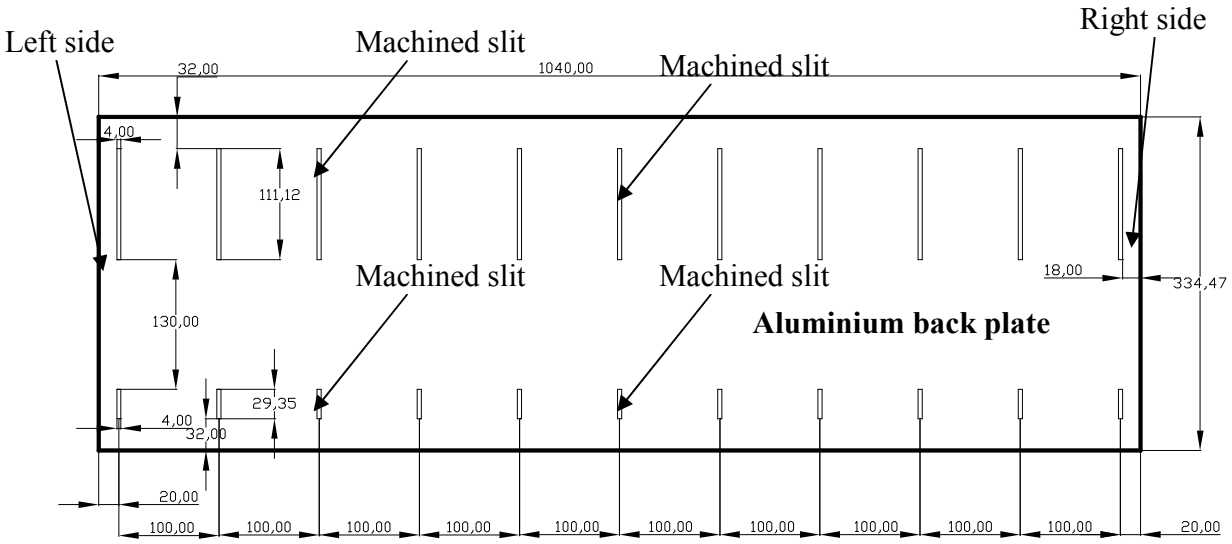

Figure 3.5 Plan view of the designed back plate for the prototype system, all dimensions in 'mm'

If the PV back ribbons made contact with the aluminium back plate, a short circuit could occur and there would be no power output from the PV system. A short circuit also creates hot spots at the rear of the solar cells and damages the cells. To prevent this happening, two 4mm wide and 2.5mm deep slots were machined in the front surface of the aluminium back plate to accommodate the PV back ribbons. The position of the two slots in the aluminium back plate are detailed in figure 3.6. Figure 3.7 is a photograph of the fabricated aluminium back plate.

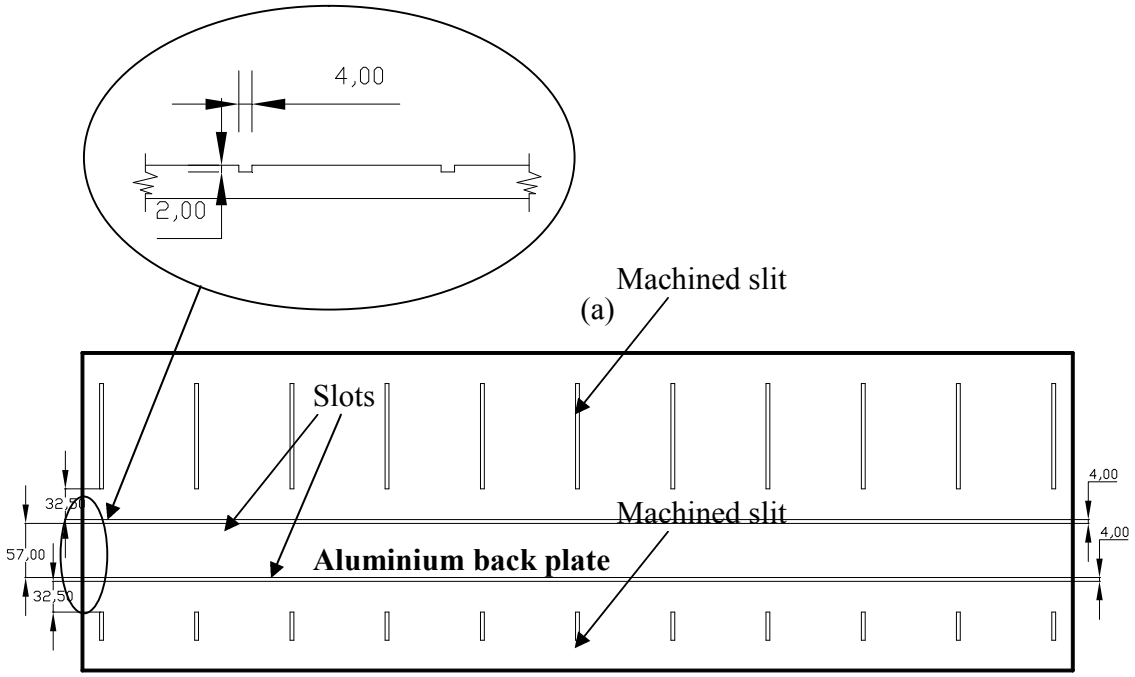

(b)

Figure 3.6 (a) Sides view of the two slots, (b) Plane view of two slots in aluminium back plate, all dimensions in 'mm'

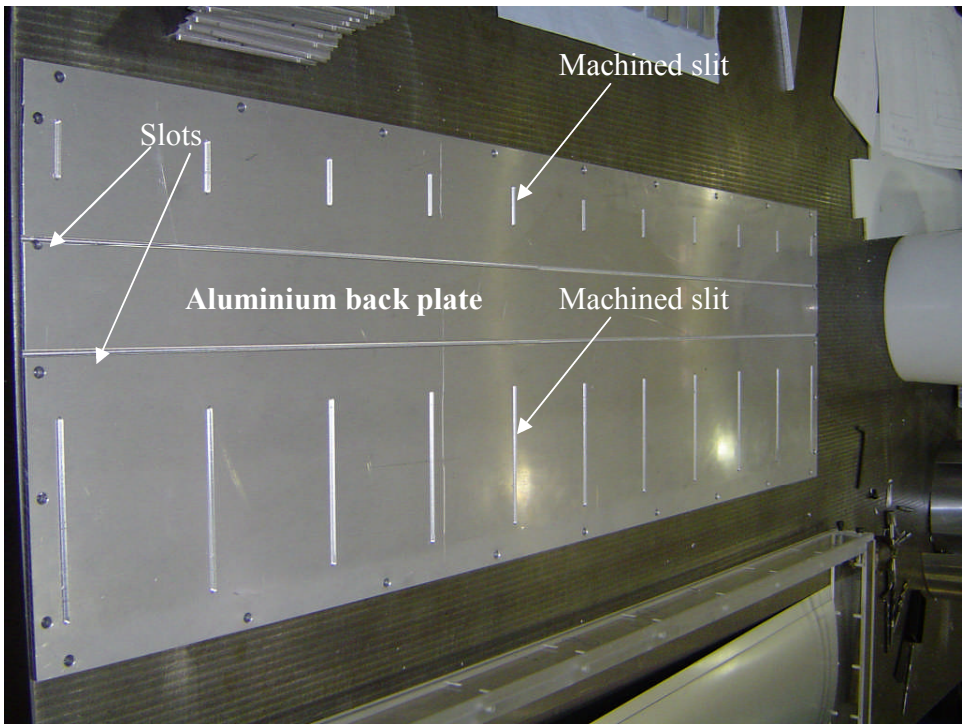

Figure 3.7 Photograph of the aluminium back plate

3.2.3 Reflector, reflector support and back plate assembly

The individual reflector supports were bonded to the aluminium back plate using 3M ™ DP-460 Epoxy Adhesive which has a thermal conductivity of 1.4W/m·K and an operating temperature of up to 110°C (Anon, 2005b). Figure 3.8 shows the reflector supports bonded to the aluminium back plate.

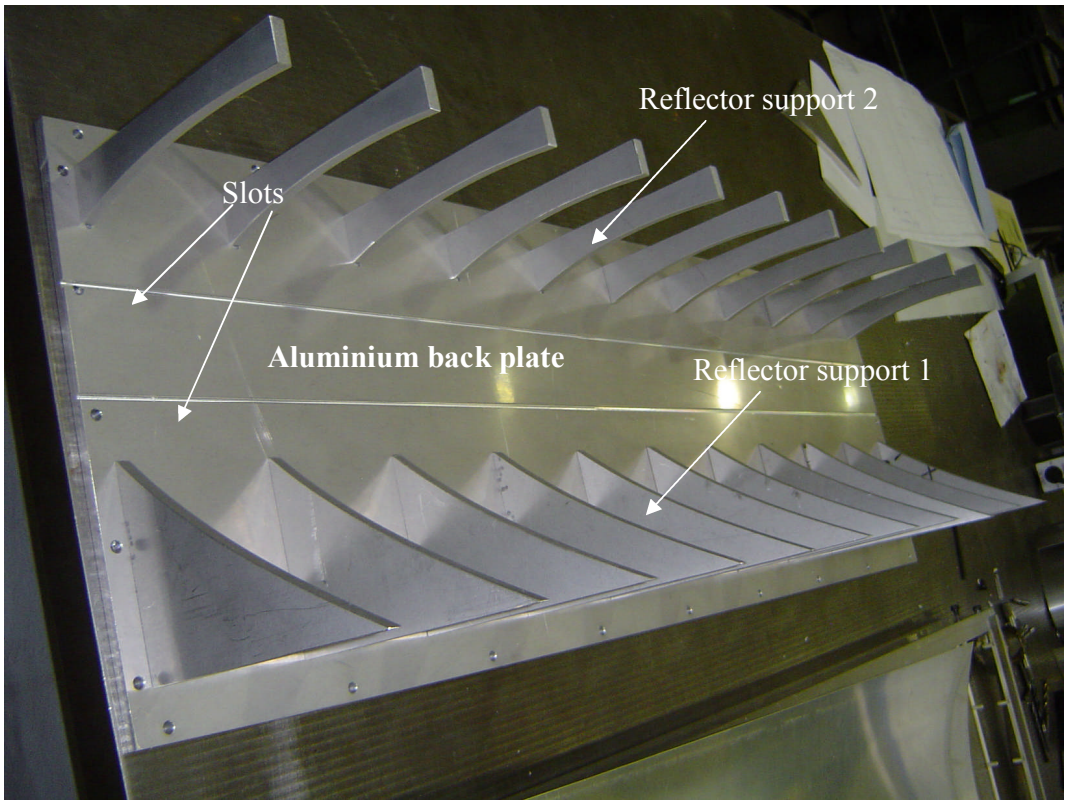

Figure 3.8 Photograph of the reflector supports bonded to the aluminium back plate

To shape the reflectors prior to bonding them on to the supports, the 0.4mm thick Miro 4270 KKSP reflectors 1 and 2 were sandwiched between two 0.4mm thick aluminium plates for protection, respectively. The sandwiches were then inserted into a rolling machine to form a parabolic profile to match the parabolic curve of the reflector supports, respectively. Adhesive was applied to the aluminium reflector supports, and then the

sandwiched Miro reflective materials were located onto the adhesive painted surface of the reflectors. A 1mm thick aluminium sheet was temporarily placed between the bottom of the Miro reflector and the aluminium back plate front surface to form the required gap for later PV installation. Full length metal clamps, enclosed in plastic pipes, were positioned on the reflectors to provide an even pressure across the reflector surfaces to ensure that an accurate system profile was obtained. The attachment procedure for the reflective material to the reflector supports is shown in figure 3.9. Figure 3.10 shows the assembled ACPPVC-55 system.

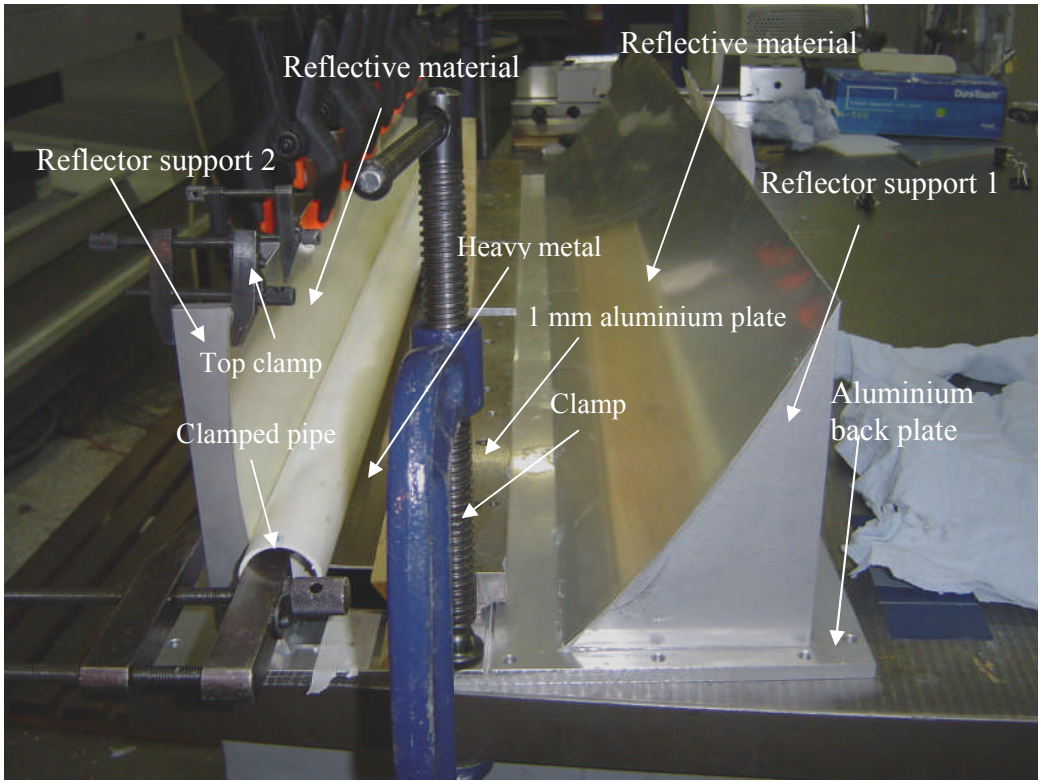

Figure 3.9 Attaching the reflective miro sheet to the reflector supports

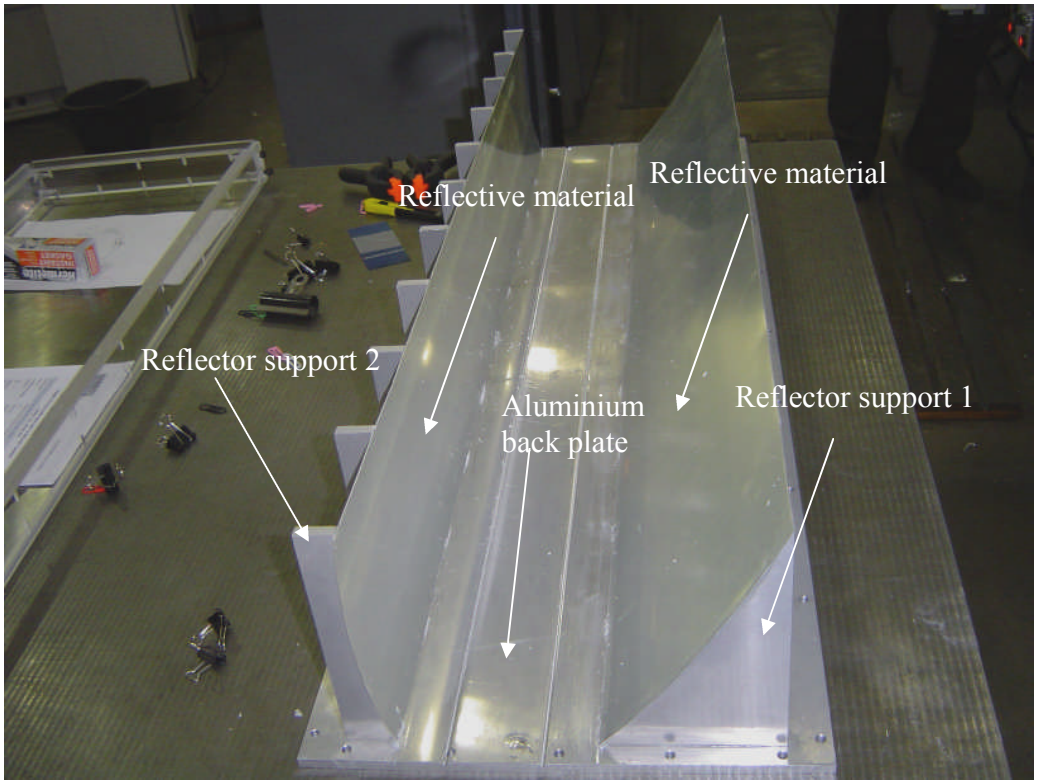

Figure 3.10 The fabricated ACPPVC-55 reflector system

3.2.4 PV selection and PV cells interconnection

BP Saturn laser grooved buried contact solar cells (Cell type: Cell-MC-S S115) were selected for the prototype experimental system. The cell dimensions were 125mm long by 125mm wide. Under standard characterising test conditions, the solar cells have an open circuit voltage of 610.1mV, a short circuit current of 5.595A, and a load current of 5.502A (Anon, 2006c). The maximum power output of the solar cell is 2.688W. The solar cells have a quoted measured maximum solar to electrical conversion efficiency of 17.42% and a fill factor of 78.76% (Anon, 2006c).

In order to obtain the desired output voltage and current requirements, PV cells can be interconnected in a number of ways as described in the following,

- Series connection, increasing the output voltage, while keeping the same output current.
- Parallel connection, increasing the output current, while keeping the same output voltage.
- A combination of series and parallel connections to increase both output voltage and current.

Six BP Saturn solar cells were series connected in one strip for the prototype ACPPVC-55 system. Copper PV ribbons 0.1mm thick and 2.0mm wide supplied by the Ulbrich Company were used to interconnect the solar cells. The ribbons' physical properties are shown in table 3.3 (Anon, 2008a).

Copper type:	CDA-110
Solder type:	62Sn/36Pb/2Ag
Coating thickness:	12-20 μm
Temper:	EXTRA SOFT

Table 3.3 Physical properties of copper ribbons (Anon, 2008a).

The following procedures were used to solder the solar cells:

- The coated copper ribbon was cleaned and cut to 252 mm lengths.
- The soldering iron was heated to 350°C.
- Sn-Pb-Ag low melting point solder of 0.71mm diameter was used. The physical and chemical properties of the solder are shown in table 3.4 (Anon, 2007).

Composition	Copper	Lead	Silver	Tin
Standards (%)	0	36	2	62

Physical State	Solid
Colour	Gray
Melting point	179°C (Solder alloy)
Specific Gravity	8.5

Table 3.4 Physical chemical properties of the Sn-Pb-Ag solder (Anon, 2007).

- A VOC free no clean flux pen MF300S was used to paint the flux on the coated copper ribbon.
- The ribbon was placed on the top of the front cell contact, and the solder iron dragged along it with a small additional amount of solder. Only a small amount of solder was used on one side of the prepared coated copper tab, since excess solder on the tab might increase the series resistance of the solar cells.
- All the tabs were soldered to the front contact of the solar cells. A solar cell with soldered front connection is shown in figure 3.11.

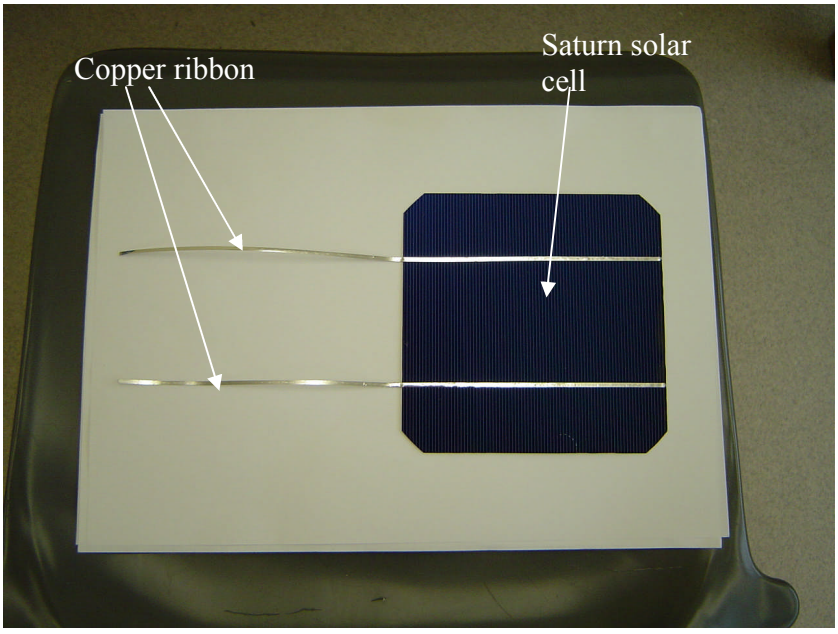

Figure 3.11 A PV cell with soldered front connection

- In the prototype ACPPVC-55 system, the PV cells were series connected. A Perspex jig was designed and fabricated to enable a string with the same spacing (2mm) between each solar cell to be made. The front soldered solar cells and the jig are shown in figure 3.12.
- The front soldered solar cells were placed in the jig with the rear surface facing upwards as shown in figure 3.12, and connected together by soldering the back

contacts using the same processes used for connecting the ribbons to the solar cell front surface. Figures 3.13 and 3.14 illustrate the rear and front view of the interconnected solar cells.

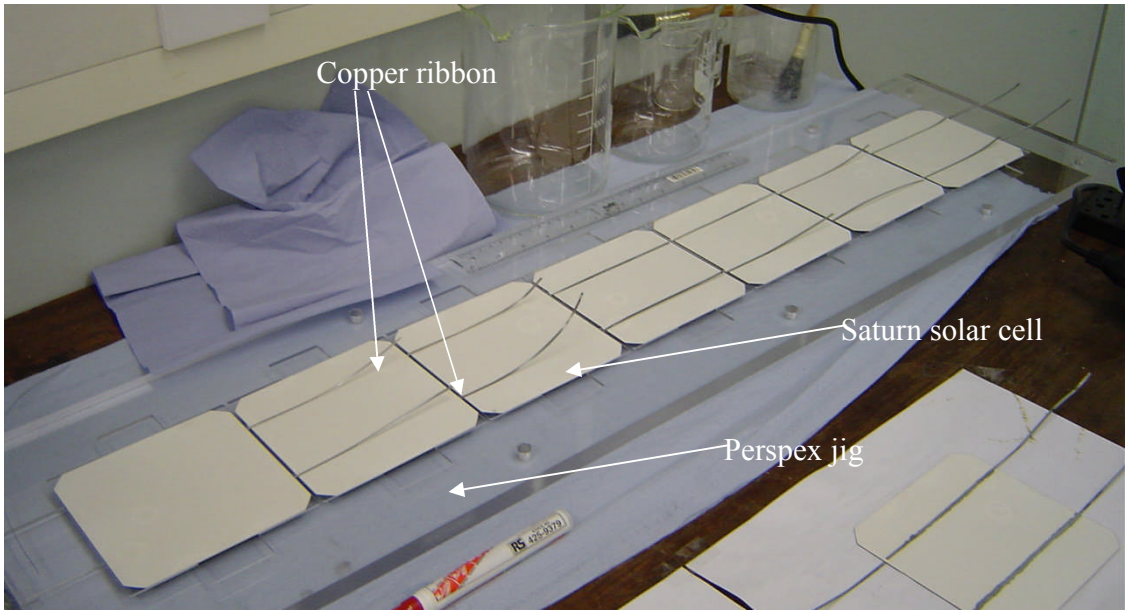

Figure 3.12 The front tabbed solar cells in the Perspex spacing jig

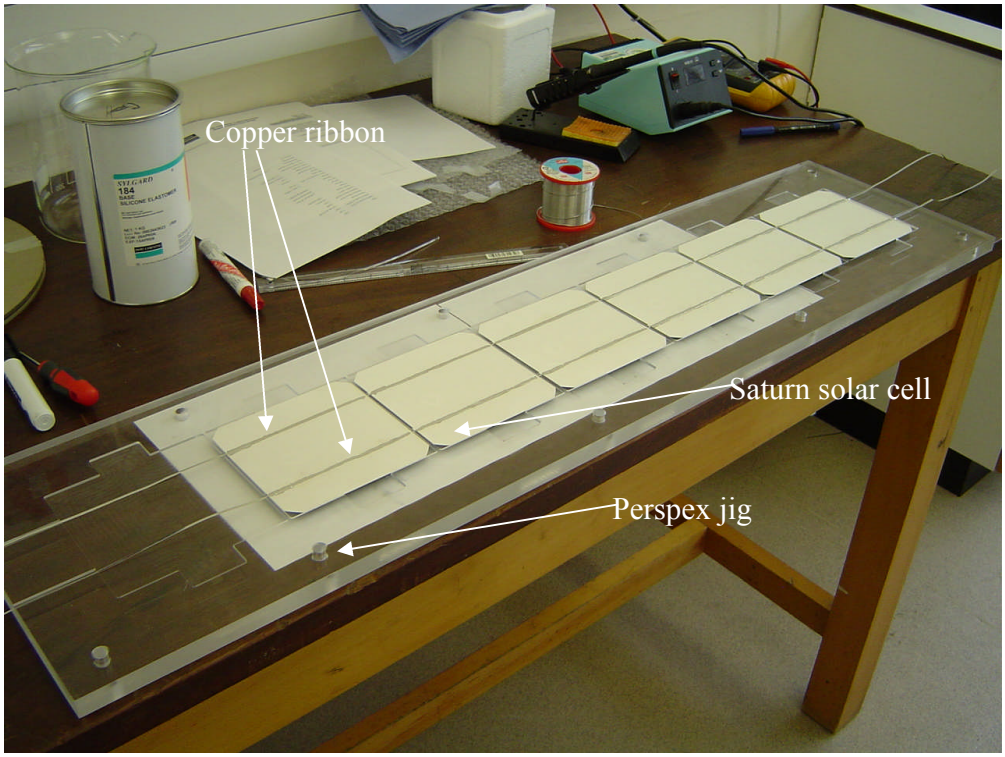

Figure 3.13 The interconnected solar cell string (back uppermost)

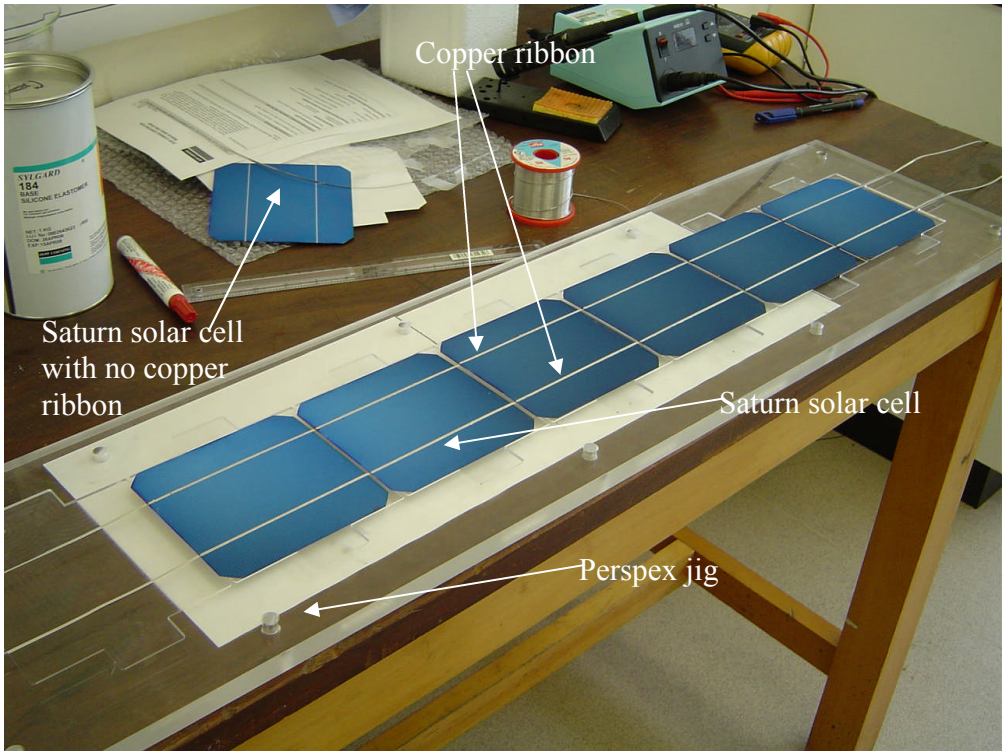

Figure 3.14 The interconnected solar cell string (front uppermost)

3.2.5 Encapsulation of the PV cell strings

A silicon elastomer (Sylgard-184) was used to encapsulate and attach the solar cells to the aluminium back plate, to prevent short circuit between the PV cells and the aluminium back plate, and to protect the PV cells from the environment. This coating provides the following benefits (Anon, 2006d):

- Effective, durable protection,
- High transparency,
- UV stable and moisture resistant,
- Easy application, by spray, brush, flow, dip or automated pattern coating and
- Continuous processing.

The procedures for encapsulation of the PV cells were as follows:

- The soldered PV cells were tested using a multimeter to determine and avoid short circuits.
- The two components of the Sylgard were thoroughly mixed using a weight ratio of 10:1 (Part A and Part B), and the mixture was placed inside a vacuum chamber for 45min to vacuum de-gas the mixture.
- The aluminium back plate surface was cleaned using acetone wipes.
- The aluminium back plate was coated with a thin layer of Dow Corning 92-023 primer followed by the Sylgard mixture.
- The PV cells were place on the coated aluminium back plate.
- Dow Corning 92-023 was used to coat the PV cells, and then covered with the Sylgard mixture.
- The system was then left for 48h at room temperature to achieve full hardness of the encapsulant.
- In the final stage, the PV cell strings were again tested to determine if short circuits were present.

3.2.6 System enclosure and cover (Weather proof cover)

In most solar energy applications, glass is used as a protective aperture cover due to its optical and mechanical properties. Compared with high iron content glass, low iron glass contains less Fe_2O_3 and absorbs less of the incident solar energy (Duffie and Beckman, 1991). Low iron glass sheet has an extinction coefficient of $4m^{-1}$ with a 4mm thick sheet having an effective transmittance of approximately 0.96 (Mallick et al, 2004). A 4mm thick low iron glass sheet was used for the front cover of the ACPPVC system. A 5 mm thick

Perspex sheet was used at the reflector end for the side covers of the ACPPVC system to reduce the risk of shading of the PV system for non perpendicular solar incidence angles.

20mm thick wooden boards were used for the upper and lower supporting structure of the system enclosure. The dimensions of the upper and lower wooden frames were all 1060mm long by 196.2mm wide. Cross slots were machined into the inner side of the wooden boards to house the side Perspex sheets and the front low iron glass cover. The side Perspex walls were sealed to the frame with silicon sealant. The front glass cover was sealed to the frame using a rubber gasket. The detailed profile and the position of the machined slots in the wooden frames are shown in figure 3.15. The air gap between the front cover glass and the reflector top was 5mm. The dimension of the side Perspex sheets were all 350.5mm× 174.2mm × 5mm. The front glass cover dimension was 1060mm × 354.5mm × 4mm. Figure 3.16 shows the fabricated prototype system enclosure.

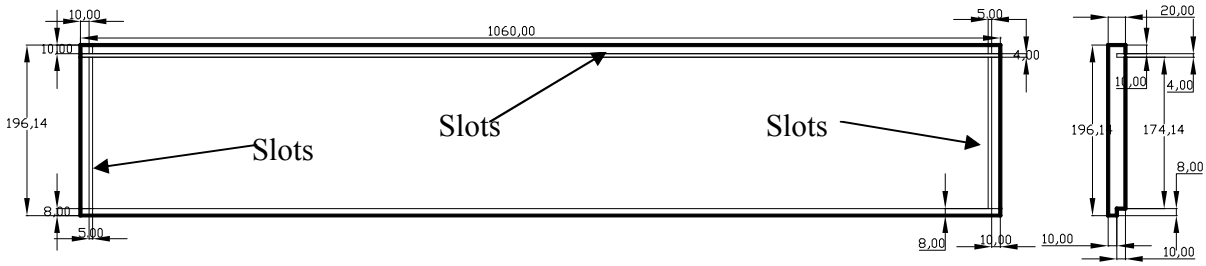

Figure 3.15 A detailed view of the wooden frame

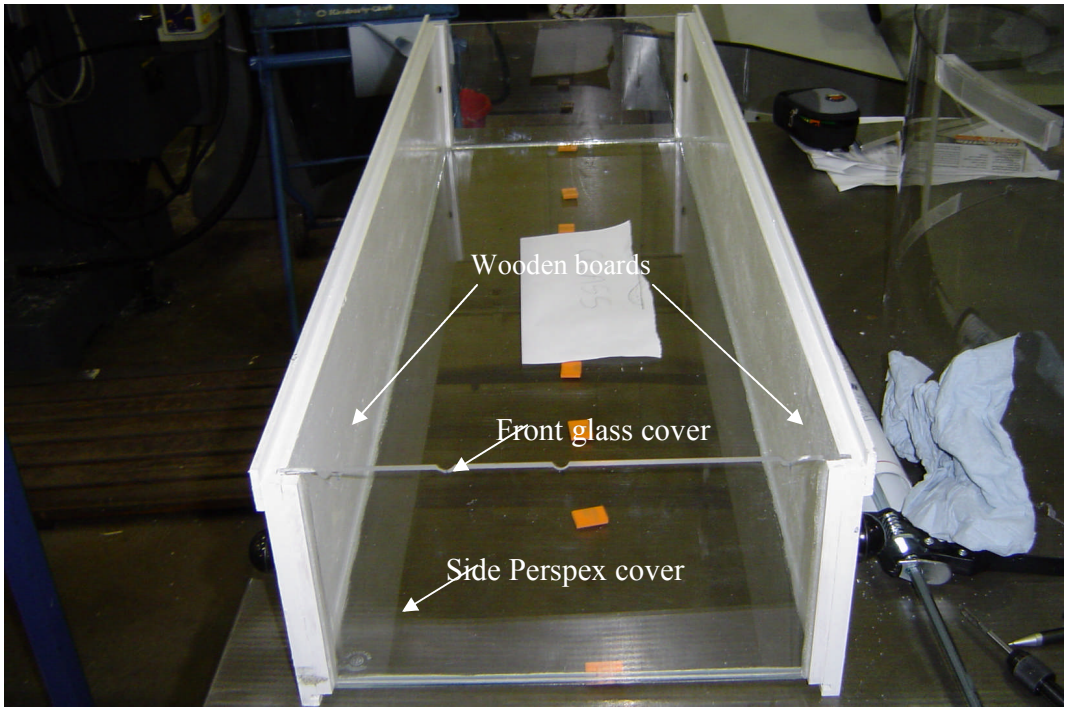

Figure 3.16 Photograph of the constructed ACPPVC-55 house

3.2.7 Phase Change Material (PCM) selection and container design

The choice of the phase change material was an important aspect in the design of the PV temperature management system. The phase change material must provide an economic advantage and be acceptable environmentally. It must have a melt point in the desired operational temperature range and the melting point must be higher than the average ambient environmental temperature to allow discharging (Pal and Joshi, 1999). It should have a high latent heat per unit mass, high thermal conductivity and a small volume change at phase transition (Abhat, 1981). The chemical and physical stability of the phase change material must also be considered so that there is no degradation after thousands of cycles (Pal and Joshi, 1999).

3.2.7.1 The PCMs employed for the prototype experiment

Organic solid to liquid phase change materials can be used for the temperature control of the ACPPVC-55/PCM system. The low thermal conductivity of organic phase change materials (0.18-0.33Wm^{-1} K^{-1}) however may cause significant problems. Low thermal conductivity affects the effective and uniform absorption of heat from the heat source to the PCM (Pal and Joshi, 1999). It can be overcome during system construction by including structures to enhance heat transfer. Inorganic PCMs have a higher thermal conductivity than the organic PCM, for example, the conductivity of $MgSO_4 \cdot 7H_2O$ is 0.4 to 0.6 $Wm^{-1}K^{-1}$, almost double that of organic paraffins. Inorganic PCMs are however usually toxic and have a complex melt behaviour. Salt hydrates are generally corrosive, and absorb and lose water during phase transition, they are not stable for long term phase change cycles (Jotshi et al, 1992).

The standard characterising temperature of PV cells is 25°C (Anon, 2005a), the appropriate phase change material should therefore have a melt temperature around 25°C and also higher than the summer average ambient air temperature in the UK. RT27 solid to liquid phase change material which has a melting temperature at 27°C was chosen for this study. The characteristics of the PCM RT 27 are shown in table 3.5 (Anon, 2006e)

Property	RT 27(liquid)
Main component	n-paraffin
Latent heat of fusion (kJ kg^{-1})	179 (Temp from 19˚C to 34˚C)
Melting temperature (˚C)	28
Density (kg m^{-3})	Solid 870 at 15˚C Liquid 750 at 70˚C
Specific heat capacity (kJ $kg^{-1}K^{-1}$)	1.8 Solid / 2.4 liquid
Heat conductivity (W m^{-1} K^{-1})	0.2
Flash point (˚C)	164
Volume expansion	16% (at△T=55K)

Table 3.5 Thermophysical properties of the chosen phase change material RT27 (Anon, 2006e).

3.2.7.2 Estimation of the required dimensions for the PCM container

The solar flux is incident on the solar cells in the concentrator system which are encapsulated onto the front surface of the rectangular aluminium back plate. A PCM container with a regular rectangular cross section which was both simple to assemble and also suitable for building façade integration was selected. The aluminium back plate of the ACPPVC-55 was used for the front cover of the PCM container to obtain good thermal contact between the solar cell and the PCM container and heat transfer to the PCM. The required volume of the PCM and thus the depth of the PCM container depended on the incident solar radiation intensity, the duration of the solar radiation, the heat loss from the ACPPVC-55/PCM system and the thermal capacity of the PCM material.

PV cells are designed to transform solar radiation into electricity, when sunlight strikes the surface of an ACPPVC-55/PCM system, part of the irradiation is converted into electricity, part is reflected and that remaining is absorbed by the PV cells and converted to heat. The energy flow in the ACPPVC-55/PCM system is presented in figure 3.17. Neglecting the ACPPVC-55/PCM system internal heat transfer and the heat loss from the reflector, heat is mainly transferred from the system aperture to the ambient environment by convective and radiative heat transfer, and from the rear of the PCM to the building fabric by conductive heat transfer.

It was assumed, for a first approximation, that the initial temperatures of the PCM and glass aperture were equal to that of the PV, the whole system was at a uniform temperature equal to T_{PV} , and that the top and the bottom boundaries were adiabatic. In time Δt the temperature change within the PCM was from $T_{pv,t}$ to $T_{pv,t+\Delta t}$. The heat transfer coefficients

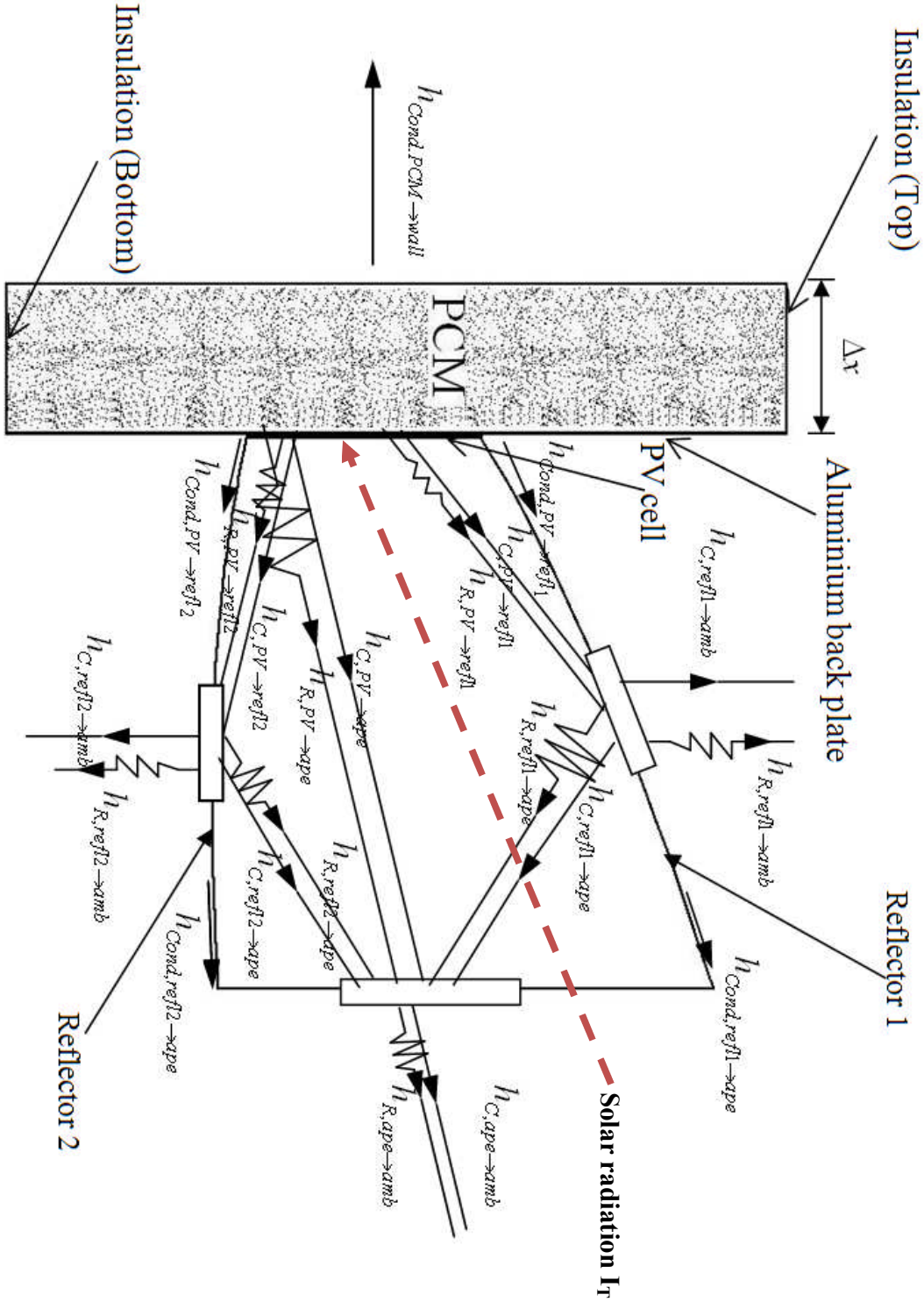

Figure 3.17 A schematic diagram illustrating the heat transfer in the ACPPVC / PCM system

from the front and rear surfaces had the fixed values h_{front} and h_{rear}. When $T_{pv,t+\Delta t}$ is smaller than the PCM melt temperature T_m, the energy balance for the system can be defined by equation 3.1 (Huang et al, 2004):

$$A \cdot I_T \cdot \Delta t = A \cdot (h_{front} + h_{rear}) \cdot (T_{PV,t} - T_{amb})\Delta t + (T_{pv,t+\Delta t} - T_{pv,t}) \cdot \rho \cdot c_p \cdot \Delta x \cdot A \quad (3.1)$$

When $T_{pv,t+\Delta t}$ was greater than the T_m, thermal energy was used for phase change and the temperature of the PCM was constant at T_m until the phase change process was complete. If the total time for phase change was $\sum \Delta t$, then the energy balance for the phase transition can be defined by equation 3.2 (Huang et al, 2004):

$$A \cdot I_T \cdot \sum \Delta t = A \cdot (h_{front} + h_{rear}) \cdot (T_m - T_{amb}) \sum \Delta t + H \cdot \Delta x \cdot A \quad (3.2)$$

Equation 3.2, the energy balance for the phase transition was used to estimate the depth of the PCM container. Assuming that the PV and PCM was constant at a temperature of 28°C from 8:00 am to 17:00, an average solar radiation intensity of 481W/m^2 calculated from weather data recorded on August in the U.K (Mallick, et al, 2007b) was used in equation 3.2. The ambient temperature was 18°C. After assuming the force convection and radiative heat transfer occurred on the front surface of the system and only nature convection took place on the rear surface of the system, the assumed heat transfer coefficient on the front and rear surface for the ACPPVC-55/PCM system were 12W/m^{2}K and 3W/m^{2}K, respectively (Mallick et al, 2007a, Huang et al, 2004). The PCM container depth was estimated to be 4.2cm for the prototype PCM which is similar to the 3cm depth PCM

container that was predicted to maintain the PV operating temperature less than 35°C for 3 days in summer in the UK (Huang, et al, 2004). The interior dimensions of the prototype PCM container were therefore 1040 mm × 431.9 mm × 42 mm.

3.2.7.3 Design of the PCM container

The design of the phase change material container considered both the structural and thermal requirements. The structure must be:

- Stable over long time cycles
- Leak-proof
- Corrosion resistant
- Accommodate the required container capacity
- Minimise construction material cost
- Allow expansion of the PCM material

The material compatibility of the phase change materials and the container materials are shown in the table 3.7 (Ure, 1998).

Material	Melting point(˚C)	Material Compatibility
Waxes	4 to 28	SS, S, Cu, Al, Al-Mg, P
Polyethylene glycols	-15 to 28	SS, S, Cu, Al, Al-Mg, P
$CaCl_2 \cdot 6H_2O$	27	S, Cu, P
Glauber's salt + additives	4 to 24	SS, S, P, (Cu, Al-Mg)*

SS=Stainless Steel, S=Mild Steel, Cu=Copper, Al=Aluminium, Al-Mg=Al/Magnesium alloys, P=Plastics, * = Materials in brackets are compatible with some mixtures

Table 3.6 Material compatibility (Ure, 1998)

Aluminium which can provide a high rate of heat transfer was chosen for the front and the back covers of the PCM container. The 8mm thick aluminium back plate of the ACPPVC system formed the front cover of the PCM container. A 5mm thick aluminium plate was

used for the back cover of the PCM system. The front and back cover were both 1040mm long by 432mm wide. A transparent Perspex sheet 25mm thick to allow observation of the phase change in the system, was selected to provide the four sides of the enclosure of the PCM container. A detailed diagram of the upper, and lower Perspex walls and the sides walls are shown in figures 3.18 and 3.19, respectively. The dimensions of the upper and lower Perspex wall were 1060mm long by 78mm wide. The Perspex side walls were 334.5mm long by 55mm wide. Steps were machined at the edge of the Perspex walls to provide a good joint between the observation walls and the aluminium covers. 50mm thick polystyrene foam sheet was used to provide insulation around the Perspex during the experimental investigation. A 3D schematic sketch picture of the PCM container is shown in figure 3.20.

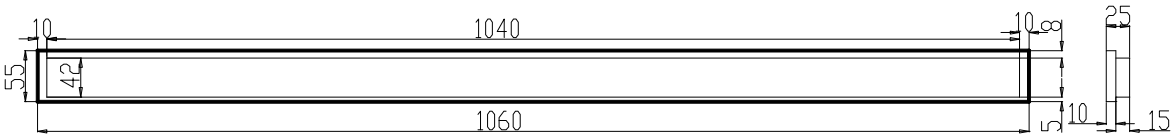

(a) (b)

Figure 3.18 (a) Detailed plan view of the upper and lower Perspex walls (b) Detailed side view of the upper and lower Perspex walls

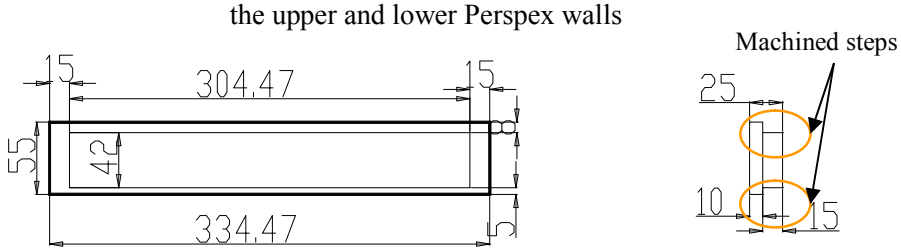

(a) (b)

Figure 3.19 (a) Detailed plan view of the Perspex side wall (b) Detailed side view of the Perspex side walls

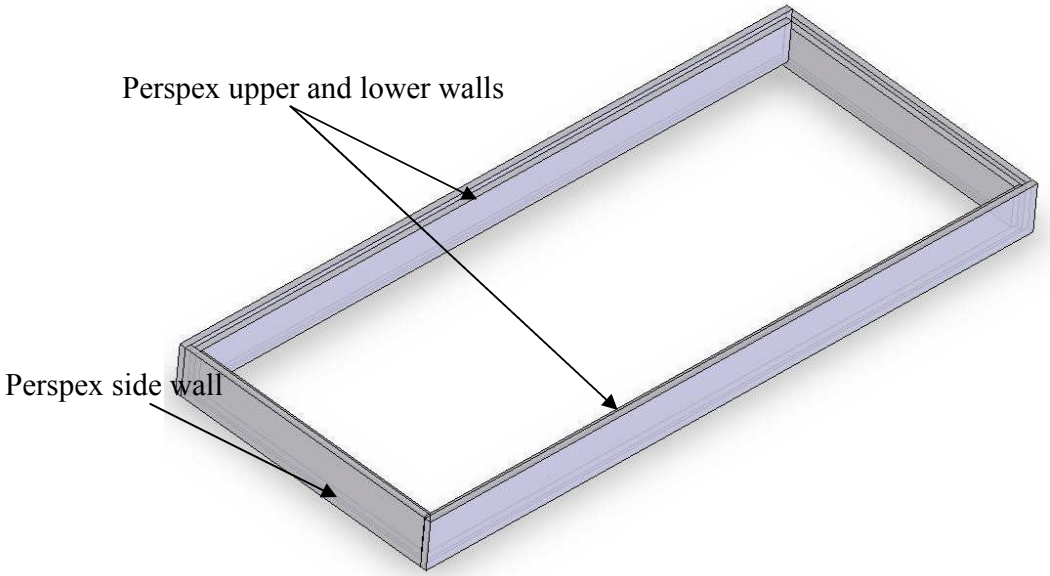

Figure 3.20 A 3D sketch picture of the PCM container Perspex walls

3.2.7.4 Assembly of the ACPPVC-55 and PCM container

A PCM container with PCM was designed to enable the transfer of heat from the PV cells and to store the thermal energy for building applications. To provide effective PV cooling, the PCM container was installed at the rear of the ACPPVC-55 system with the ACPPVC-55 aluminium back plate forming the front cover of the PCM container. An exploded view of the ACPPVC-55/PCM system showing its different components can be seen in figure 3.21.

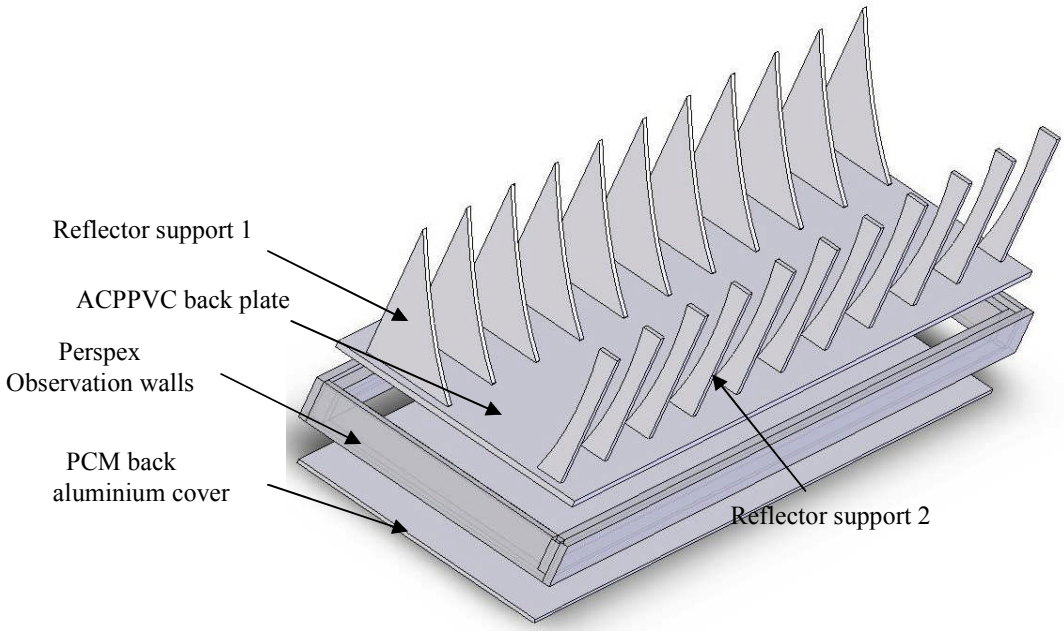

Figure 3.21 An exploded view of the ACPPVC-55/PCM system

It was necessary to use sealant to reduce the probability of leakage at the interfaces between materials when the PCM was in the liquid state. Silicon sealants were used at all junctions of the observation walls to prevent leakage. Socket screws, M6×30mm, as shown in figure 3.22 with washers were used to connect the aluminium cover to the Perspex observation walls with silicon sealants were used at the inside and the outside of the joints of the screws. Construction details for the corners of the PCM container are shown in figure 3.22. Figures

3.23 and 3.24 show the pre-assembled ACPPVC-55/PCM and the assembled ACPPVC-55/PCM system, respectively.

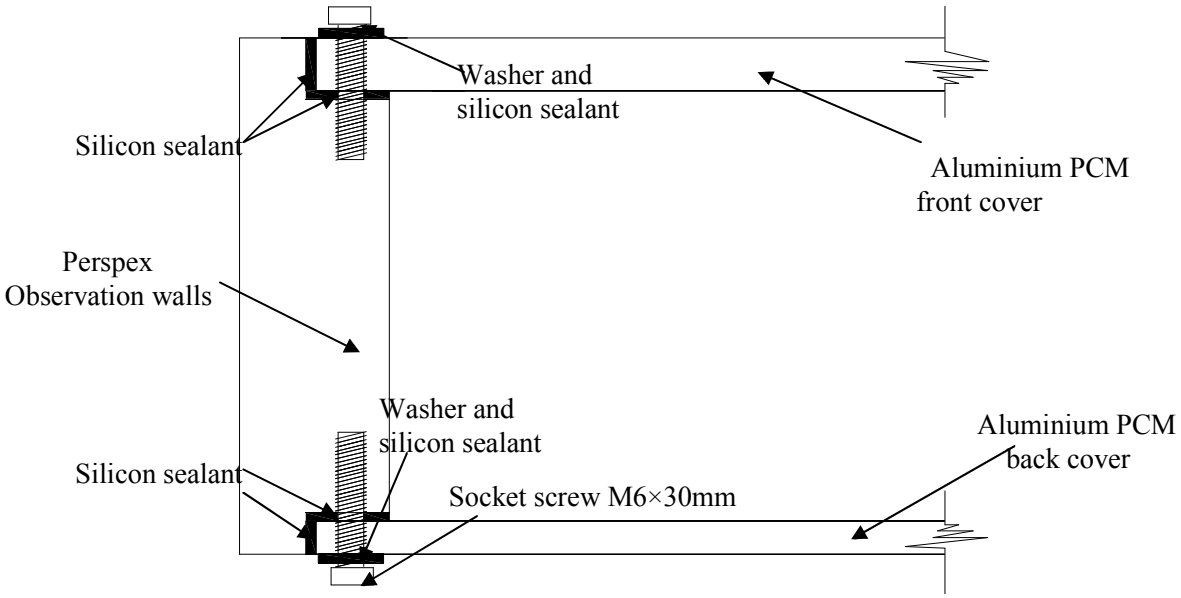

Figure 3.22 Profiles of the joint between Perspex observation walls and aluminium sheets

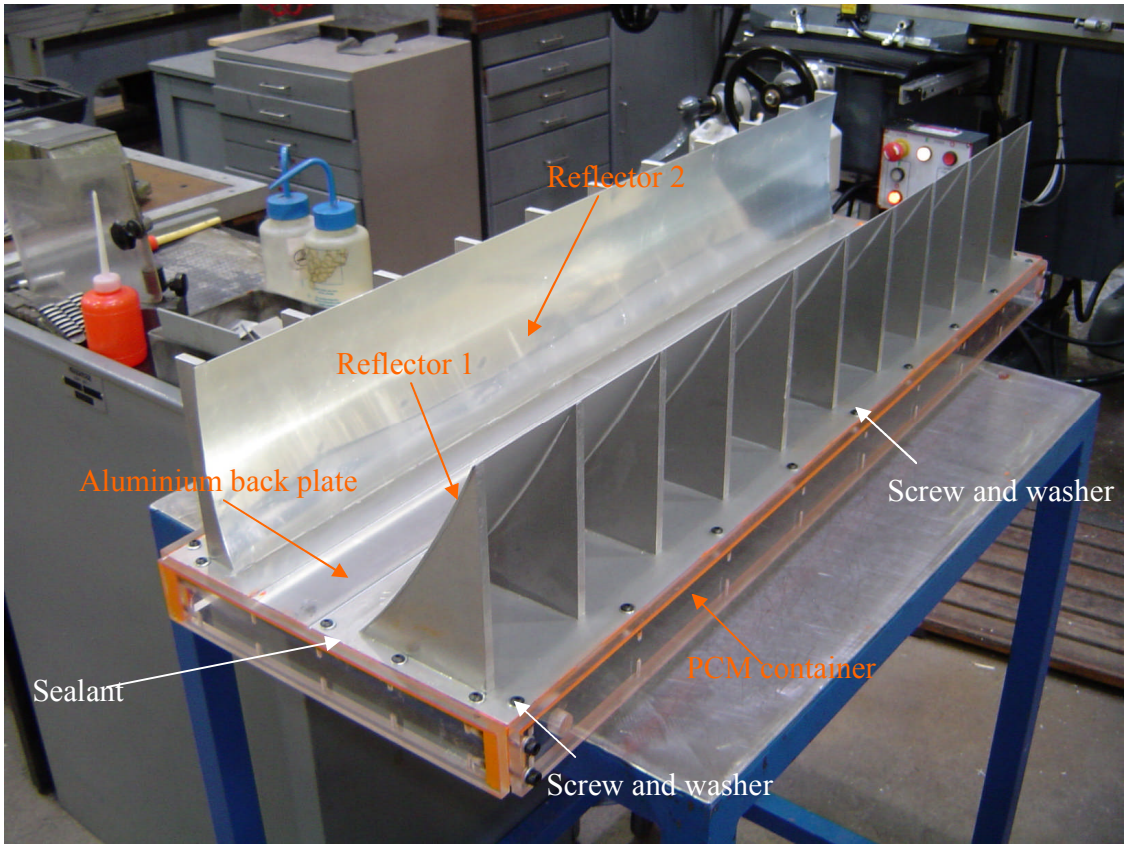

Figure 3.23 Photograph showing the ACPPVC system with integrated PCM container

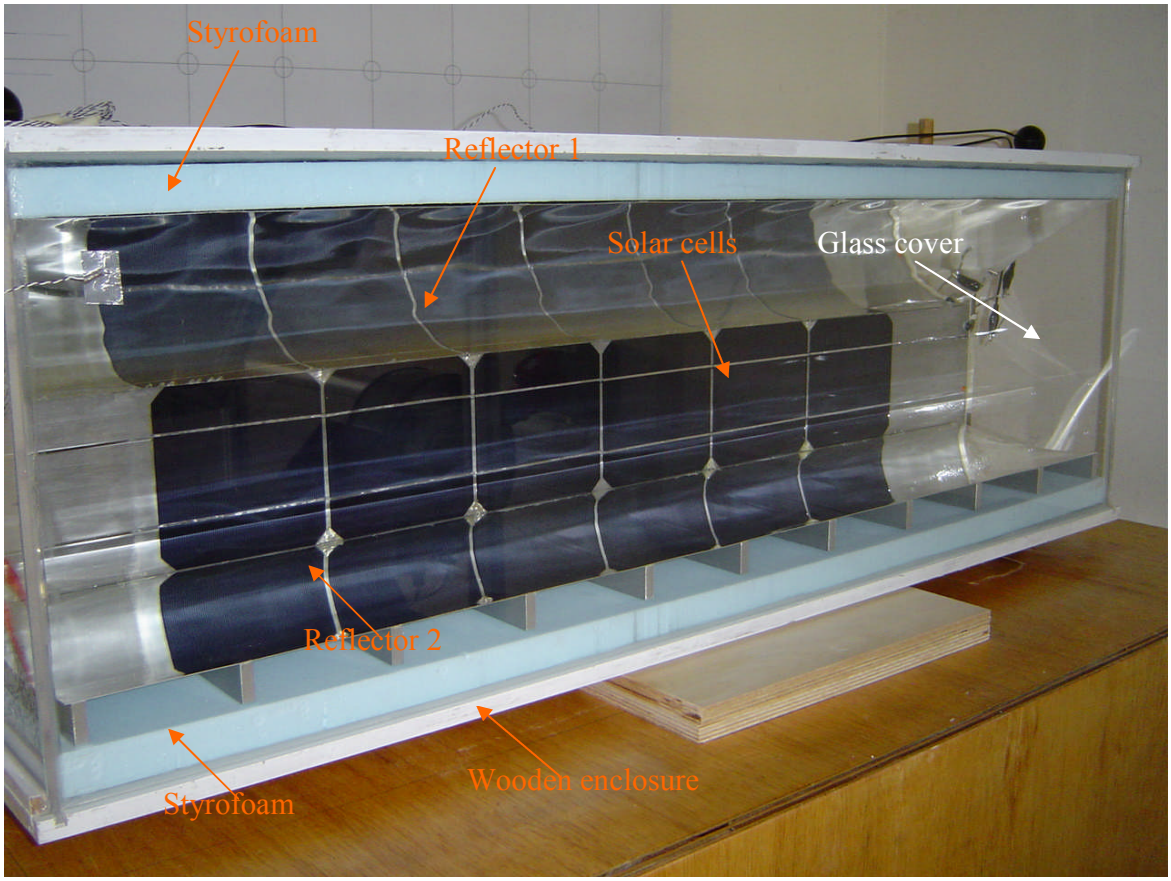

Figure 3.24 Photograph of ACPPVC-55/PCM system with enclosure cover

3.3 Conclusion

A suitable design and fabrication method was developed to produce an ACPPVC/PCM test system. The designed ACPPVC-55 system with a concentration ratio of 2.0 requires half of the expensive PV material compared to a similar flat PV panel, but may provide similar output power.

Chapter 4 Description of the solar simulator design

4.1 Introduction

Solar simulators are usually used to simulate natural sunlight for indoor experiments. An ideal solar simulator should have less than ±1% variation in the solar radiation level, less than ±1% spatial variation in irradiance both in and several cm above the test plane (Luque and Hegedus, 2003). The performance requirements for solar simulator in different classes are shown in table 4.1 (Anon, 2008d).

	Class A	Class B	Class C
Spectral match (Ratio of percentage distribution	0.75-1.25	0.6-1.4	0.4-2.0
Non-uniformity (+/-)	≤2%	≤5%	≤10%
Temporal stability (+/-)	≤2%	≤5%	≤10%

Table 4.1 Solar simulator performance requirements (Anon, 2008d).

In this project, a highly collimated solar simulator with uniform output irradiation distribution was designed and fabricated for indoor experimental tests. The materials selection for the different components, and the individual component design and fabrication for the solar simulator are described in the following sections.

4.2 Prototype solar simulator design

Solar simulators using a parabolic reflector provide good collimation. However, their output flux distribution is non-uniform along the width of the test plane (detailed discussion is presented in Section 4.2.6), this can be addressed in the system design. For the prototype solar simulator, parabolic reflectors were designed to provide a collimated beam output and a graduated reflective coated secondary reflector was designed to maintain flux output less than ±2% variation.

A detailed cross sectional view of the solar simulator and schematic output ray paths from the lamp is shown in figure 4.1. The focal length of the chosen parabolic reflector (Reflector 2) was 200mm, and the central portion of the parabolic reflector shown on the diagram was removed to allow lamp cooling. A semi-circular reflector (Reflector 1) which had a radius of 100mm was used to reflect half of lamp output radiation back to their origin and onto the parabolic reflector (reflector 2), to reduce radiation output loss. Figure 4.2 illustrates a 3D sketch of the solar simulator. The prototype solar simulator comprised a Xenon long arc lamp and its cooling system, reflectors and support frame.

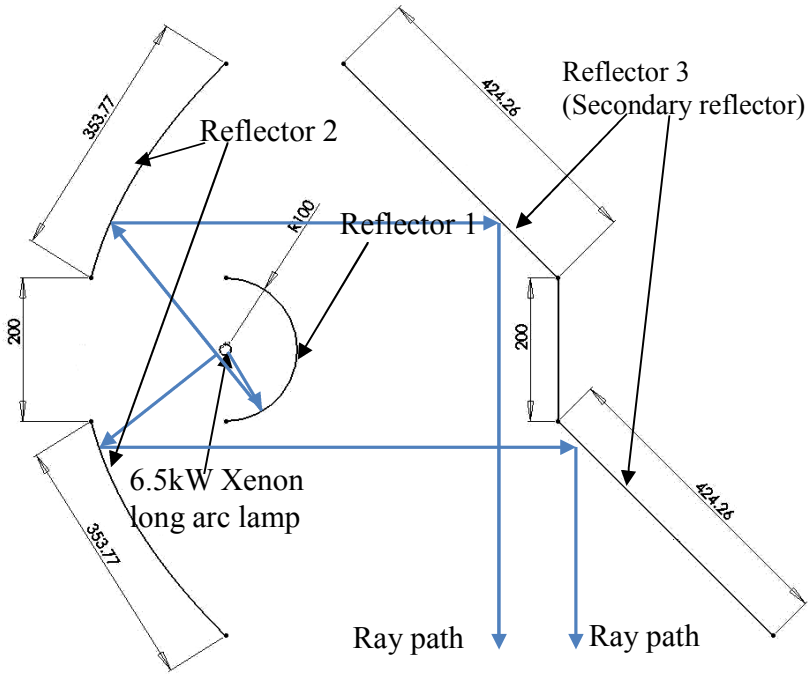

Figure 4.1 A detailed cross sectional view of the solar simulator, all dimensions in 'mm'

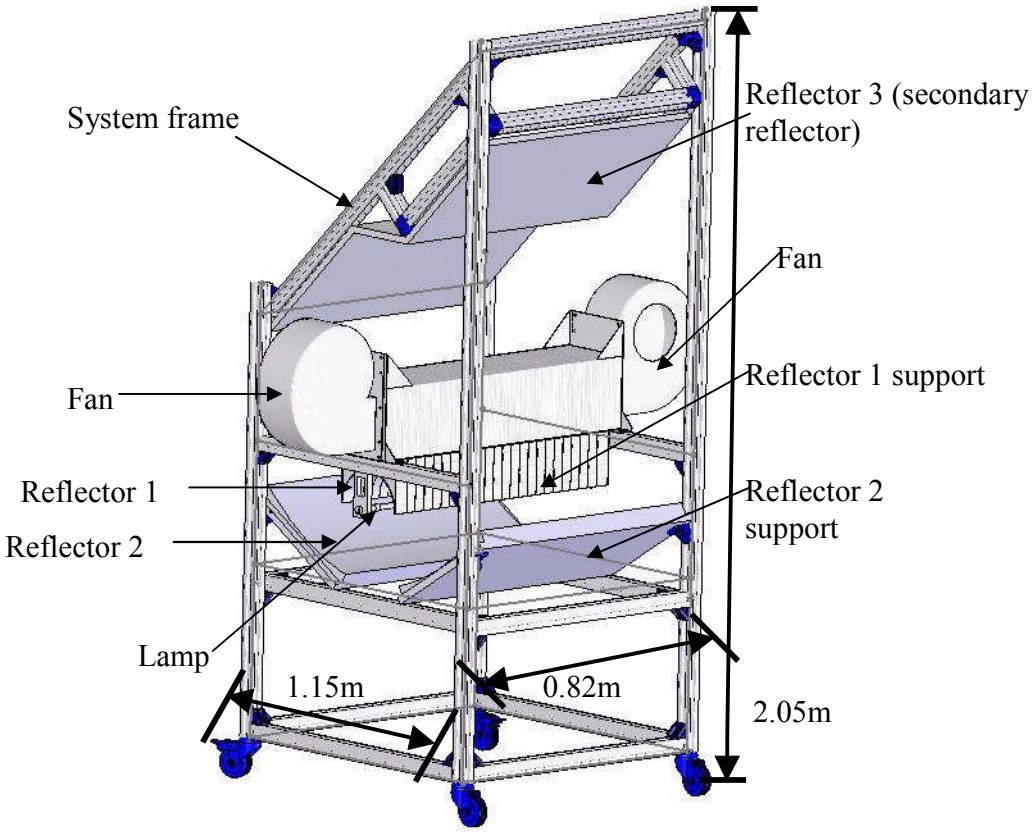

Figure 4.2 A 3D schematic sketch of the prototype solar simulator

4.2.1 Lamp selection

A solar simulator light source can be typically categorised as continuous arc or pulsed arc. The continuous light source provides a constant illumination output for the desired period of time. The pulsed source provides a desired intensity within a very short period of time due to the intermittent action of the light source (Luque and Hegedus, 2003). A SQP-HLA660 Xenon long pulsed arc lamp having a spectrum close to the solar spectrum at AM1.5, which is the standard solar spectrum for indoor PV characterisation, has been chosen as the light source for the developed solar simulator. The spectral distribution of the SQP-HLA660 lamp was measured by a HR2000+ high resource spectrometer shown in figure 4.3. The lamp has a rated power of 6.5kW, total length of 819mm with a 680mm

long illuminated area. The diameter of the illuminated area is 14mm. From figure 4.3, it can be seen that the spectral intensity of the SQP-HLA660 lamp is higher than that of the AM 1.5 in the range of wavelength from 800nm to 1000nm.When use the SQP-HLA660 light source to simulate the solar radiation for indoor PV experimental tests, the measured electricity output of the PV may be higher than that tested at solar spectrum AM 1.5.

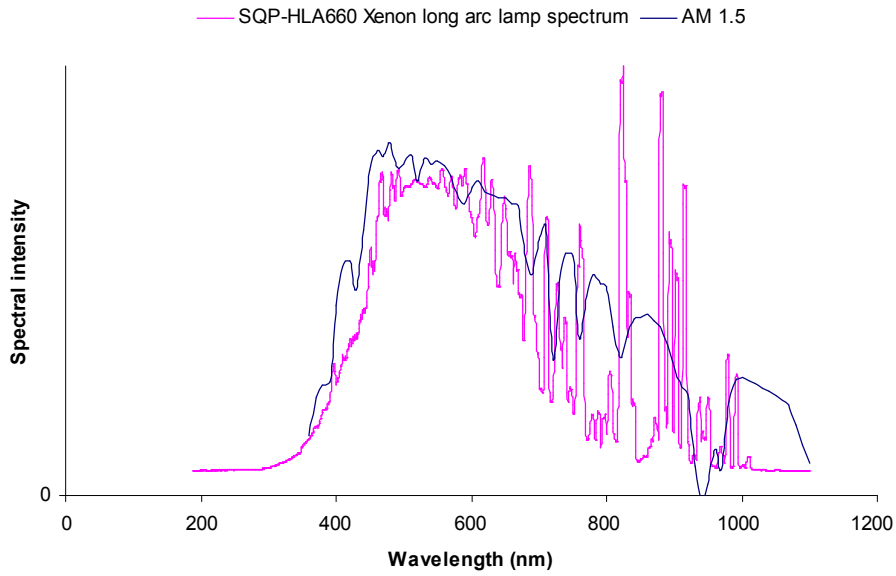

Figure 4.3 Measured spectral distribution of the SQP-HLA660 Xenon long pulsed arc lamp measured using a HR2000+high resource spectrometer and AM 1.5 (Duffie and Beckman, 2006)

4.2.2 Reflective material employed for reflectors 1 and 2

Miro-Silver 4270 AG 0.2mm thick having a reflectivity greater than 98% and maximum operating temperature of up to 150°C (Anon, 2006b) was employed as the reflective material for reflectors 1 and 2.

4.2.3 Design and construction of reflector 1 and lamp cooling system

An exploded view of the lamp housing is shown in figure 4.4. The lamp house comprised of the reflector 1 support, reflector 1, lamp cooling duct (plenum chamber) and fans. Twenty five 1mm thick aluminium reflector 1 supports were designed and manufactured. A

detailed sketch of the reflector 1 support design is shown in figure 4.5. Fins 20 mm long and 1.5 mm wide were included at the edges of reflector 1 supports and were used to fix the reflector supports to their aluminium back plate. To make the supports, all the profile data points were transferred to 'AUTOCAD', and the parts produced using laser cutting. The dimensions of the reflective material used for reflector 1 were 740mm long by 314mm wide by 0.2mm thick.

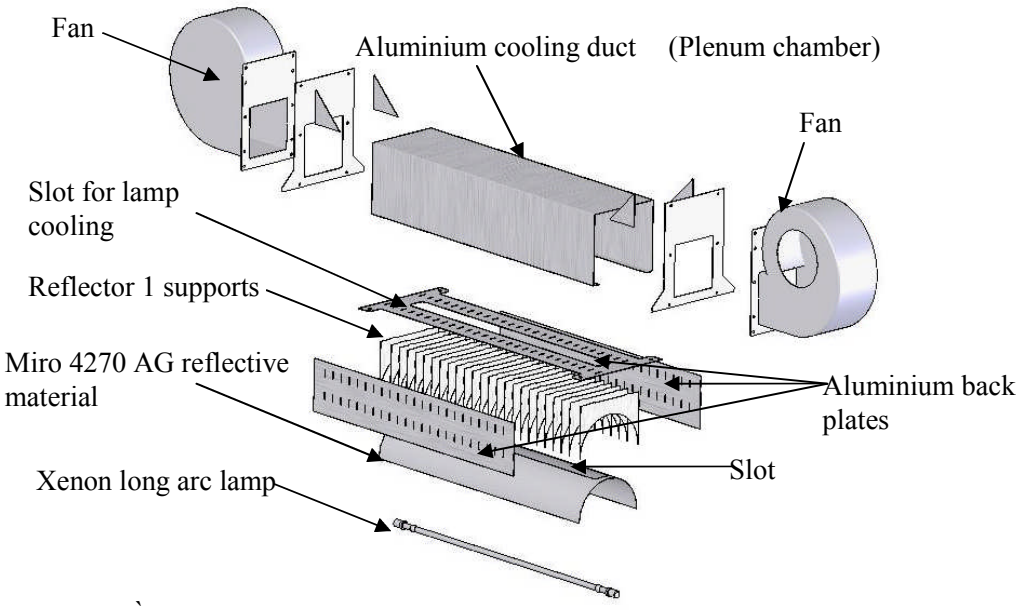

Figure 4.4 An exploded view of the reflector 1 supports, back and side aluminium plates and the lamp cooling system

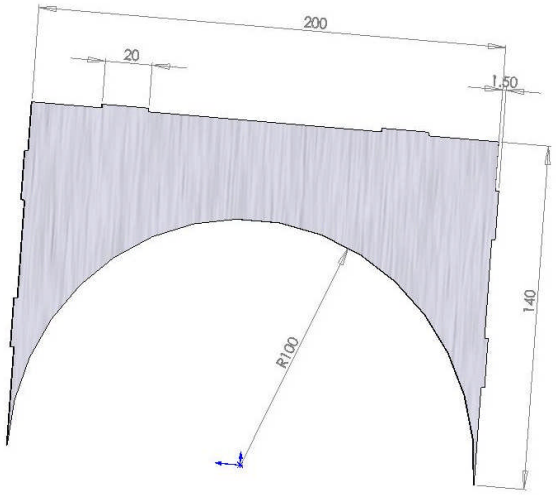

Figure 4.5 Detailed sketch of the reflector 1 support, all dimensions in 'mm'

A lamp cooling duct was designed with dimensions 820mm long by 200mm wide by 185mm high, fabricated from aluminium. Fans were installed at both ends of the duct to blow air into it. A slot 680mm long and 50 wide was cut into the base of the tunnel to blow air over the lamp and ensure effective lamp cooling. A schematic view of the air flow in the lamp house is shown in figure 4.6. A similar bonding processes discussed in section 3.2.3 for assembling the reflector and its support in the ACPPVC-55 system were undertaken to assemble the reflector 1 and it supports for the solar simulator. The assembled reflector 1 and the lamp cooling tunnel are shown in figure 4.7.

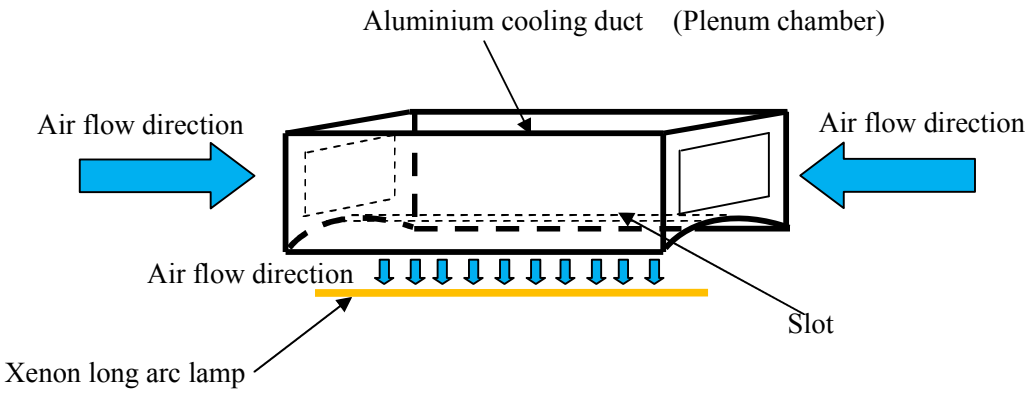

Figure 4.6 Schematic view of air flow direction in the lamp house

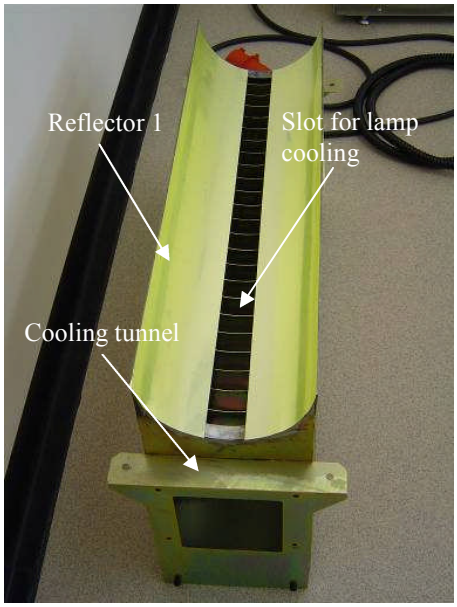

Figure 4.7 Photograph of the assembled reflector 1, reflector support and lamp cooling duct

4.2.4 Prediction of the lamp operating temperature and selection of the cooling fan capacity

The energy flux absorbed by the SQP-HLA 660 lamp surface was comprised of two parts as shown in figure 4.8, (i) the energy output from the plasma inside the lamp, (ii) energy reflected back to the lamp by reflector 1. The parameters used to predict the lamp surface temperature are shown in table 4.2.

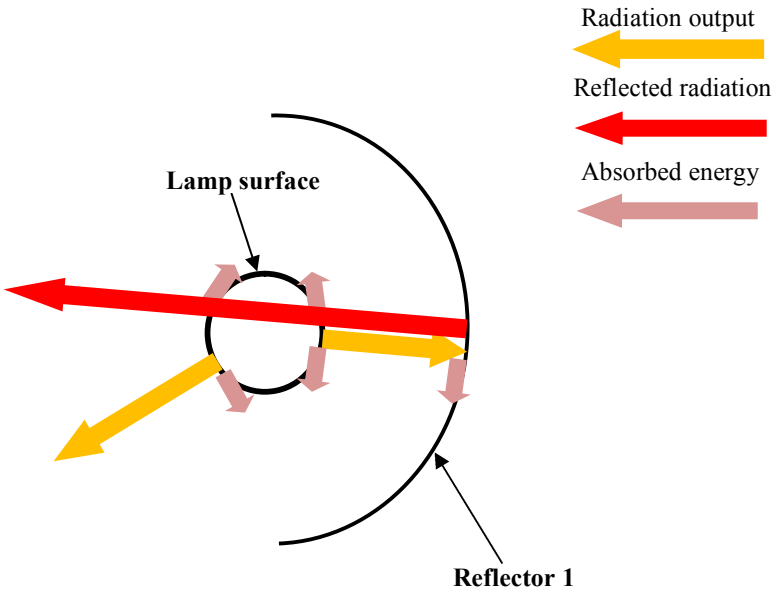

Figure 4.8 A schematic diagram illustrating the energy absorbed by the lamp

Symbol	Values
α_{lamp}	0.06
ε_{lamp}	0.06
$E_{power\ supply}$	0.92
ρ_{refl}	0.98
T_{amb}	20°C

Table 4.2 The parameters used to predict the lamp surface temperature

The power factor of the SQP-HLA 660 lamp was 0.92. The lamp surface was 2mm thick quartz with absorption of 0.06 (Anon, 2008e). The diameter of the lamp was 0.014m and the length of the lamp was 0.679m. Based on above informations, the total absorbed energy flux at the lamp surface was calculated by equation 4.1,

$$Q_{lamp} = Q_{plasma \to lamp} + Q_{ref1 \to lamp} \tag{4.1}$$

$$= 6.5kW \cdot E_{power\,sup\,ply} \cdot \alpha_{lamp} + 6.5kW \cdot E_{power\,sup\,ply} \cdot \frac{1}{2} \cdot (1-\alpha_{lamp}) \cdot \rho_{ref1} \cdot \left[\alpha_{lamp} + (1-\alpha_{lamp}) \cdot \alpha_{lamp}\right]$$

$$= 6.5kW \times 0.92 \times 0.06 + 6.5kW \times 0.92 \times 0.5 \times (1-0.06) \times 0.98 \times \left[0.06 + (1-0.06) \times 0.06\right]$$

$$= 0.6794kW = 679.4W$$

The average absorbed radiation intensity by the lamp surface was calculated by equation 4.2,

$$q_{lamp} = \frac{Q_{lamp}}{A_{lamp}} = \frac{Q_{lamp}}{\pi d_{lamp} l} = \frac{679.4W}{3.14 \times 0.014m \times 0.67945m} = 22746.3W/m^2 \tag{4.2}$$

Due to the high power of the lamp, the lamp surface could have temperatures much higher than the ambient temperature. Therefore, the natural convective heat transfer around the lamp surface can be neglected compared to the radiative heat transfer from the lamp (Ede A. J., 1967). The temperature of the lamp was calculated using equation 4.3,

$$q_{lamp} = \varepsilon\sigma(T_{lamp}^4 - T_{amb}^4) \tag{4.3}$$

And $T_{lamp} \approx 1608K = 1335°C$

The lamp supplier suggested that the lamp operation temperature should be under 850 °C. However, the predicted lamp temperature T_{lamp} was higher than this maximum lamp operating temperature. A cooling system was therefore required for the lamp to reduce the lamp surface temperature.

The average forced convective heat transfer coefficient can be calculated by Zukauskas relation as shown in equation 4.4,

$$\bar{h} = \bar{N}u_D \frac{\lambda}{D} = \frac{\lambda}{D} C \,\mathrm{Re}_D^m \,\mathrm{Pr}^n (\frac{\mathrm{Pr}}{\mathrm{Pr}_{lamp}})^{1/4} \quad (4.4)$$

If $\mathrm{Pr} \le 10$, n=0.37; $\mathrm{Pr} \ge 10$, n=0.36

To enable a calculation to be made, it was estimated that a constant air temperature of 20°C flowing across the long central axis of the lamp with a velocity of 10m/s would reduce the lamp temperature to 600°C

The following factors were used (Incropera et al, 2007)

$\mathrm{Pr} = 0.6744$

$\nu = 49.756 \times 10^{-6} m^2 / s$

$\lambda = 4.662 \times 10^{-2} W/(m \cdot K)$

$\mathrm{Pr}_{lamp} = 0.699$

Re was calculated as follows,

$$\mathrm{Re}_D = \frac{uD_{lamp}}{\nu} = \frac{10m/s \times 0.014\,m}{49.756 \times 10^{-6} m^2/s} = 2813.7 \quad (4.5)$$

Then, the average forced convective heat transfer coefficient for lamp surface: $\bar{h} = 45W/(m^2 \cdot K)$.

Using the calculated coefficient 45W/m^{2}K, the predicted lamp surface temperature can be calculated using equation 4.6,

$$q_{lamp} = \varepsilon\sigma(T_{lamp}^4 - T_{amb}^4) + \bar{h}(T_{lamp} - T_{amb}) \quad (4.6)$$

Which provides $T_{lamp} \approx 772K = 499°C$ less than the presumed 600°C.

This implies that for air of 20°C temperature with a velocity of 10m/s flowing across the long central axis of the lamp, the lamp surface temperature will be significantly less than the maximum permissible 850°C.

Based on the above calculation, two EBMPAPST G4E180-GS11-01 having air flow rate of 1030m^3/h and fan diameter of 180mm, were chosen to provide the lamp cooling. A photograph of the fan is shown in figure 4.9. The outlet area of cooling duct was 680mm long by 60mm wide. The calculated average air flow rate at the outlet slot was 14.0m/s higher than the desired minimum of 10m/s. The operating lamp surface temperature with cooling was measured using an IR camera as shown in figure 4.10. From figure 4.10, it can be seen that the lamp surface temperature is less than 750°C, lower than the maximum lamp operating temperature. It is however higher than the predicted lamp surface temperature, this may possibly be due to the low emissivity and high transmittance of the quartz envelop, leading to the IR camera predominately imaging the flux emitted from the plasma inside the lamp. It can be concluded that the developed cooling system provides effective lamp cooling.

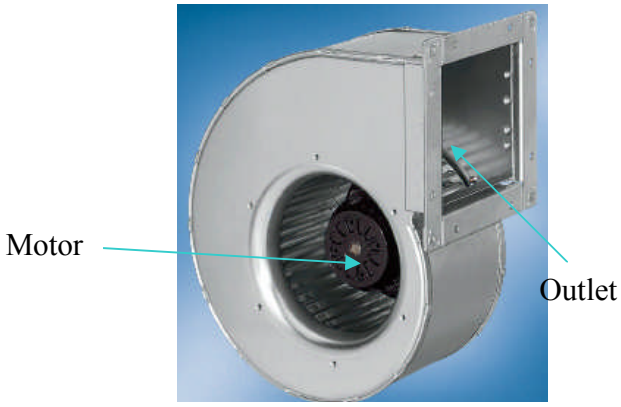

Figure 4.9 Photograph of the EBMPAPST G4E180-GS11-01 fan

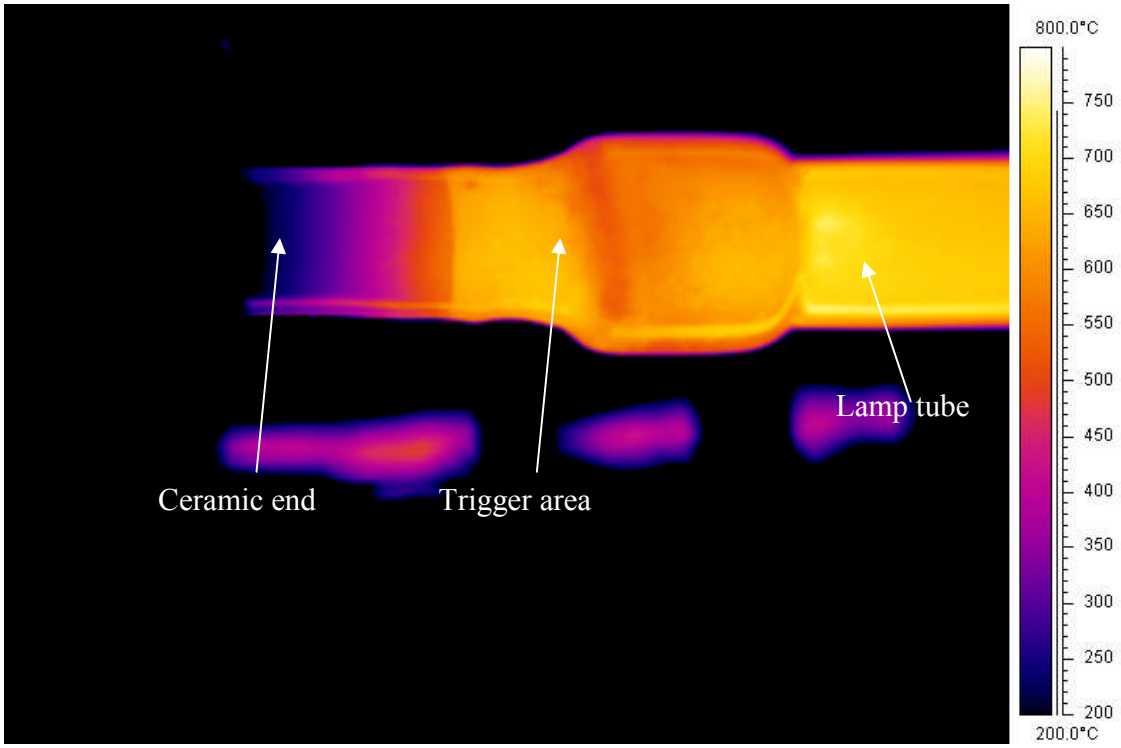

Figure 4.10 IR image of the lamp mounting end

4.2.5 Fabricating reflector 2 (Parabolic reflectors)

An aluminium block with dimensions of 738mm long by 354mm wide by 60mm thick was used to fabricate the reflector 2 support using a CNC machine. A sketch of the reflector 2 support is shown in figure 4.11. To bond the reflector to the support, Loctite 330 having a maximum operating temperature of up to 100°C was uniformly painted onto the front surface of the reflector 2 support, and the activator Loctite 7380 was sprayed on the rear surface of the Miro 4270 AG reflective material. The reflective material was placed on the glue painted surface of the reflector 2 support, and then a wooden rod was rolled on the reflective material surface to allow an even pressure across the reflector surfaces and ensure that an accurate system profile was obtained as shown in figure 4.12.

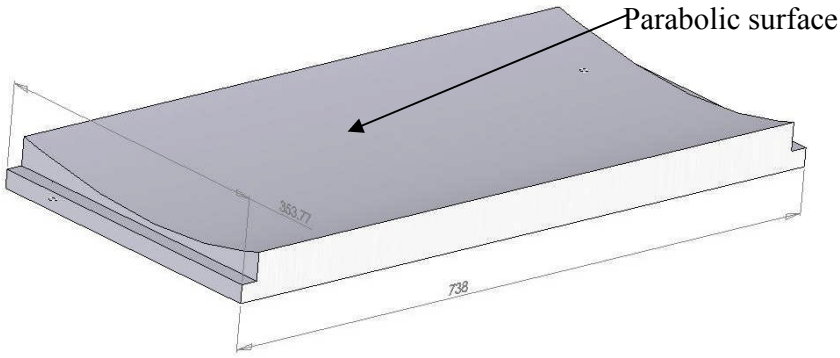

Figure 4.11 3D sketch of the reflector 2 support, all dimensions in 'mm'

Figure 4.12 Attachment of mirror reflector to the reflector 2 support

4.2.6 Design and fabrication of reflector 3 (Secondary reflectors)

A ray trace was used to determine modifications to the secondary reflector that will improve the uniformity of the solar simulator energy flux output. All rays were assumed specular in the ray trace model, the light output angle (θ) was measured from the horizontal. The output flux of the lamp was composed of two parts: half of the output flux traveled to reflector 1 and was then reflected back to reflector 2, finally reaching the secondary reflector; the remaining half of the output flux directly travelled to reflector 2 and then reached the secondary reflector. The ray trace diagram illustrating the solar simulator optical behaviour is shown in figure 4.13 with 360 rays traced from 1° to 360° at

1° interval. It can be observed that the rays are not uniformly distributed along the test plane width, being denser at the centre of the test plane than that at the sides.

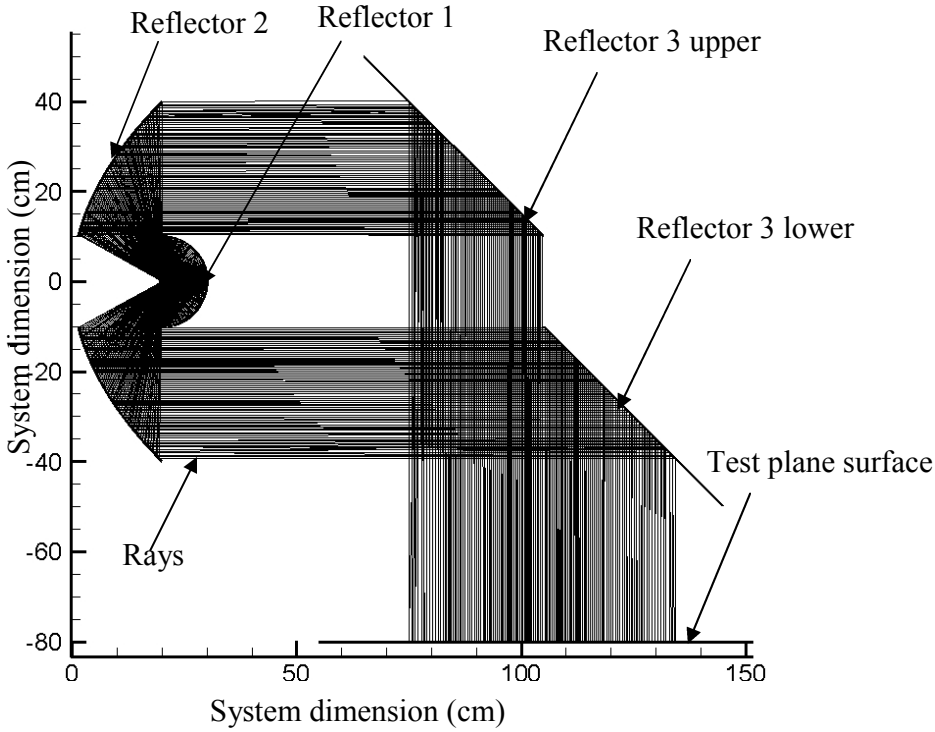

Figure 4.13 Ray trace diagram illustrating the optical behaviour of the solar simulator design, 360 rays from 1° to 360° are illustrated

720,000 rays were traced in the ray trace to calculate the energy distribution along the test plane width. The average reflectivity of reflector 1 and 2 was 98%. The power factor of the selected Xenon long pulsed arc lamp was 0.92, and the rated power of the lamp was 6.5kW. It was known that the energy distribution on the test plane surface demonstrates left-right symmetry. In order to simplify the simulation, only the rays reflected on the upper reflector 3 were used in the ray trace technique. The predicted energy distribution on the test plane surface is shown in figure 4.14. From figure 4.14 is can be seen that if the luminous efficacy of the lamp is 15%, the highest energy flux is 1244W/m^2, at the centre of the test plane, gradually reducing to 667W/m^2 across the width of the test plane. The maximum flux

difference at the test plane surface is approximately 46%. It can be reduced by optimizing reflector 3 with a graduated reflective coating on its surface designed to modify the flux intensity coming from reflector 2 to achieve a uniform level. Based on the predicted energy distribution on the absorber surface, the designed reflectivities for the reflector 3 upper and lower region along its width are presented in figure 4.15.

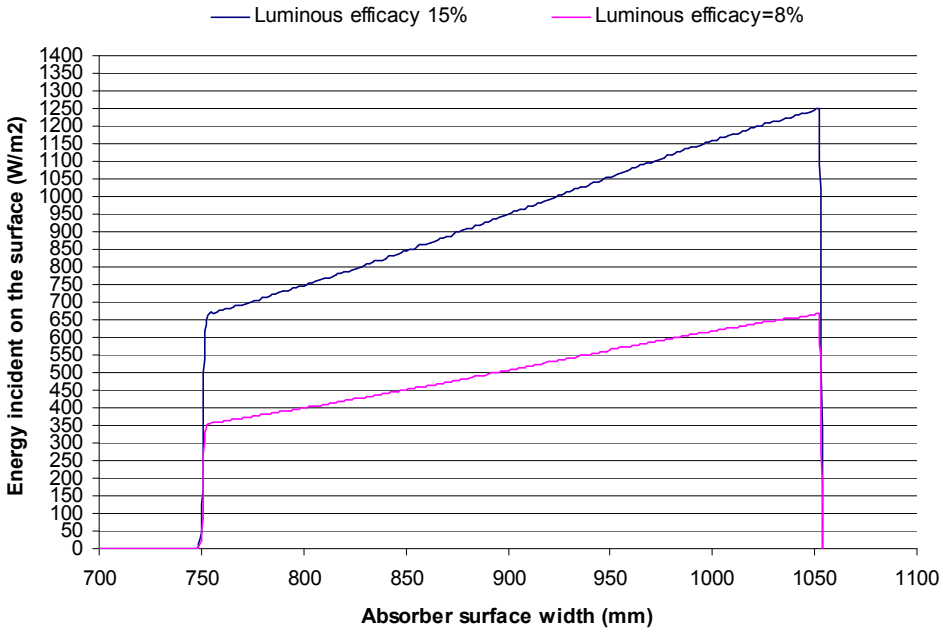

Figure 4.14 Energy distributions along the absorber width

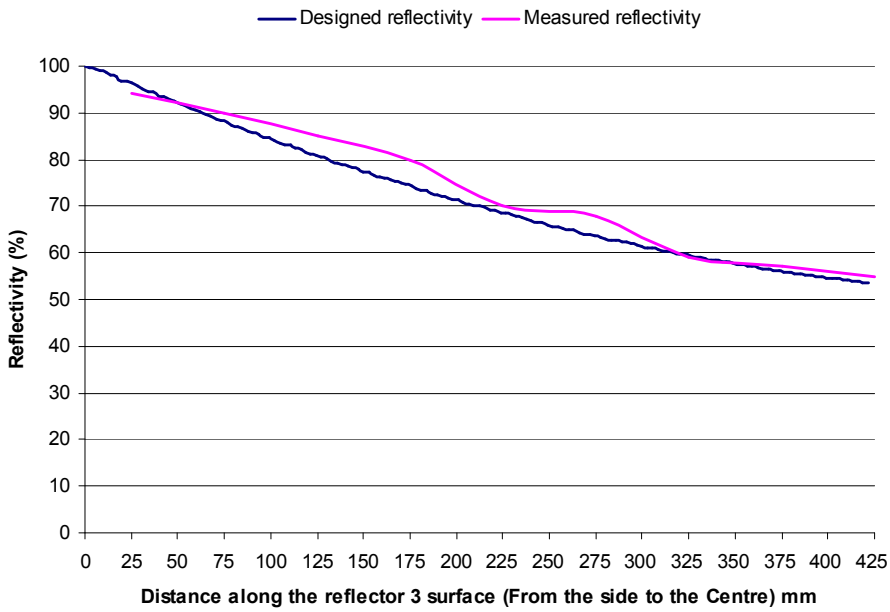

Figure 4.15 The measured reflectivity and the designed reflectivity along the reflector 3 width

Reflector 3 was comprised of 4 pieces of 2 mm thick float glass (dimension 425mm × 350mm) mirror coated by Siltint Company. Figure 4.16 shows piece of the mirror coated glass. The designed and measured reflectivities along the width of the mirror are shown in figure 4.15. From figure 4.15, it can be seen that the measured reflectivity in the range between 0 mm to 50 mm is lower than that designed, and is higher than that designed in the range between 50mm to 300mm. In the range from 300mm to 425mm, they are almost the same. The desired solar simulator energy flux output uniformity might not be achieved due to the deviation in measured mirror coating from that required.

Figure 4.16 Photograph of the graduated mirror coated float glass

Two coated float glass sheets were glued onto a 6mm thick by 740mm long by 450mm wide toughened glass using loctite 358 adhesive which is designed for glass to glass application. A photograph of the coated float glass bonded to the glass back plate is shown in figure 4.17. They formed mirrors were subsequently attached onto the solar simulator frame using 3m 4941 VHB acrylic foam double sided tape.

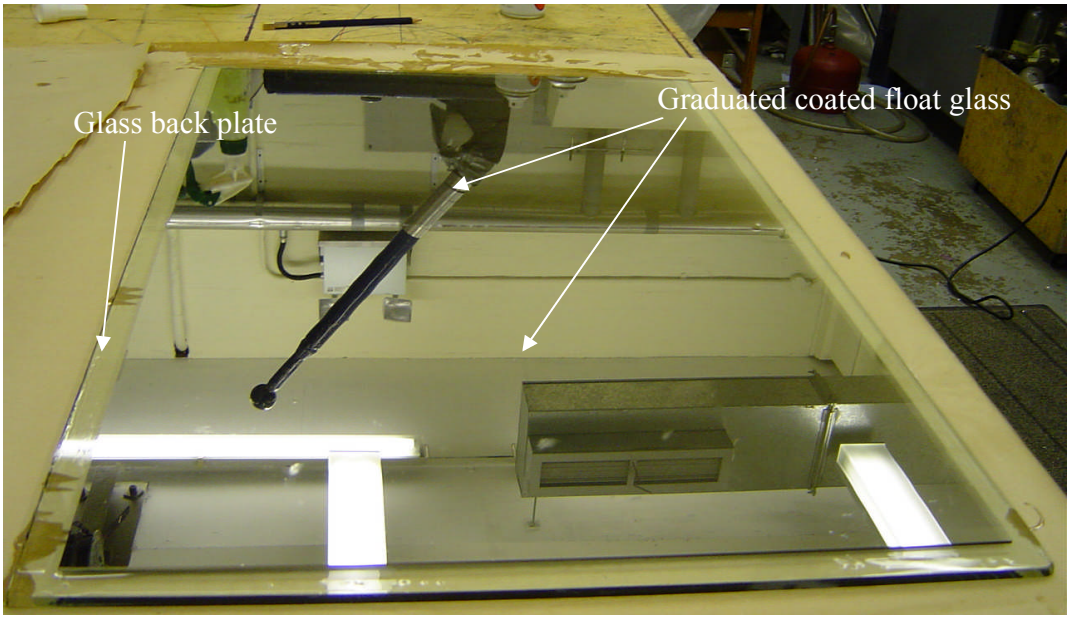

Figure 4.17 A photograph of the graduated coated glass glued to the glass back plate.

4.3 Optical alignment of the solar simulator system

Correct alignment of the lamp and mirrors were required for the solar simulator to perform in the way predicted. In the first instance, spirit levels and rulers were used for the alignment process. Initially the lamp was located along the long central axis of the semi-circular reflector (Reflector 1). The lamp in the semi-circular reflector was then located at the focal point of the parabolic reflectors (Reflector 2). Verification of the optical alignment accuracy was undertaken using laser pens. Two laser pens were suspended above reflector 2 and turned on as shown in figure 4.18. When the reflector 2 and lamp are accurately aligned, the laser beam can be found to intersect the lamp tube perpendicularly. A similar verification method was also applied for reflector 3 alignment. The assembled solar simulator is shown in figure 4.19.

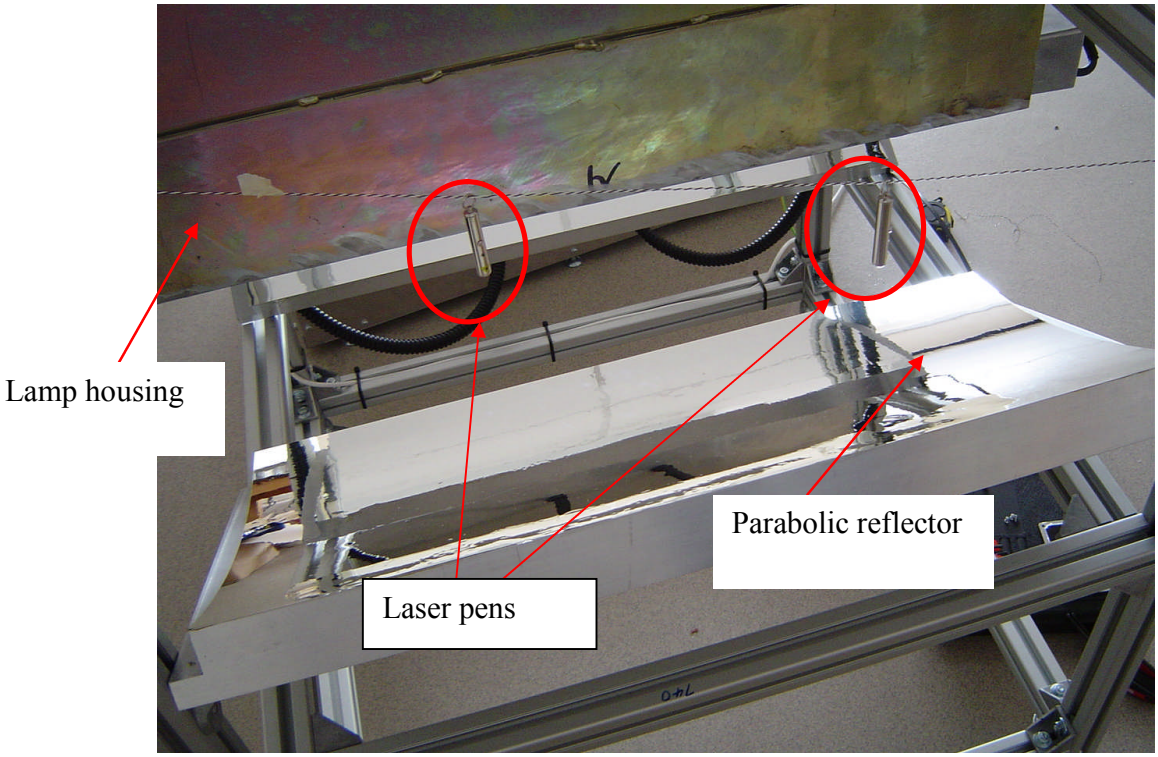

Figure 4.18 A photograph showing suspended laser pens used to verify for optical alignment

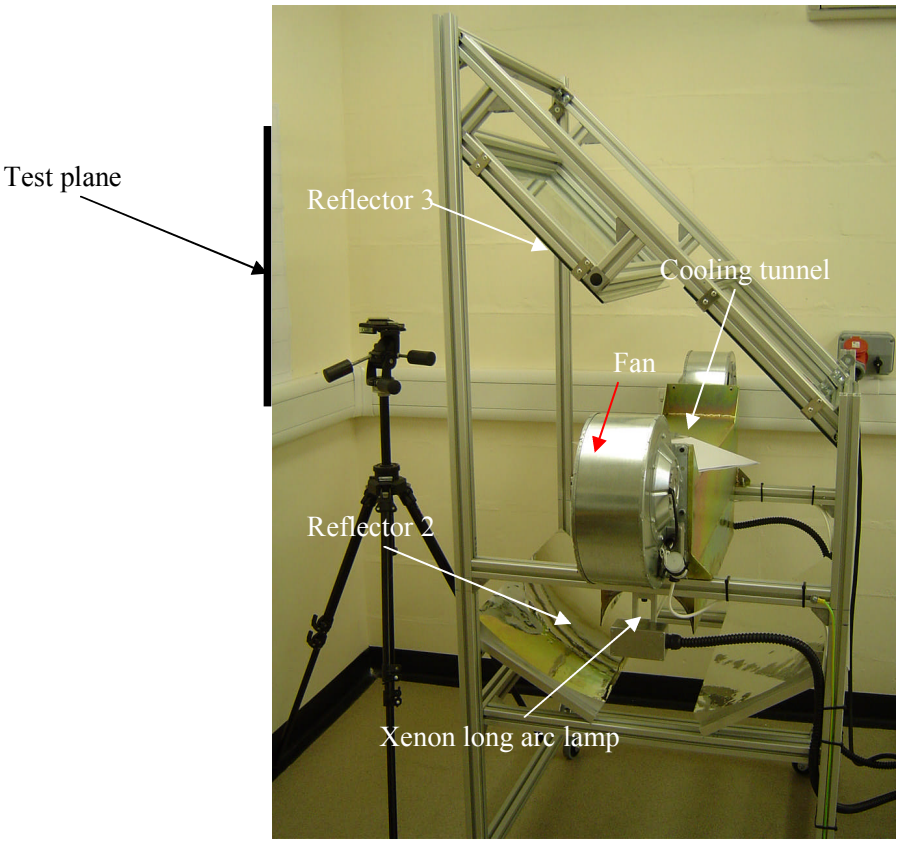

Figure 4.19 A photograph showing the developed solar simulator

4.4 Determination of the characteristics of the solar simulator

The spatial distribution of the solar radiation on the test plane was measured using a CM11 pyranometer connected with a Keithley 2750 data logger. The test plane was located at a distance of 1m from the solar simulator aperture, and the intensity of flux measured at 63 locations spaced on a regular grid of size 60cm by 80cm to divide the test plane as shown in figure 4.20. The lamp was set to the lower operation output of 2kW power input and after a 30 minute lamp warm-up period, the radiation was measured at each grid point as shown in figure 4.21. From figure 4.21, it can be seen that the radiation intensity in the upper region of the test plane is higher than that in the lower region of the test plane. The centre area between 25cm to 40cm in the vertical axis of the test plane has the lowest solar radiation intensity at approximately 30W/m^2. This may be caused by the edge mirror error of reflectors 2 and 3, or the solar simulator being incorrectly aligned.

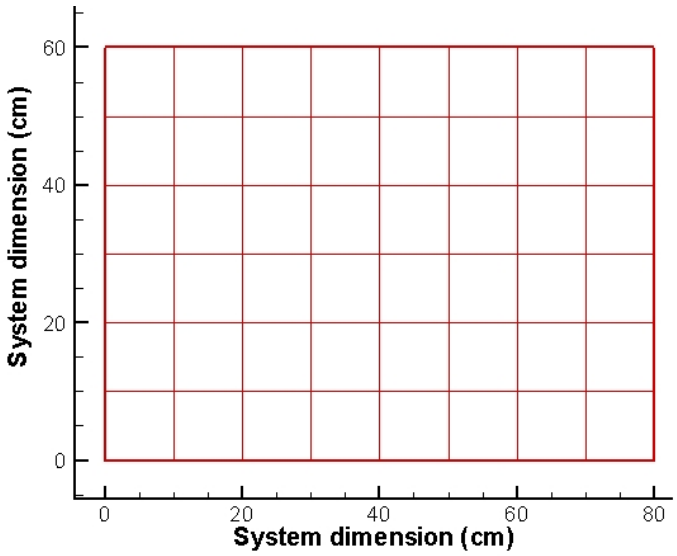

Figure 4.20 Location of points on the test plane used to determine insolation distribution

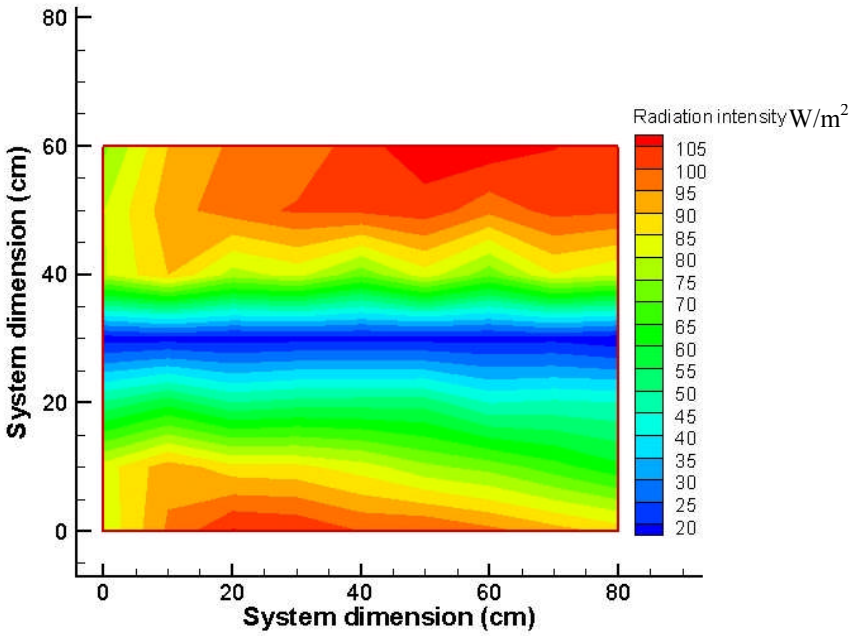

Figure 4.21 Spatial distribution of insolation on test plane

From the above, it was apparent that the use of conventional rulers and spirit levels was insufficient to align the solar simulator system accurately. More accurate measurement methods were required to achieve adequate solar simulator component alignment. A Platinum Faro Arm which can be used to collect individual 3D data points of an object in a space using a point probe on an articulating arm was used to improve the solar simulator alignment as shown in figure 4.22. The measurement accuracy of a Platinum Faro Arm is ±0.013mm. A 3D coordinate map was built for the solar simulator using the Faro Arm with the centre of the left lamp holder hole chosen as the origin for the coordinate system. After several applications to confirm the coordinate points and re-alignment of the solar simulator component, the designed and final measured coordinate points of the solar simulator components are shown in figure 4.23. From figure 4.23, it can be seen that the installation deviation is within ±2.5mm, which is still large and may affect the solar simulator output irradiation performance.

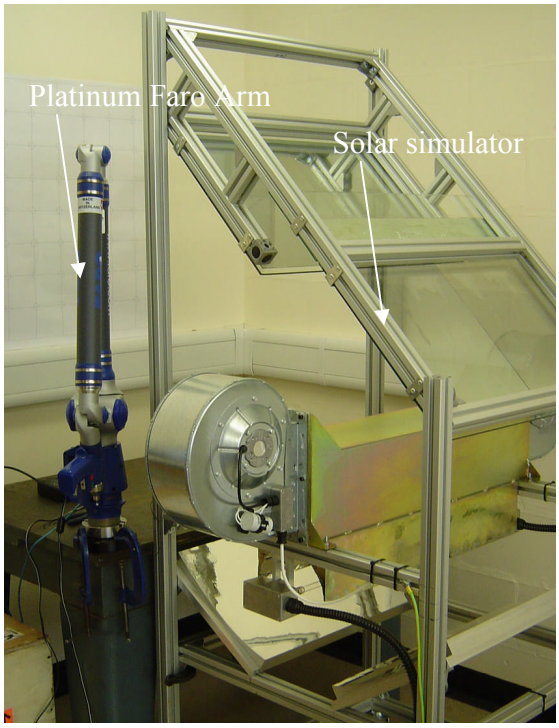

Figure 4.22 A photograph showing a Faro arm and the developed solar simulator

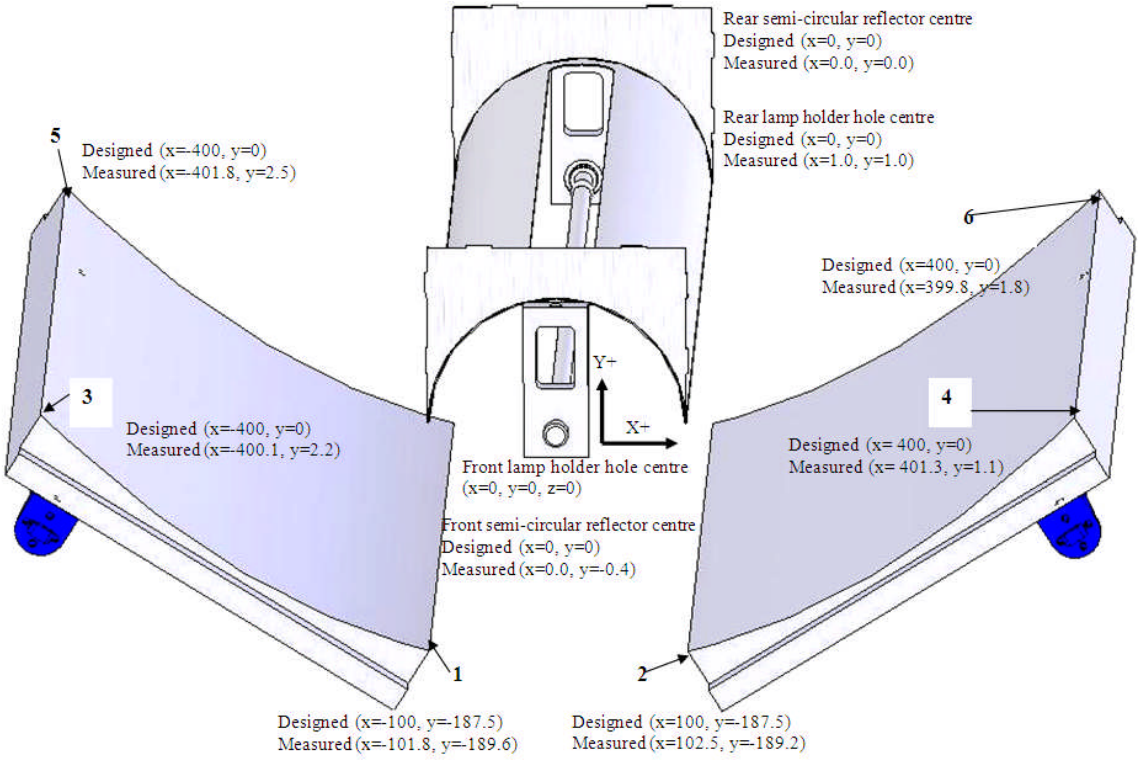

Figure 4.23 Designed and measured coordinate points of the solar simulator, all dimensions in 'mm'

The final spatial distribution of the solar radiation on the test plane for low and high power settings are shown in figure 4.24 and 4.25, respectively, using the measurement method discussed in section 4.4.

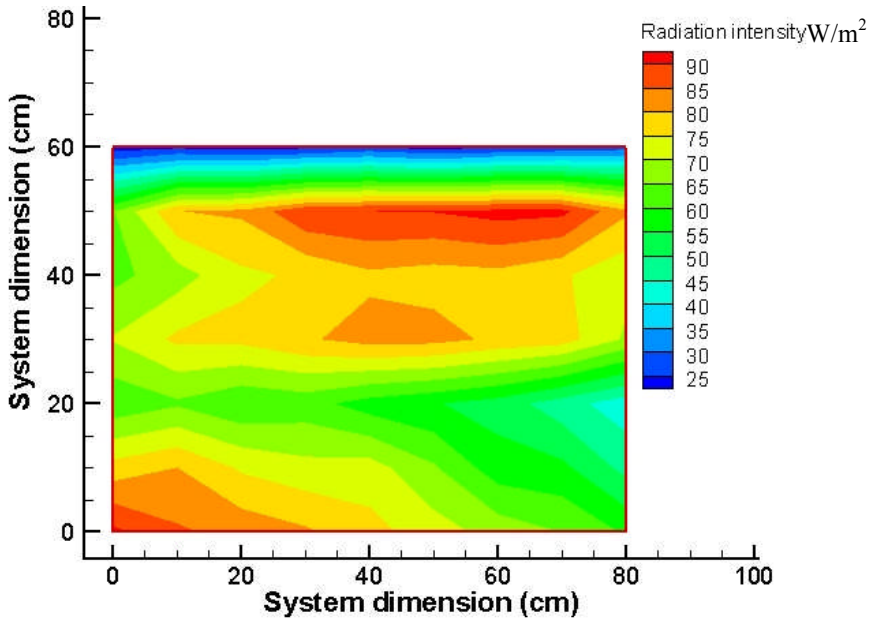

Figure 4.24 Spatial distribution of insolation at test plane under solar simulator at low power setting

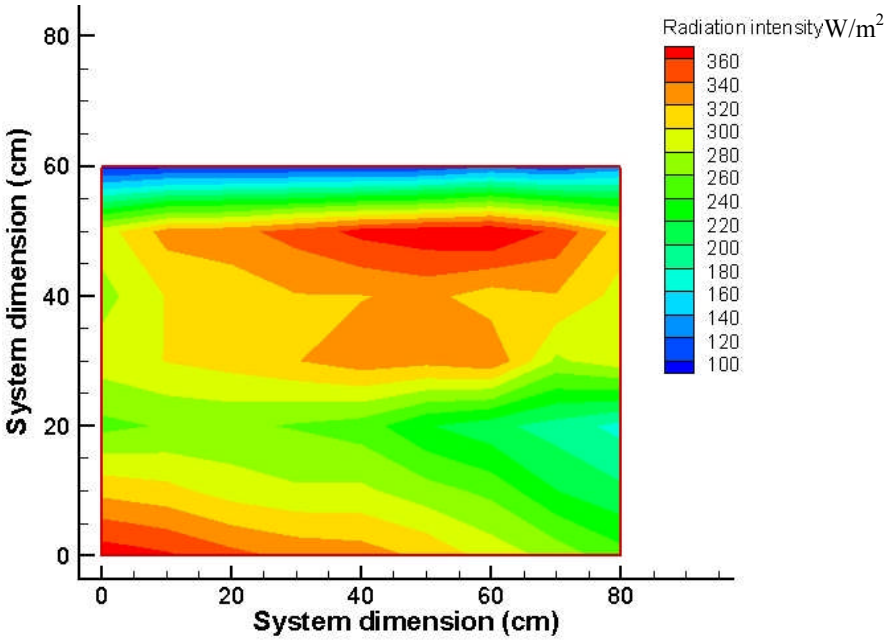

Figure 4.25 Spatial distribution of insolation at test plane under solar simulator at high power setting

From figures 4.24 and 4.25 it can be seen that the flux distribution is not uniform on the absorber plane. The measured maximum flux intensity on the test plane is approximately 90W/m^2, when the lamp runs in low power setting which is 2kW, and approximately 360W/m^2 at high power setting being 6.5kW. The measured output beam uniformity was within ±13% deviation on the test plane. The centre region on the test plane has lower insolation than that on the upper and the lower regions of the test plane. The measured radiation output was lower than that predicted. This is due to the reflectivity of reflector 3 being significantly reduced at the solar incidence angle of 45°, compared to when reflecting solar radiation incident perpendicular to its surface. When the solar radiation was incident perpendicular in the centre region of reflector 3, the measured reflectivity was 56%, compared to a measured reflectivity of approximately 20% with a solar radiation incidence angle of 45° to its surface at the same position.

For the indoor experimental characterisation of the ACPPVC-55/PCM, when a maximum solar radiation intensity of 360W/m^2 was incident on the aperture of the ACPPVC-55/PCM system, the time required to obtain phase change of all the PCM in the system may be long. In order to increase the solar radiation intensity output of the solar simulator, Miro-Silver 4270 AG 0.2mm thick having a reflectivity greater than 98%, even with a solar radiation incidence angle of 45° to its surface, was subsequently employed as the reflective material replacing the graduated coated reflector 3. An average solar radiation intensity of 672W/m^2 was measured at the aperture of the ACPPVC-55/PCM.

A ‘T’ shaped aluminium test piece was used to measure the solar simulator collimation, to do this it was placed on the test plane for which the solar simulator flux output had been

measured as illustrated in figure 4.26. The height of the aluminium piece 'h' was 60mm, by measuring the shadow length, the collimation of the solar simulator 'θ' can be subsequently calculated using equation 4.7.

$$\tan\theta = S / h \tag{4.7}$$

The measured collimation angles were all 0° in the vertical directions. The measured collimation angles in the horizontal directions at the test positions are presented in figure 4.27. From the figure 4.27, it is can be seen that the collimation angles are at maximum ±8° along the horizontal direction, this is due to the design of the solar simulator not achieving collimation of the output energy in the horizontal direction

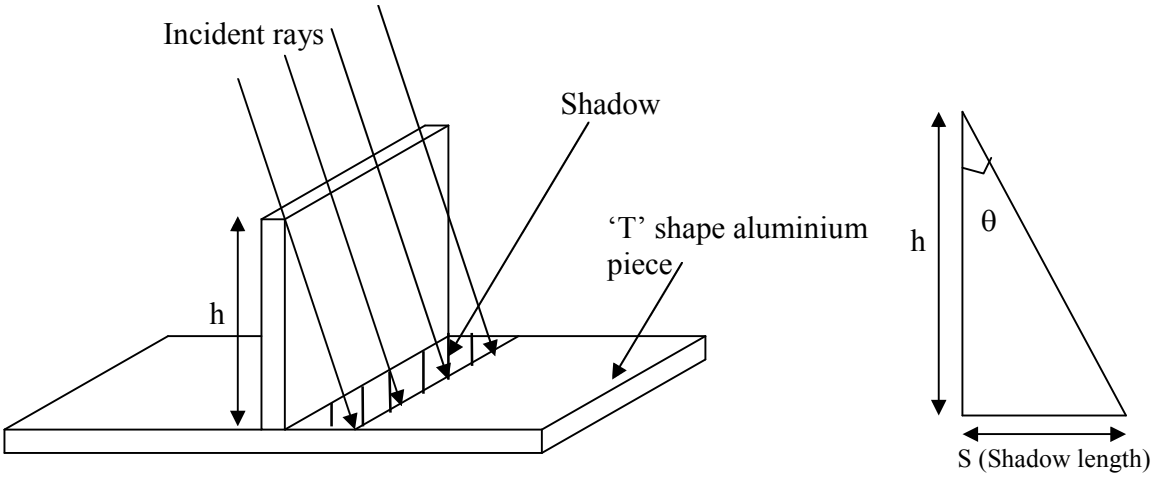

Figure 4.26 'T' Shaped aluminium test piece used to measure the solar simulator collimation

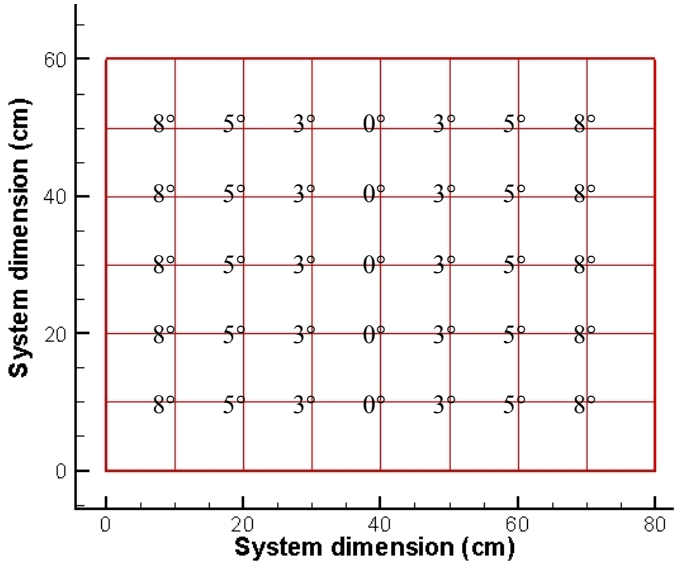

Figure 4.27 Solar simulator collimation angles in the horizontal direction

4.5 Conclusion

A design to produce a highly collimated large illumination area solar simulator was developed and fabricated. The parabolic reflectors provided good collimation output for the solar simulator, and the designed graduated reflective coated secondary reflector improved the irradiation output uniformity.

The measured output beam uniformity for the designed solar simulator was within ±13% deviation on a 60cm wide 80cm long test plane, which is higher than the target value, this is due to the deviation in the performance of the secondary reflector and non optimal system alignment. The measured collimation angles were all 0° in the vertical directions and at maximum ±8° in the horizontal direction. The designed solar simulator, which is close to the solar simulator performance Class C, is suitable for assisting indoor PV experimental characterisations.

Chapter 5 Experimental characterisation of low concentration ratio building integrated PV concentrators

5.1 Introduction

Extensive indoor experimental characterisation of a number of PV systems was undertaken for a range of incident solar radiation intensities using the developed solar simulator. The systems tested are described below:

- **System A**, a flat non-concentrating panel with six 125mm × 125mm BP SATURN solar cells connected in series
- **System B**, a concentrating trough ACPPVC-55 panel with six 125mm × 125mm BP SATURN solar cells connected in series as described in chapters 2 and 3.
- **System C**, a concentrating trough ACPPVC-55 panel with six 125mm × 125mm BP SATURN solar cells connected in series combined with a passive cooling PCM system as described in chapter 3.

An electronic Keithley 2430 source-meter, which replaced the simple PV performance test circuit shown in figure 5.1, was used in the following tests to achieve the desired accuracy. In the simple PV performance test circuit, an ammeter connected in series measured the current produced by the PV, and a voltmeter connected in parallel concurrently measured the voltage produced by the PV. A rheostat applied in parallel connection across the voltmeter was used to change the internal resistance of the circuit and thus the electrical output. The behaviour of the PV can be characterised by the measured Current-Voltage curve generated by applying a variable load. The voltage source circuit configuration of the Keithley 2430 source meter is shown in figure 5.2. The current and the voltage of the solar cells were measured by sourcing the voltage from the Keithley 2430 system. 'T' Type thermocouples connected with a Keithley 2750 data logger were used to record the thermal performance of the systems in the following tests.

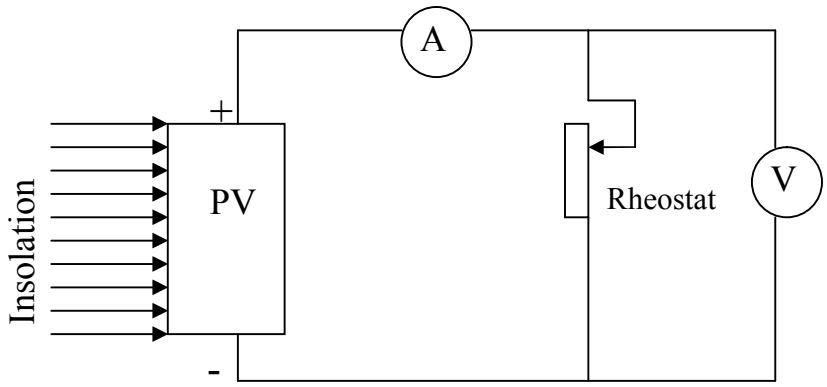

Figure 5.1 Standard circuit diagram for I-V curve characterization of PV system

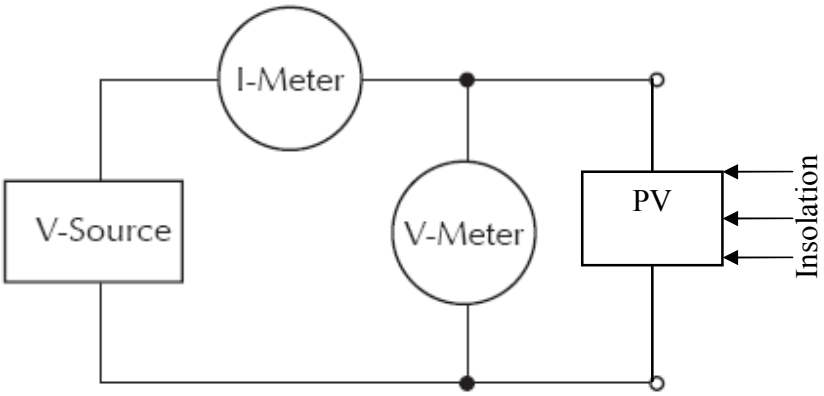

Figure 5.2 The basic circuit configuration of Keithley 2430 by source voltage

5.2 The I-V characteristics of BP SATURN solar cells

Exploratory experimental tests for BP Saturn solar cells were undertaken using a highly collimated Model SS 1.6kW solar simulator manufactured by Sciencetech Company. The spectral distribution of the solar simulator measured by a HR2000+ high resource spectrometer is shown in figure 5.3. Voltage - current data, maximum power point, electrical conversion efficiency and fill factor were determined from the tests. Figure 5.4 (a) shows the test system with a SATURN solar cell and 5.4 (b) presents an enlarged view of the SATURN solar cell under test. A pyranometer was used to measure the solar radiation for each of the tests. A block diagram illustrating the connection between the solar cell and the test facilities is shown in figure 5.5.

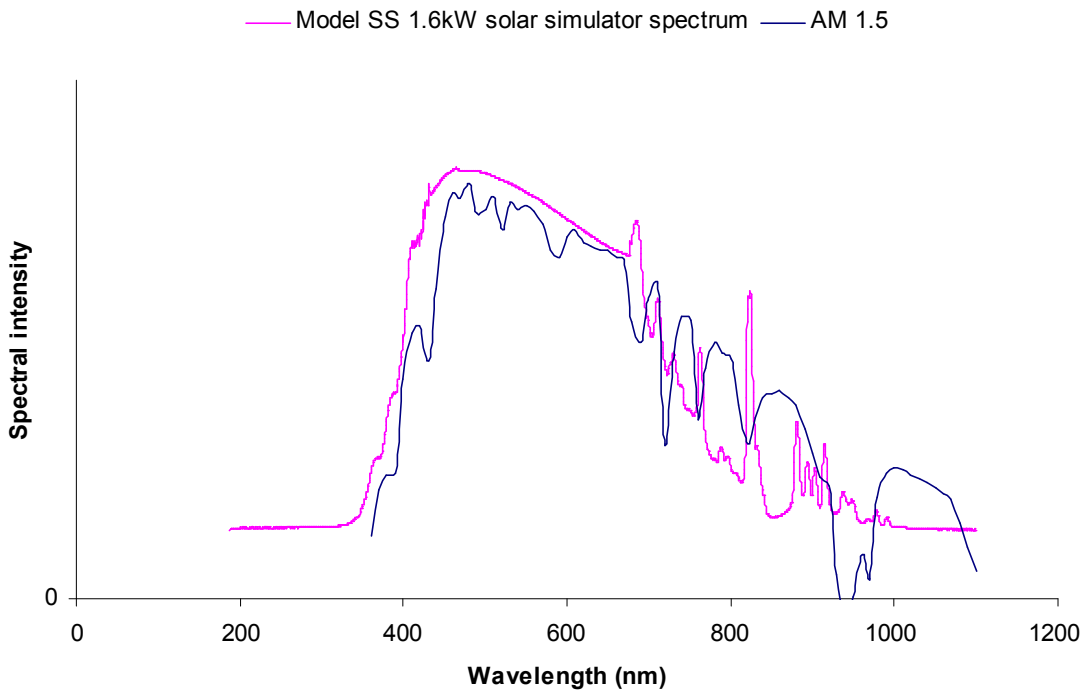

Figure 5.3 Measured spectral distribution using HR2000+high resource spectrometer of the solar simulator with a 1.6kW Xenon short arc length lamp and AM1.5.

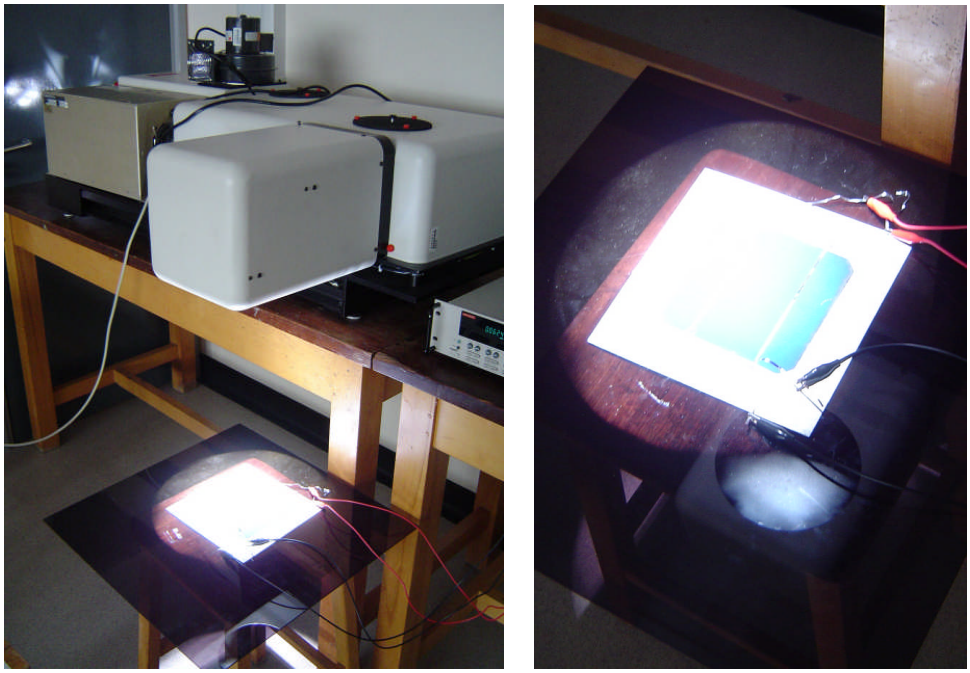

(a) (b)

Figure 5.4 (a) Experimental characterization of a full size SATURN solar cell (b) test plane enlarged view.

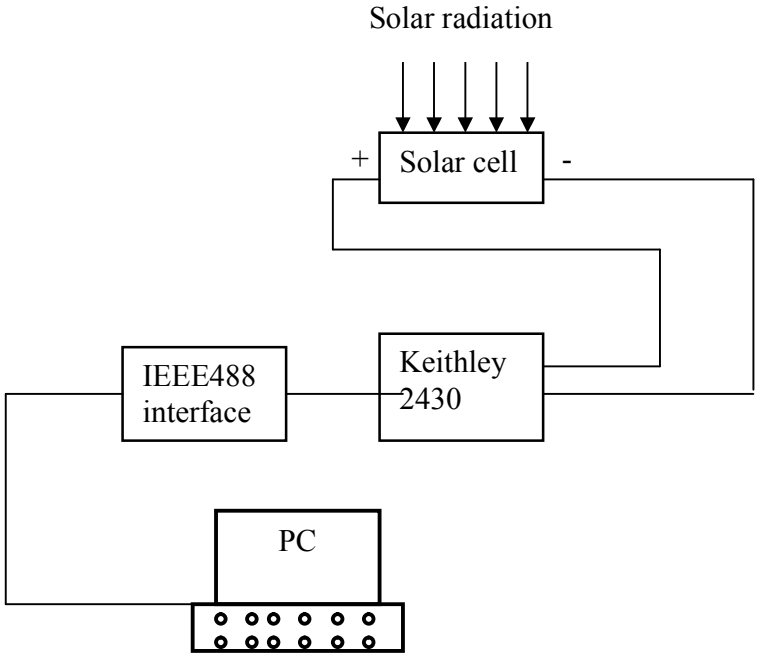

Figure 5.5 Block diagram for the I-V measurement of a photovoltaic system under illumination conditions.

Experimental tests were carried out for one full size BP SATURN solar cell with and without a Sylgard 184 coating on the front surface at different solar radiation intensities of 555W/m^2, 714W/m^2, 848W/m^2 and 926Wm^2 to investigate the effect of the Sylgard 184 front coating on the cell performance. Ambient room temperature was maintained at 20°C, the doors and windows of the test room were closed to reduce unwanted air flow and temperature variations. The radiation was perpendicular (0° solar incidence angle) to the solar cell. The measured I-V data of the solar cell are presented in figure 5.6 and 5.7, and table 5.1.

From figures 5.6 and 5.7, and table 5.1, it can be seen that the full size BP SATURN solar cell had a decrease in short circuit current of 6% when coated with Sylgard on the front surface, compared to no coating for similar radiation levels. The open circuit voltages were almost the same in both cases. Although the coating reduced the short circuit current of the solar cell, the reduction in maximum power output was only 1%.

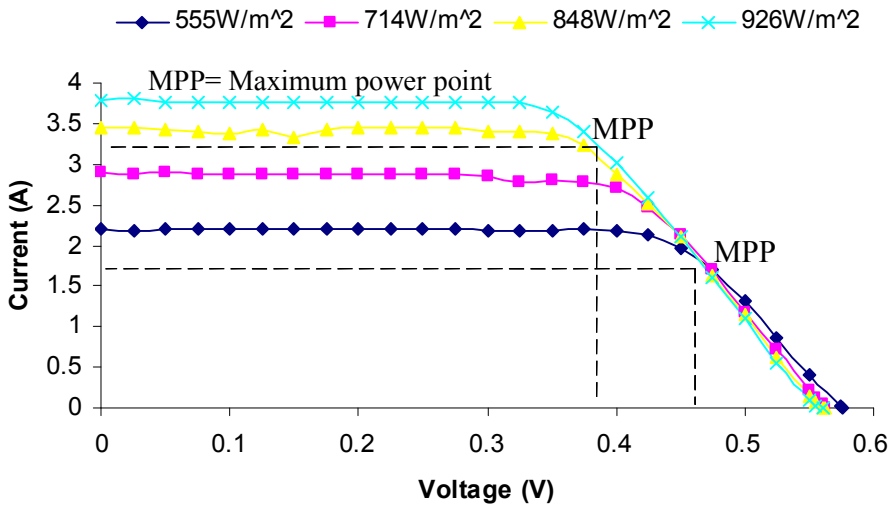

Figure 5.6 I-V characteristics for a full size SATURN solar cell with no Sylgard 184 coating on the front surface. The ambient room temperature was 20°C and solar incidence angle was 0°

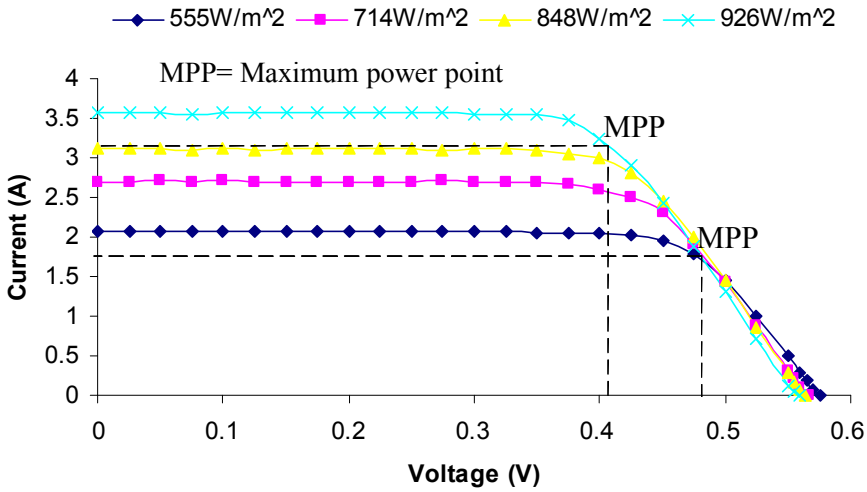

Figure 5.7 I-V characteristics for a full size SATURN solar cell coated with Sylgard 184 at the front surface. The ambient room temperature was 20°C and solar incidence angle was 0°

	Solar radiation intensity (W/m^2)	**Isc (A)**	**Voc (V)**	**MPP (W)**
uncoated solar cell	555	2.20	0.576	0.90
	714	2.89	0.562	1.08
	848	3.45	0.562	1.21
	926	3.78	0.560	1.28
Front surface coated solar cell	555	2.08	0.576	0.88
	714	2.70	0.567	1.06
	848	3.12	0.564	1.20
	926	3.56	0.560	1.27

Table 5.1 The short circuit current, open circuit voltage and maximum power point for a solar cell tested with and without Sylgard 184 coating on the front surface for different solar radiation intensities.

The fill factors can be calculated by equation 5.1,

$$ff = \frac{I_{\max} V_{\max}}{I_{sc} V_{oc}} \tag{5.1}$$

The PV efficiency is given as follows equation 5.2,

$$\eta = \frac{P_{\max}}{GA} \tag{5.2}$$

Where, I_{max} is the current at maximum power point, V_{max} is the voltage at the maximum power point, G is the incident solar radiation and A is the effective solar cell area.

The fill factors (ff) of one solar cell with and without the sylgard 184 front coating are shown in figure 5.8. It can be seen that the solar cell with the front surface coating had a higher fill factor than that without a front surface coating with similar intensities of solar radiation. The fill factor for both decreased with increasing incident solar radiation intensity. The fill factor at different radiation intensities along with a linear line fit for both systems is also shown in figure 5.8. The fill factor decreased by 0.0002 for every 1W/m^2 rise in solar radiation intensity for the solar cell with no coating at the front surface, and decreased by 0.0003 for every 1W/m^2 rise in solar radiation intensity for the same cell with the front surface coated. The electrical conversion efficiency of one solar cell with and without the coating on the front surface is shown in figure 5.9. It can be seen that the electrical conversion efficiencies decreased with increasing solar radiation intensity, this is due to the increased cell temperature. The efficiencies are 10.39% for the solar cell with no coating on the front surface, and 10.12% for the same cell with a Sylgard 184 coating on the front surface at an incident solar radiation intensity of 555W/m^2.

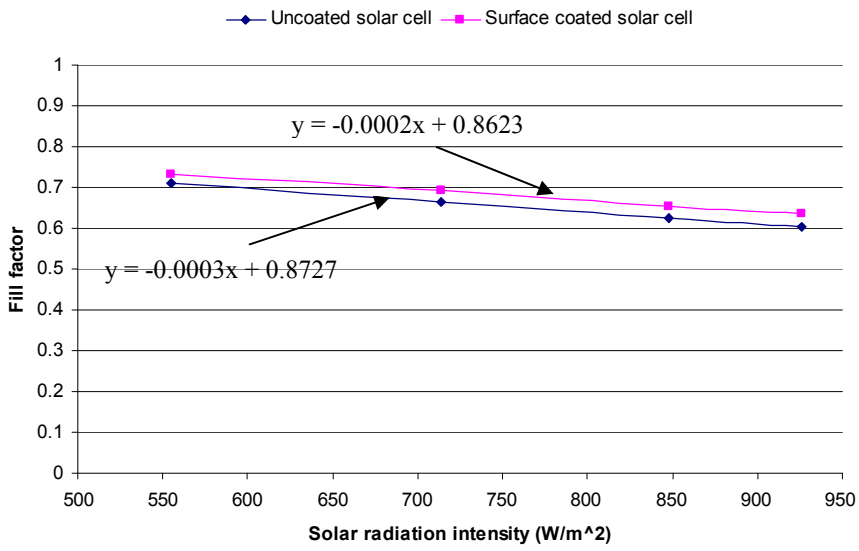

Figure 5.8 The variation of fill factor for one BP SATURN solar cell with and without Sylgard 184 coating at different incident solar radiation intensities.

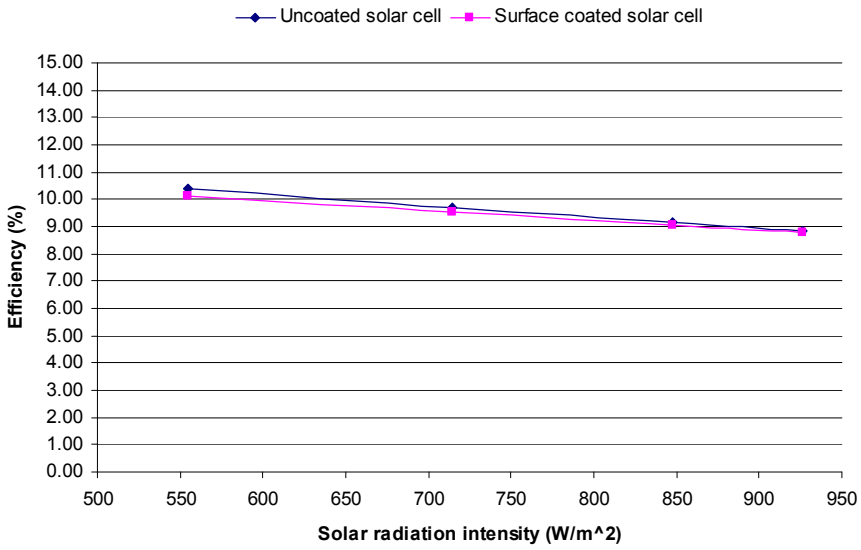

Figure 5.9 The variation of electrical conversion efficiency of one BP SATURN solar cell with and without Sylgard 184 coating at different incident solar radiation intensities.

5.3 Exploratory test using RT27 phase change material in an aluminium container

An experiment was undertaken to observe the variation in the temperature distribution in RT27 as it melted in an aluminium container with inner dimension of 105mm × 56mm × 15mm.

A wire support matrix was used to support an array of thermocouples inside the container as suggested by Ettouney et al (2005). The wire matrix, however, could affect the heat transfer inside the container potentially altering behaviour (Huang, 2002, Ettouney et al, 2005). In order to reduce this problem, thermocouples were bonded by 3.2mm diameter heat shrink to a 1.8 mm diameter straight bamboo rod to produce a thin stable sensor holder

as shown in figure 5.10 and fixed through the rear plates of the aluminium container to monitor the temperatures in the exploratory test.

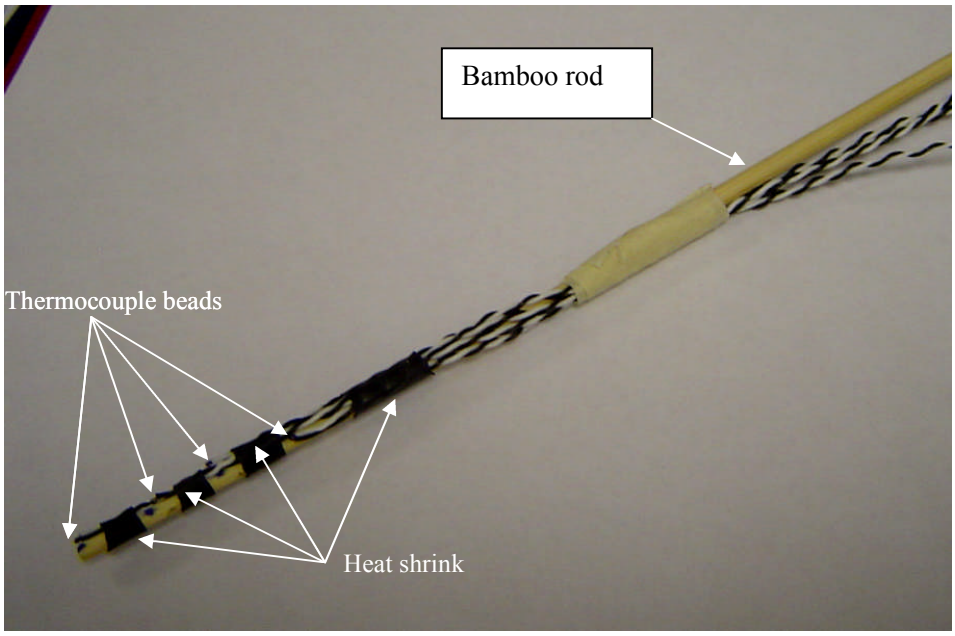

Figure 5.10 Image of thermocouples bonded to bamboo

In the exploratory test, two sets of the above thermocouple rods were located in the middle 1/3 and 2/3 section along the length of the aluminium box. Each rod with four thermocouples was passed through the holes in the rear of the aluminium box as shown in figure 5.11. Rubber stoppers and silicon sealant was used to seal the holes in the rear of the box. The thermocouple rods were inserted so that the thermocouples were at distances of 2mm, 20mm, 38mm, and 50mm from the front plate. The locations of the thermocouples T1 to T8 are shown in figure 5.12. Thermocouple T9 was used to measure the front surface temperature of the aluminium box. Thermocouples T10 and T11 were located at the rear surface of the aluminium box. The ambient room temperature was measured by thermocouple T12.

The aluminium box was heated by two TO-220 resistance heaters each with a rated power output of 35W and dimensions of 14.5mm×10mm×4mm mounted to the exterior front surface of the aluminium box as shown in figure 5.11. 5.0W was delivered by each heater in this test. Temperature readings were taken every 30 second using a Keithely 2750 data logger. Ambient room temperature was maintained at 20°C, the door and windows were closed to reduce unwanted air flow and temperature variations.

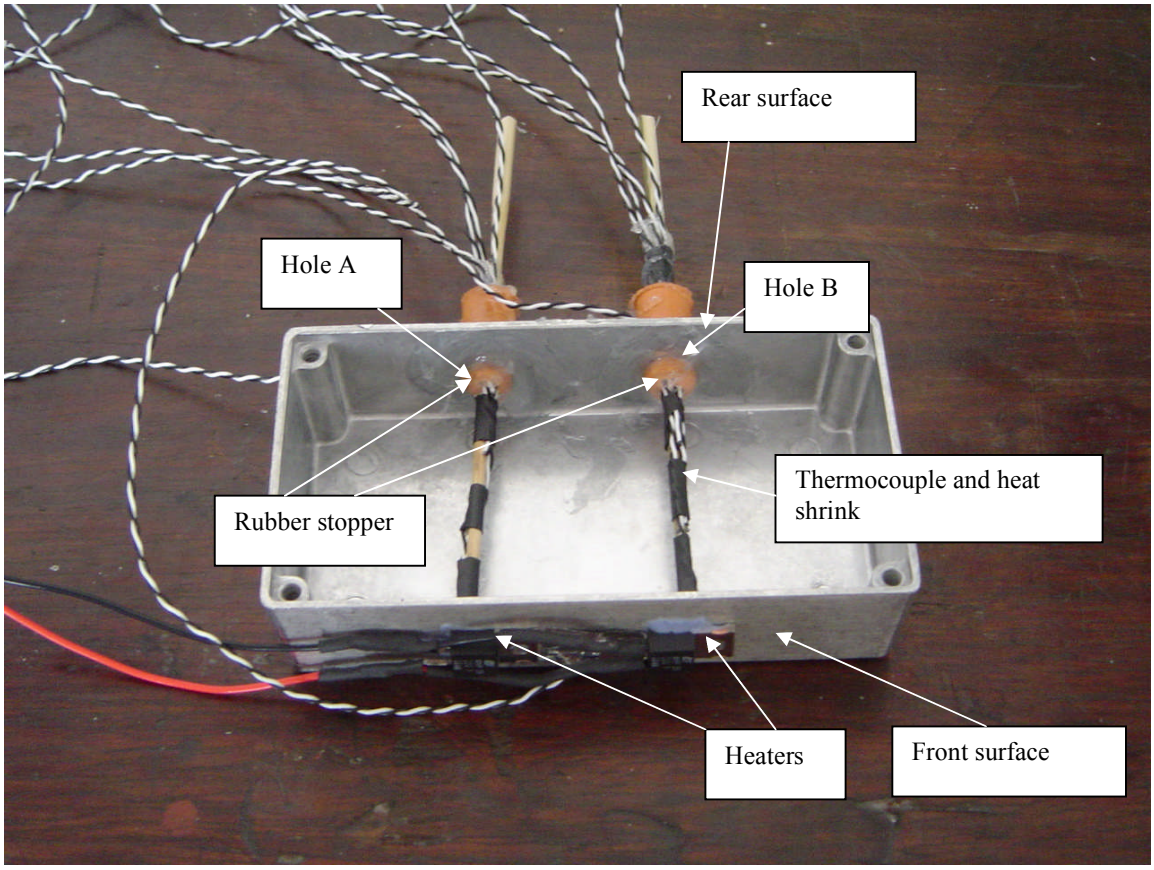

Figure 5.11 Photograph of thermocouples fixed inside the aluminium container

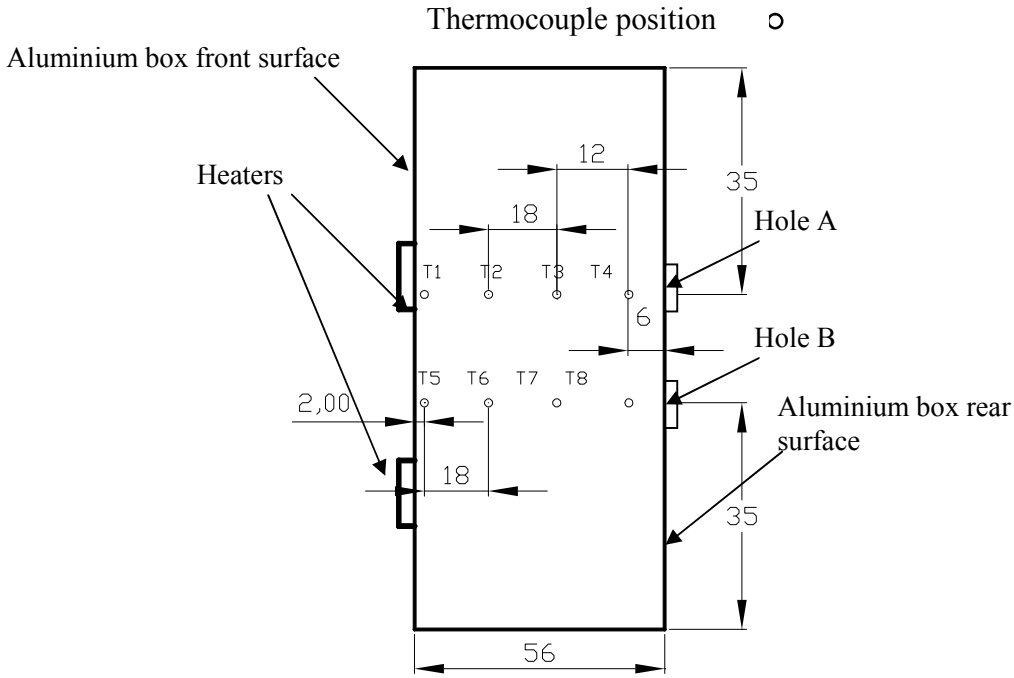

Figure 5.12 A plan of the aluminium box illustrating the locations of thermocouples T1 to T8 in the middle plane of the test box, all dimensions in 'mm'.

The measured temperatures at the exterior front surface of the aluminium case with and without a filling of RT27 are shown in figure 5.13. The measured temperatures illustrating the melt process in the RT27 are shown in figure 5.14.

The following can be observed from figures 5.13 and 5.14:

- The temperature rise at the aluminium case exterior front surface was significantly reduced by the inclusion of RT27 PCM, when the RT27 underwent phase change.
- RT27 kept the front surface temperature less than 50°C for more than 45mins during the phase change stage.
- Melting began from the hot front surface.
- Based on the temperature gradient for T1 to T8 shown in figure 5.14, the melting temperature of RT27 ranged between 26°C and 28°C.

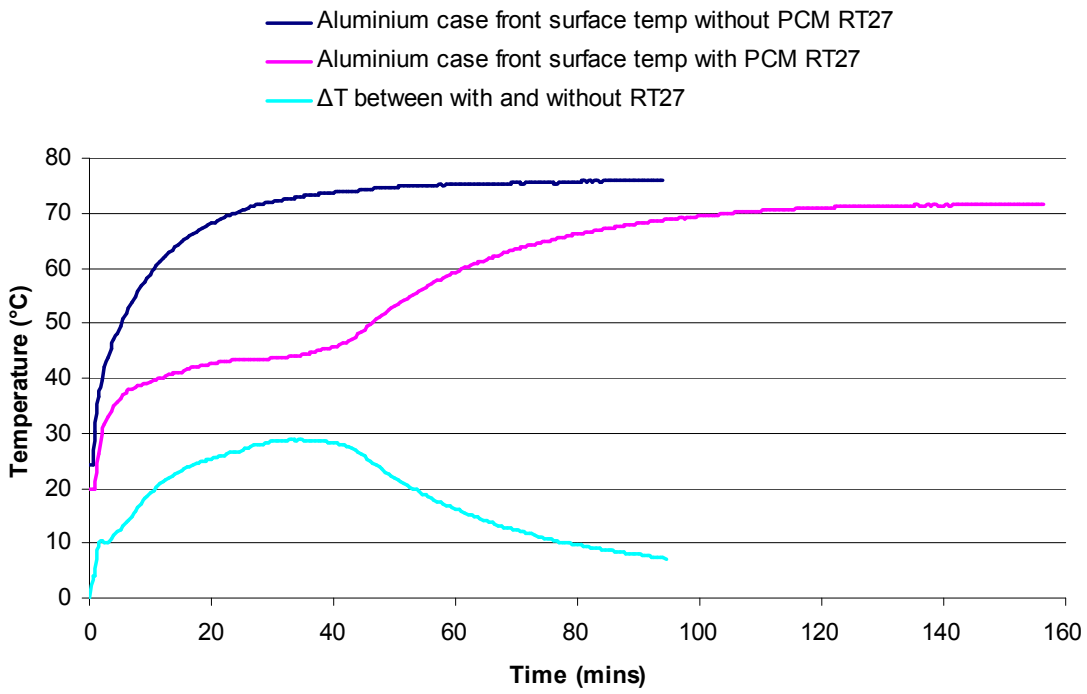

Figure 5.13 The measured variation of temperature with time for the aluminium case exterior front surface

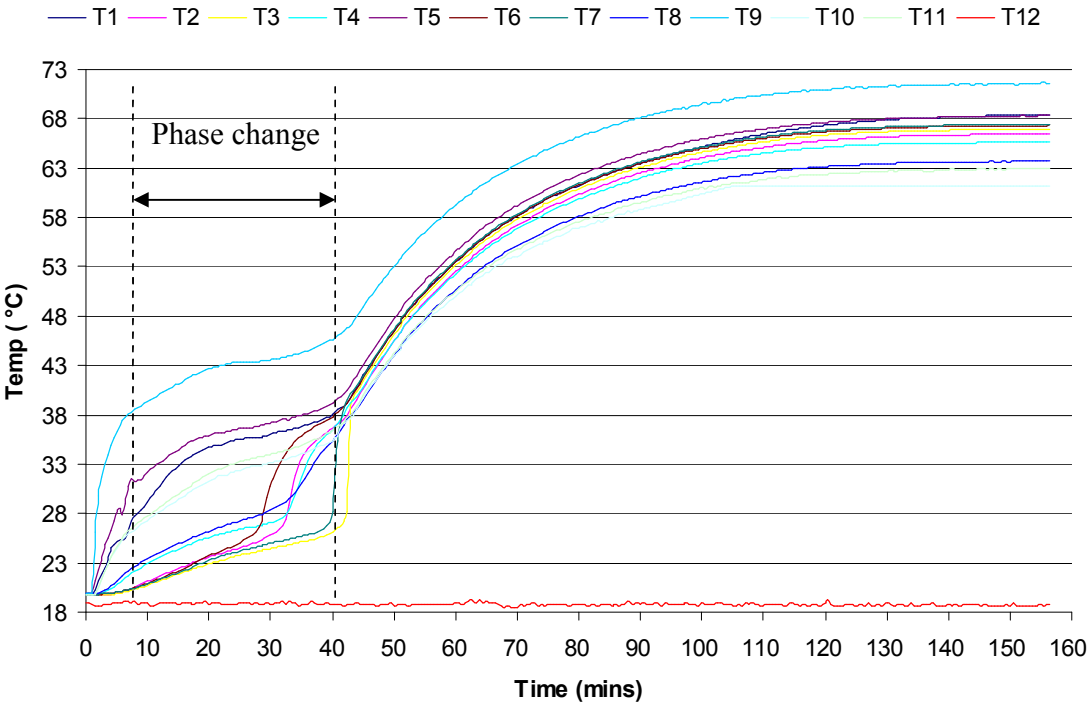

Figure 5.14 The measured variation of temperature with time at different locations in the aluminium container filled with RT27

5.4 Measured I-V and thermal characteristics of the non-concentrating PV system

The thermal characteristics of the non-concentrating PV systems were investigated by illuminating the system with the solar simulator until it reached steady state. Thermocouples were located on both the front (T1 to T8) and rear (T9 to T12) surfaces of the aluminium back plate as shown in figures 5.15 and 5.16, respectively. T13 and T14 were used to measure the front glass cover and ambient room temperature, respectively. Figure 5.17 shows the non-concentrating PV system under test using the developed solar simulator. The circuit diagram illustrating the equipment used to measure I-V data and thermal performance of the non-concentrating PV system is shown in figure 5.18. The output from the non-concentrating PV system was connected directly to the Keithley data acquisition and source meter through an IEEE488 interface linked to a PC. Temperature readings were taken every 30 seconds. The applied experimental conditions had average insolation intensities of 69W/m^2, 280W/m^2 and 672W/m^2, which represented the low, medium and high solar radiation intensities obtained from the developed solar simulator, respectively. An air conditioning unit temperature was set at 20°C to control the ambient room temperature.

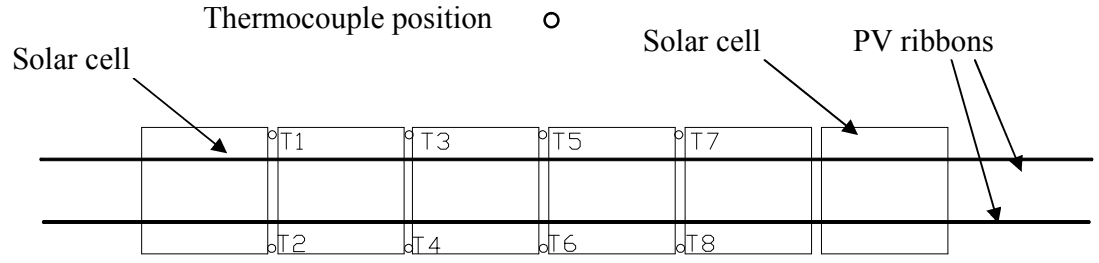

Figure 5.15 Diagram showing the location of the thermocouples on the front surface of the aluminium back plate for the non-concentrating PV system

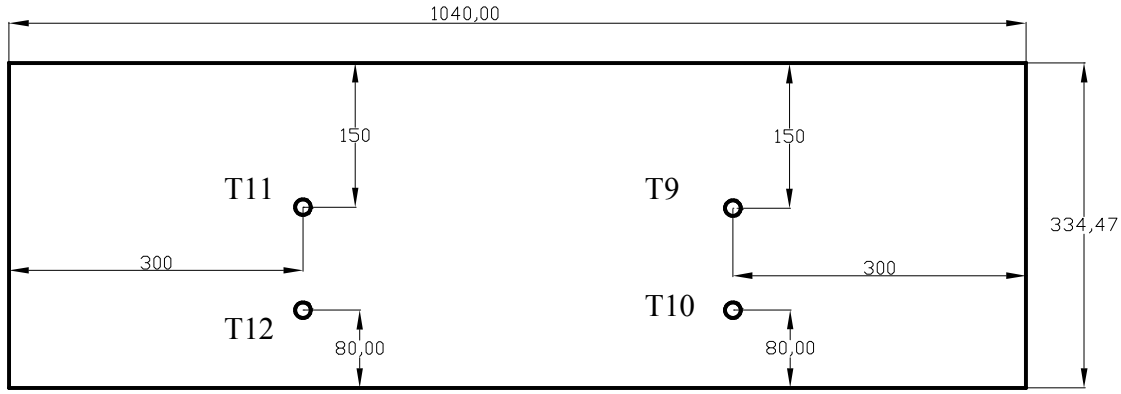

Figure 5.16 Diagram illustrating the location of the thermocouples on the rear surface of the aluminium back support plate of the non-concentrating PV system, all dimensions in 'mm'

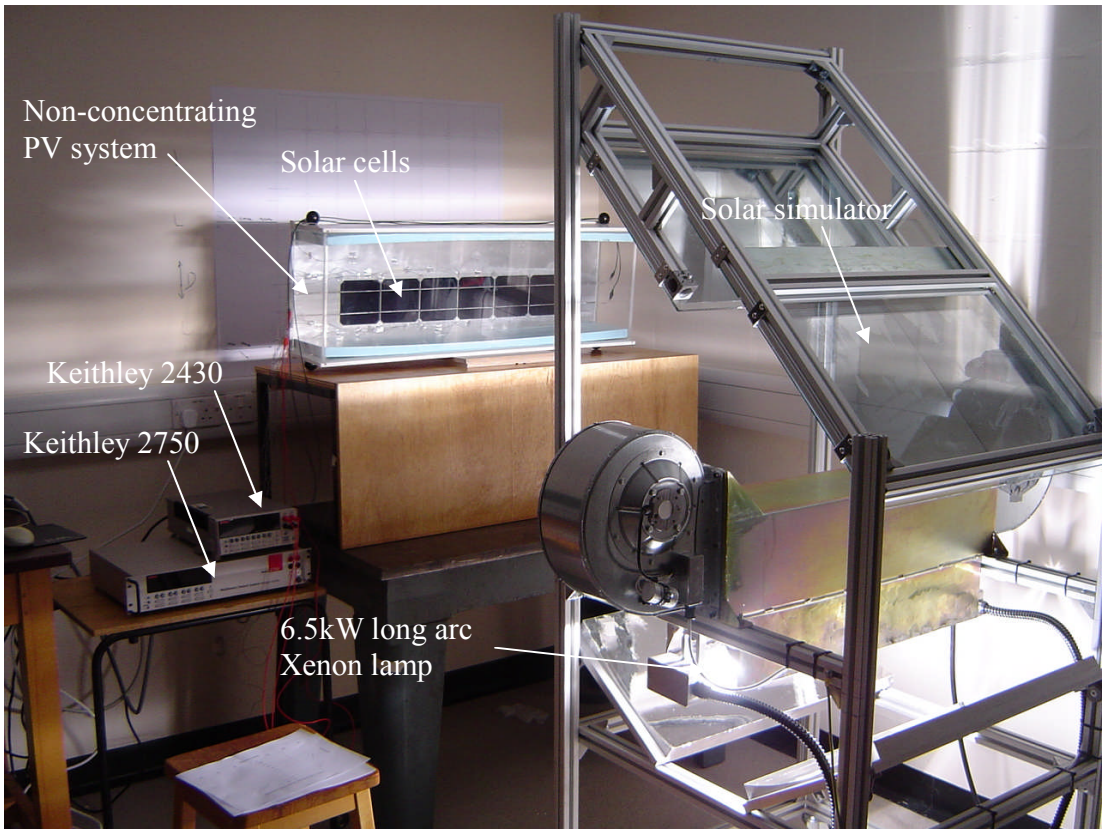

Figure 5.17 Experimental characterization of the non-concentrating PV system using the developed solar simulator

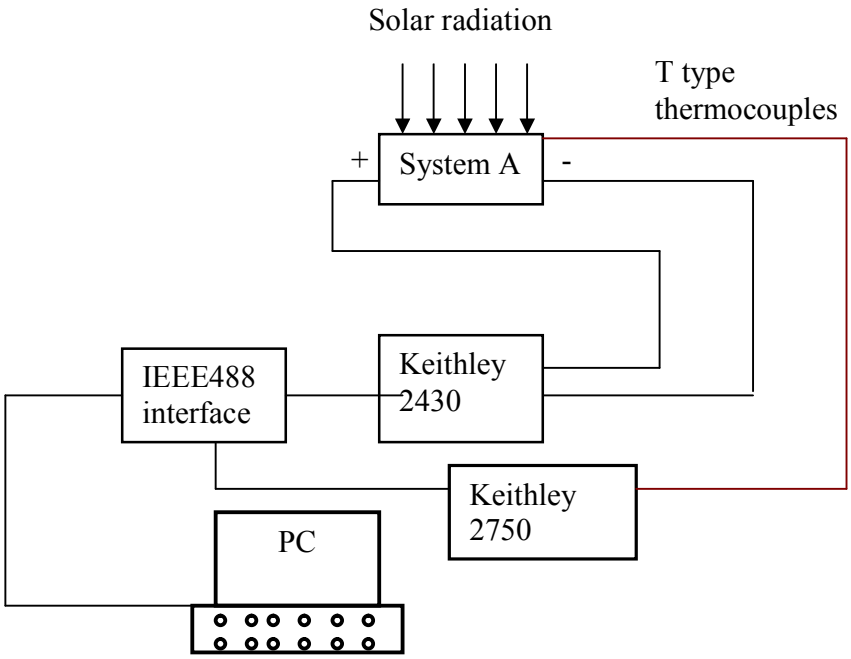

Figure 5.18 A schematic circuit diagram for continuous I-V and temperature measurement of the photovoltaic system under illumination conditions.

5.4.1 Thermal behaviour of the non-concentrating PV system at insolation levels of 69W/m^2, 280W/m^2 and 672W/m^2

The measured temperatures for the non-concentrating PV system at an average solar radiation intensity of 69W/m^2, 280W/m^2 and 672W/m^2 are shown in figures 5.19, 5.20 and 5.21, respectively. The temperature difference between the measured temperatures in the non-concentrating PV system and the ambient room temperature for the non-concentrating PV system tested at average solar radiation intensity of 69W/m^2, 280W/m^2 and 672 W/m^2 are presented in figure 5.22.

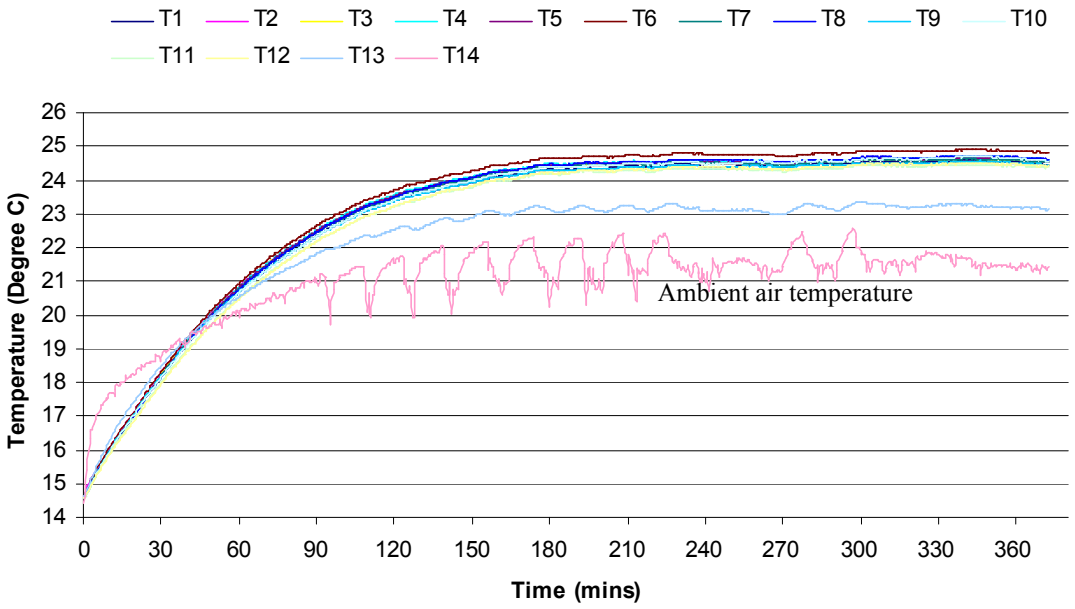

Figure 5.19 Measured variation of temperature with time for the non-concentrating PV system at a solar radiation intensity of 69W/m^2

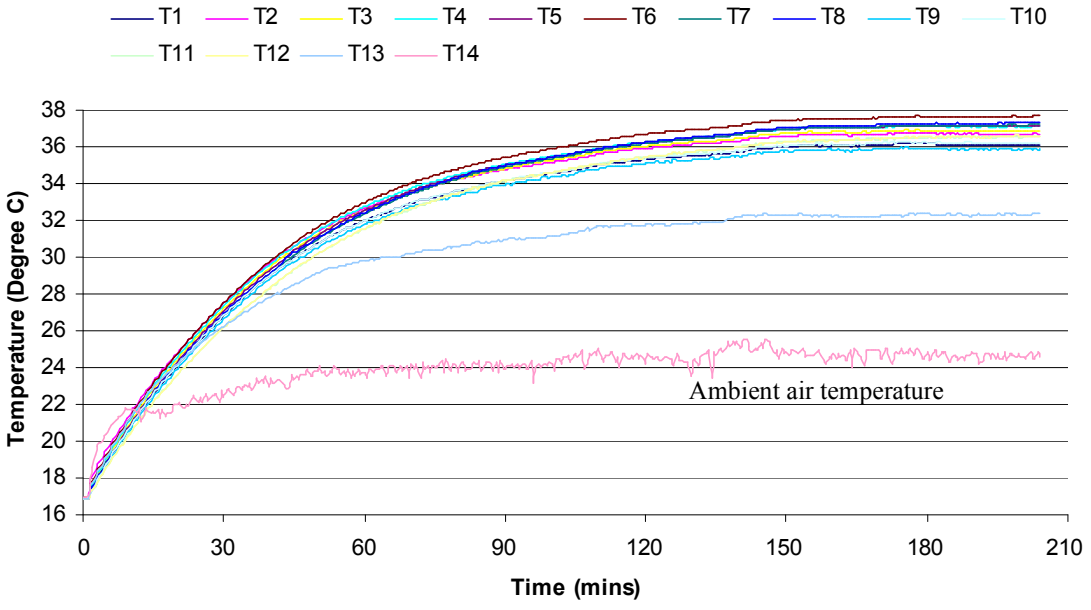

Figure 5.20 Measured variation of temperature with time for the non-concentrating PV system at a solar radiation intensity of 280W/m^2

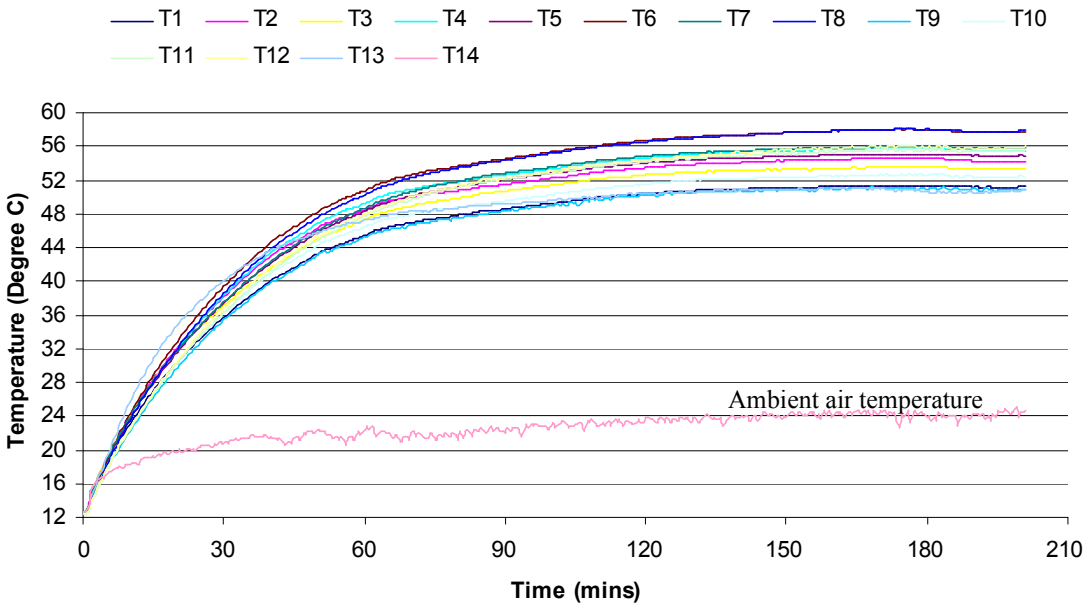

Figure 5.21 Measured variation of temperature with time for the non-concentrating PV system at a solar radiation intensity of 692W/m^2

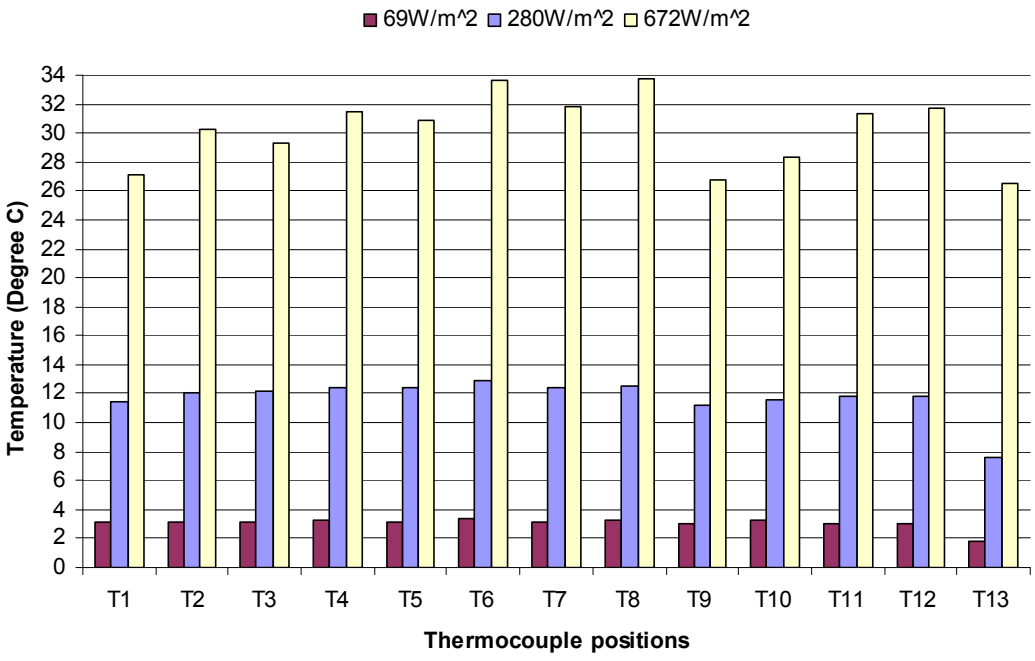

Figure 5.22 Measured temperature difference between locations T1 to T13 on the non-concentrating PV system and the ambient room temperature at solar radiation intensities of 69 W/m^2, 280 W/m^2 and 692 W/m^2

Average radiation intensity of 69W/m^2

From figures 5.19 and 5.22, it can be seen that all temperatures at the beginning of the test are around 14.5°C, and steady state temperatures are achieved after 200minutes. The ambient room temperature increases due to the heat emitted by the SQP-HLA660 lamp. Initially, it oscillated between 20.5°C and 22.5°C caused by the uncontinuous cooling from the air conditioning system, and finally achieved a constant value of around 21.4°C. There is no significant temperature difference between the solar cells and the rear surface of the aluminium back plate, and all temperatures are around 24.6°C which is approximately 3°C higher than the ambient room temperature. The temperature of the front glass is 23.2°C, 1.8°C higher than the ambient room temperature.

Average radiation intensity of 280W/m^2

From figures 5.20 and 5.22, it can be seen that the ambient room temperature is constant at around 25°C, when steady state temperatures are reached. The temperatures of the aluminium back plate and solar cells are at a steady value of 37°C, around 12°C higher than the ambient room temperature. The temperature of the front glass cover is 32.3°C around 7°C higher than the ambient room temperature.

Average radiation intensity of 672W/m^2

From figures 5.21 and 5.22, it can be seen that the ambient room temperature is constant at around 24°C, when steady state temperatures are reached. The measured average temperature for the front aluminium back plate surface and solar cells is at a steady value of 55.1°C which is around 31°C higher than the ambient room temperature. The temperature on the lower region of the aluminium back plate is approximately 2°C higher than that on the upper region which may be the result of non-uniform incident solar radiation.

5.4.2 I-V characteristics of the non-concentrating PV system at insolation of 69W/m^2, 280W/m^2 and 672W/m^2

The measured I-V characteristics and the output power with output voltage for the non-concentrating PV system at average solar radiation intensities of 69W/m^2, 280W/m^2 and 672W/m^2 are shown in figure 5.23 and 5.24, respectively. The short circuit current, open circuit voltage, maximum power output, fill factors and electrical conversion efficiency for the non-concentrating PV system are presented in table 5.2. From figures 5.23, 5.24 and table 5.2, it can be seen that the short circuit current increases by 258% when the average solar radiation increases from 69W/m^2 to 280W/m^2. A 357% increase in power can be observed when the incident radiation intensity increases from 69W/m^2 to 280W/m^2. When incident radiation increases from 280W/m^2 to 672W/m^2, the short circuit current increases by 87% and the maximum power output increases by 72%. With increasing radiation, both fill factor and electrical conversion efficiency decrease possibly due to the increased solar cell temperature.

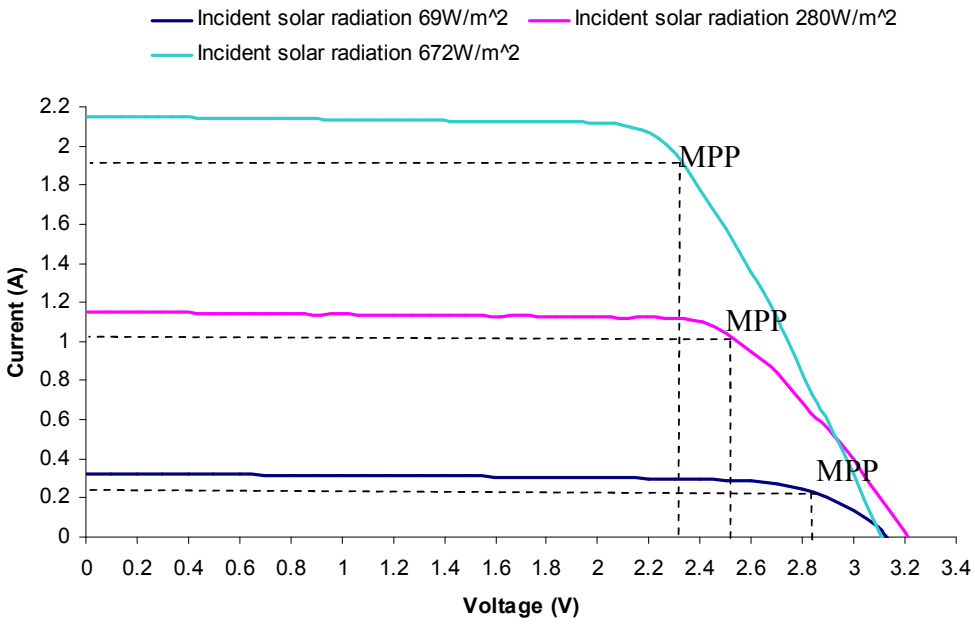

Figure 5.23 I-V characteristics of the non-concentrating PV system at radiation intensities of 69W/m^2, 280W/m^2 and 672W/m^2

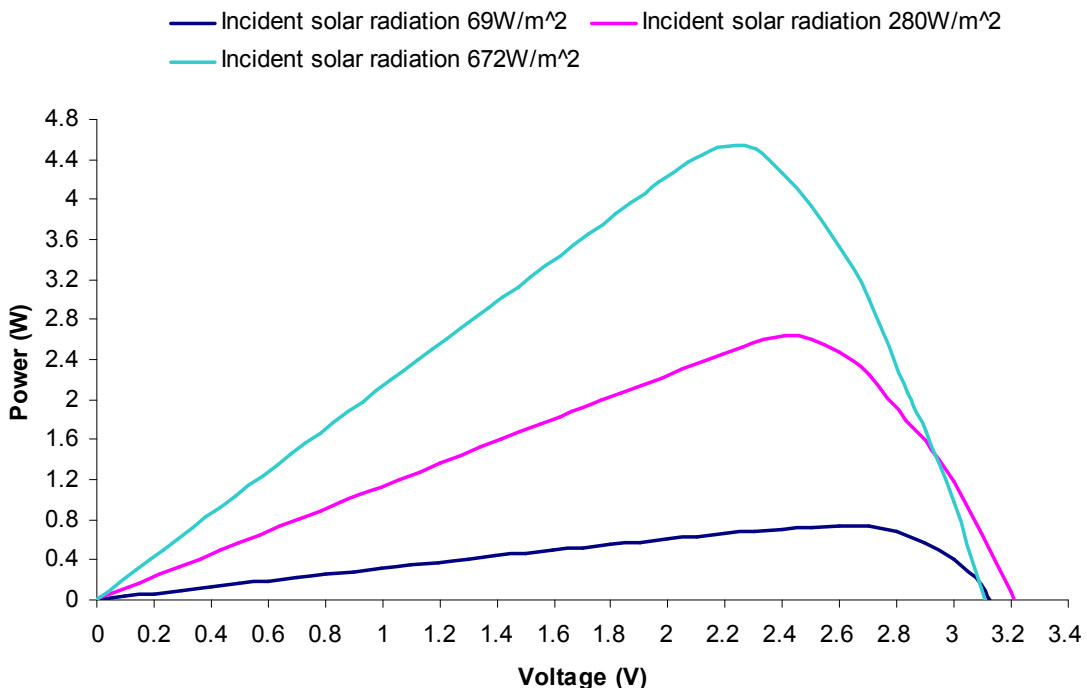

Figure 5.24 Variation of instantaneous power with sweep voltage for non-concentrating PV system at the selected radiation intensities

	Solar radiation intensity	Isc (A)	Voc (V)	MPP (W)	FF	η (%)	T_{cell} (°C)
Non-concentrating PV system	69W/m^2	0.32	3.12	0.74	0.737	11.5	24.6
	280W/m^2	1.15	3.21	2.64	0.714	10.1	37
	672W/m^2	2.15	3.11	4.55	0.680	7.2	55.1

Table 5.2 The power output of the non-concentrating PV system

5.5 Measured I-V and thermal behaviour of the ACPPVC-55 system

The thermal behaviour of the ACPPVC-55 was investigated by illuminating the system using the solar simulator until it reached steady state. The thermocouple positions on the front of the aluminimum back plate, rear of the reflector surface and rear surface of the aluminium back support plate are shown in figure 5.25, 5.26 and 5.27, respectively.

Thermocouples T1 to T8 were located in the same positions as for the non-concentrating PV system and were used to measure the temperature on the front surface of the aluminium back plate, thermocouple T9 to T14 were used to measure the temperatures on the rear surface of reflectors 1 and 2. Thermocouples T15 to T18 were located at the same positions as in the non concentrating PV system and were used to measure the temperature on the rear surface of the aluminium back plate. T19 and T20 were used to measure the front glass cover and ambient temperatures, respectively. Temperature readings were taken every 30 seconds. The applied experimental conditions were the same for the non-concentrating PV system, the applied solar radiation intensities were 69W/m^2, 280 W/m^2 and 672W/m^2. An air conditioning system was set to 20°C to control the ambient room temperature.

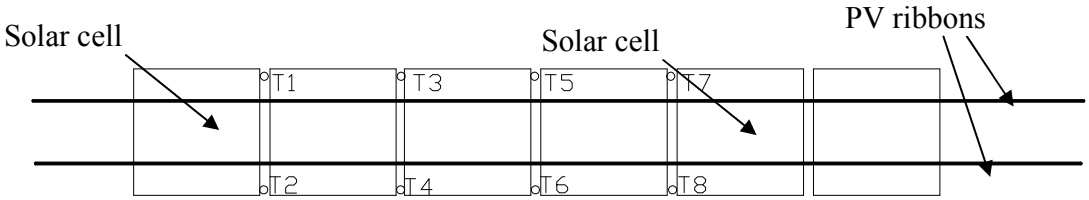

Figure 5.25 A schematic diagram showing the locations of the thermocouples on the aluminium back plate for the ACPPVC-55 system

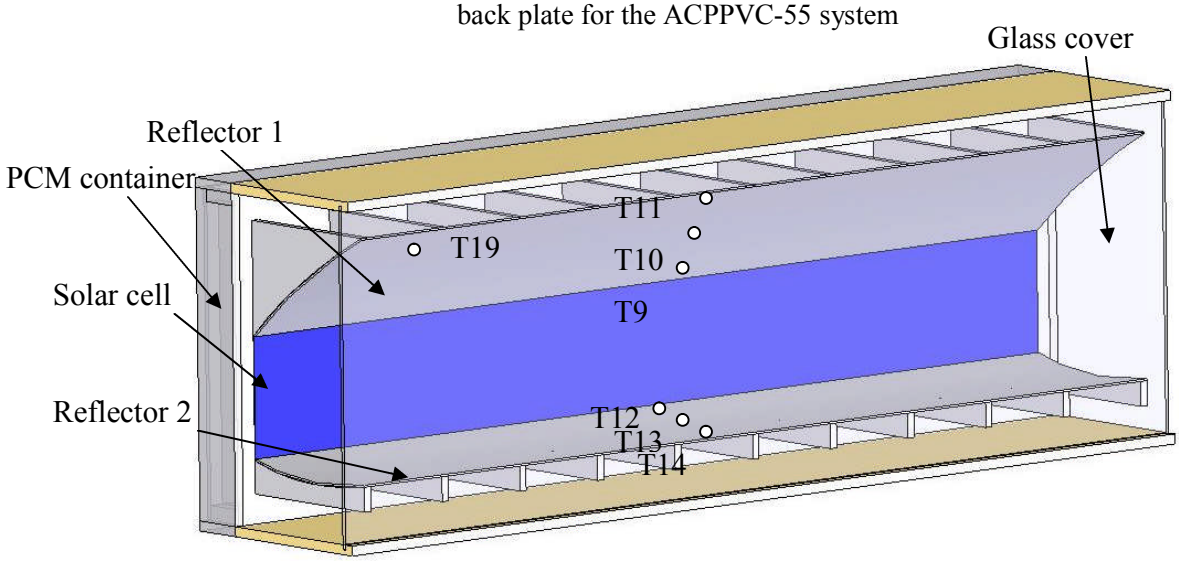

Figure 5.26 A 3D diagram illustrating the thermocouple locations on the rear surface of the reflectors for the ACPPVC-55 system

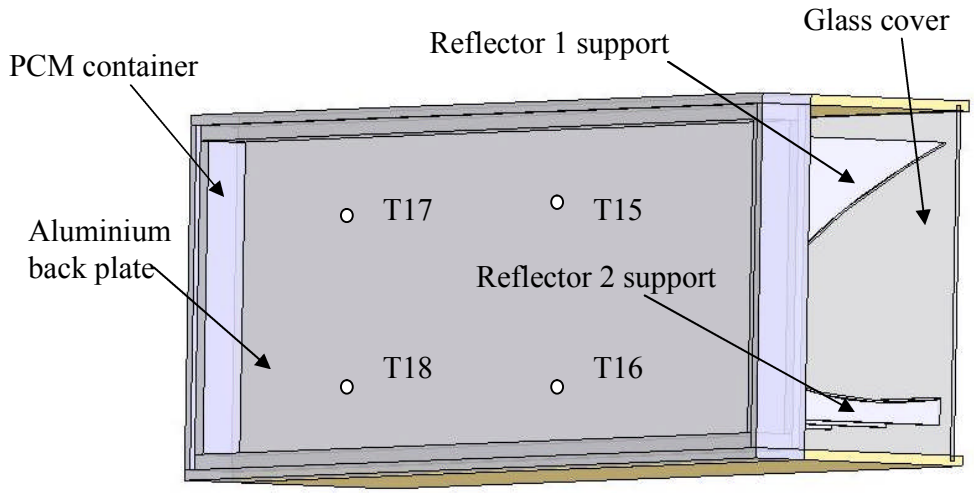

Figure 5.27 A 3D diagram showing the thermocouple locations on the rear surface of the aluminium back plate for the ACPPVC-55 system

5.5.1 Optical and thermal performance of the ACPPVC-55 system at an average incident radiation intensity of 69W/m^2

Figure 5.28, 5.30 and 5.32 present enlarged views of the ACPPVC-55 system used for indoor experimental characterisation at solar incidence angles of 0°, 5° and 10° and average incident radiation intensity of 69W/m^2. From figure 5.28, when the solar incidence angle is 0° (from the horizontal), a strip of high intensity radiation can be seen at the lower edge of the solar cells, this is the light reflected from reflector 1. It was also observed that a small portion of the incident solar radiation was reflected back out of the aperture from the ACPPVC system, this is possibly due to the mirror edge errors of the reflectors. The ray trace diagram for the ACPPVC-55 system at a solar incidence angle of 0° is shown in figure 5.29(a). It can be seen that most of the rays are incident on the PV cells, whilst only a small portion is reflected back out. A high intensity flux can be seen near the lower edge of the PV cells, this may lead to an increase in the local temperature of the PV cell, and potentially result in a decrease in the electrical conversion efficiency. The ray trace technique was also used to predict the solar energy flux across the PV cells and is shown in figure 5.29(b), the cosine effect on the radiation incident on the aperture of the ACPPVC is

included. One peak in the solar flux, a combination of the direct radiation and radiation reflected from reflector 1 occurred on the PV cells for solar incidence angle of 0°. The predicted peak flux was 225 W/m^2, over 3 times higher than the incident solar radiation on the central and upper regions of the PV cells.

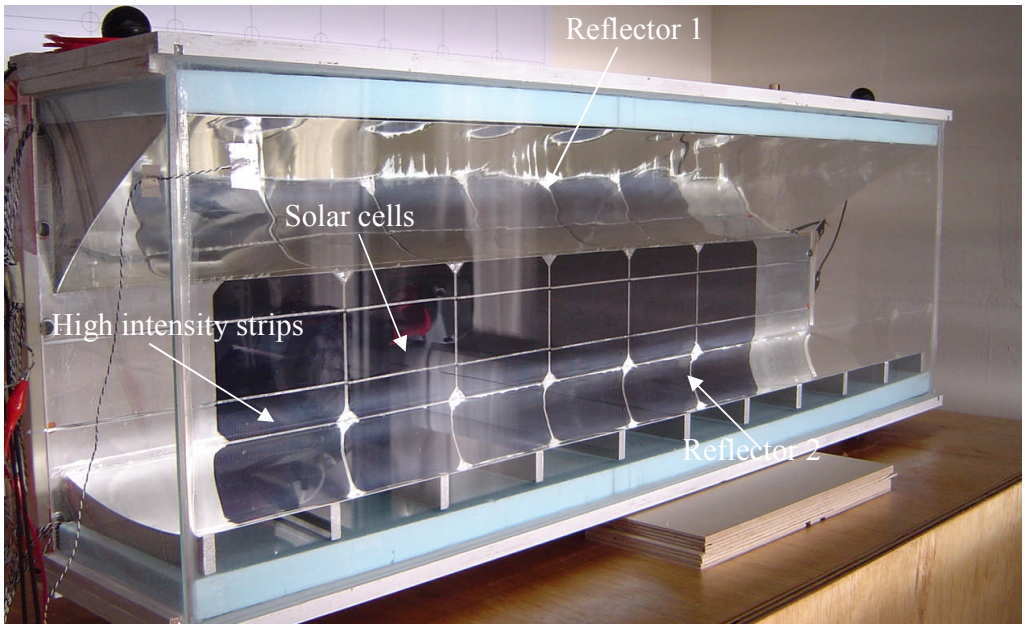

Figure 5.28 Experimental characterization of an ACPPVC-55 system at a solar incidence angle of 0° (from the horizontal) using the developed collimated solar simulator detailed in Chapter 4

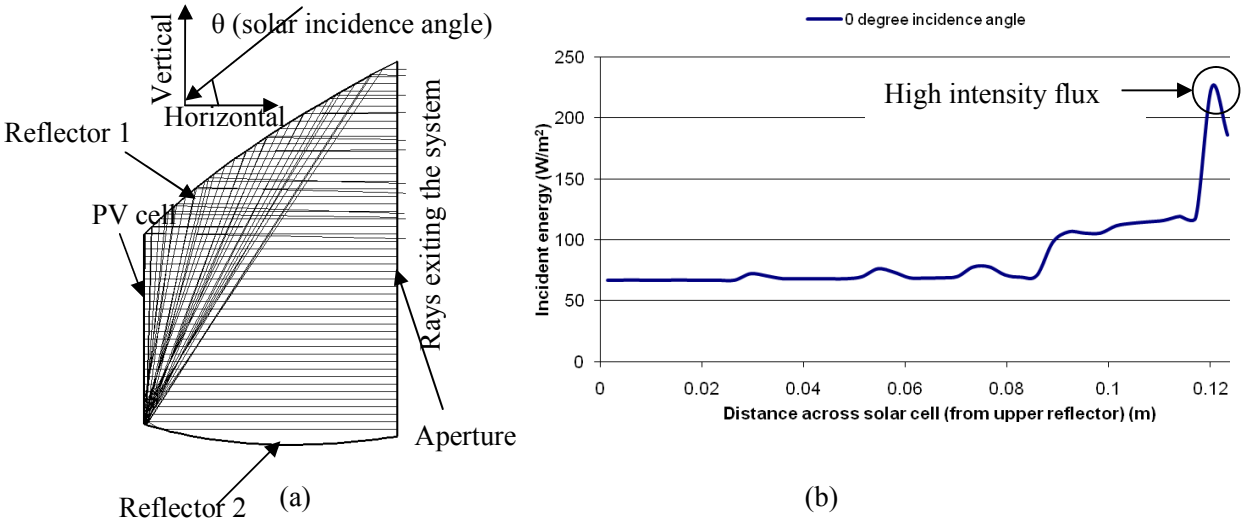

Figure 5.29 (a) Ray trace diagrams for the ACPPVC-55, incidence angle 0°, 50 rays are shown. (b) Predicted energy distribution across the photovoltaic cell of the ACPPVC-55 system for a solar incidence angle of 0° with a incident radiation intensity at the system aperture of 69W/m^2.

From figure 5.30, two high intensity strips of radiation can be seen in the middle and at the lower edges of the solar cells for a solar incidence angle of 5° (from the horizontal). These are due to the light reflected from reflectors 1 and 2. The ray trace diagram for the ACPPVC-55 system at a solar incidence angle of 5° is shown in figure 5.31 (a) with the predicted solar energy flux across the PV cells shown in figure 5.31 (b). From figure 5.29, it can be seen that all of the rays at the aperture are incident on the PV cells. Two peaks are predicted in the solar flux on the PV cells, with the one nearer the lower reflector having a higher intensity than the one in the central region. The predicted peak flux of 313 W/m^2, is over 4 times higher than the solar radiation flux incident in the upper regions of the PV cells.

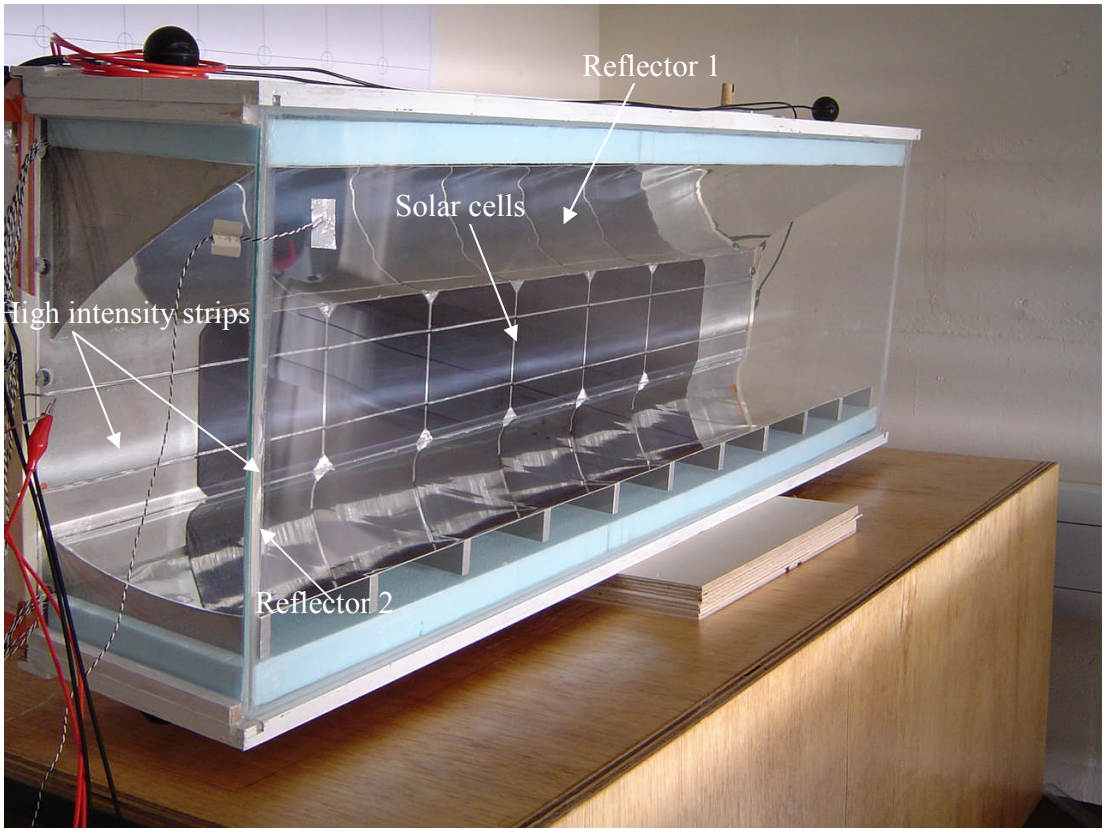

Figure 5.30 Experimental characterization of an ACPPVC-55 system at a solar incidence angle of 5° (from the horizontal) using the developed collimated solar simulator detailed in Chapter 4

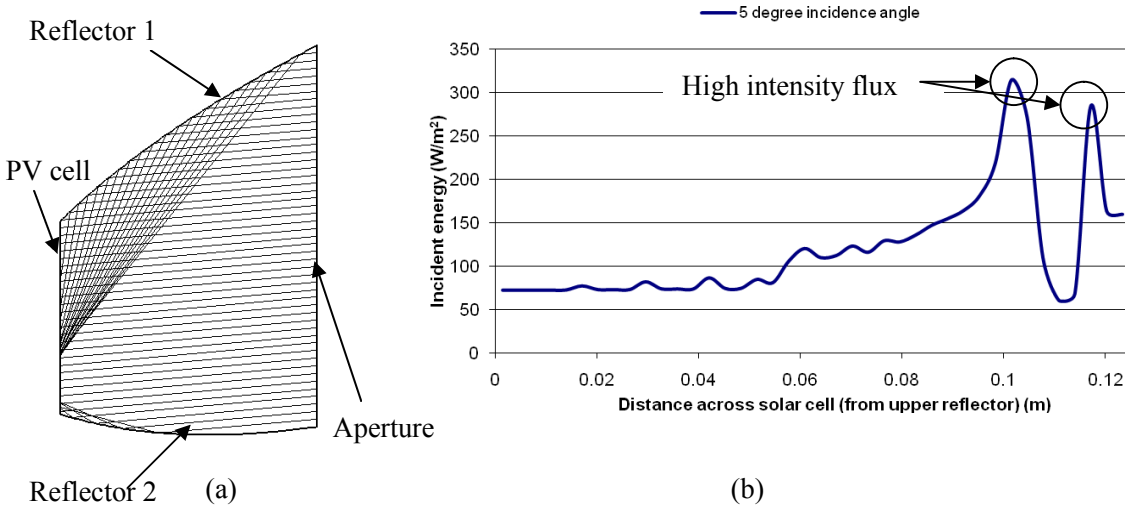

Figure 5.31 (a) Ray trace diagrams for the ACPPVC-55, incidence angle 5°, 50 rays are shown. (b) Predicted energy distribution across the photovoltaic cell of the ACPPVC-55 system for a solar incidence angle of 5° with a incident radiation intensity at the system aperture of 69W/m^2.

Figure 5.32 Experimental characterization of an ACPPVC-55 system at a solar incidence angle of 10° (from the horizontal) using the developed collimated solar simulator detailed in Chapter 4

From figure 5.32, for the 10° solar incidence angle, the energy distribution has similar characteristics to that for the 5° solar incidence angle, two peaks in solar flux are seen on the PV cells. The ray trace diagram for the ACPPVC-55 system at a solar incidence angle of 10° is shown in figure 5.33 (a) with the predicted solar energy flux across the PV cells shown in figure 5.33 (b). The predicted peak flux was 321 W/m^2, over 4 times higher than the solar radiation incident in the central and upper regions of the PV cells.

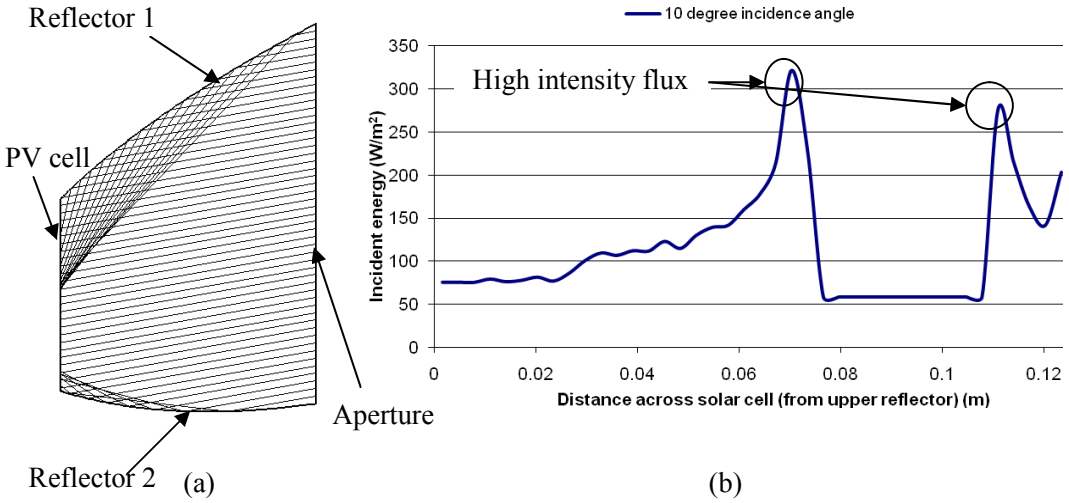

Figure 5.33 (a) Ray trace diagrams for the ACPPVC-55, incidence angle 10°, 50 rays are shown. (b) Predicted energy distribution across the photovoltaic cell of the ACPPVC-55 system for a solar incidence angle of 10° with a incident radiation intensity at the system aperture of 69W/m^2.

The measured temperatures for the ACPPVC-55 system and the temperature difference between the measured temperatures and the ambient room temperature for selected solar incidence angles are presented in figure 5.34 and 5.35, respectively.

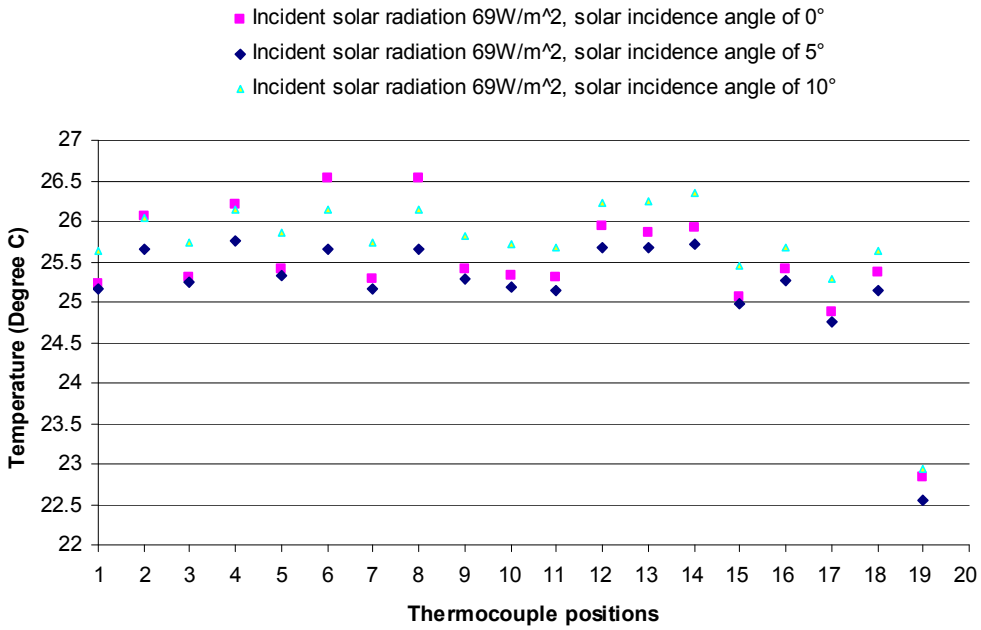

Figure 5.34 The measured temperature for the ACPPVC-55 system tested at a radiation intensity of 69W/m^2.

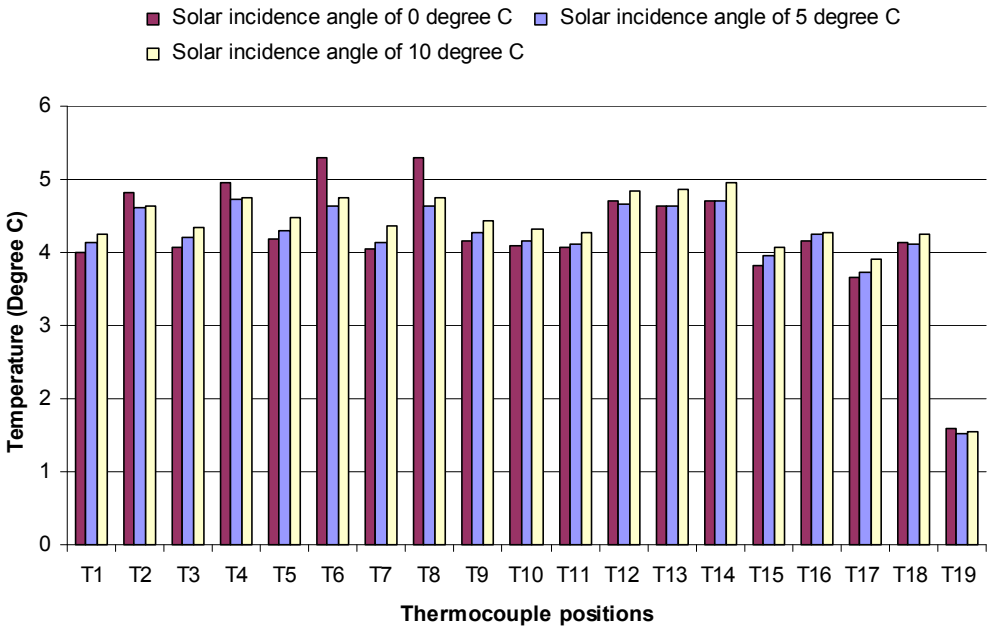

Figure 5.35 The temperature difference between the measured temperatures in the ACPPVC-55 system and the ambient room temperature at incident radiation intensity of 69W/m^2

The measured temperatures for the ACPPVC-55 system when tested at a solar incidence angle of 0°

When the ACPPVC-55 system was tested at a solar incidence angle of 0°, the temperatures of the ACPPVC-55 system reached steady state after 200 minutes. The ambient room temperature was constant at 21.2°C. From figure 5.34 and 5.35, it can be seen that the temperatures on the lower region of the solar cells (average value of 26.3°C) are approximately 1°C higher than those on the upper region (average value of 25.3°C), this is a consequence of the local high intensity flux on the lower region and the effective smaller back plate cooling fin. The measured temperature on the rear of the aluminium back plate has the same characteristics as that on the front surface of the aluminium back plate. Simultaneously, there is no significant temperature difference between the solar cells and the rear surface of the aluminium back plate. The average temperature for reflector 2 (25.9°C) is 0.5°C higher than that for reflector 1, this is due to reflector 1 having a larger area of reflector support to dissipate heat compared to reflector 2 as shown in figure 5.36. The measured front glass temperature is 22.8°C which is 1.6°C higher than the ambient room temperature.

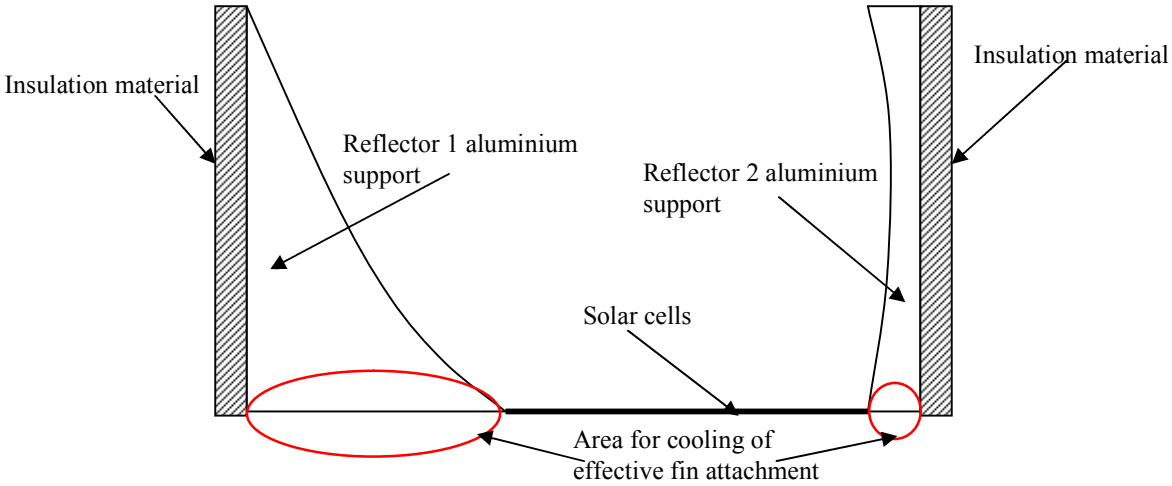

Figure 5.36 A cross sectional view of the ACPPVC-55 system illustrating the regions suitable for cooling at the back plate

The measured temperatures for the ACPPVC-55 system when tested at a solar incidence angles of 5° and 10°

From figure 5.34 and 5.35, it can be seen that the ACPPVC-55 system tested at solar incidence angles of 5° and 10° has a similar thermal behaviours to that at a solar incidence angle of 0°. There was no significant difference in temperatures measured for the ACPPVC-55 system when tested at solar incidence angles of 0°, 5° and 10°.

5.5.2 I-V characteristics of the ACPPVC- 55 system at an average incident solar radiation of 69W/m^2

The measured I-V characteristics and the output power and output voltage of the ACPPVC-55 system tested at an average solar radiation intensity of 69W/m^2 and selected solar incidence angles are shown in figures 5.37 and 5.38, respectively. The short circuit current, open circuit voltage, maximum power output and fill factor of the non-concentrating PV system and the ACPPVC-55 system are presented in table 5.3. From figures 5.37, 5.38 and table 5.3, it can be seen that, for the ACPPVC-55 system, at solar incidence angles of 5° and 10°, the short circuit current and output power of the ACPPVC-55 system are higher than those at the solar radiation incidence angle of 0°, this is possibly due to the mirror edge error at a solar radiation incidence angle of 0° reducing the incident solar radiation intensity, a small portion of incident solar radiation does not reach the solar cells. At a solar incidence angle of 5°, the short circuit current and output power of the ACPPVC-55 system were slightly higher than those at the solar incidence angle of 10°, this is possibly due to the incident solar radiation intensity at the aperture cover being reduced, due to the increasing cosine effect and increased reflection at the aperture cover with increasing solar incidence angles. The solar radiation intensity in horizontal direction for solar radiation

incidence angle of 10° was 68.0W/m^2, a 1% reduction than the solar radiation incidence angle of 5°.

A short circuit current of 0.55A was measured for an average solar radiation intensity of 69W/m^2 at the solar incidence angle of 5° compared to the 0.32A short circuit current produced by the counterpart non-concentrating PV system at the same insolation level. At the same time, the open circuit voltage of the ACPPVC-55 system and its non-concentrating counterpart PV system were 3.24V and 3.12V, respectively. The ratio of the maximum power output was 1.88 between the ACPPVC-55 system at a solar radiation incidence angle of 5° and its non-concentrating counterpart PV system for the same incident solar radiation level. The experimental results indicated that significant additional power losses occured for the ACPPVC-55 system. They are discussed in section 5.8.

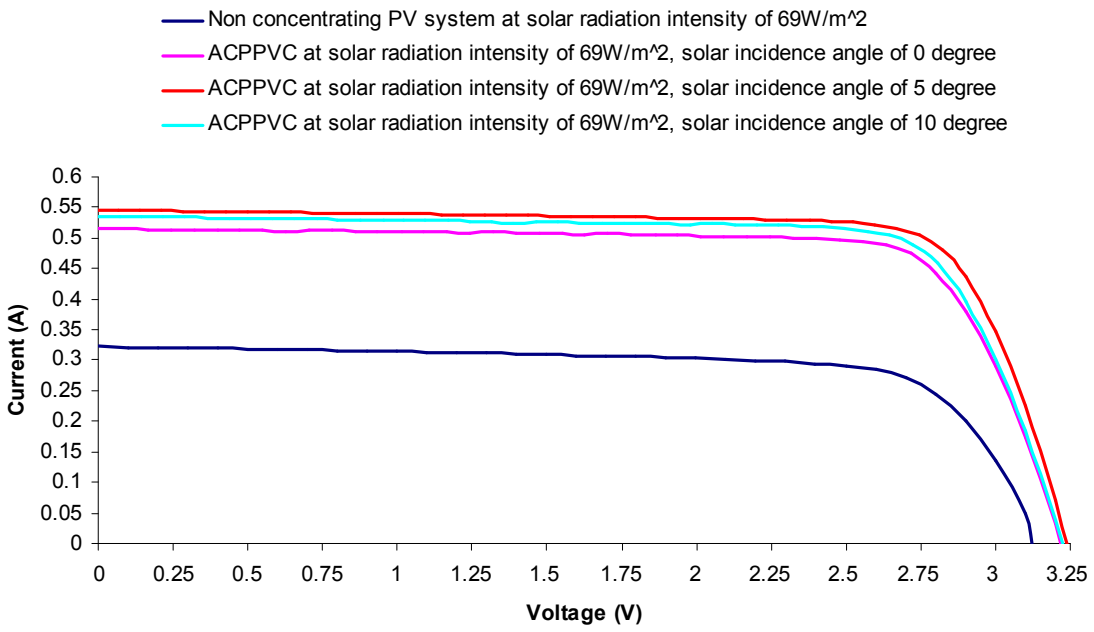

Figure 5.37 Measured I-V characteristics of ACPPVC-55 system at solar radiation intensity of 69 W/m^2 and solar radiation incidence angles of 0°, 5° and 10°.

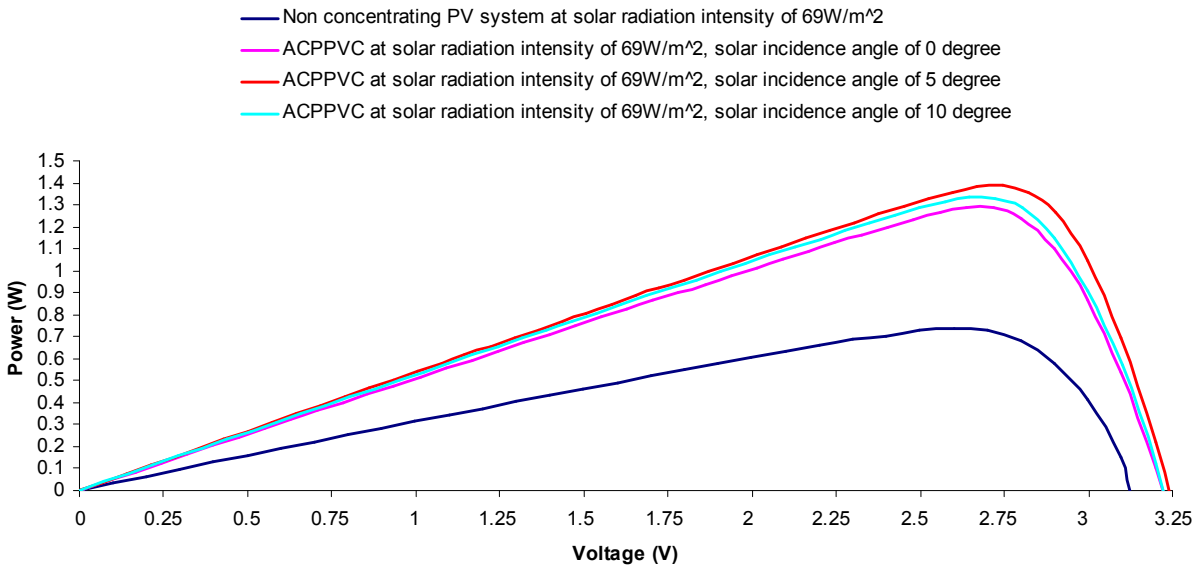

Figure 5.38 Variation of instantaneous power with sweep voltage for non-concentrating PV system and the ACPPVC-55 system at incident solar radiation intensity of 69W/m^2

	Incident solar radiation at aperture	Isc (A)	Voc (V)	MPP (W)	FF
Non-concentrating system	69W/m^2	0.32	3.12	0.74	0.736
ACPPVC-55 (0° Solar incidence angle)	69W/m^2	0.52	3.22	1.29	0.775
ACPPVC-55 (5° Solar incidence angle)	68.7W/m^2	0.55	3.24	1.39	0.784
ACPPVC-55 (10° Solar incidence angle)	68.0W/m^2	0.54	3.22	1.34	0.774

Table 5.3 The power output of the non-concentrating PV system and the ACPPVC-55 system for incident solar radiation of 69W/m^2.

5.5.3 The thermal behaviour of the ACPPVC- 55 system at an average incident solar radiation intensity of 280W/m^2

The measured temperatures for the ACPPVC-55 system and the temperature difference between the measured temperature and the ambient room temperature at solar incidence angles of 0°, 5° and 10° are shown in figure 5.39 and 5.40, respectively.

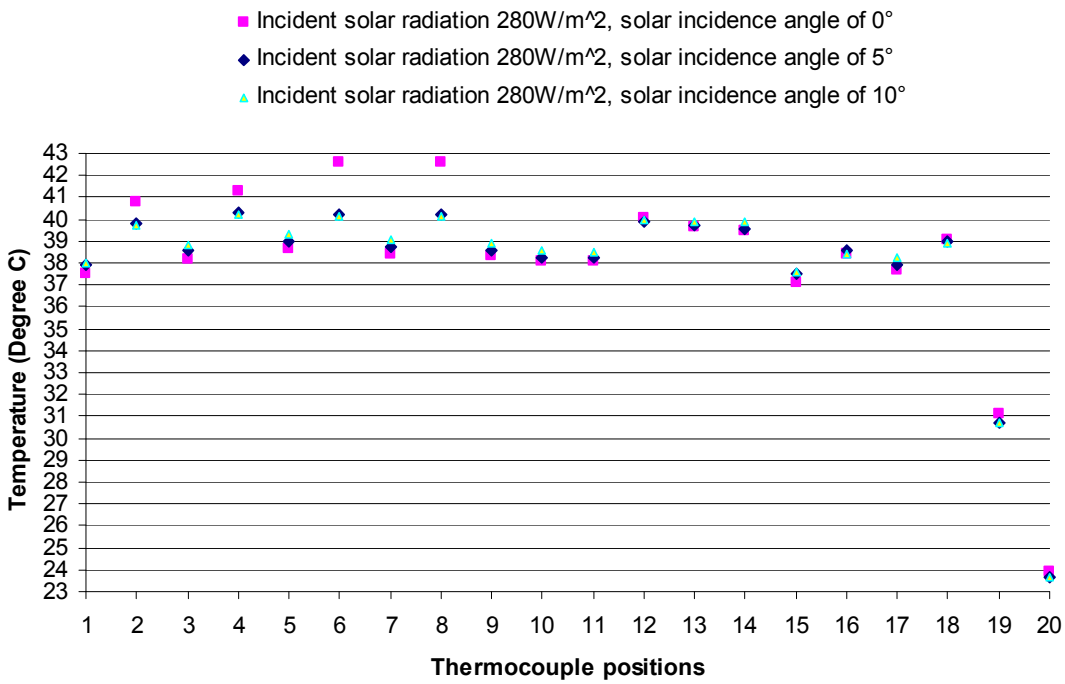

Figure 5.39 The measured temperatures of the ACPPVC-55 system when tested at a radiation intensity of 280W/m^2.

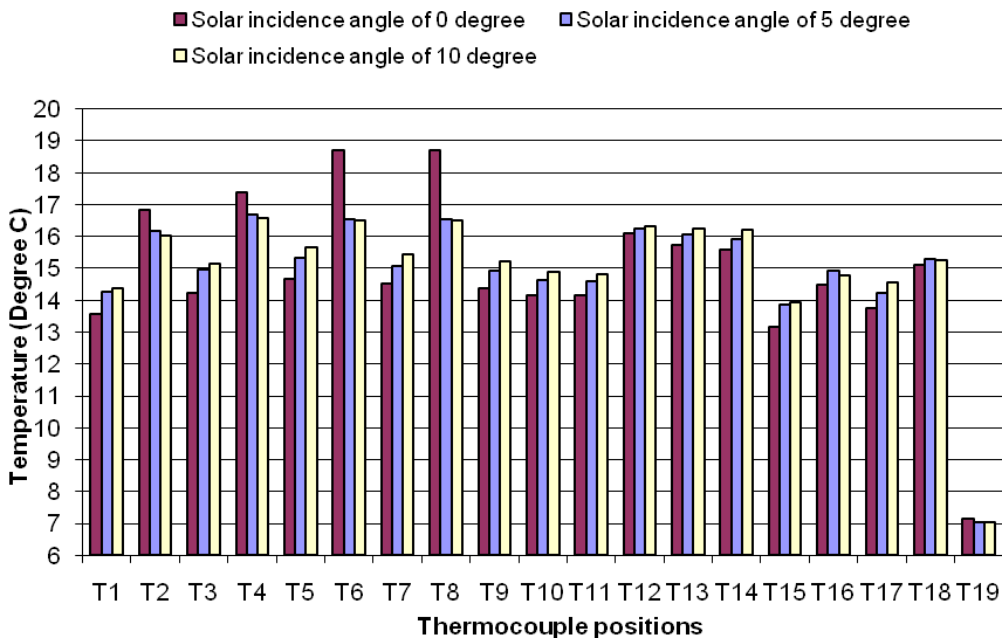

Figure 5.40 The temperature difference between the measured temperature in the ACPPVC-55 system and the ambient room temperature at a radiation intensity of 280W/m^2.

The ACPPVC-55 temperatures reached steady state after 240 minutes. The ambient room temperature was constant at 23.9°C. From figures 5.39 and 5.40, it can be seen that when the incident solar radiation intensity is 280W/m^2 on the aperture cover of the ACPPVC-55 system, the measured temperatures in the ACPPVC-55 system have similar characteristics to those when tested at an incident solar radiation intensity of 69W/m^2. The temperatures on the lower region of the solar cells are higher than those on the upper region. There is also no significant temperature difference between the solar cells and the rear surface of the aluminium back plate. The average temperature of reflector 2 is higher than that of reflector 1. The measured temperatures of T6 and T8 at the solar incidence angle of 0° are higher than that at the solar incidence angle of 5 and 10°, it may be caused by the non-uniform output solar radiation from the solar simulator.

5.5.4 I-V characteristics of the ACPPVC- 55 system at an average incident solar radiation of 280W/m^2

The measured I-V characteristics and the output power and output voltage of the ACPPVC-55 system tested at solar radiation intensity of 280W/m^2 and selected solar incidence angles are shown in Appendix B in figure B.1 and B.2, respectively. The short circuit current, open circuit voltage, maximum power output and fill factor of the non-concentrating PV system and the ACPPVC-55 system are presented in table 5.4. From figures B.1, B.2 and table 5.4, it can be seen that the short circuit current and power output have similar characteristics to the system when tested at a solar radiation of 69W/m^2. For the solar radiation of 280W/m^2, at the solar incidence angles of 5° and 10°, the short circuit current and output power of the ACPPVC-55 system were higher than those at the solar incidence angle of 0°.

A short circuit current of 1.86A was measured for an average solar radiation intensity of 280 W/m^2 at a solar incidence angle of 5° compared to 1.15A short circuit current produced by the counterpart non-concentrating PV system at the same insolation level. The open circuit voltage of the ACPPVC-55 system and its non-concentrating counterpart PV system were 3.23V and 3.21V, respectively. The ratio of the maximum power output was 1.43 between the ACPPVC-55 system at a solar radiation incidence angle of 5° and its non-concentrating counterpart PV system for the same incident solar radiation level. The experimental results indicated significant additional power losses for the ACPPVC-55 system which are discussed in section 5.8.

	Incident solar radiation	Isc (A)	Voc (V)	MPP (W)	FF
Non-concentrating system	280W/m^2	1.15	3.21	2.64	0.714
ACPPVC-55 (0° Solar incidence angle)	280W/m^2	1.77	3.21	3.51	0.618
ACPPVC-55 (5° Solar incidence angle)	278.9W/m^2	1.86	3.23	3.78	0.627
ACPPVC-55 (10° Solar incidence angle)	275.7W/m^2	1.86	3.23	3.71	0.619

Table 5.4 The power output of the non-concentrating PV system and the ACPPVC-55 system for incident solar radiation of 280W/m^2.

5.5.5 The thermal behaviour of the ACPPVC- 55 system at an average incident solar radiation intensity of 672W/m^2

The measured ACPPVC-55 system temperatures and the temperature difference between these measured temperatures and the ambient room temperature at solar incidence angles of 0°, 5° and 10° are illustrated in figure 5.41 and 5.42, respectively. The ACPPVC-55 system tested at a radiation intensity of 672W/m^2 with solar incidence angles of 0° 5° and 10° behaved in a similar way thermally. There was no significant temperature difference between the ACPPVC-55 system tested at solar incidence angles of 0°, 5° and 10°. When the ACPPVC-55 system was tested at a solar incidence angle of 0°, the ambient room

temperature was constant at 24.6°C after reaching steady state. The temperatures of the lower region of the solar cells (average value of 67.8°C) were approximately 10°C higher than those of the upper region (average value of 57.2°C). There is no significant temperature difference between the solar cells and the rear surface of the aluminium back plate. The average temperature of reflector 2 (63.5°C) was 5°C higher than that of reflector 1. The measured front glass temperature of 49.5°C was 24.9°C higher than the ambient room temperature.

Under the incident solar radiation intensity of 672 W/m^2, the output current of the ACPPVC-55 was higher than the maximum direct current measurement range of 3.5A for the source meter. Due to the restriction of the measurement facility, the I-V characteristics of the ACPPVC-55 system could not be obtained at the incident radiation intensity of 672W/m^2 on the ACPPVC-55 aperture.

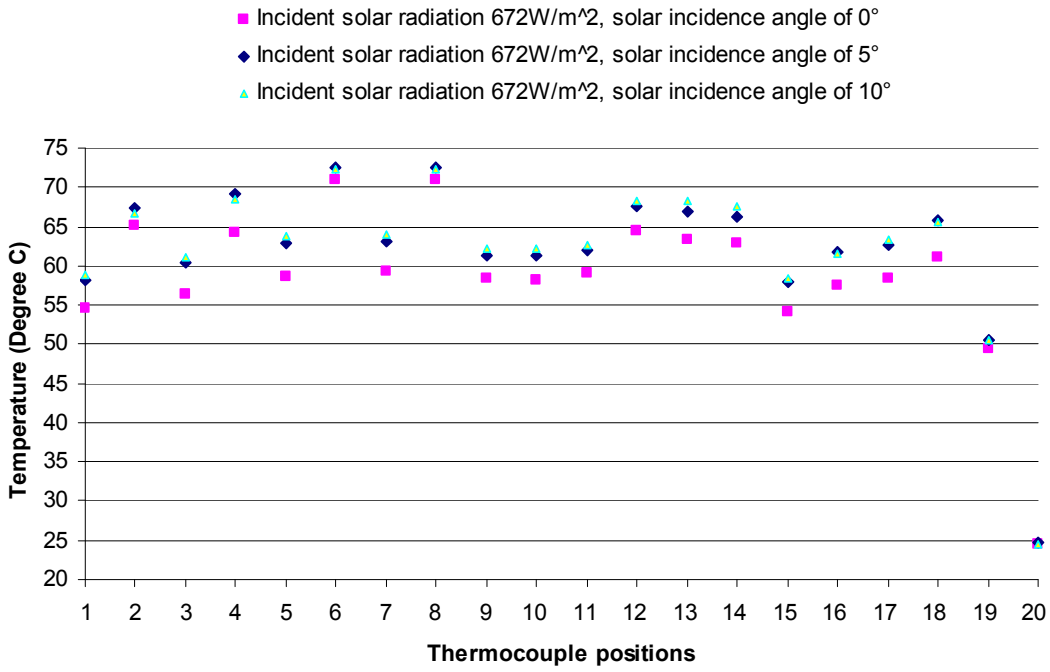

Figure 5.41 The measured temperatures of the ACPPVC-55 system when tested at a radiation intensity of 672W/m^2.

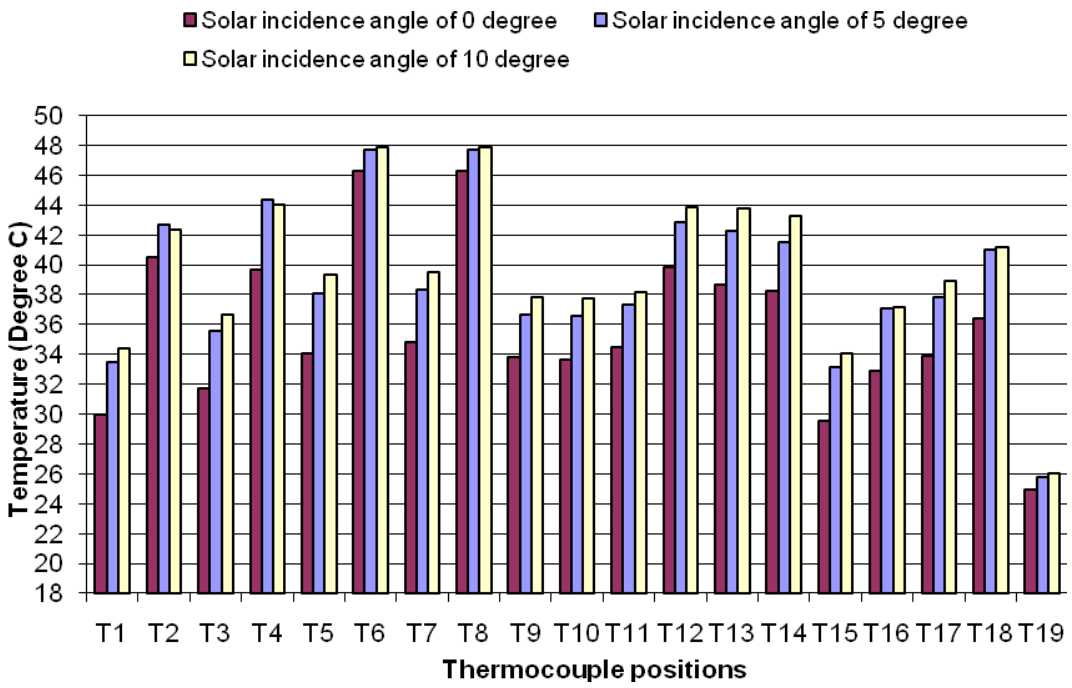

Figure 5.42 The temperature difference between the measured temperature in the ACPPVC-55 system and the ambient room temperature at a radiation intensity of 672W/m^2.

5.6 Measured I-V and thermal behaviours of the ACPPVC- 55 system combined with a PCM module for passive cooling

The PCM container was filled with 9.08kg of RT27, which was melted and poured into the cavity with 10% of the container volume left for expansion during phase change. The thermal performance of the ACPPVC-55/PCM system was investigated by illuminating the system with the solar simulator until it reached steady state. The applied experimental conditions used insolation of 280W/m^2 and 672 W/m^2. The thermocouple positions on the front of the aluminium back plate and the rear of the reflector were the same as those for the ACPPVC-55 system with no PCM as shown in figures 5.43 and 5.44. A total of 20 thermocouples were inserted into the PCM container using the method described in section

5.3. The rationale behind the choice of the thermocouple location in the PCM was a desire to measure and analyse the temperature changes at the rear of the solar cells and reflector supports. Five thermocouple sets were chosen in the rear plate of the ACPPVC-55/PCM system. For each hole, four thermocouples were inserted at distances 2mm, 14mm, 26mm, and 38 mm from front plate. A detailed 3D sketch of the thermocouple insertion holes in the rear plate of the system is shown in figure 5.45. Figure 5.46 illustrates the cross-sectional view showing locations of thermocouples T15 to T34 inside the PCM container. T35 to T38 were used to measure the temperature of the PCM rear cover of the ACPPVC-55/PCM system. The front glass aperture and the ambient room temperature were measured by T39 and T40, respectively.

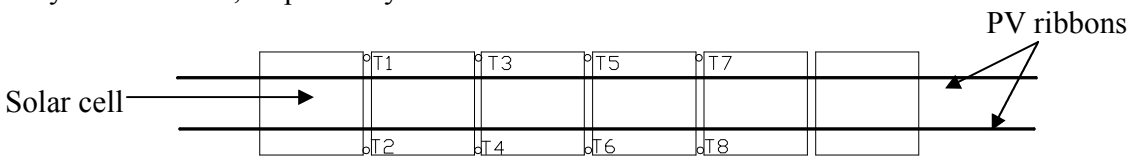

Figure 5.43 A schematic diagram showing the location of the thermocouples on the solar cells of the ACPPVC-55/PCM system

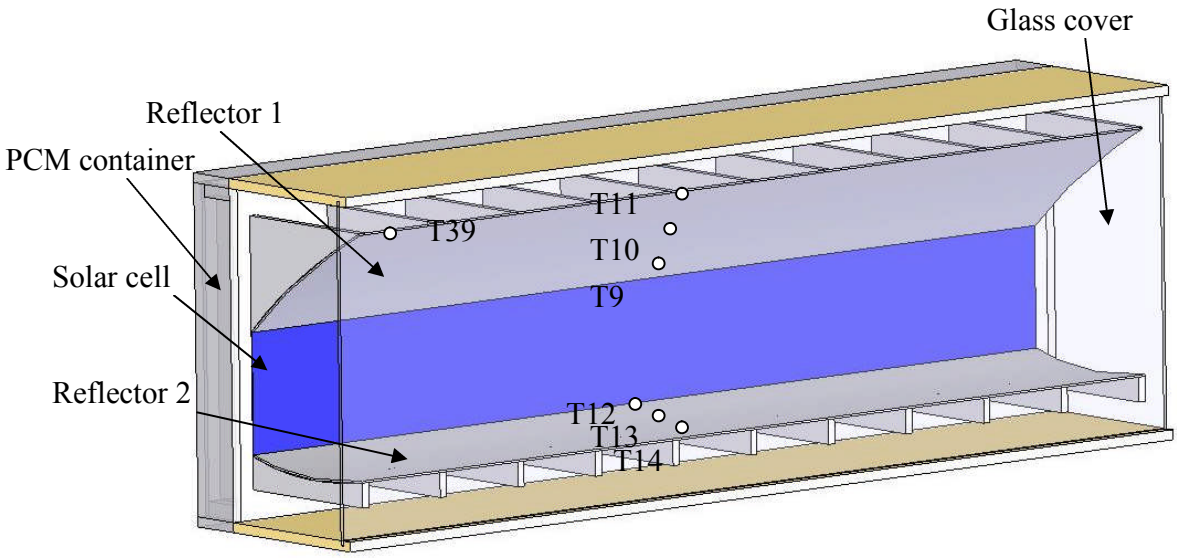

Figure 5.44 A 3D diagram illustrating the thermocouple locations on the rear surface of the reflectors of the ACPPVC-55/PCM system

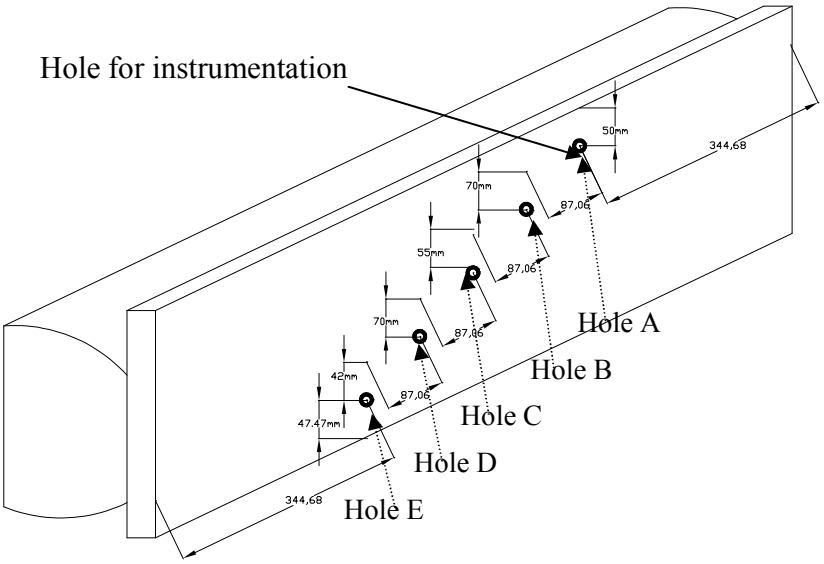

Figure 5.45 A 3D diagram of the ACPPVC-55/PCM system illustrating the thermocouple insertion holes, all dimensions in 'mm'.

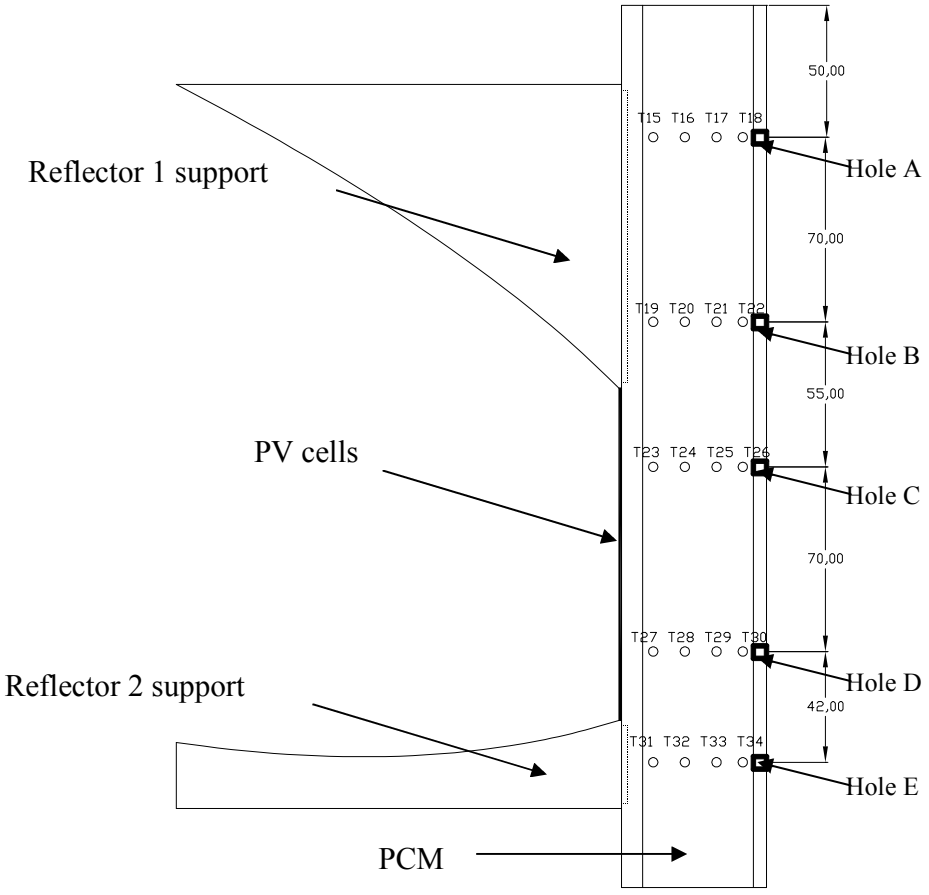

Figure 5.46 A cross-sectional view illustrating the locations of the thermocouples T15 to T34 inside the PCM container, all dimensions in 'mm'.

5.6.1 Measured I-V and thermal behaviour of the ACPPVC-55/PCM system at an average incident solar radiation intensity of 280W/m^2

The experiments with solid-liquid phase change materials RT27 were undertaken for the ACPPVC-55/PCM system for solar incidence angles of 0°, 5° and 10°. The applied experimental conditions were insolation of 280W/m^2. The room air conditioning was set to 20°C to control the ambient room temperature.

5.6.1.1 Thermal behavirour of the ACPPVC-55/PCM system at an average incident solar radiation intensity of 280W/m^2

The measured variation of the average solar cell temperatures with time for the ACPPVC-55 and ACPPVC/PCM system at a solar radiation incidence angle of 0° are shown in figure 5.47. From figure 5.47, it can be seen that the average solar cell temperature on the front surface of the ACPPVC-55/PCM system was maintained below 34°C for 10 hours. The average solar cell temperature of the ACPPVC-55/PCM system was steady at 33.2°C for more than 400 mins, while the RT27 underwent phase change. Comparing this with the average solar cell temperature rise for the ACPPVC-55 system with no PCM, the RT27 clearly delayed the PV cell temperature rise. The potential to use a PCM to reduce the temperature rise of a PV system can be seen from figure 5.47. The ACPPVC-55/PCM system tested at solar radiation incidence angles of 5° and 10° have similar thermal behaviour as when tested at a solar incidence angle of 0°. Their thermal behaviours are shown in Appendix B in figures B.3 and B.4, respectively. From figures 5.47, B.3 and B.4, it is clear that during phase change, the solar cell temperature of the ACPPVC-55/PCM is maintained approximately 7°C lower than that of the ACPPVC-55 system with no PCM for the same incident solar radiation intensity.

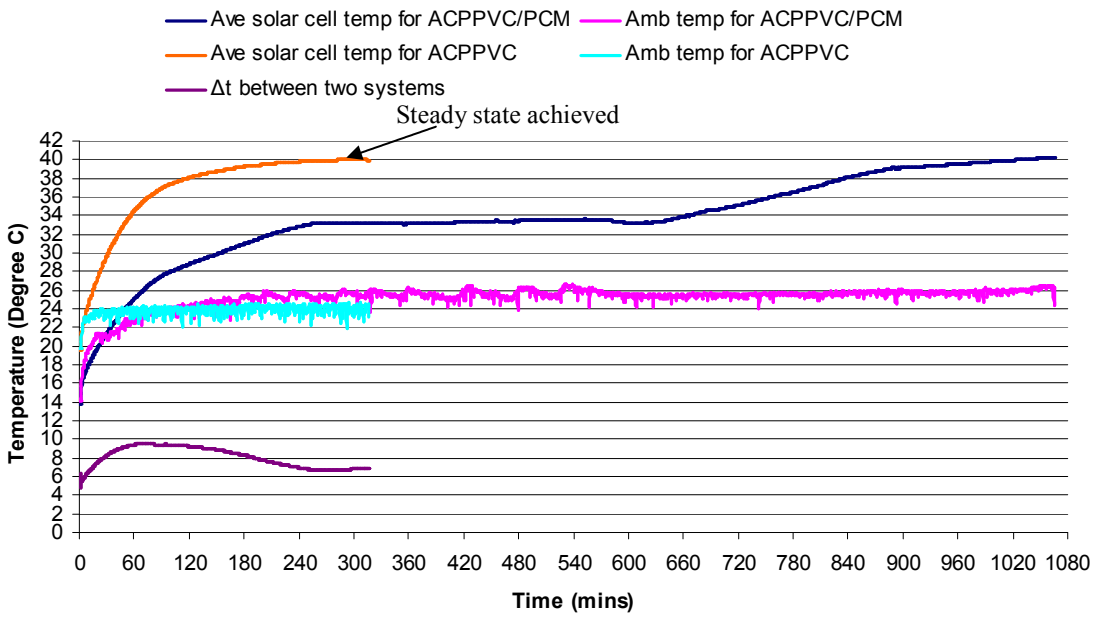

Figure 5.47 The measured average solar cell temperature with time for the ACPPVC and ACPPVC/PCM system for incident solar radiation intensity of 280W/m^2 and solar radiation incidence angle of 0°

The measured temperatures in the ACPPVC-55 and ACPPVC-55/PCM system, and the temperature difference between the measured temperatures and the ambient room temperature after the systems had been illuminated with the developed solar simulator for 250mins are shown in figures 5.48 and 5.49. At this time, in the ACPPVC-55/PCM system, the RT27 adjacent to the solar cell is melting, the temperature of the aluminium back plate front surface for both systems is at steady state. From figure 5.48 and 5.49, it can be seen that both systems have similar thermal behaviours, the temperatures in the lower region of the solar cells are higher than those of the upper region. The measured temperature of the solar cells and reflector surfaces of the ACPPVC-55/PCM system are 7°C less when compared to those of the ACPPVC-55 system. The front glass temperature difference between the two systems is approximately 2°C.

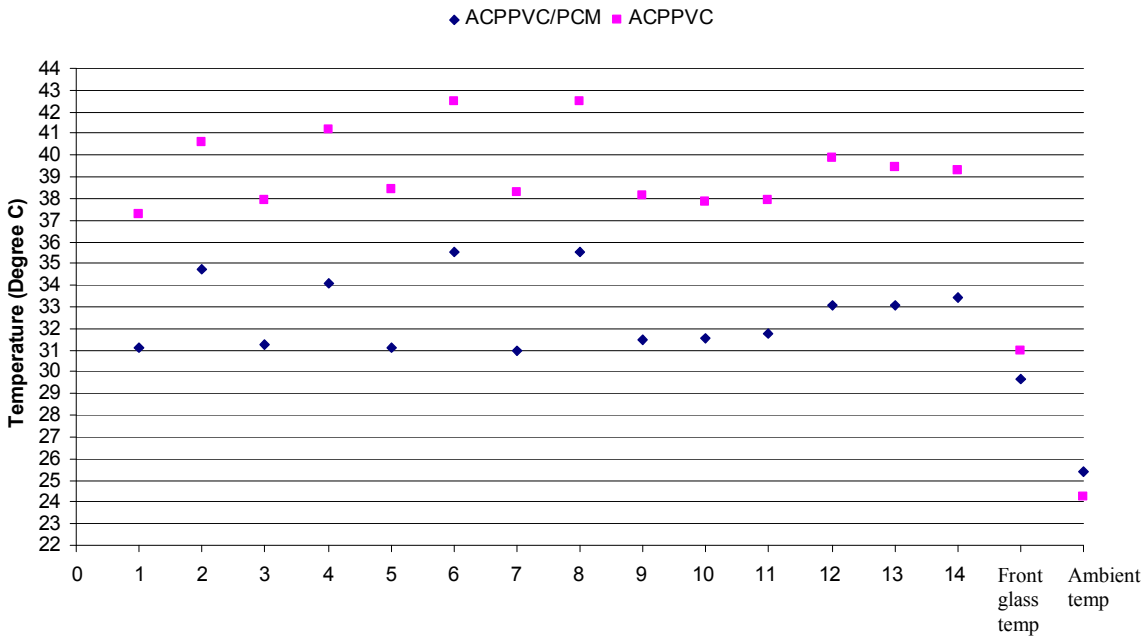

Figure 5.48 The measured temperatures of the ACPPVC-55 and ACPPVC-55/PCM system after illumination with the developed solar simulator for 250mins at a radiation intensity of 280W/m^2.

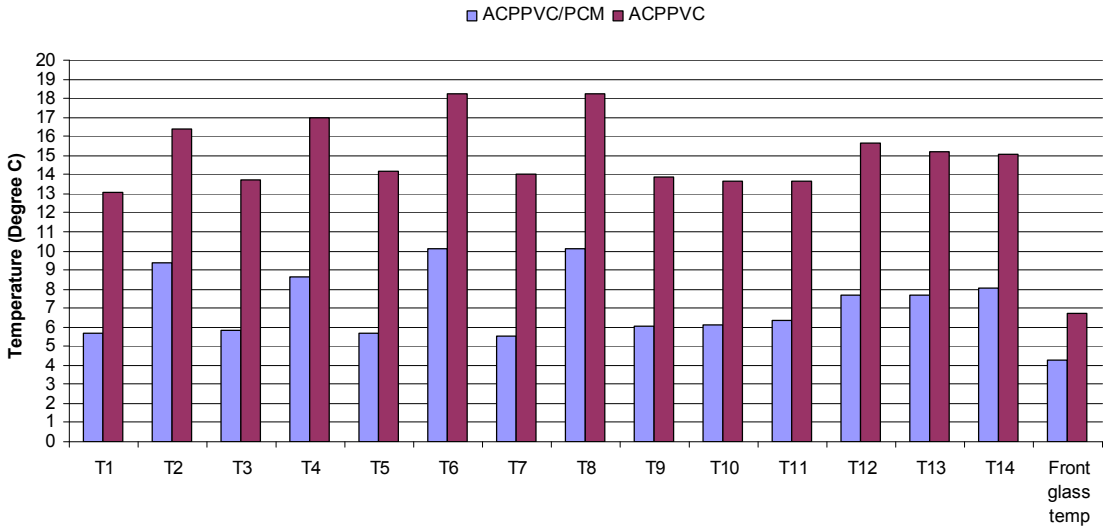

Figure 5.49 The temperature difference between the measured temperatures and the ambient room temperature for the ACPPVC/PCM and ACPPVC system after illumination with the developed solar simulator for 250mins at a radiation intensity of 280W/m^2.

Photographs and isotherms plotted from the measured temperatures during the phase change process for the ACPPVC-55/PCM system at times of 250, 300, 400, 500 and 600mins are presented in figure 5.50. The phase change can be clearly seen after the system is illuminated by the solar simulator for 250mins, the RT27 adjacent to the back plate on which the solar cells were mounted melted quicker than in any other region. With increasing time, the heated liquid flowed to the upper region of the PCM container, the upper front region of the RT27 then began to melt more quickly than the lower front region. This can be clearly seen at times 300mins, 400mins, 500mins and 600mins in figure 5.50. At times 250mins and 300mins, it can be seen that the temperature of a portion of the solid RT27 at the inner central region of the PCM container were lower than the rest of the PCM. This is due to the heat fluxes transferred into the RT27 from the heated front solar cells, and that transferred through the rear aluminium back plate from the ambient air.

After 600mins, the phase change process is nearly complete, with only a small region of RT27 remaining at the back bottom corner inside the PCM container shown in figure 5.50 at t=600mins. The temperatures of the aluminium back plate began to increase after 600 mins.

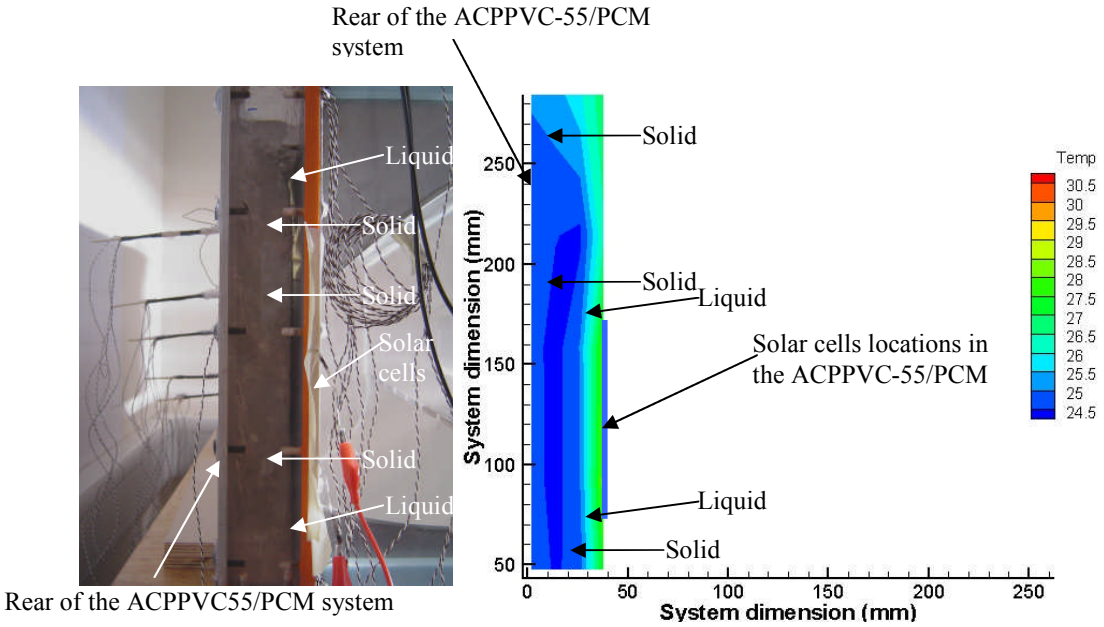

t=250mins

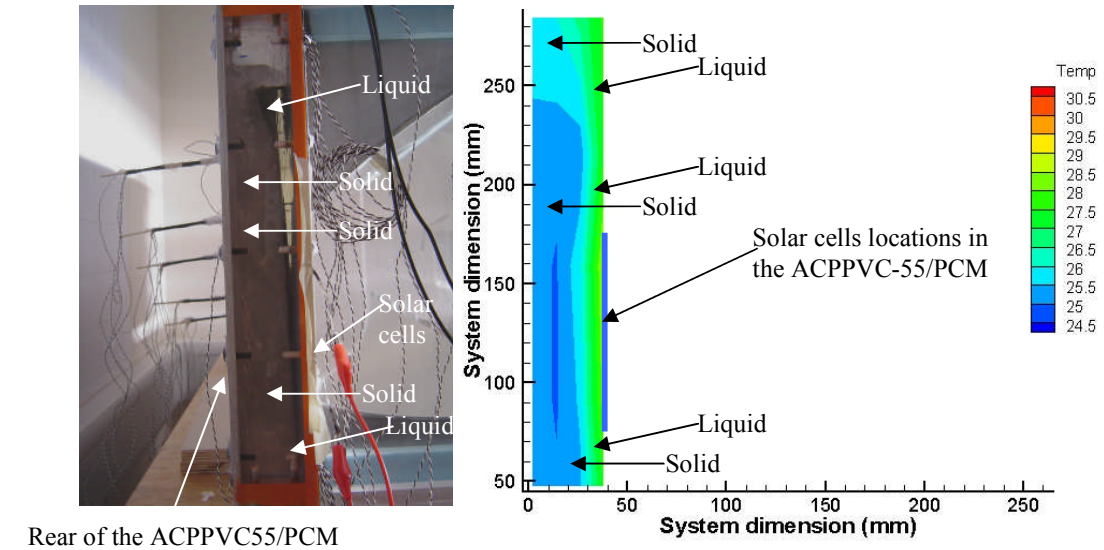

t=300mins

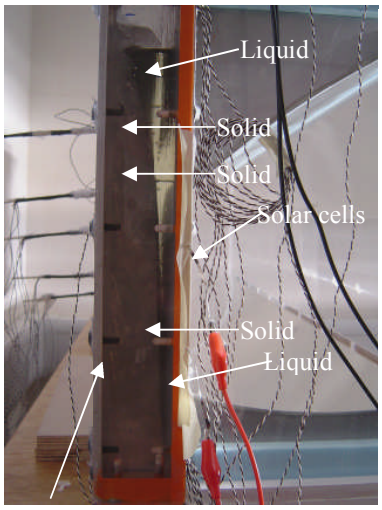

Rear of the ACPPVC55/PCM system

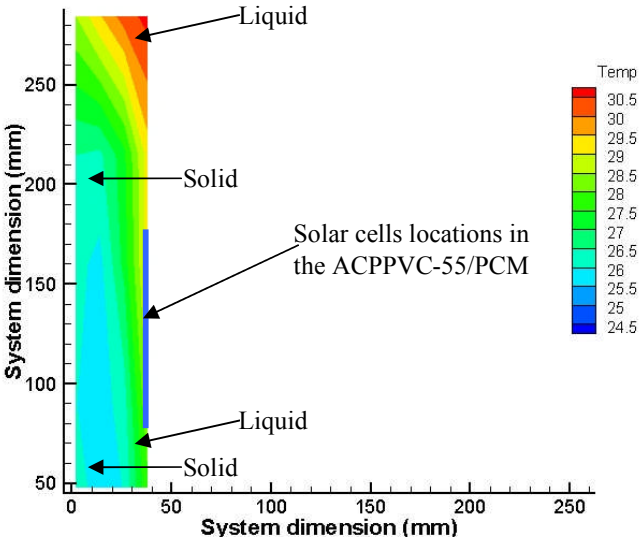

t=400mins

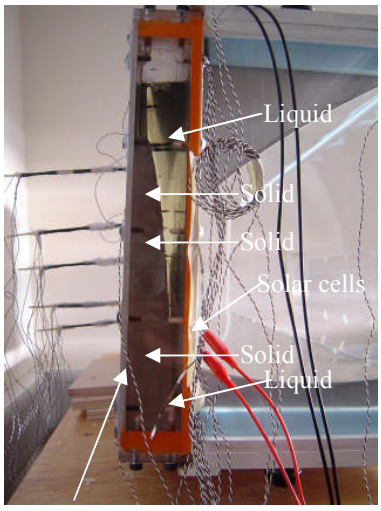

Rear of the ACPPVC55/PCM system

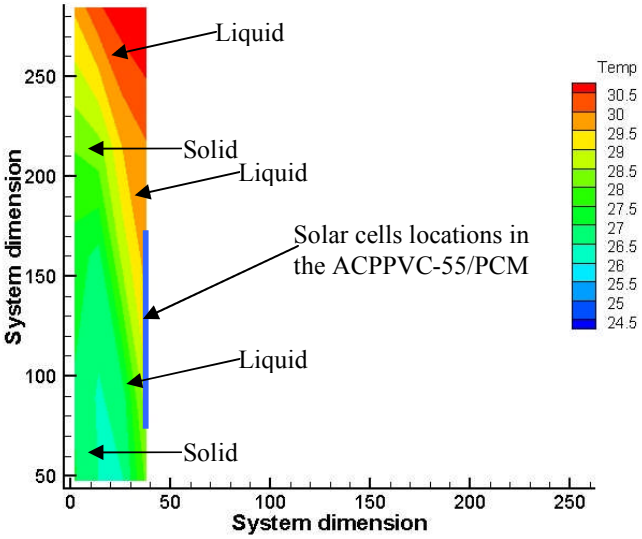

t=500mins

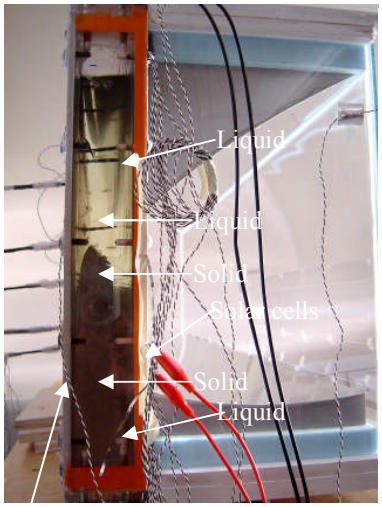

Rear of the ACPPVC55/PCM system

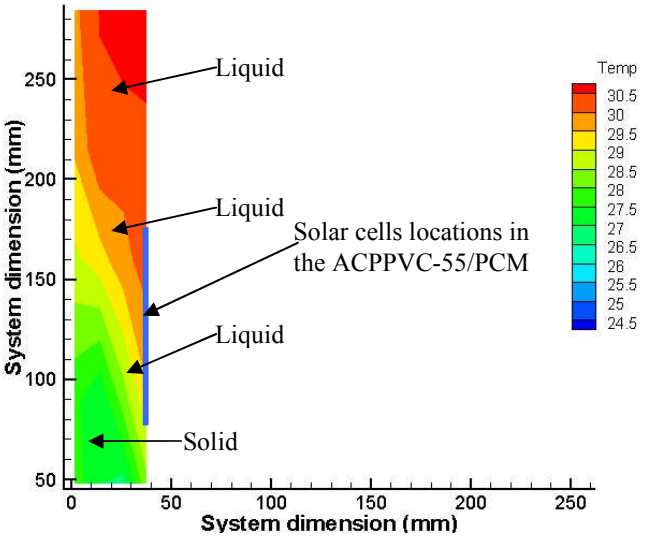

t=600mins

Figure 5.50 Photographs and measured isotherms illustrating the phase change process in the PCM of the ACPPVC/PCM system for selected times when the average insolation was 280 W/m^2 and solar incidence angle was 0°.

5.6.1.2 I-V characteristics of the ACPPVC-55/PCM system at an average incident solar radiation intensity of 280W/m^2

After illuminating the ACPPVC-55 and the ACPPVC-55/PCM system with the solar simulator at an average solar radiation intensity of 280W/m^2 and solar radiation incidence angle of 0° for 250mins, the temperature of solar cells in ACPPVC-55 systems reached steady state values and the RT27 adjacent to the solar cells in the ACPPVC-55/PCM system was melting. The measured average solar cell temperature was 40.2°C for the ACPPVC-55 system, and 32.5°C for the ACPPVC-55/PCM. The measured I-V characteristics and the output power with output voltage of the ACPPVC-55 system and the ACPPVC-55/PCM system tested at an average solar radiation intensity of 280W/m^2 and solar incidence angle of 0° are shown in figure 5.51. From figure 5.51, it can be seen that the measured open circuit voltage and maximum power output of the ACPPVC-55/PCM system were both higher than those for the ACPPVC-55 system, this is due to the ACPPVC-55/PCM system having lower solar cell temperatures. Similar characteristics were found at solar radiation incidence angles of 5° and 10°. The measured short circuit current, open circuit voltage, maximum power output, fill factor and electrical conversion efficiency of the ACPPVC-55 system and the ACPPVC-55/PCM system at selected solar radiation incidence angles are presented in table 5.3. From Figure 5.51 and table 5.5, it can be seen that the electrical conversion efficiency of the ACPPVC-55 system increased by 5.4% at the solar radiation incidence angle of 0°, and by approximately 5% at solar radiation incidence angle of 5 and 10°, when the PCM unit was coupled to the ACPPVC-55 system.

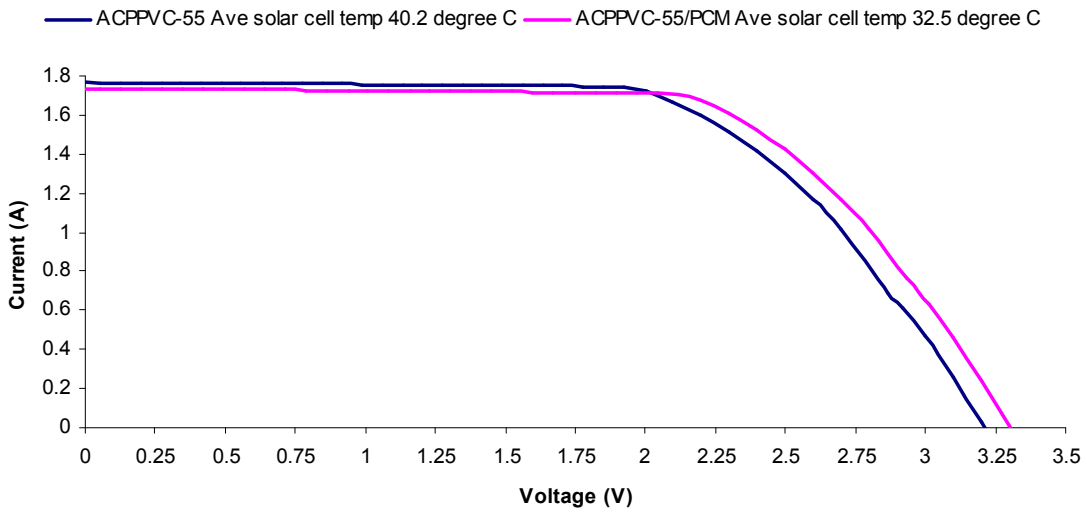

Figure 5.51 Measured I-V characteristics of ACPPVC-55 and ACPPVC-55/PCM system at solar radiation intensity of 280 W/m^2 and solar radiation incidence angle of 0°.

	Solar radiation incidence angle	Isc (A)	Voc (V)	MPP (W)	FF	η (%)
ACPPVC-55	0°	1.77	3.21	3.51	0.618	13.4
	5°	1.86	3.23	3.78	0.627	14.4
	10°	1.86	3.23	3.71	0.619	14.2
ACPPVC-55/PCM	0°	1.74	3.30	3.70	0.644	14.1
	5°	1.84	3.31	3.96	0.650	15.1
	10°	1.82	3.31	3.88	0.644	14.8

Table 5.5 The measured power output of the ACPPVC-55 and ACPPVC-55/PCM system after illumination using the developed solar simulator at an average solar radiation intensity of 280W/m^2 for 250mins

5.6.2 The thermal behaviour of the ACPPVC-55/PCM system at an average incident solar radiation intensity of 672W/m^2

Experiments with solid-liquid phase change material RT27 were undertaken for the ACPPVC-55/PCM system for solar incidence angles of 0°, 5° and 10°. The applied experimental conditions were insolation intensity of 672W/m^2 and air conditioning temperature set to 20°C to control the ambient room temperature.

The measured variation of the average solar cell temperatures with time for the ACPPVC-55 and ACPPVC-55/PCM system at a solar radiation intensity of 672W/m^2 and solar radiation incidence angle of 0° are shown in figure 5.52. From figure 5.52, it can be seen that the average solar cell temperature on the front surface of the ACPPVC-55/PCM is maintained below 42°C for 4 hours. The RT27 maintains the average solar cell temperature of the ACPPVC-55 system steady at 41.6°C for around 180mins, while it undergoes phase change. Comparing this with the temperature rise of the ACPPVC-55 system with no PCM, the RT27 clearly delayed the temperature rise. At a solar radiation intensity of 672W/m^2, RT27 within the ACPPVC-55/PCM system began to melt earlier than when tested at a solar radiation intensity of 280W/m^2, and required a shorter time to complete the phase change process, only 4 hours compared to 10 hours for a radiation intensity of 280W/m^2

The ACPPVC-55/PCM system tested at solar radiation incidence angles of 5° and 10° had similar measured temperatures to those tested at a solar incidence angle of 0°. Their measured temperatures are shown in Appendix B, figures B.5 and B.6, respectively. From figures 5.52, B.5 and B.6, it is clear that during phase change, solar cell temperature was significantly reduced by using the PCM. The solar cell temperature of the ACPPVC-55/PCM was maintained approximately 18°C lower than that of the ACPPVC-55 system with no PCM for the same incident solar radiation intensity.

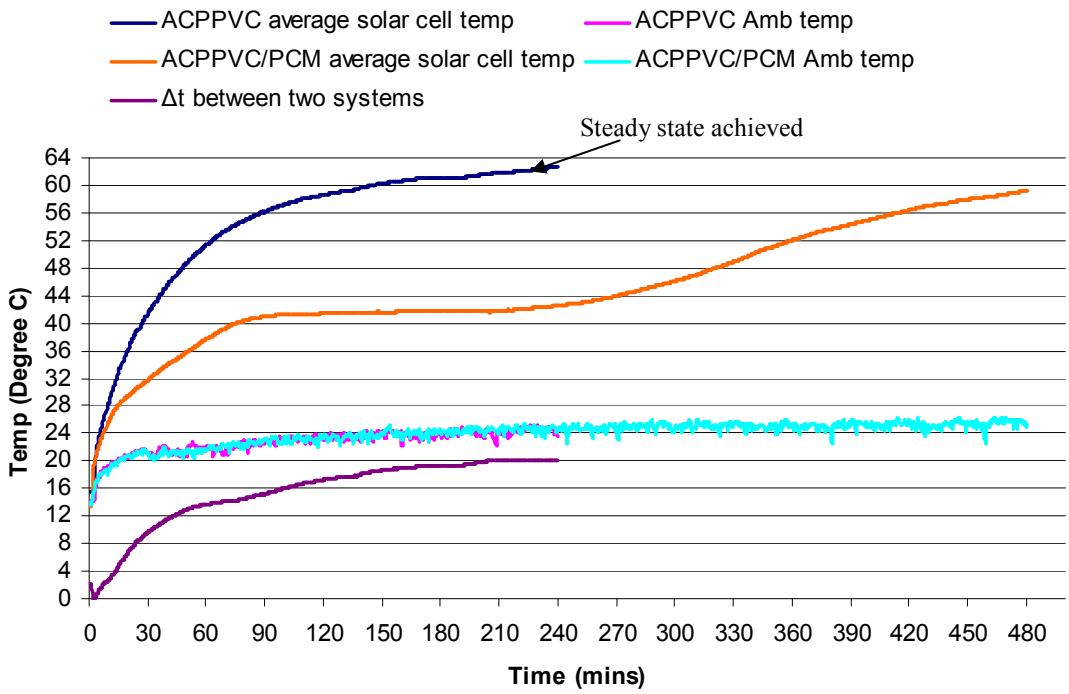

Figure 5.52 Measured average solar cell temperatures with time for the ACPPVC and ACPPVC/PCM system with incident solar radiation of 672W/m^2 and incidence angle of 0°

Photographs and isotherms produced from the measured temperatures during the phase change process for the ACPPVC/PCM system at times of 90, 120, 150, 180, 210, 240 and 270mins are presented in figure 5.53. Phase change can be clearly seen after the system was illuminated by the developed solar simulator for 90mins, RT27 which was adjacent to the solar cells melted more quickly than in any other region in the system. With increasing time, the heated liquid flowed to the upper region of the PCM container, then the upper front region of RT27 began to melt quicker than the lower front region, this can be clearly seen at times 150, 180, 210, 240 and 270mins shown in figure 5.53. After 270mins, the phase change process was nearly complete, only a small region of RT27 remained at the back bottom corner inside the PCM container. The temperatures of the aluminium back plate began to increase after 270mins.

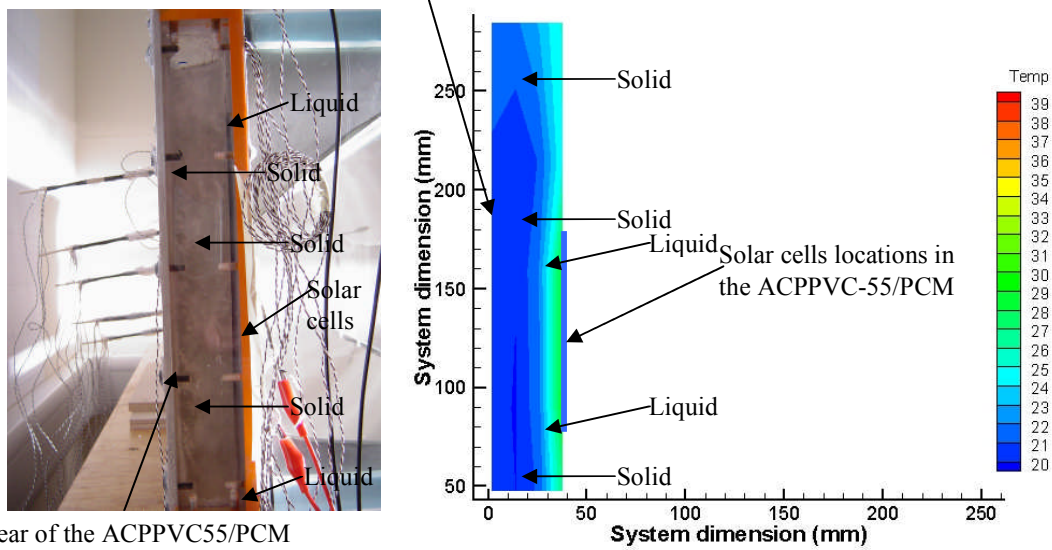

t=90mins

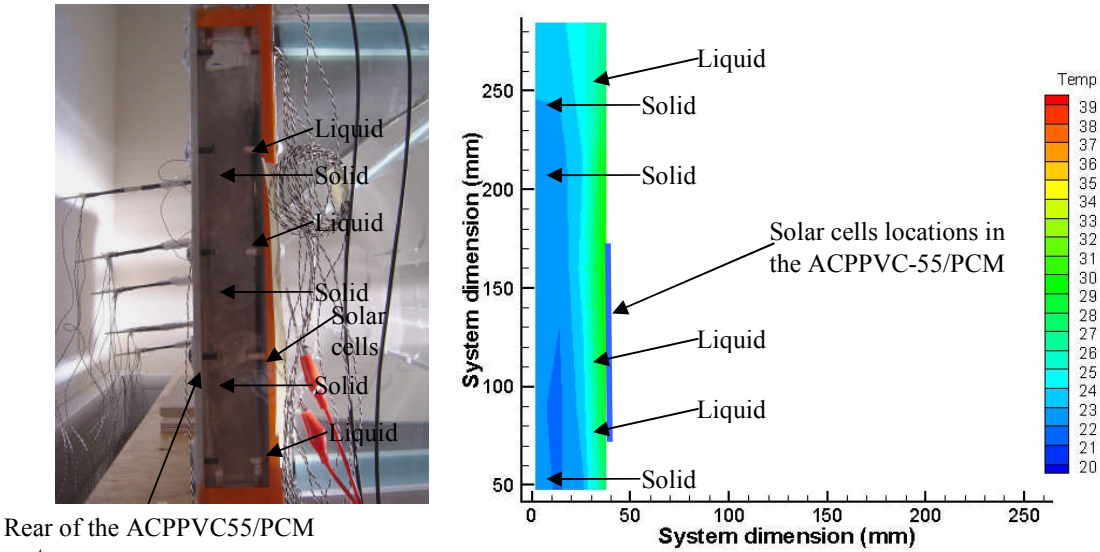

t=120mins

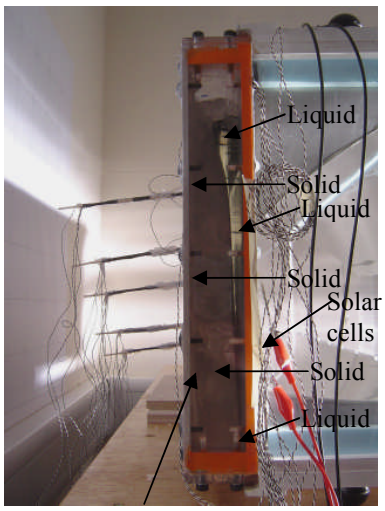

Rear of the ACPPVC55/PCM system

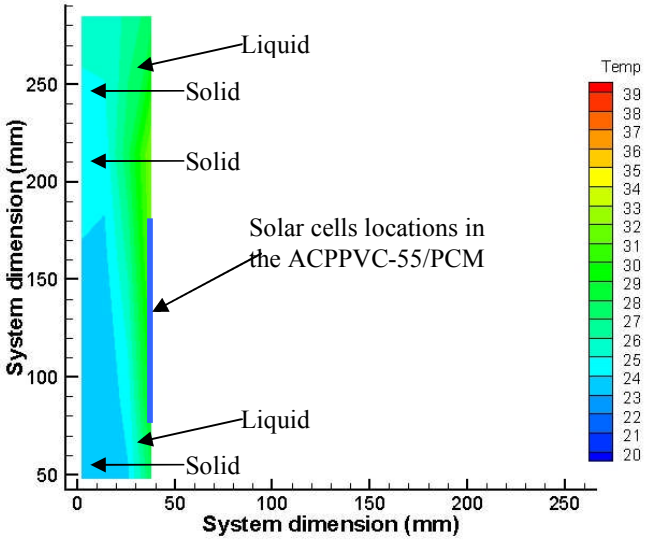

t=150mins

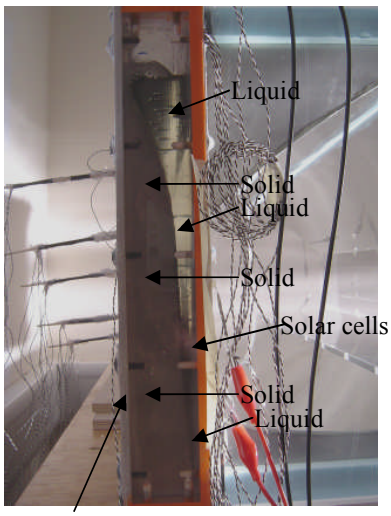

Rear of the ACPPVC55/PCM

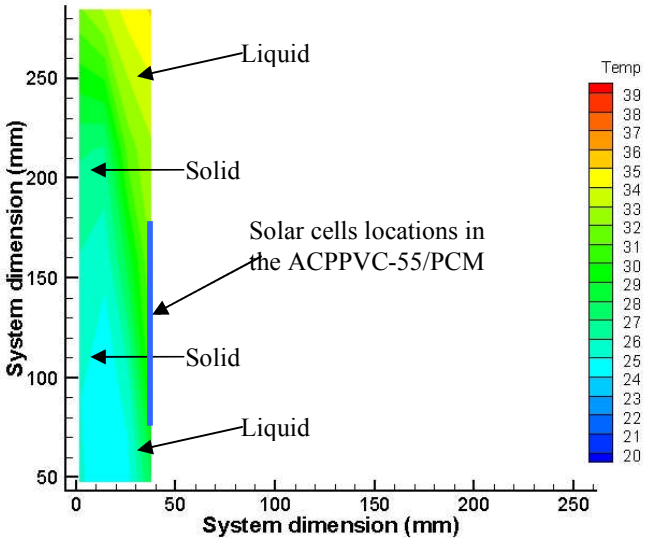

t=180mins

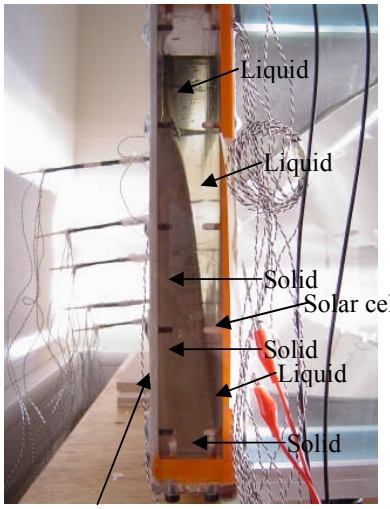

Rear of the ACPPVC55/PCM system

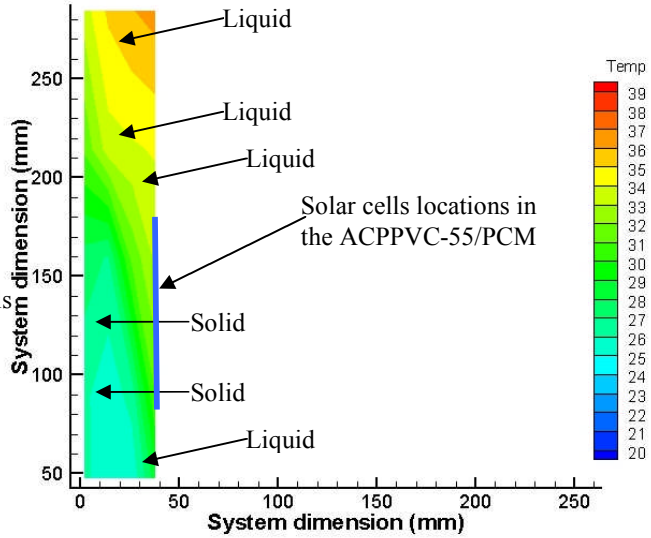

t=210mins

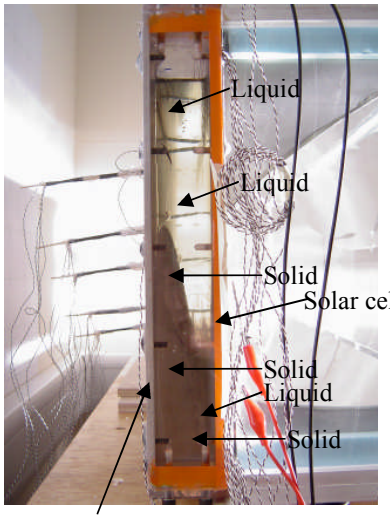

Rear of the ACPPVC55/PCM system

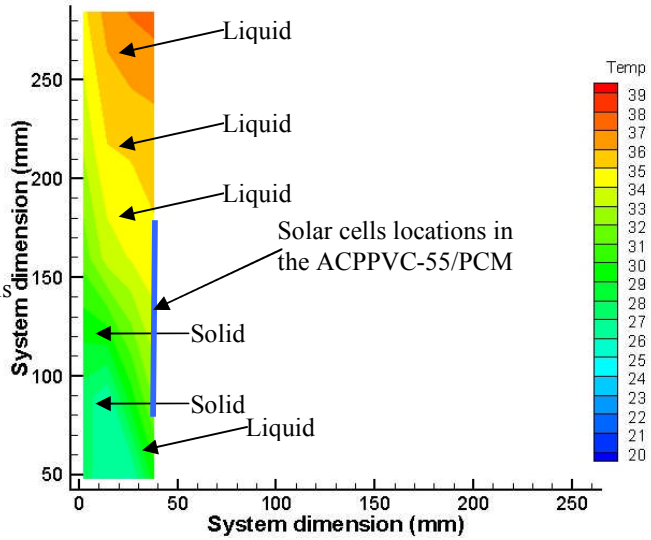

t=240mins

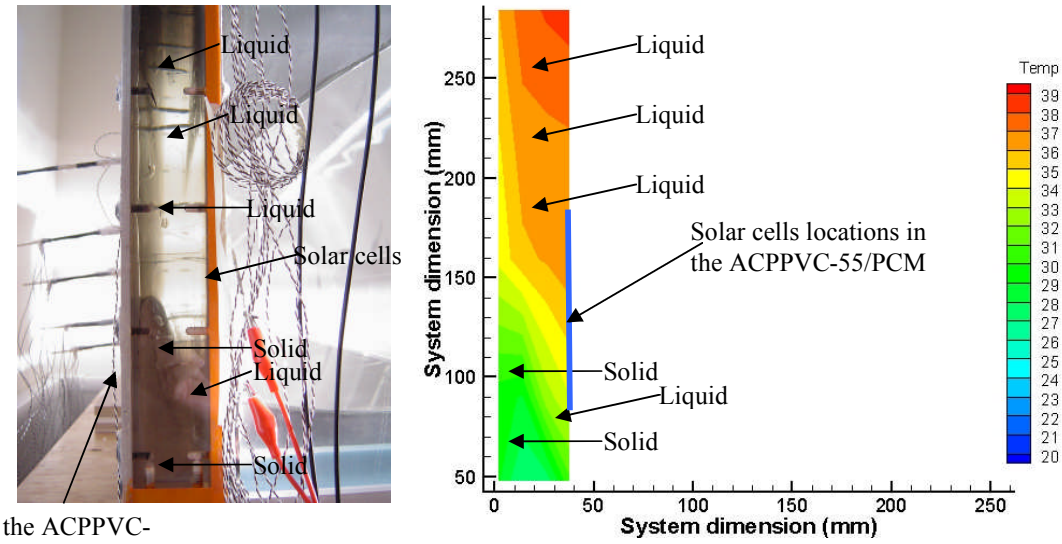

Figure 5.53 Photographs and measured isotherms illustrating the phase change process in the PCM of the ACPPVC/PCM system for selected times when the average insolation was 672 W/m^2 and solar incidence angle was 0°.

Due to the restriction of the measurement facility, the I-V characteristics of the ACPPVC-55/PCM system could not be obtained at the incident radiation intensity of 672W/m^2 on the ACPPVC-55 aperture. However, the solar cells temperature for the ACPPVC-55 system was reduced by 18°C, when the PCM RT27 underwent phase change. The predicted electrical conversion efficiency of the ACPPVC-55/PCM system would be increased by approximately 10% compared to that of the ACPPVC-55 with no RT27 PCM at the same incident radiation intensity of 672W/m^2.

5.7 Temperature dependency of solar to electrical conversion efficiency for the ACPPVC-55 system

The measured I-V characteristics of the ACPPVC-55 at difference solar cell temperatures for a solar incidence angle of 0° are shown in figure 5.54. From figures 5.54, it can be seen

that at average solar radiation intensity of 280W/m^2 on the aperture, the maximum power and open circuit voltage decrease with increasing solar cell temperature. When the average solar cell temperature was 24.5°C, an open circuit voltage of 3.41V is measured. Increasing the solar cell temperature by 8°C, reduced the open circuit voltage by 0.11V.

The fill factors of the ACPPVC-55 system at solar incidence angles of 0° at different solar cell temperatures are shown in figure 5.55. From figure 5.55, it can be seen that the fill factor decreases with increasing solar cell temperature. The fill factors at different solar cell temperatures along with a linear line fit are also shown in figure 5.55. For a solar radiation incidence angle of 0°, the fill factor decreased by 0.002 for every 1°C rise in solar cell temperature.

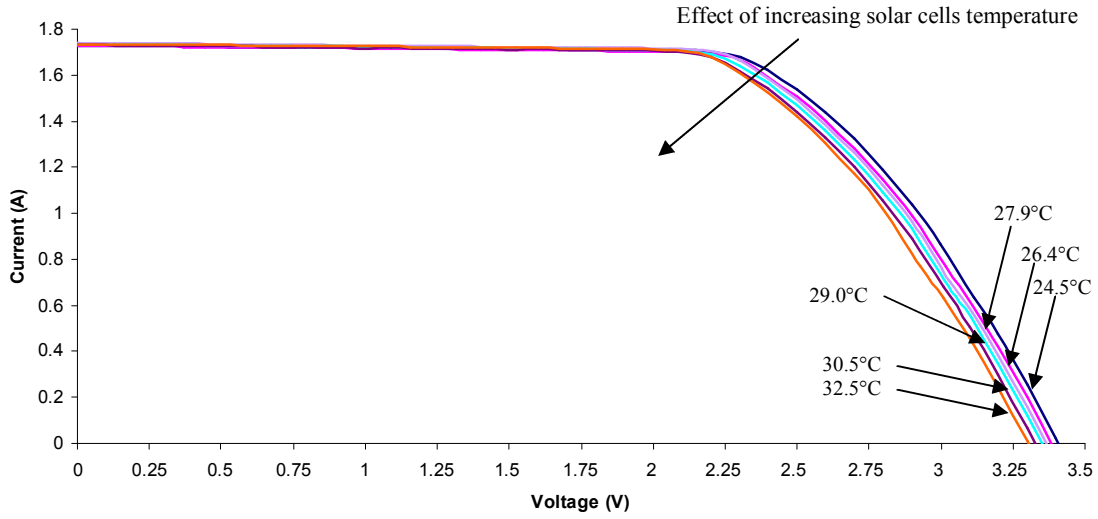

Figure 5.54 I-V characteristics of the ACPPVC-55 system for different solar cell temperatures at a solar radiation intensity of 280W/m^2 and solar incidence angle of 0°

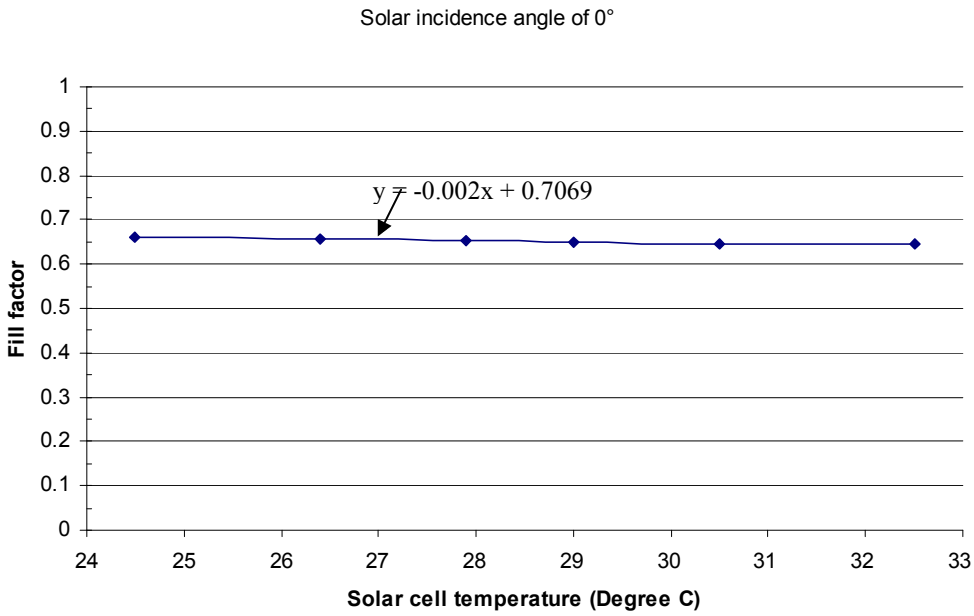

Figure 5.55 The variation of fill factor with solar cell temperature for the ACPPVC-55 system under incident solar radiation intensity of 280W/m^2

The electrical conversion efficiency of the ACPPVC-55 system at a solar radiation intensity of 280W/m^2 and an incidence angles of 0° are shown in figure 5.56. From figure 5.56, it can be seen that the electrical conversion efficiencies decrease with increasing solar cell temperatures. When the average solar cell temperature was around 24.5°C, the efficiency was 14.9%. The efficiency decreased to 14.1% when the solar cell temperature increased to 32.5°C. The electrical conversion efficiency decreases by approximately 6.3% for every 10°C rise in solar cell temperature. For crystalline silicon cells, the cell efficiency decreases by approximately 5% with a 10°C temperature increase (Anon, 2005a). The ACPPVC-55 system had a higher efficiency decrease with increasing the solar cell temperature, this was possibly caused by the temperature differences across the solar cells and non-uniform flux distributions. The power loss caused by temperature differences across the solar cells is discussed in section 5.8.4.

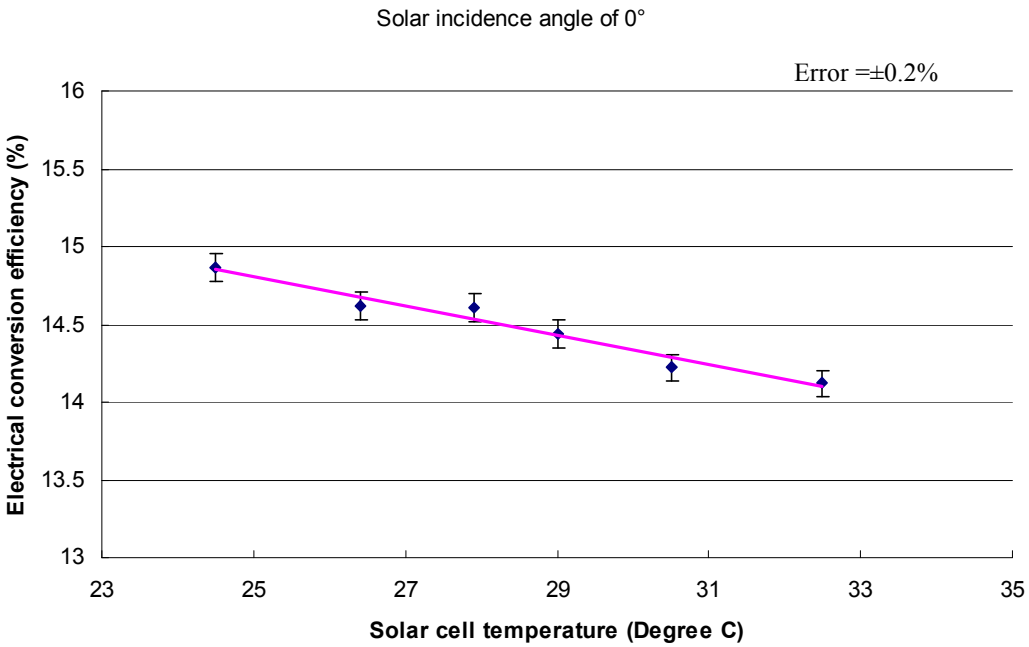

Figure 5.56 The variation of electrical conversion efficiency for the ACPPVC-55 system with different solar cell temperature for solar incident radiation intensity of 280W/m^2.

5.8 Analysis of the electrical power losses for the ACPPVC-55 system

For a concentration ratio of 2.0, the effective solar radiation intensity at the absorber should increase by a factor of 2.0, if the geometry was perfect and no reflection losses occur. This implies that the maximum power point of the ACPPVC-55 system can be double compared to its non-concentrating counterpart PV system. The maximum power ratio between the two systems was less than 2.0 at solar radiation intensities of 69 W/m^2 and 280W/m^2. This indicates significant additional losses for the ACPPVC-55 system, which may be caused by the non-uniform solar radiation distribution on the solar cells surface, higher solar cell temperature, non-uniform solar cell temperatures, increased resistance loss from the PV

ribbon and cables and reflection losses at the reflectors. The power losses in ACPPVC-55 system are discussed in the following paragraphs.

5.8.1 Optical losses

Power losses occur for the ACPPVC-55 system due to optical losses in the system at the aperture cover glass, the reflectors and that resulting from the solar radiation incidence angle due to the cosine effect. The prediction of optical performance of the ACPPVC-55 was presented in Chapter 2 and showed that the maximum predicted optical efficiency of the ACPPVC-55 system was 88.67%. At a solar radiation incidence angle of 5°C, the predicted power loss of the ACPPVC-55 system due to optical losses in the system was approximately 12%, which was approximately twice higher than that of its non-concentrating counterpart system.

5.8.2 Ohmic losses from cable

Ohmic losses occur due to the resistance in the external cables used to connect the ACPPVC-55 system and the Keithley 2430 source meter, and the internal connections (PV ribbons) between the individual solar cells. If the system total resistance is 'r' and the system current output is 'i', then the power loss is i^2r. The power loss from external cables was verified by experimental tests on one BP Saturn solar cell (dimension 125mm×125mm) connect to the Keithley 2430 source meter using different lengths of external cables at solar radiation intensities of 137W/m^2 and 240W/m^2, respectively. The systems tested are described below:

- One solar cell connected to Keithley 2430 source meter using a total length of 4.6m of external cables which were the same as the cables used for the ACPPVC-55 system
- One solar cell connected to a Keithley 2430 source meter with a total length of 2.0m of external cable

Figure 5.57 shows the variation of the current with the voltage for one solar cell when tested at solar radiation intensities of 137W/m^2 and 240W/m^2. The maximum power output and the fill factors are presented in table 5.7. From figure 5.57 and table 5.7, it can be seen that there are no significant differences in short circuit current and open circuit voltage for the solar cell connected with 2.0m and 4.6m of long external cables at the same solar radiation intensity level. However, the solar cell connected with the 4.6m long external cable has a reduced maximum power output than when connected with 2.0m long external cable. The solar cell has a decrease of 9% in its maximum power output when connected with the 4.6m long external cable, compared to being connected with the 2.0m long external cable for an incident solar radiation intensity of 137 W/m^2, and has a decrease of approximately 13% for an incident solar radiation intensity of 240W/m^2.

The measured resistance of the 4.6m long external cable used for the ACPPVC-55 and its non-concentrating counterpart systems is approximately 0.40Ω. When the incident solar radiation intensity was 280W/m^2, power losses of 1.28W and 0.48W caused by ohmic losses in the external cable were calculated from 'i^2r' for the ACPPVC-55 and its non-concentrating counterpart systems, respectively. An additional power loss of approximately 30.3% of that for the ACPPVC-55 system was obtained, when compared to its non-concentrating counterpart system at an incident solar radiation intensity of 280W/m^2.

Mallick et al (2007b) indicated an average of 3.4% electrical power loss of a non-concentrating PV system may be due to resistance in the interconnections between each individual solar cell. It can be concluded that the power loss due to the resistance of the measuring circuit is significant, and increases with increasing incident solar radiation intensity.

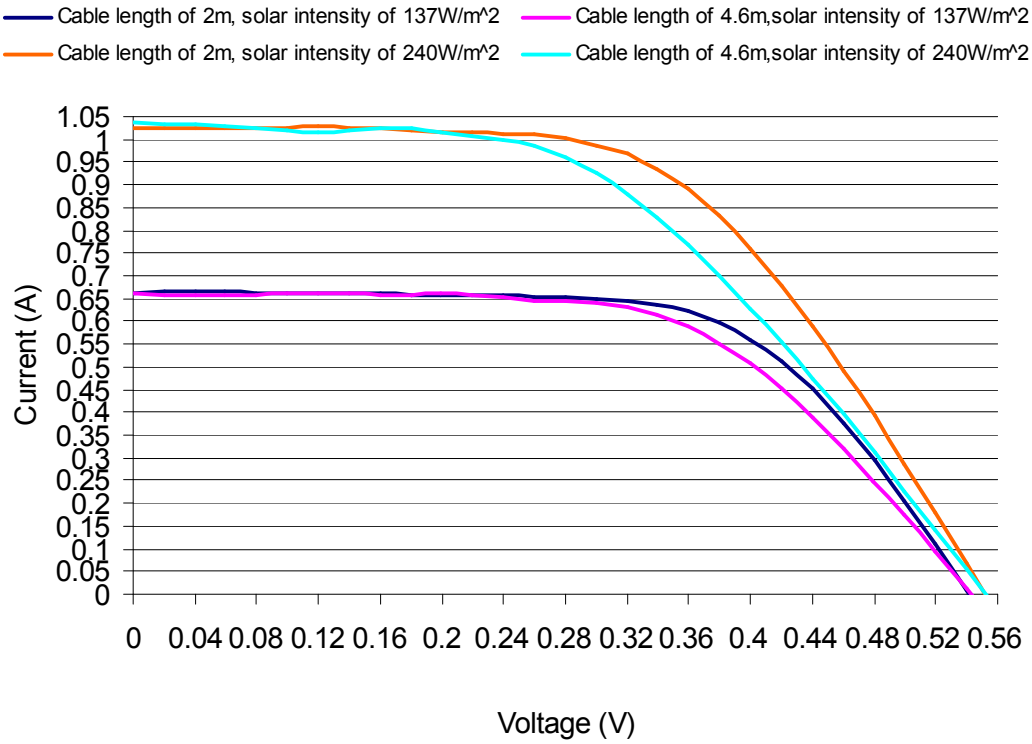

Figure 5.57 I-V characteristics of one solar cell with different external cable lengths for solar radiation intensities of 137W/m^2 and 240 W/m^2.

	Cable length of 2m, insolation 137W/m^2	Cable length of 4.6m, insolation 137W/m^2	Cable length of 2m, insolation 240W/m^2	Cable length of 4.6m, insolation 240W/m^2
Fill Factor (%)	63.2	59.4	57.0	49.4
Max power point	0.23	0.21	0.32	0.28

Table 5.6 The fill factors and maximum power points for a solar cell tested using different external cable lengths and solar radiation intensities.

5.8.3 Power losses caused by high local radiation intensities

The electrical power loss of the ACPPVC-55 system may be caused by the high local radiation intensity that occurred as a strip on the solar cells. It was tested by performing experiments in which a solar cell was exposed to radiation with and without a high intensity flux strip on its surface, in both experiments similar area weighted average incident solar radiation intensity was used. A mask was fabricated specifically for this test using two overlapped 400mm long by 200mm wide alumimnium mesh sheets with a 150mm long by 10mm wide slot cut in their centre region sandwiched between two pieces of 6mm thick Perspex sheet. Figure 5.58 shows an enlarged view of the solar cell under test using the developed mask. The solar concentration ratio on the solar cell surface when covered with the mask is shown in figure 5.59. The radiation flux which passes through the slot in the mask and incident on the solar cell surface was approximately 5 times higher than those in other areas of the solar cell surface. The area weighted average solar concentration ratio was 1.32.

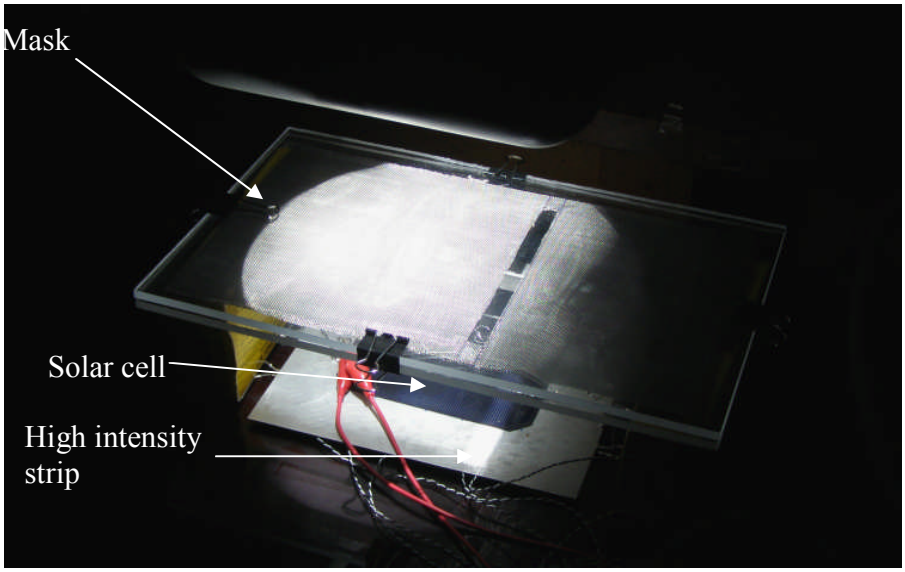

Figure 5.58 An enlarged view of experimental characterisation of one full size SATURN solar cell using the developed mask

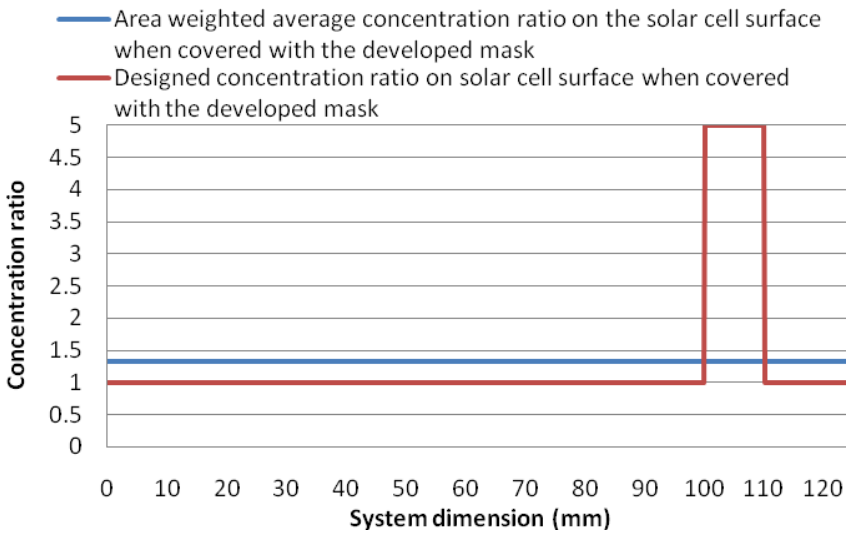

Figure 5.59 The concentration ratio on the solar cell surface when covered with the developed mask

Figure 5.60 presents that the variation of current with voltage for one solar cell with and without the high intensity flux strip. An experiment was undertaken with the area weighted average solar radiation intensity of 200W/m^2. The measured short circuit currents, open circuit voltages, maximum power output and the fill factors are presented in table 5.8. From figure 5.60 and table 5.8, it can be seen that the solar cell with no high intensity flux strip has a higher short circuit current and maximum power output than that with the high intensity flux strip. There are no significant differences for the fill factors of the solar cell with and without the high intensity strip at the same average incident radiation intensity. When the area weighted average incident solar radiation intensity is 200W/m^2, a power loss of approximately 2% is found for the solar cell with a high intensity flux strip.

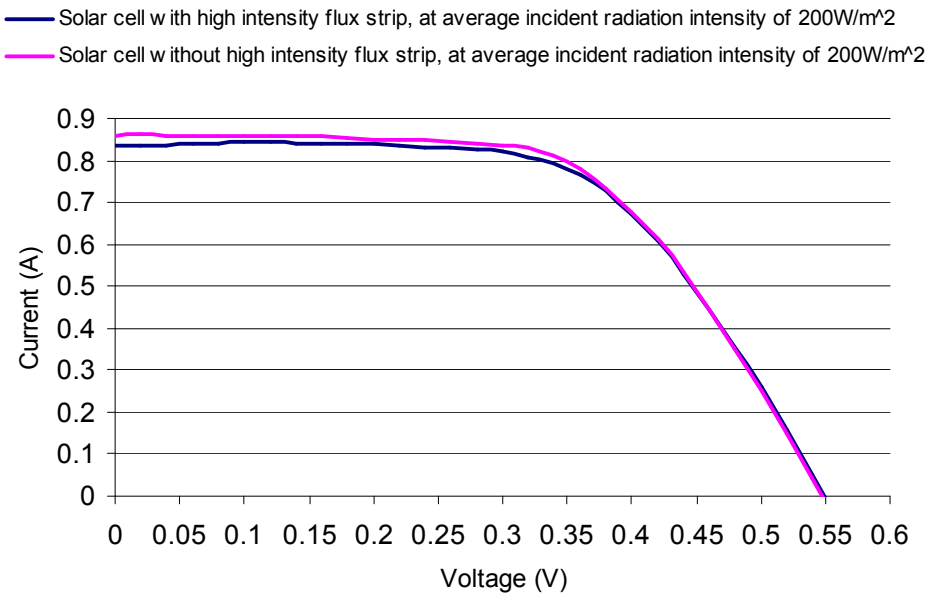

Figure 5.60 I-V characteristics of a solar cell for an area weighed average solar radiation intensity of 200W/m^2 with and without high intensity strips on.

	Incident solar radiation	Isc (A)	Voc (V)	MPP (W)	FF(%)
Solar cell with high intensity strip	200W/m^2	0.83	0.55	0.276	60.1
Solar cell without high intensity strip	200W/m^2	0.86	0.55	0.281	59.3

Table 5.7 The short circuit currents, open circuit voltages, fill factors and maximum power points for a solar cell tested with and without high flux intensity, at an area weighted average solar radiation intensity of 200W/m^2.

5.8.4 Hot spot effect

From sections 5.4 and 5.5, it can be seen that the average solar cell temperature difference between the ACPPVC-55 and the non-concentrating PV system was approximately 1.2°C and 3°C at solar radiation intensities of 69W/m^2 and 280W/m^2, respectively. With every 10°C increase in silicon solar cell temperature, the electrical conversion efficiency decreases by 5% (Anon, 2005a). This implies a possible electrical conversion efficiency

decreases of around 0.5% and 1.5% for the ACPPVC-55 system when compared to the non-concentrating PV counterpart system, at incident solar radiation intensities of 69W/m^2 and 280W/m^2.

5.9 Conclusion

Three different PV systems were fabricated and characterised using a developed collimated solar simulator at selected solar radiation intensities and solar incidence angles. The experimental results showed that the electrical output from the ACPPVC-55 was approximately 1.8 of that of a non-concentrating PV system with similar PV cells area. The electrical conversion efficiency for the ACPPVC-55 system was further increased, when RT27 PCM was incorporated to its rear. The stored thermal energy in the PCM can be used for potential building application. The detailed conclusions are as follows:

- The incident energy is non-uniformly distributed along the width of the solar cell surface for the ACPPVC-55 system, this is due to a combination of the direct radiation and radiation reflected from the reflectors onto the PV cells.
- For solar incident radiation of 69W/m^2, an 88% increase in maximum power was observed for the ACPPVC-55 system compared with its non-concentrating counterpart.
- For a solar incident radiation intensity of 280W/m^2, only a 43% increase in maximum power was observed for the ACPPVC-55 system compared to its non-concentrating counterpart, this was possibly due to the approximately an additional 30.3% ohmic loss in the external cables, a 1.5% power loss caused by the higher solar cell temperature and other losses including power loss caused by the resistance in the interconnections between each individual solar cell and power loss caused by the non-uniform incident solar radiation for the ACPPVC-55 system.

- The maximum power output from the ACPPVC-55 system decreased by around 6.3% for every 10°C increase in solar cell temperature at a solar radiation intensity of 280W/m^2, this may be due to an approximately 3°C temperature differences that occurred across the solar cells surface.
- The fill factor decreased by 0.002 for every 1°C increase in solar cell temperature.
- For the ACPPVC-55/PCM system, it was observed the solar cell temperature was significantly reduced by using a PCM.
    - For an incident solar radiation intensity of 280W/m^2, the average solar cell temperature of the ACPPVC-55 system was reduced by 7°C for approximately 10 hours when using RT27. The electrical conversion efficiency of the ACPPVC-55 system increased by approximately 5%.
    - For an incident solar radiation intensity of 672W/m^2, the average solar cell temperature of the ACPPVC-55 system was reduced by 18°C for approximately 4 hours when using RT27. The predicted electrical conversion efficiency of the ACPPVC-55 system increased by around 10%.

The designed ACPPVC-55 system with a concentration ratio of 2.0 requires half of the expensive PV material compared to a similar flat PV panel, and provide similar output power. For further reducing the PV system's initial cost, a high concentration ratio Fresnel lens PV Concentrator can be applied, however, the significant increased incident solar radiation intensity on the cell surface may lead to an increase in the local temperature of the PV cell, and potentially result in a significant decrease in the electrical conversion efficiency.

Chapter 6 Experimental characterisation for a high concentration ratio Fresnel lens PV Concentrator (FPVC)

6.1 Introduction

The Fresnel lens PV Concentrator (FPVC) system is a promising technology for increasing the solar radiation intensity on solar cells thus reducing the system's capital cost. FPVC systems developed by 'Whitfield Solar' are shown in figure 6.1. The aluminium concentrator trough works as a heat sink and enhances heat transfer from the solar cells to the ambient environment. Considerable research has been undertaken to improve the optical efficiency of the Fresnel lens aperture and in optimising the Fresnel lens design to obtain a uniform radiation intensity distribution on the solar cell of the FPVC concentration (Nabelek et al, 1991, Ryu et al, 2006). To date however, most of the FPVC systems had a concentration ratio of more than 100, it may lead to an increase in the local temperature of the PV cell, potentially result in a significant decrease in the solar to electrical conversion efficiency of the FPVC system, few researches have studied the thermal performance of the FPVC system. In this Chapter, details of extensive indoor experimental characterisation of the heat loss from a Fresnel lens PV Concentrator (FPVC) supplied by Whitfield Solar Company are reported for a range of simulated solar radiation intensities, different ambient air temperatures, and both natural and forced convection.

The tested FPVC is illustrated in figure 6.2. It has a design concentration ratio of 100. The concentrator trough is made of aluminium with wall thickness of 0.6mm, and is 1000mm in length. Its aperture is 100mm wide, and the base is 20mm wide. The height of the trough is 87mm. Ten solar cells with dimensions of 12mm long by 10mm wide are installed on a 1000mm long, 1.5mm thick 20mm wide IMS circuit board in the FPVC system.

Figure 6.1 A photograph of the Fresnel Lens PV Concentrator (FPVC) systems developed by 'Whitfiled Solar' Company

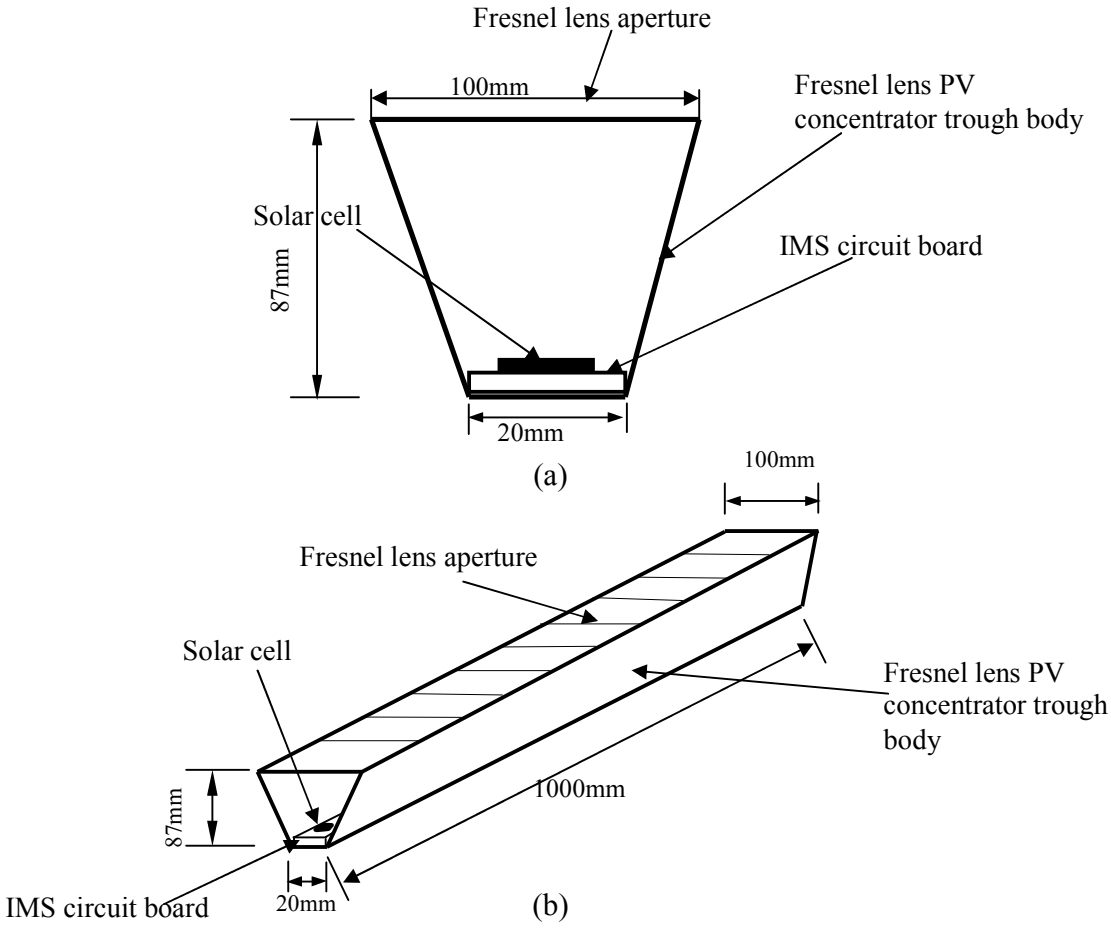

Figure 6.2 (a) Cross sectional view of the experimentally characterised FPVC system (b) 3D diagram of the experimentally characterised FPVC system

6.2 Design and selection of the experimental testing facilities

The indoor experimental thermal characterisation required that the Fresnel lens PV Concentrator (FPVC) was tested inside a heated insulated enclosure which was used to maintain a constant environmental temperature. Ten Electrical Resistance Heaters (ERHs), similar in dimension to the solar cells used in the FPVC system, replaced the solar cells, and thus simulated the heat generated at the solar cells in the FPVC system when exposed to solar radiation.

6.2.1 Selection of the Electrical Resistance Heaters (ERHs)

The heat to be dissipated from a solar cell in the Fresnel lens PV concentrator can be calculated using equation 6.1.

$$Q = A \cdot I \cdot \eta_{opt} \cdot (1 - \eta_{PV}) \tag{6.1}$$

Where A is the area of the Fresnel lens, I is the incident solar radiation intensity, η_{opt} is the optical efficiency of the FPVC system and η_{PV} is the solar-electrical conversion efficiency.

Assuming that the maximum incident solar radiation intensity on the FPVC aperture was 1000W/m^2, the optical efficiency of the FPVC system was 85% (Andreev, 2004) and the electrical conversion efficiency of the solar cell was 15%. From equation 6.1, it can be found that each solar cell in the FPVC system would, at steady state, need to dissipate 7.225W of heat. Ten 20W 20Ω ERHs TO-126 with dimensions of 12mm × 8mm × 3mm having a rated output greater than 7.225W were selected to simulate the heat to be

dissipated from the PV cells in the FPVC and used in the following experiments. A variable output power supply was used to control the power input into each of the resistance heaters.

6.2.2 Design and fabrication of the temperature controlled test chamber and the support frame for the FPVC system

A thermally insulated test chamber was designed and fabricated and used to provide constant temperature experimental conditions for the FPVC system. The test chamber was 1500mm long by 1400mm wide by 1400mm high, it provided sufficient space to contain the FPVC system and incline it over a range of angles. The test chamber frame was fabricated from 30mm × 30mm cross section Bosch Aluminium Profiles. A sketch of the box frame is shown in figure 6.3. The floor of the chamber was comprised of a 3mm aluminium base plate, onto which a 15mm thick plywood board was bonded, the walls of the box were made from 15mm thick plywood boards. Celotex insulation boards 25mm thick with a thermal conductivity of 0.024W/m·K were bonded to the inner surface of all of the walls to reduce heat loss from the inside of the test chamber to the outside ambient environment. A photograph of the test chamber is shown in figure 6.4.

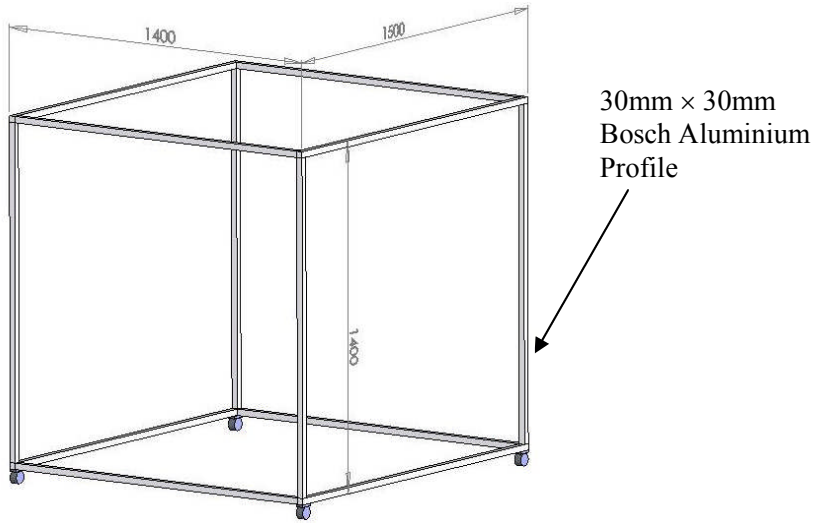

Figure 6.3 A schematic of the test chamber frame, all units in ‘mm’

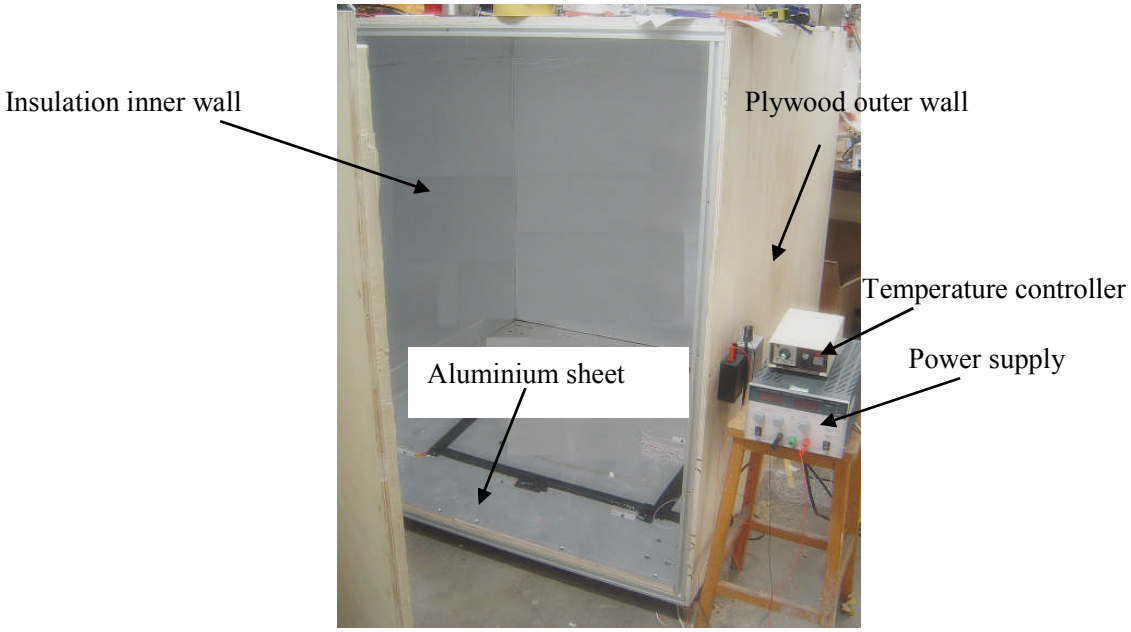

Figure 6.4 A photograph of the test chamber

In order to incline the FPVC system at a range of different angles in the experimental characterisation, a support frame was designed and fabricated for the FPVC system as shown in figure 6.5. The support frame allowed rotation in all three dimensions.

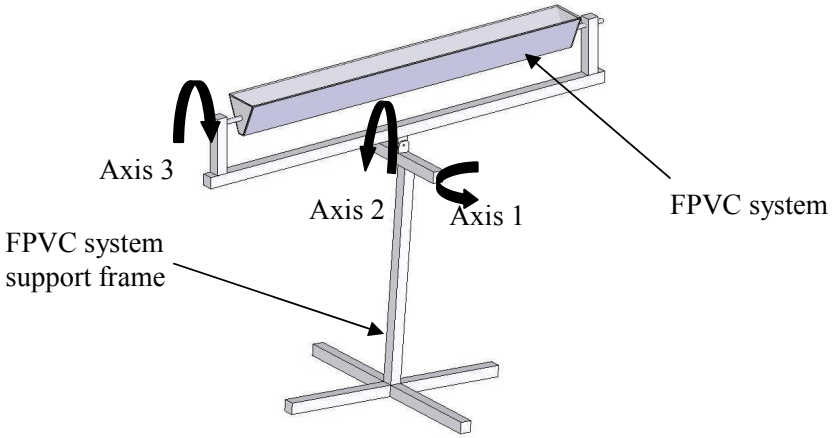

Figure 6.5 A diagram of the FPVC and the developed concentrator support.

6.2.3 Selection of the heaters to maintain the required ambient air temperature

The first stage of experimental tests required only natural convection. The ambient air temperature in the test chamber was maintained at a controlled level by heaters. Eight 200W PTC element enclosure heaters which were connected in parallel to a FTST 400K temperature controller were used to increase the ambient temperature in the test chamber. The maximum generated heat flux on the aluminium base surface was around 830W/m^2.

6.2.4 Design of the experimental facilities to allow in forced convective heat transfer conditions in the FPVC system

In the second stage of experimental testing, the thermal characterisation of the FPVC system was undertaken using forced convective heat transfer. Twelve W2E 200-HH 38-01 exhaust fans having a maximum air volume flow rate of 1030 m^3/h (average air speed 5.65m/s) and fan diameter of 200mm were mounted onto the outer surface of the test chamber, opposite to the chamber door as shown in figure 6.6. The air flow rate was controlled using a fan speed controller. A 2D cross sectional view of the air flow direction in the test chamber is shown in figure 6.7. The air extracted by the exhaust fans, entered from the chamber door and passed through the FPVC systems.

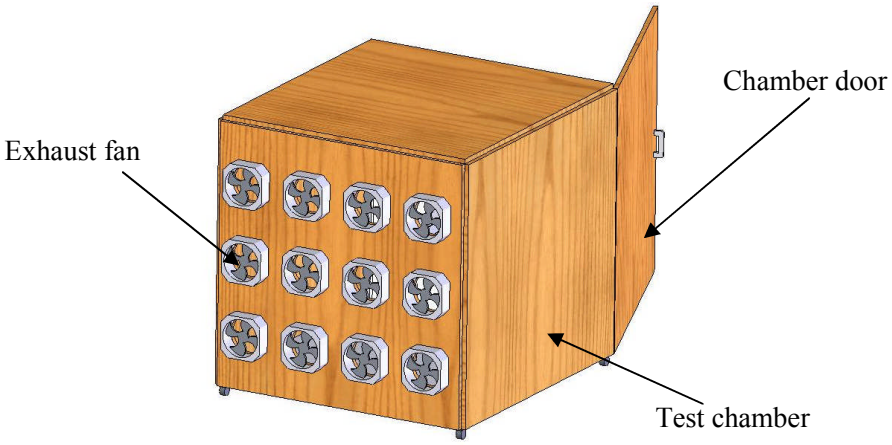

Figure 6.6 A 3D diagram illustrating of the fans mounted on the side of the test chamber

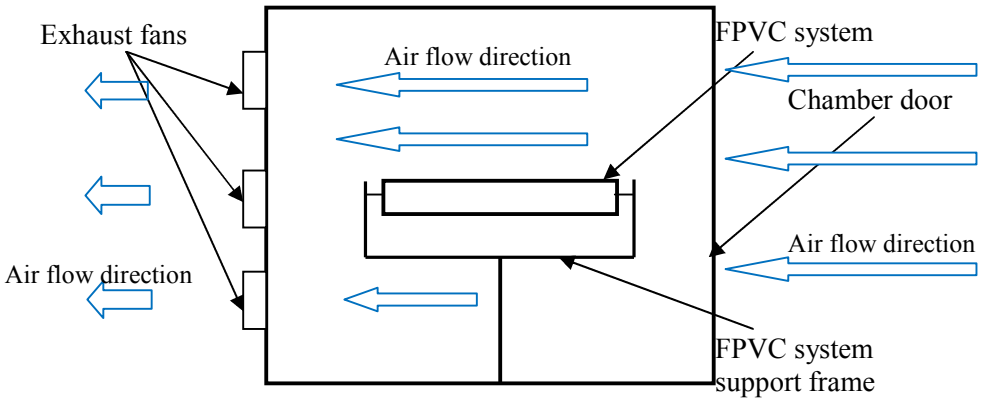

Figure 6.7 Cross sectional view illustrating the air flow direction in the test chamber

6.3 Experimental apparatus setup used for indoor heat loss characterisation

6.3.1 Installation of the resistance heaters to the FPVC system

Ten TO-126 ERHs were connected in parallel and placed in thermal contact with the IMS circuit board and bonded to it using a thermally conductive Loctite adhesive. The IMS circuit board is a heat-conducting electrically-isolating material. The Loctite adhesive had a maximum operational temperature of 150°C and thermal conductivity of 0.815 W/m·K

(Anon, 2008b). Following discussion with Whitfield Solar, a double-sided tape (Technibond T555) was used to fix the IMS circuit board to the inner base of the PV concentrator. Photographs of the TO-126 ERHs and the IMS strips mounted in the FPVC system and a 2D cross sectional view illustrating the components structure of the FPVC are shown in figure 6.8 and 6.9, respectively.

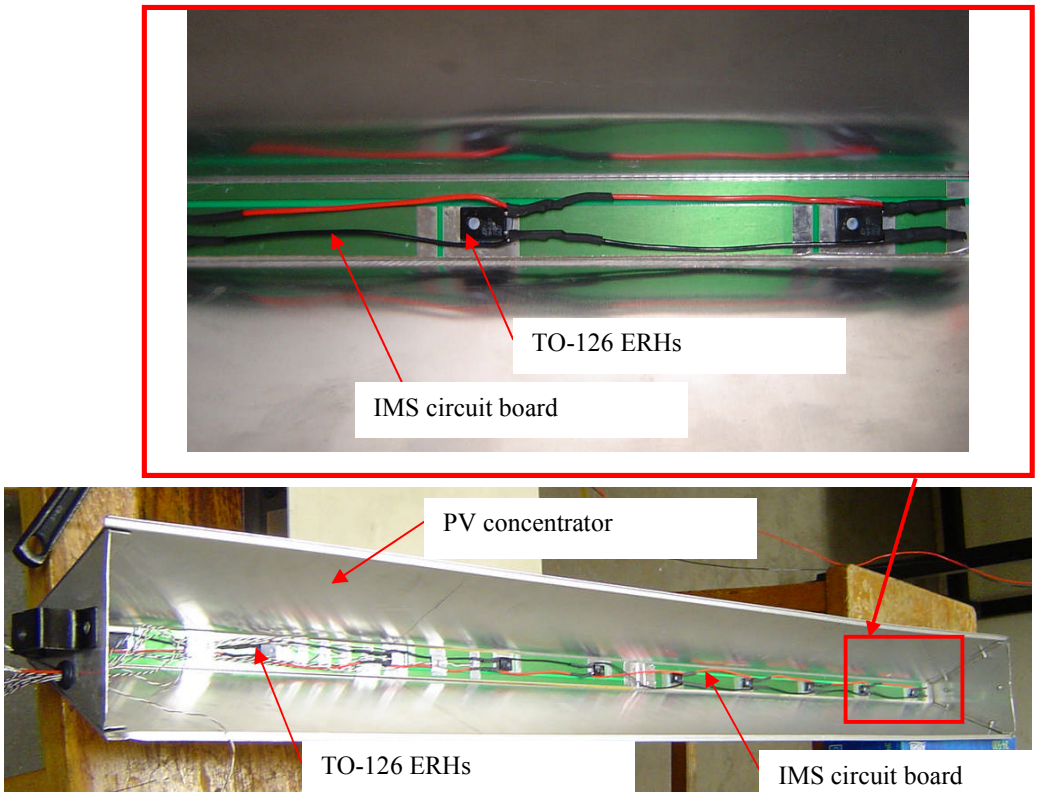

Figure 6.8 Photographs of the ERHs and the IMS strips in the FPVC

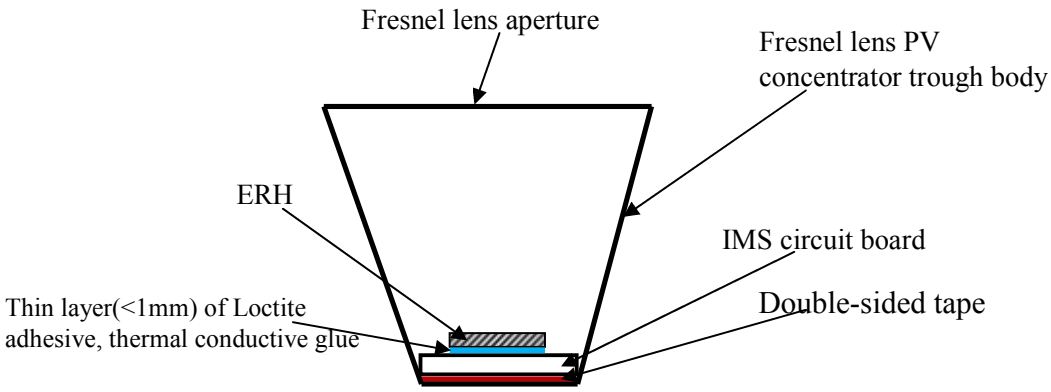

Figure 6.9 Cross sectional view of the ERHs and the IMS strips in the FPVC

6.3.2 Temperature measurements and full experimental test apparatus

"T" type thermocouples were used to measure the temperatures in the FPVC system. Figure 6.10 and table 6.1 show the thermocouple positions in the FPVC system. A photograph of the test chamber, FPVC system, power supply and the temperature controller are presented in figure 6.11. The K type temperature sensor used to control the temperature controller was located at the same position as thermocouple 16 (T16) shown in figure 6.11. A circuit diagram illustrating the equipment used to measure the thermal performance of the FPVC system, to simulate the heat generated in the solar cells, and to control the ambient air temperature in the test chamber is shown in figure 6.12.

Thermocouple	Thermocouple positions
T1 to T4	Distributed between No.2 and No.3 solar cells on the IMS board
T5 and T6	On both sides of the No.3 solar cell
T7	On the No.3 solar cell
T8	17.6mm from the No.4 solar cell
T9 to T14	On the FPVC long trough walls
T15	At the rear of the trough base
T16	At the same horizontal plane as the trough base used to measure the ambient air temperature (shown in figure 6.11)
T17	7mm from T1
T18 and T19	7mm from T20
T20	17.6mm from the No.3 solar cell

Table 6.1 Thermocouple locations in the FPVC system and the test Chamber

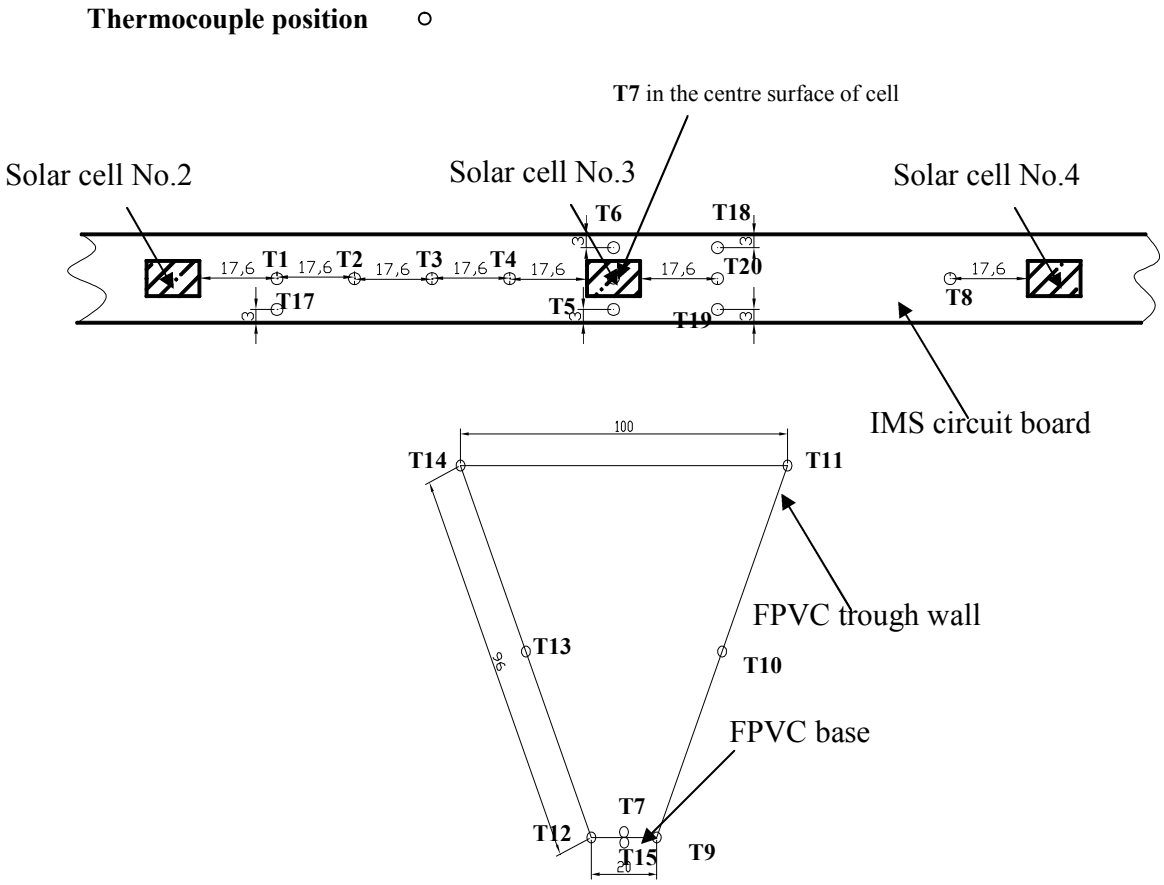

Figure 6.10 Detailed view of the thermocouple positions in the FPVC system, all dimensions in 'mm'

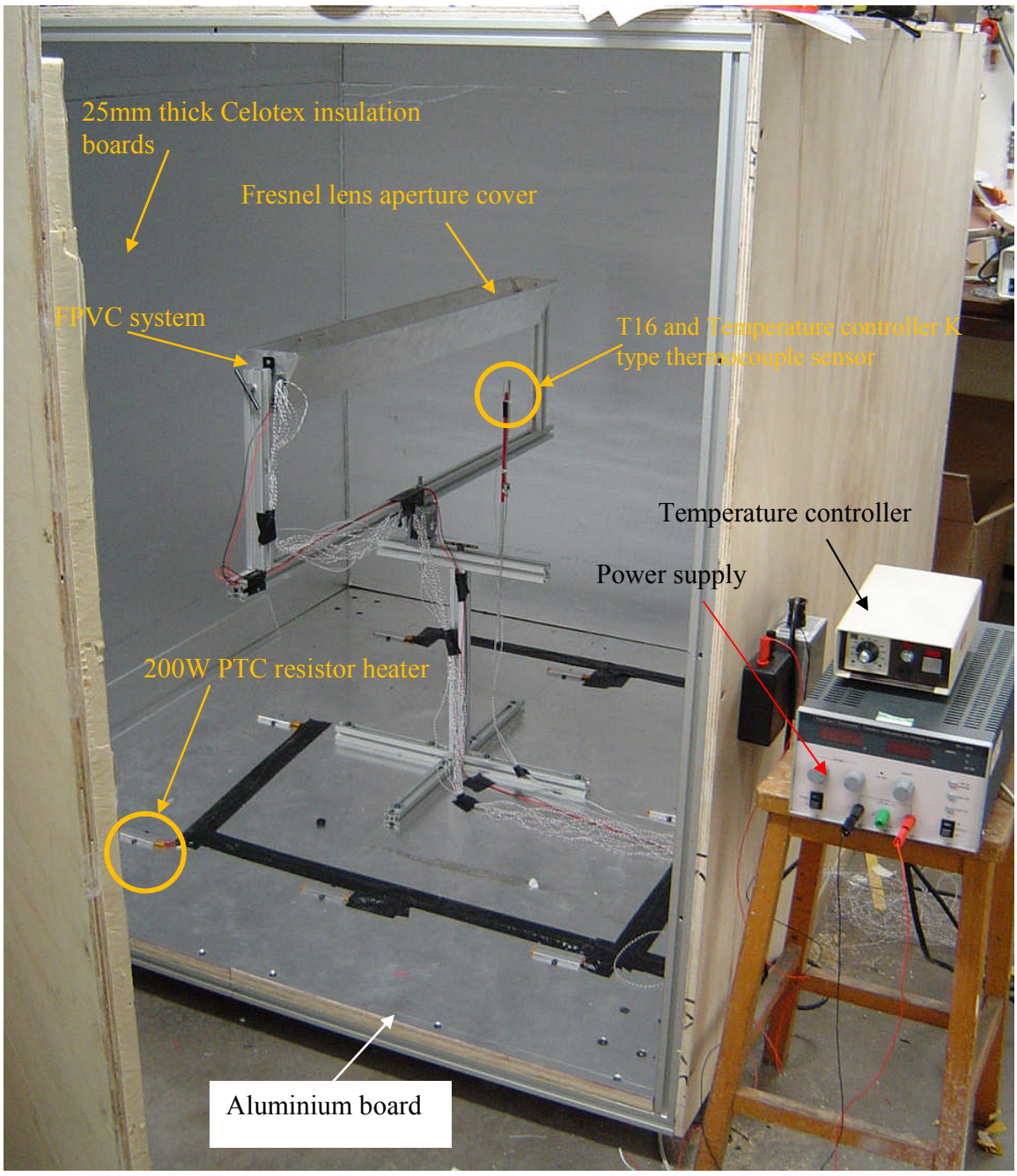

Figure 6.11 A photograph of the test facilities for the FPVC system showing the test chamber, temperature controller, power supply and FPVC system

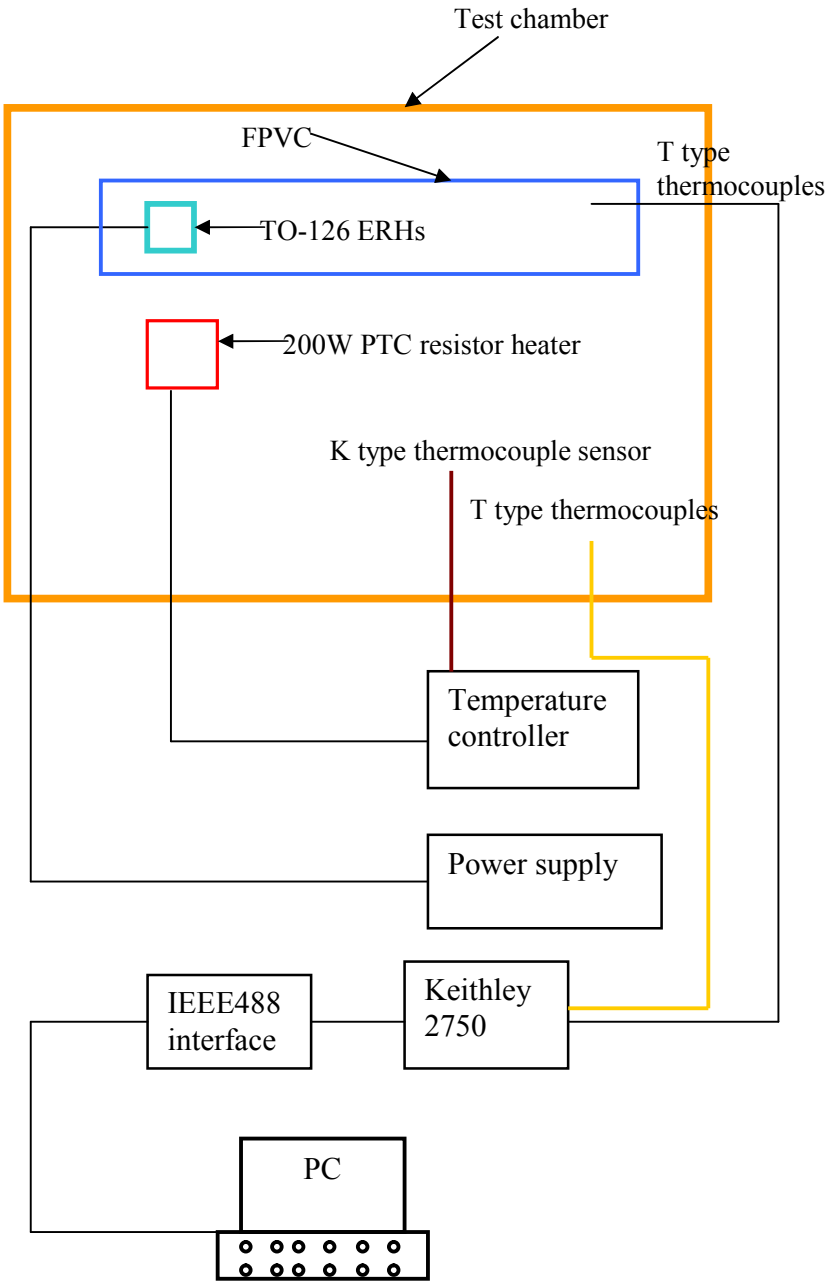

Figure 6.12 Block diagram of the FPVC system and the test facilities

6.4 Thermal behaviour of the FPVC system at an ambient temperature of 20°C with natural convective heat transfer only

The thermal characteristics of the FPVC system were determined for simulated solar radiation intensities at the Fresnel lens of 200, 400, 600, 800 and 1000W/m^2 for natural convective heat loss by running the heaters in both the FPVC system and the test chamber until the FPVC system reached steady state. The final ambient temperature of the test chamber was set at 20°C by controlling the heat input from the chamber heaters. Temperature readings were taken every 30 seconds. The measured variation in temperatures with time for the FPVC at a simulated solar radiation intensity of 1000W/m^2 are shown in figure 6.13. Initially, all temperatures were around 20°C, and the temperature for the FPVC system increased due to the heat emitted from the TO-126 ERHs. After approximately 30mins, steady state temperatures were reached for all sensors in the FPVC system.

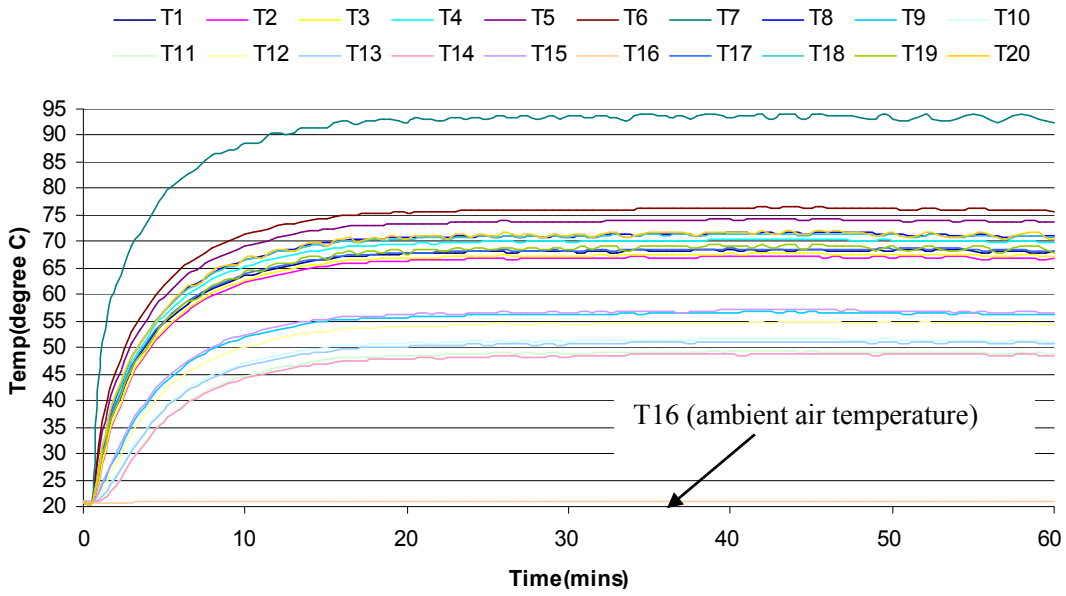

Figure 6.13 The measured variation of temperature with time in the FPVC system for 1000 W/m^2 simulated radiation and an ambient air temperature of 20°C.

From the measured temperatures, isotherm at intervals of 4°C have been plotted in the plane of the No.3 solar cell along with the IMS circuit board at simulated solar radiation intensities of 200, 400, 600, 800 and 1000W/m^2 as shown in figure 6.14. Figure 6.15 presents the change in temperature in the horizontal long central axis (X-direction) for the 3rd solar cell and the IMS circuit board at solar radiation intensities of 200, 400, 600, 800 and 1000W/m^2. From figures 6.14 and 6.15, it can be seen that when the simulated solar radiation intensity is 1000W/m^2, the PV cell achieves the highest temperate of 92.4°C in the FPVC system. It is 72.4°C degree higher than the ambient temperature, and also over 20°C higher than those recorded on the IMS strips. The temperatures of X=-23.6mm, 23.6mm and 76.4mm are all similar at around 70°C, this is expected since they are all located at similar distances from the simulated solar cells. They are however approximately 3°C higher than that of X=-76.4mm, which is closer to the side end of the FPVC trough. Similar thermal behaviour was found on the solar cell and the IMS circuit board at simulated solar radiation intensities of 200, 400, 600 and 800W/m^2. The area around the cell has higher temperatures than any other part of the IMS board. There are no significant temperature differences measured on the IMS board when they are over 18mm away from the simulated solar cells.

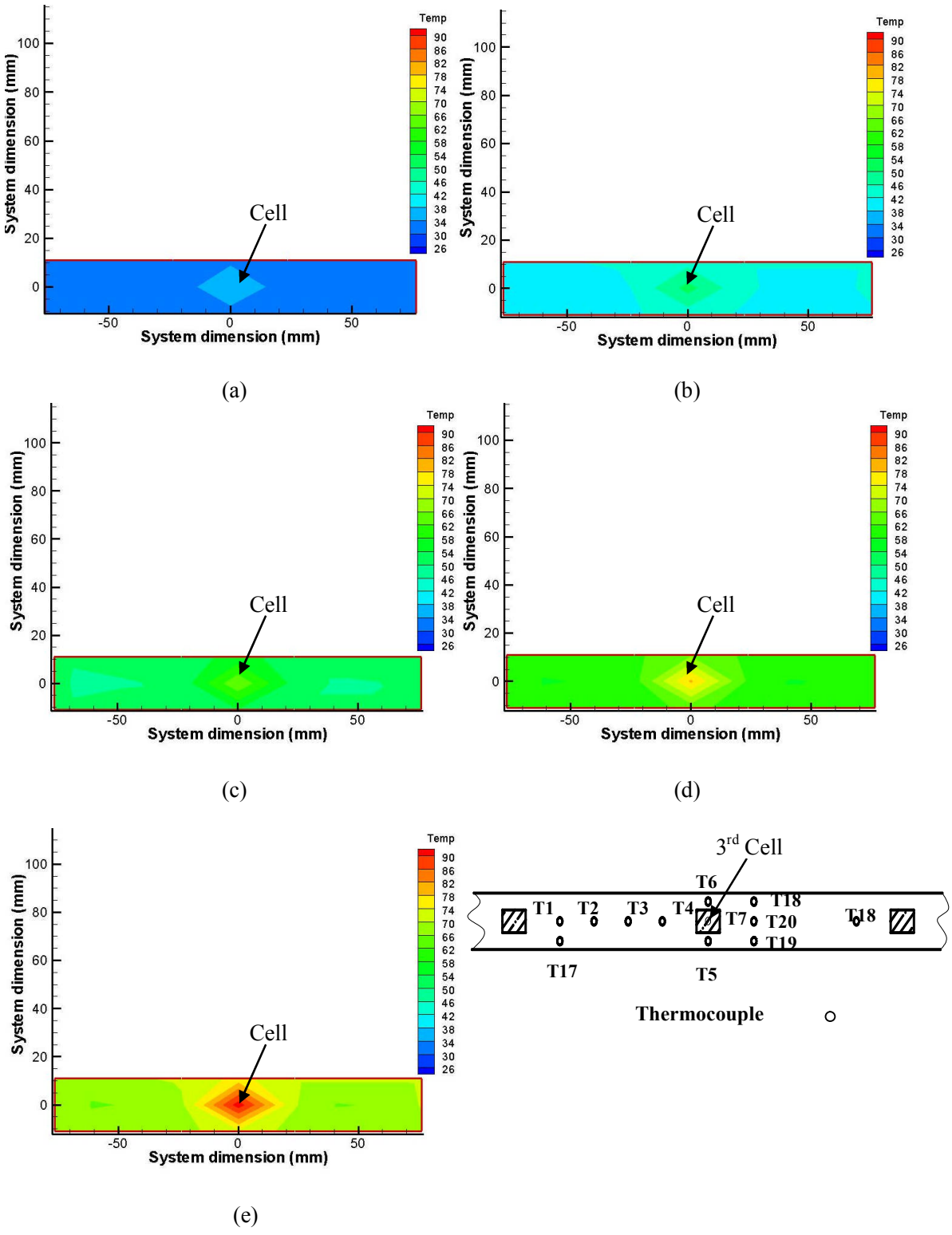

Figure 6.14 Isotherms generated from experimental measurements around the 3rd solar cell along the IMS circuit board. Simulated solar radiation intensity was (a) 200, (b)400, (c)600, (d)800 and (e)1000W/m^2 with an ambient air temperature of 20°C.

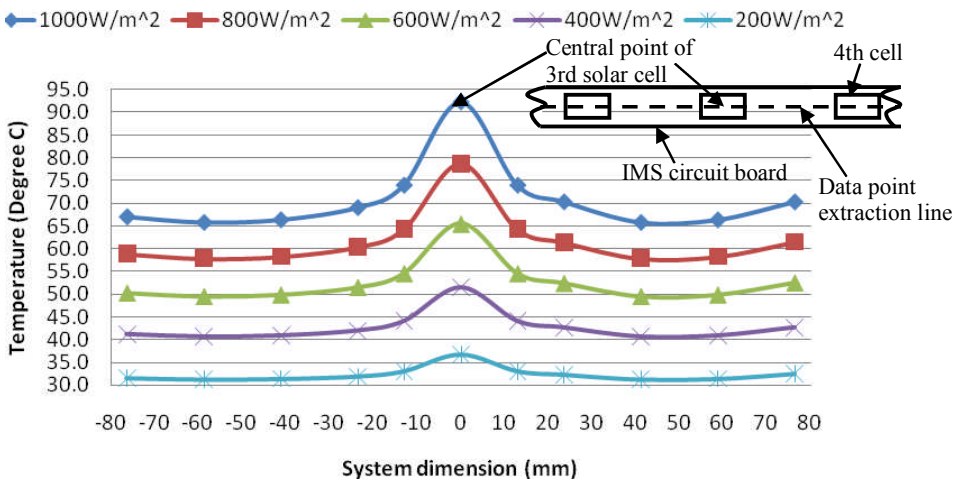

Figure 6.15 Temperature distribution in the horizontal long central axis(X-direction) around the 3rd solar cell along the IMS circuit board for solar radiation intensities of 200, 400, 600, 800 and 1000W/m^2, and an ambient air temperature of 20°C.

The measured temperatures for the solar cell, the FPVC trough base rear, the bottom and the top of the FPVC trough wall and the temperature difference between the solar cell and the trough base rear are plotted in figure 6.16. The following can be observed from figure 6.16, when the ambient air temperature is 20°C, the solar cell temperature linearly increases with the increase in the intensity of simulated solar radiation. Due to long-wave radiative heat transfer relating to T^4, it can be deduced that conductive and convective heat transfer dominate the heat transfer in the FPVC system. When the simulated solar radiation intensity was 1000W/m^2, the temperature difference between the solar cell and the trough base rear was 36.5°C, and 7.7°C at a simulated solar radiation intensity of 200W/m^2. This temperature difference between the solar cell and the trough base rear is significant compared with the distance between the solar cell and the rear of the trough base, and is possibly due to the high thermal resistance between the IMS strips and the trough base.

There were no significant temperature differences between the trough base rear and the bottom of the trough wall in all situations. The temperatures at the trough base are approximately around 7°C higher than those on the top of the trough wall at a simulated solar radiation intensify of 1000W/m^2, and 2°C higher at 200W/m^2.

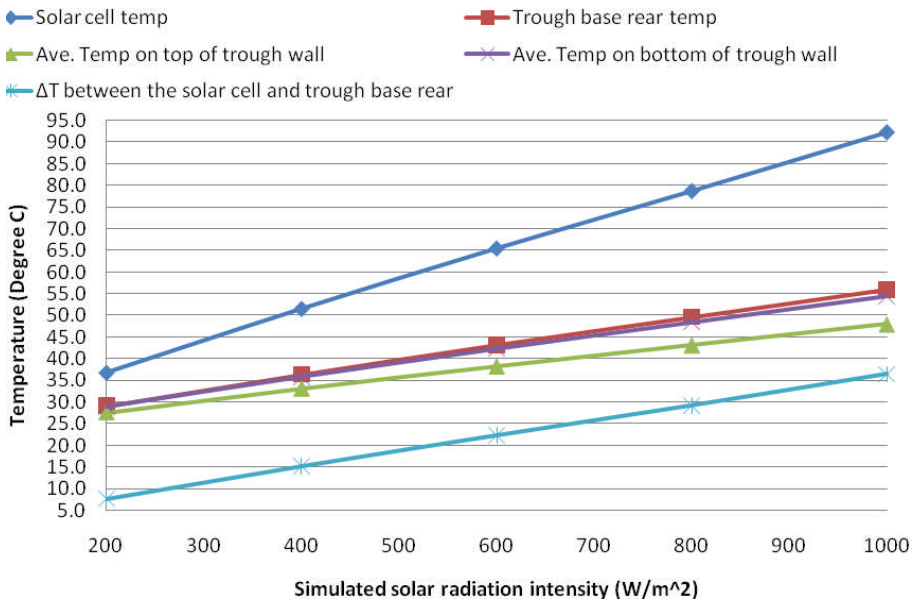

Figure 6.16 The measured temperatures in the FPVC system at selected simulated solar radiation intensities with an ambient air temperature of 20°C

6.5 Thermal behaviour of the FPVC system at an ambient temperature of 50°C with natural convective heat transfer only

To investigate the thermal performance of the FPVC system in a hot climate, a ambient air temperature of 50°C was maintained in the test chamber, which is little higher than the average summer ambient air temperature of 45°C in the Arabian Gulf (Anon, 2008c). Simulated solar radiation intensities of 200, 400, 600, 800 and 1000W/m^2 were used in the FPVC system with a natural convective heat loss condition by running the heaters in both the FPVC system and the test chamber until it reached steady state. Temperature readings were taken every 30 seconds.

From the measured temperatures, isotherms at intervals of 4°C have been plotted in the plane of the No.3 solar cell along with the IMS circuit board at simulated solar radiation intensities of 200, 400, 600, 800 and 1000W/m^2 as shown in figure 6.17. From figure 6.17, it can be seen that the temperature distributions on the IMS circuit board around the No.3 solar cell for a 50°C ambient air temperature have similar general distributions to those on the IMS circuit board at 20°C ambient air temperature. The area around the cell has higher temperatures than any other part of the IMS strips. There are no significant temperature differences on the IMS board over a distance of 18mm from the cells.

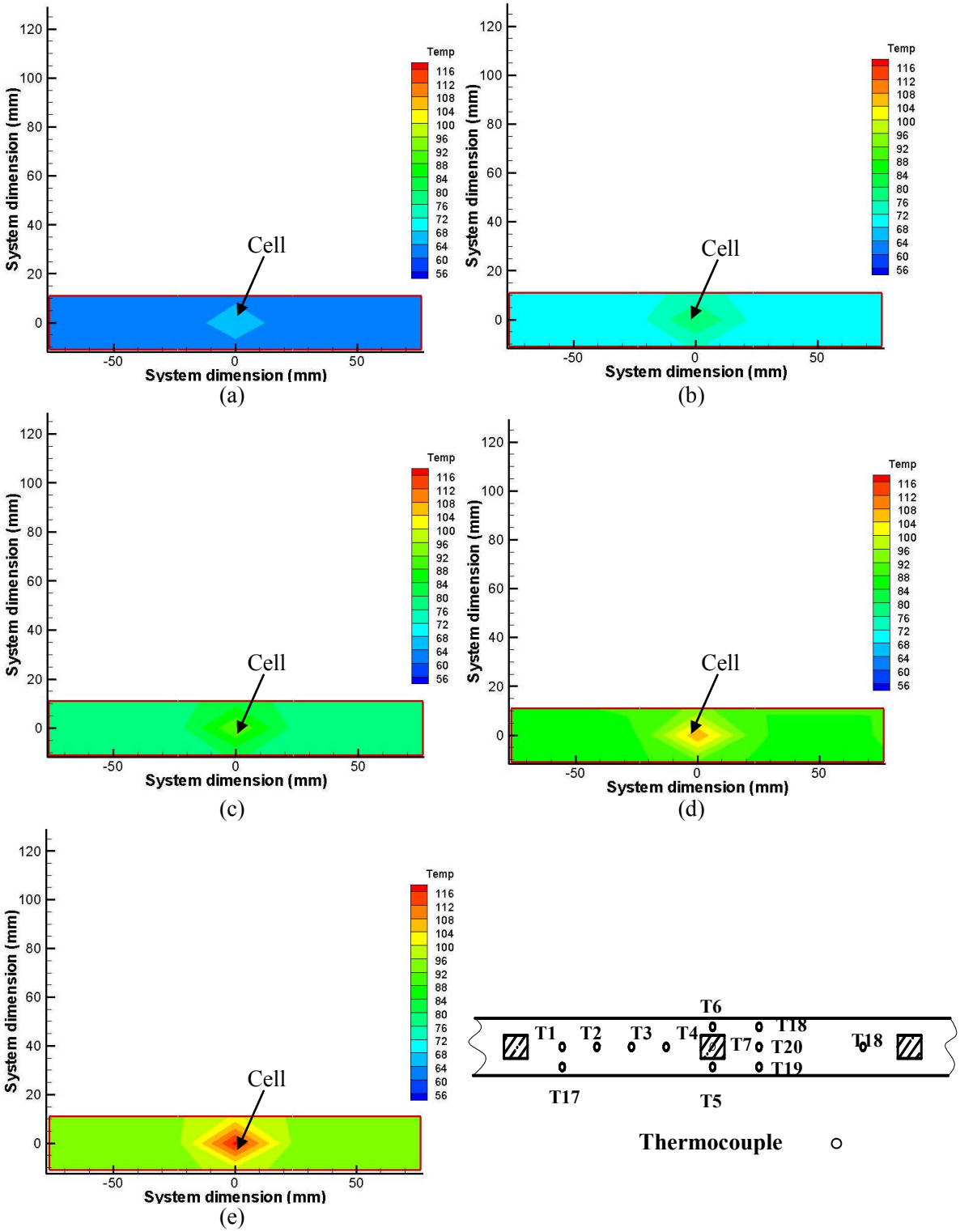

Figure 6.17 Isotherms generated from experimental measurements around the 3rd solar cell along the IMS circuit board. Simulated solar radiation intensity was (a) 200, (b)400, (c)600, (d)800 and (e)1000W/m^2 with an ambient air temperature of 50°C.

The measured temperatures of the solar cell, the FPVC trough base rear, the bottom and the top of the FPVC trough wall and the temperature difference between the solar cell and the trough base rear are plotted in figure 6.18. From figure 6.18, it can be seen that when the ambient air temperature is 50°C, the FPVC system demonstrates similar thermal behaviour as when the ambient air temperature is 20°C. The linearity of the temperature increase with input power indicates that conductive and convective heat transfer again dominates the heat transfer in the FPVC system. The temperature difference between the solar cell and the trough base rear is significant.

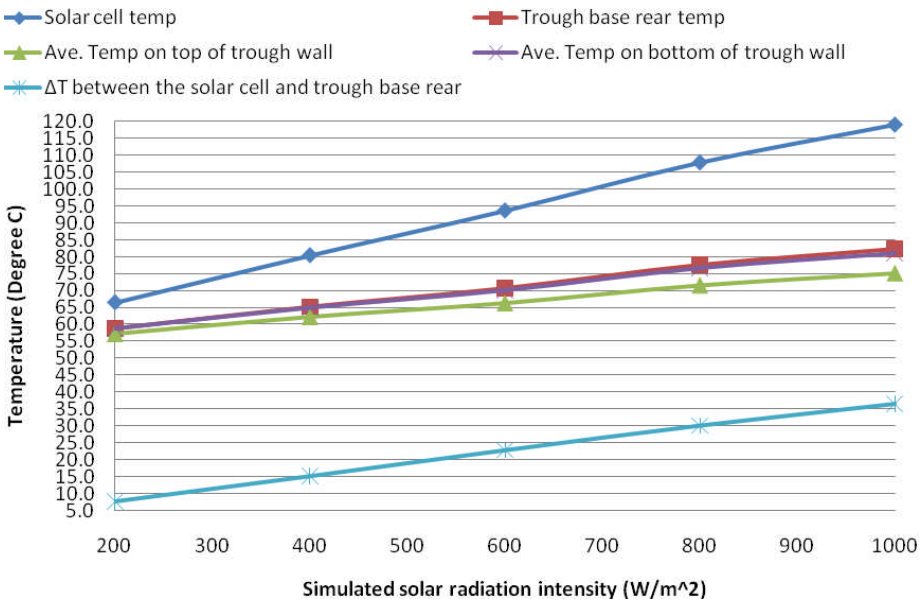

Figure 6.18 The measured temperatures of the FPVC system for selected solar radiation intensities, and an ambient air temperature of 50°C

The temperature difference between the measured temperature of the simulated solar cell, the trough base rear and the ambient air at selected ambient air temperature conditions are presented in figure 6.19. When the system was tested at different ambient air temperatures of 20°C and 50°C with similar simulated solar radiation intensities, the temperature

differences between the cell and the ambient air temperatures were similar. It was approximately 70°C at a simulated solar radiation intensity of 1000W/m^2 with an ambient air temperature of 50°C, and was 72°C at the similar radiation intensity level with ambient air temperature of 20°C. They were all 17°C at a solar radiation intensity of 200W/m^2, when the ambient air temperatures were 20°C and 50°C, respectively.

A similar difference was found for the measured temperature difference between the trough base rear and the ambient air temperature, when the system was tested at different ambient air temperature of 20°C and 50°C with similar simulated solar radiation intensities.

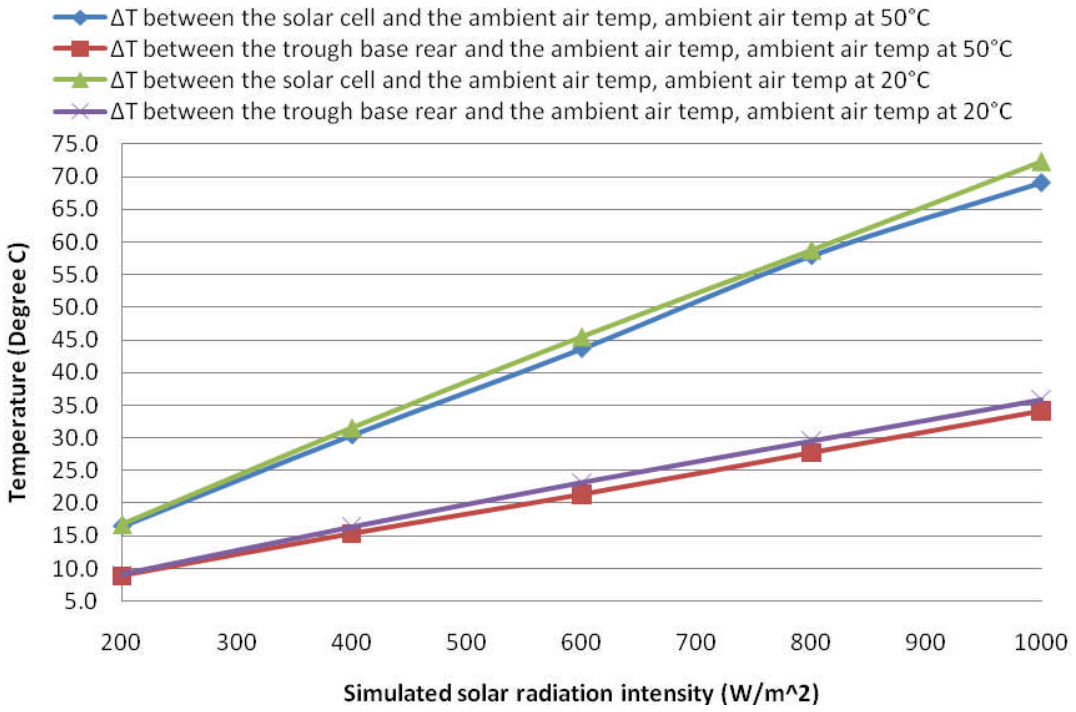

Figure 6.19 The measured temperatures difference between the solar cell, the trough base rear in FPVC system and the ambient air temperature, with different experimental ambient air temperature of 20°C and 50°C

6.6 Thermal characteristics of the FPVC system with an ambient air temperature of 20°C and forced convection

6.6.1 Forced air flow along the long axis of the FPVC system

The thermal characteristics of the FPVC were investigated for simulated solar radiation intensities of 200, 400, 600, 800 and 1000W/m^2 with forced convective cooling by running the heaters in the FPVC system until it reaching steady state while air flowed along the long axis of the PV concentrator with an average air velocity of 2.0m/s as shown in figure 6.20. The finial ambient temperature in the test chamber was 20°C. Temperature readings were taken every 30 seconds.

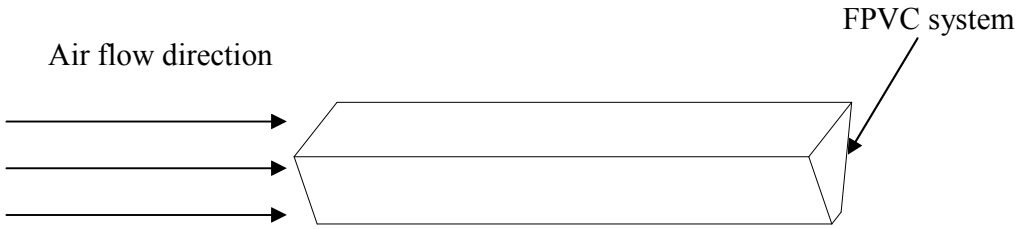

Figure 6.20 Sketch illustrating the air flow direction along the long axis of the FPVC system

The change of temperature in the horizontal, long central axis (X-direction) for the 3rd solar cell and IMS circuit board at solar radiation intensities of 200, 400, 600, 800 and 1000W/m^2 are presented in figure 6.21. The measured temperature for the solar cell, the FPVC trough base rear, the bottom and the top of the FPVC trough wall and the temperature difference between the solar cell and the trough base rear are plotted in figure 6.22. From figure 6.21 and 6.22, it can be seen that when the FPVC system was tested at an ambient air temperature of 20°C under 2.0m/s forced air flow along the long axis of the

FPVC system, the FPVC system demonstrated similar thermal behaviour when compared to that at 20°C ambient air temperature with natural convective cooling only. However, the simulated solar cell temperatures were lower. The area around the cell has higher temperatures than any other part of the IMS board. Conductive and convective heat transfer again dominates the heat transfer for the FPVC system, due to the linearity of the temperature for the simulated solar cell increase with input power. The temperature difference between the solar cell and the trough base rear is significant. When the simulated solar radiation is 1000W/m^2, the temperatures of similar distances from the solar cells are shown in table 6.2

Distance from the No. Solar cell	X=-76.4	X=-23.6	X=23.6	X=76.4
Temperature (°C)	50.6	52.3	54.2	54.5

Table 6.2 Measured temperatures around the simulated No.3 solar cell at simulated solar radiation intensity of 1000W/m^2

From table 6.2, it can be seen that the temperatures at the +X side on the IMS circuit board are higher those at the -X side at the same distances from the No.3 solar cell, this is due to the air flow direction being from -X to +X. A similar characteristic behaviour is found at solar radiation intensities of 200, 400, 600 and 800W/m2, with temperature higher at the +X side than at the –X side at the same distances from the No.3 solar cell.

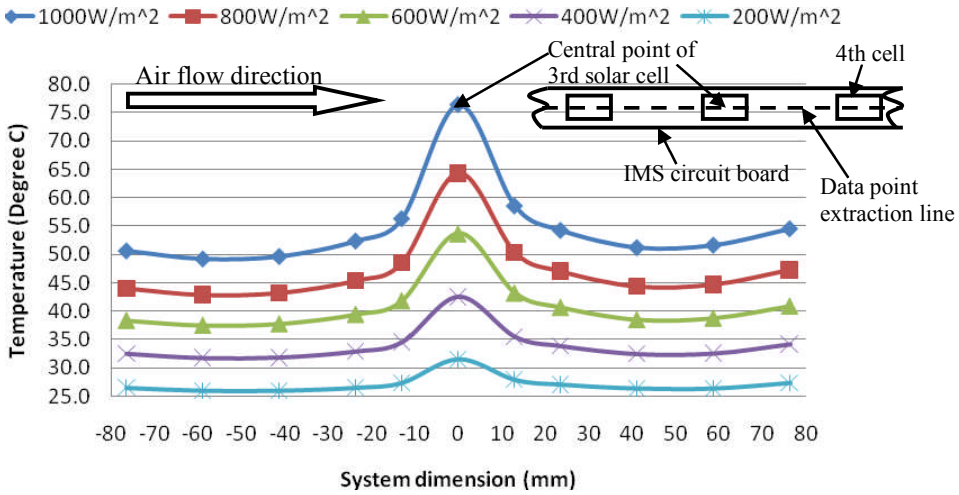

Figure 6.21 Temperature distribution in the horizontal long central axis (X-direction) for the 3rd solar cell and the IMS circuit board at simulated solar radiation intensities of 200, 400, 600, 800 and 1000W/m^2, and an ambient temperature of 20°C with forced convection along the long axis of the FPVC system.

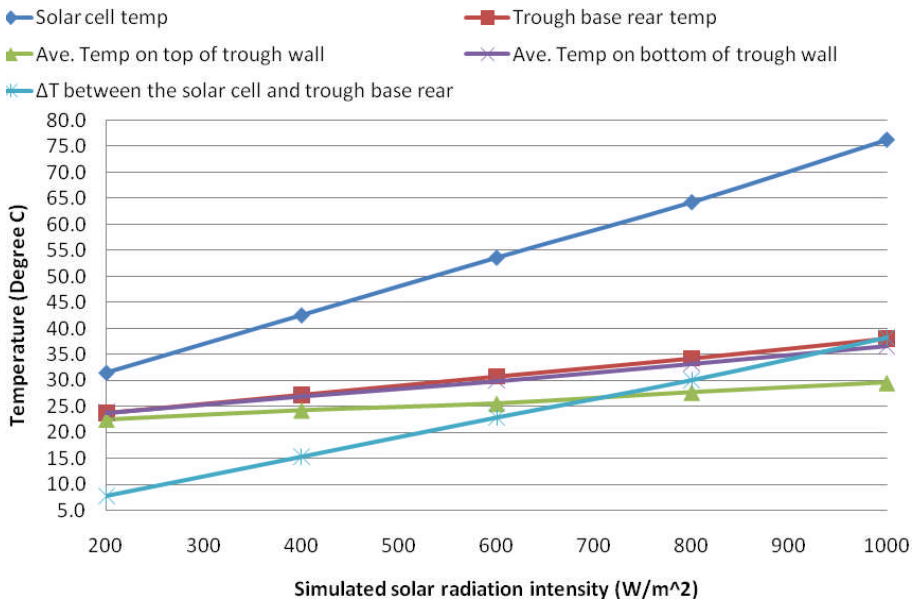

Figure 6.22 The measured temperatures of the FPVC system for selected solar radiation intensities and an ambient air temperature of 20°C with forced convection along the long axis of the FPVC system.

6.6.2 Air flow over the cross section of the FPVC

The thermal characteristics of the FPVC were investigated for forced convection with the air flow over the cross section of the FPVC system. For the experimental characterisation, similar experimental conditions to those for air flow along the long axis of the FPVC system were used. Simulated solar radiation intensities used were 200, 400, 600, 800 and 1000W/m^2, and an air velocity of 2.0m/s. A schematic diagram illustrating the air flow direction across the FPVC system is shown in figure 6.23,

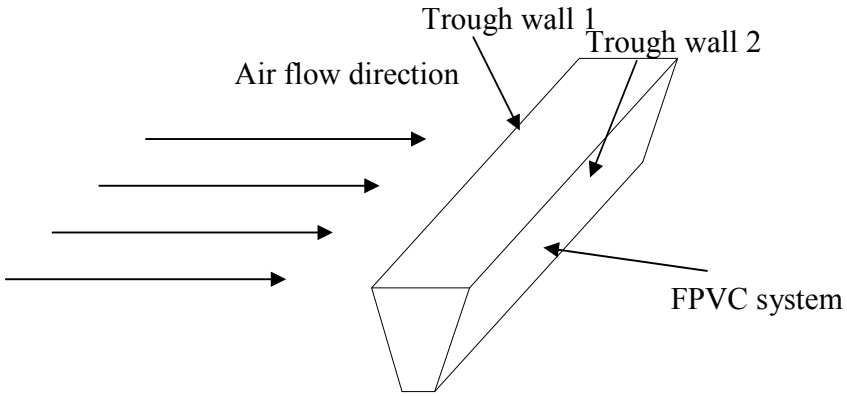

Figure 6.23 Sketch of the air flow direction along the cross section of the FPVC

The change of temperature in the horizontal long central axis (X-direction) for the 3rd solar cell and IMS circuit board at solar radiation intensities of 200, 400, 600, 800 and 1000W/m^2 are presented in figure 6.24. From figure 6.24, it can be seen that when the FPVC system was tested at an ambient air temperature of 20°C with 2.0m/s forced air flow over the cross section of the FPVC system, the FPVC system had similar thermal behaviour when compared to that at 20°C ambient air temperature and the natural convective condition, but had the lowest simulated solar cell temperatures compared to any other conditions at a similar simulated solar radiation intensity. The area around the cell has

higher temperatures than any other part of the IMS strips. There are no significant temperature differences on the IMS board when they are over 18mm away from the cells.

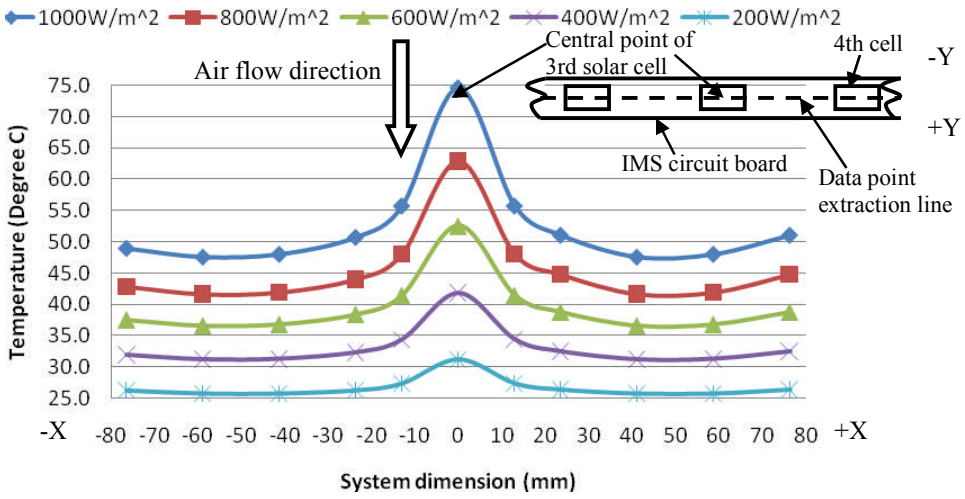

Figure 6.24 Temperature distribution in horizontal long central axis (X-direction) for the 3rd solar cell and IMS circuit board at solar radiation intensities of 200, 400, 600, 800 and 1000W/m^2, and an ambient temperature of 20°C with forced convection over the cross section of the FPVC system.

The change of temperature along the cross section of the FPVC No.3 solar cell and trough wall at solar radiation intensities of 200, 400, 600, 800 and 1000W/m^2 and an ambient temperature of 20°C with forced convection along the cross section of the FPVC system are presented in figure 6.25. From figure 6.25, it can be seen that the temperatures at the +Y side are higher than those at –Y at the same distance from the solar cell, this is due to the air flow from -Y to +Y direction. When the solar radiation intensity is 1000W/m^2, the temperature difference between Y=-7mm and Y=7mm which are near the edges of the IMS circuit board is more than 3°C. The temperature differece is around 3°C between Y=-10mm and 10mm which are at the bottom of the trough walls, are around 3°C between Y=-116mm and 116mm which are at the top of the trough walls. Similar temperature distribution for the FPVC system were also found at other simulated solar radiation intensities.

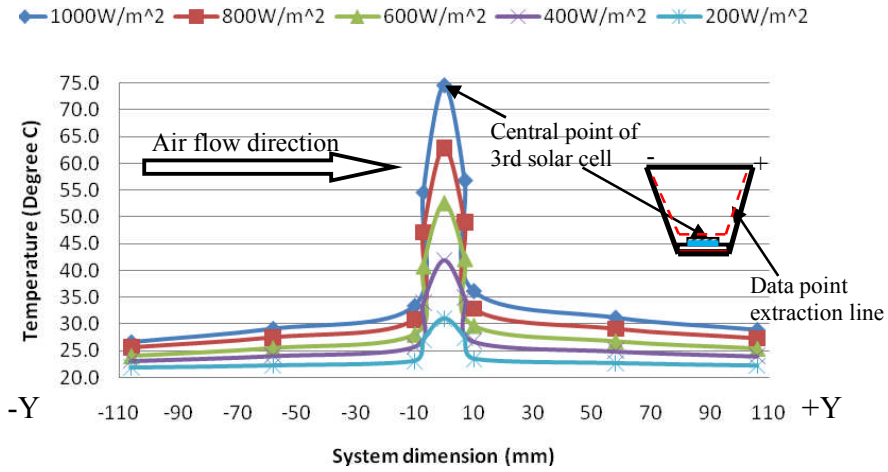

Figure 6.25 Temperature distribution along the cross section for the FPVC system 3rd solar cell and trough walls at solar radiation intensities of 200, 400, 600, 800 and 1000W/m^2, and an ambient temperature of 20°C with forced convection over the cross section of the FPVC system.

The measured temperature of the solar cell, FPVC trough base rear, the bottom and the top of the FPVC trough wall and the temperature difference between the solar cell and the trough base rear are plotted in figure 6.26. A significant temperature difference is also seen between the solar cell and the trough base rear.

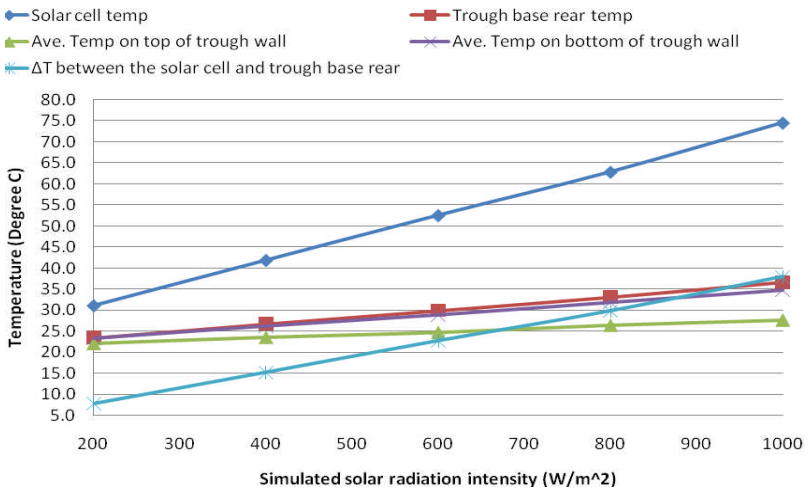

Figure 6.26 The measured temperatures for the FPVC system at selected solar radiations, and an ambient air temperature of 20°C under forced convection over cross section of the FPVC system

6.6.3 Discussion

The measured temperatures of the No.3 solar cell and the FPVC trough base rear at selected solar radiation and an ambient air temperature of 20°C under natural convection and forced convection are plotted in figure 6.27. The temperature difference between the No.3 solar cell and the trough base rear are presented in figure 6.28. From figures 6.27 and 6.28, it can be seen that the cell temperature is significantly reduced by using forced convection heat transfer when compared to that for natural convection.

At an ambient temperature of 20°C and under the natural convective conditions, the solar cell temperature is higher than that with 2.0m/s air flow over the FPVC system. When the air flows along the long axis of the FPVC trough, the cell temperature is slightly higher than that measured for air flow over the cross section. When the simulated solar radiation intenity is 1000W/m^2, the measured cell temperature was 92.4°C for the natural convection case, and 76.4 and 74.6°C for forced convection with 2.0 m/s air flow along the long axis, and over the cross section of the FPVC, respectively. The temperature of the trough base rear has similar temperature distributions to that of the cell under natural and forced convection. Temperatures are higher for natural convection than that measured for forced convection.

The temperature difference between the cell and trough base rear is similar at the same simulated solar radiation and under natural and forced convective conditions. When the solar radiation is 1000W/m^2, the temperature difference between the cell and the trough base rear is around 38°C, and approximately 8°C at 200W/m^2.

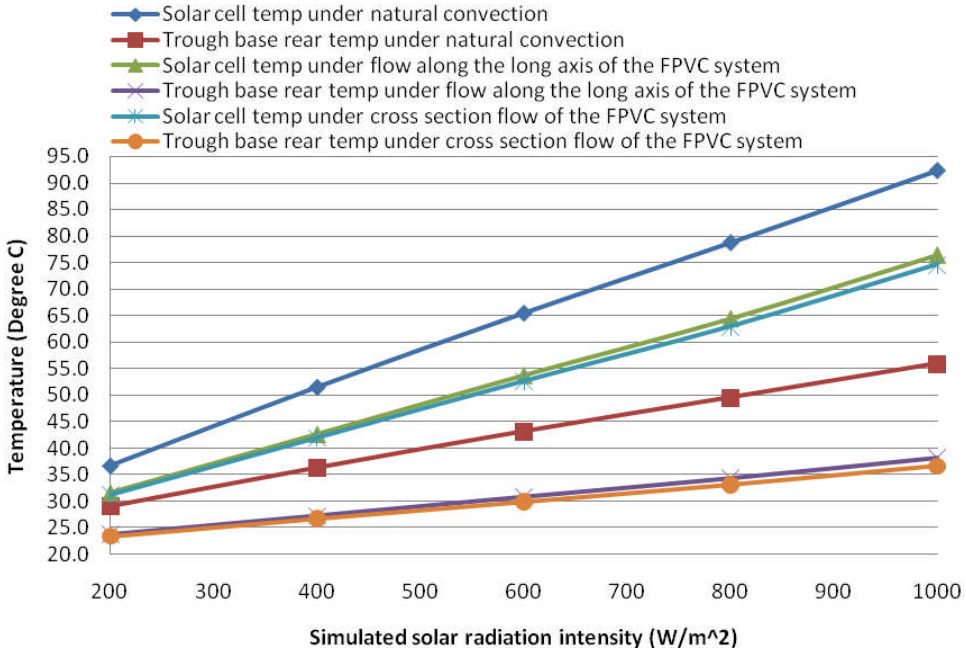

Figure 6.27 The measured temperatures for the FPVC system at selected solar radiation intensities with an ambient air temperature of 20°C for natural convection and forced convections

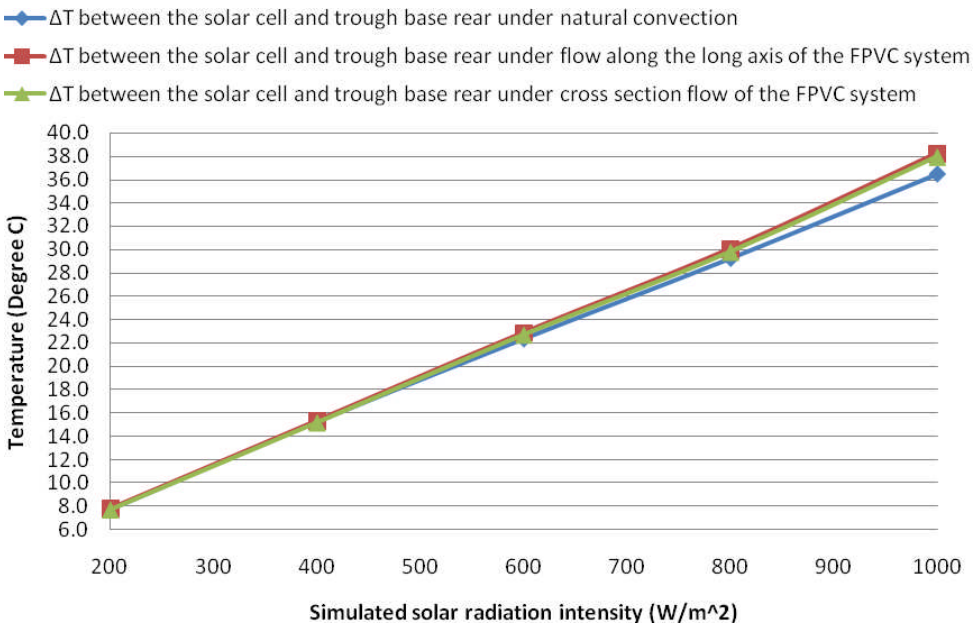

Figure 6.28 The measured temperatures difference between the No.3 solar cell and the trough base rear at selected solar radiation intensities and an ambient air temperature of 20°C for natural convection and forced convections

6.7 Electrical conversion efficiency prediction of the FPVC system

For crystalline silicon cells, the cell efficiency decreases by approximately 5% with a 10°C temperature increase (Anon, 2005a). The electrical conversion efficiency of the FPVC system can be calculated by equation 6.2 (Anon, 2005a).

$$\eta_{PV} = \eta_{PV.STC} \times [1 + 0.005 \times (25 - T_{cell})] \quad (6.2)$$

Where $\eta_{PV.STC}$ is the standard test condition PV electricity conversion efficiency ($\eta_{PV.STC} = 15\%$).

Based on the measured solar cell temperatures in sections 6.4, 6.5 and 6.6, the electrical conversion efficiency of the 3rd cell in FPVC system at simulated solar radiation intensities of 200W/m^2, 400W/m^2, 600W/m^2, 800W/m^2 and 1000W/m^2 for different ambient air temperatures, and both natural and forced convection are calculated using equation 6.2 shown in table 6.3. From table 6.3, it can be seen that in the simulated worst case scenario, when the FPVC system was only under natural convection at simulated solar radiation intensity of 1000W/m^2 and ambient air temperature of 50°C, the solar cell efficiency in the FPVC system was 7.95%. It increased to 9.95%, for an ambient air temperature of 20°C, for a similar simulated solar radiation intensity of 1000W/m^2 and natural convection only. When the ambient air temperature was 20°C, the 3rd solar cell efficiencies were 11.15% and 11.28% under forced air (air velocity of 2m/s) flow along the length of the FPVC and with air flow across the cross section, respectively.

Solar radiation intensities	Electrical conversion efficiency (%)			
	Natural convective heat transfer only		Forced convection (air velocity of 2m/s) and ambient air temperature of 20°C	
	Ambient temperature of 20°C	Ambient temperature of 50°C	Forced air flow along the long axis of the FPVC system	Forced air flow over the cross section of the FPVC system
200W/m^2	14.12	11.89	14.51	14.54
400W/m^2	13.01	10.85	13.68	13.73
600W/m^2	11.96	9.86	12.85	12.93
800W/m^2	10.97	8.79	12.05	12.16
1000W/m^2	9.95	7.95	11.15	11.28

Table 6.3 The electrical conversion efficiency of the No.3 solar cell at simulated solar radiation intensities of 200W/m^2, 400W/m^2, 600W/m^2, 800W/m^2 and 1000W/m^2 for different ambient air temperatures, and both natural and forced convection

6.8 Conclusion

A detailed indoor experimental characterisation of a 0.6 mm thick aluminium trough wall Fresnel PV concentrator (FPVC) with a concentration ratio of 100 was undertaken at different simulated solar radiation intensities, different ambient temperatures, natural and forced convective heat transfer conditions. The following conclusions can be drawn,

- The area around the cell had significantly higher temperatures than any other part of the IMS strips, there were no significant temperature differences measured on the IMS board when they were over 18mm away from the cells for all experimental conditions.
- The solar cell temperature linearly increased with the increase of the simulated solar radiation from 200W/m^2 to 1000W/m^2 in all experimental tests. Due to the long wave radiative heat transfer relating to T^4, conductive and convective heat transfers dominated the heat transfer in and from the FPVC system.
- The temperature differences between the solar cell and the ambient air temperatures were similar for system tested at different ambient air temperature conditions.

- The temperature difference between the solar cell and the trough base rear was significant compared to the distance between them, and possibly may be due to the high thermal resistance between the IMS board and the trough base. They were almost the same at similar solar radiation intensities for both natural and forced air flow condition. When the solar radiation was 1000W/m^2, the temperature difference between the solar cell and the trough base rear was around 38°C, and approximately 8°C at 200W/m^2.
- Under forced convection, the solar cell temperature was significantly reduced compared to that for similar solar radiation intensities and natural convective conditions.
- There was no significant temperature difference between the No.3 solar cell, when tested at similar solar radiation intensities and ambient air temperatures under air flow along the long axis of the FPVC system and with air flow across the cross section.
- In the simulated worst case scenario, when the FPVC system was tested for a simulated solar radiation intensity of 1000W/m^2, ambient air temperature of 50°C and natural convection only, the predicted solar cell efficiency in the FPVC system was 7.95%.
- In order to increase the solar to electrical conversion efficiency of the FPVC systems, the FPVC systems should be installed at the place with frequent wind flow.

Chapter 7 Conclusions and recommendations for further work

7.1 Conclusions

Optical concentrator systems that increase the solar radiation intensity on the PV system may reduce the system cost, however temperature control becomes more important. A two-dimension ray trace technique has been used to predict the optical performance of the Asymmetrical Compound Parabolic Photovoltaic Concentrator (ACPPVC) systems. Extensive indoor experiments used to investigate the thermal behaviour and the I-V characterisations of a truncated Asymmetrical Compound Parabolic Photovoltaic Concentrator with acceptance-half angles of 0° and 55° (ACPPVC-55) and its non-concentrating counterpart flat PV system have been undertaken using a developed highly collimated solar simulator. The feasibility of utilising PCMs integrated into the ACPPVC-55 to minimise the PV cells' temperature rise and store thermal energy in the PCM for potential use has also been studied. The thermal behaviour of a 0.6 mm thick aluminium trough wall Fresnel lens PV concentrator (FPVC) with a concentration ratio of 100 have been conducted at different simulated solar radiation intensities, different ambient temperatures, with both natural and forced convective heat transfer conditions.

7.1.1 Conclusions from the design and manufacture of the solar simulator

A suitable design and fabrication method was developed to produce a highly collimated large illumination area solar simulator. The parabolic reflectors used in the solar simulator provided good collimation output for the solar simulator, and the designed graduated reflective coated secondary reflector in the solar simulator improved the irradiation output uniformity. The selected SQP-HLA660 Xenon long arc lamp had a spectrum close to the solar spectrum at AM1.5, which is suitable for the PV standard characterisation. The developed cooling system provided effective lamp cooling.

The measured output beam uniformity for the designed solar simulator was within ±13% deviation on a dimension of 60cm wide and 80cm long test plane. The measured collimation angles were all 0° in the vertical directions and at maximum ±8° along the horizontal direction. The designed solar simulator, which is close to the solar simulator performance Class C, is suitable for assisting the indoor PV experimental characterisations.

7.1.2 Conclusions from the optical performance analysis and predictions of ACPPVC system

A two-dimension ray trace analysis to predict the optical performance for three ACPPVC systems was undertaken. The systems studied were an ACPPVC-50 system with acceptance-half angles of 0° and 50°, an ACPPVC-55 system with acceptance-half angles of 0° and 55°, and an ACPPVC-60 system with acceptance-half angles of 0° and 60°. The PV absorber widths in all cases were 0.125m.

The predictions indicated that the angular acceptance was 1 within the range of incidence angles between the original acceptance-half angles for the untruncated and truncated systems. Increased truncation leads to increased angular acceptance with reduced maximum geometric concentration. The highest optical efficiency predicted was 88.67% for all ACPPVC systems. The ACPPVC-60 had the greatest range of angular acceptance for solar incidence angles between 0° and 90°, due to the designed highest acceptance-half angle of 60° in the three selected ACPPVC systems.

The solar concentrations were non-uniformly distribution on the PV cell. Predicted peak solar concentrations of higher than 5 were found on the PV for the untruncated and

truncated ACPPVC systems at selected solar incidence angles. The peak solar concentration occurring on the PV cells decreased with decreasing system geometric concentration ratio.

It was concluded that the truncated ACPPVC-55 system with a geometric concentration ratio of 2.0 was more suitable for the UK climate compared to the other ACPPVC systems simulated, due to the range of angular acceptance.

7.1.3 Conclusions from the experimental characterisation of low concentration ratio building integrated PV concentrators

Indoor experimental characterisations were undertaken for three different PV systems: truncated ACPPVC-55, truncated ACPPVC-55/ PCM and their non-concentrating counterpart flat PV system, at different solar radiation intensities and solar incidence angles.

From the experimental results, it was concluded that the incident energy is non-uniformly distributed along the width of the solar cell surface for the truncated ACPPVC-55 system, this is due to a combination of the direct radiation and radiation reflected from reflectors onto the PV cells. The electrical output from the ACPPVC-55 was approximately 1.8 of that of a non-concentrating PV system with similar PV cells area. The electrical conversion efficiency for the ACPPVC-55 system was further increased, when RT27 PCM was incorporated to its rear. The stored thermal energy in the PCM can be used for potential building application. For solar incident radiation of 69W/m^2, an 88% increase in maximum power was observed for the ACPPVC-55 system compared with its non-concentrating counterpart. Only a 43% increase in maximum power was obtained at a solar incident

radiation intensity of 280W/m^2, this was possibly due to an additional 30.3% ohmic loss in the external cable, a 1.5% power loss caused by the higher solar cell temperature and other losses including power loss caused by the resistance in the interconnections between each individual solar cell and power loss caused by the non-uniform incident solar radiation for the ACPPVC-55 system.

For the ACPPVC-55/PCM system, it was observed the solar cell temperature was significantly reduced by using a PCM. For an incident solar radiation intensity of 280W/m^2, the average solar cell temperature of the ACPPVC-55 system was reduced by 7°C for approximately 10 hours when using the PCM RT27. The electrical conversion efficiency of the ACPPVC-55 system increased by approximately 5%. For an incident solar radiation intensity of 672W/m^2, the average solar cell temperature of the ACPPVC-55 system was reduced by 18°C for approximately 4 hours when using the PCM RT27. The predicted electrical conversion efficiency of the ACPPVC-55 system increased by around 10%.

7.1.4 Conclusions from the experimental characterisation of a high concentration ratio Fresnel lens PV Concentrator (FPVC)

Extensive indoor experimental characterisation of the heat loss from a 0.6 mm thick aluminium trough wall Fresnel PV concentrator (FPVC) with a concentration ratio of 100 supplied by Whitfield Solar Company were investigated for a range of simulated solar radiation intensities, different ambient air temperatures, and both natural and forced convection.

During the indoor experimental characterisation, the Fresnel lens PV Concentrator (FPVC) was tested inside a heated insulated enclosure which was used to maintain a constant environmental temperature. Ten Electrical Resistance Heaters (ERHs), which had similar dimensions to the solar cells used in the FPVC system replaced the solar cells, and were used to simulate the heat generated at the solar cells in the FPVC system when exposed to solar radiation.

From the experimental results, it was concluded that the simulated solar cell temperature linearly increased with increase in simulated solar radiation intensity from 200W/m^2 to 1000W/m^2 in all experimental tests. Due to long wave radiative heat transfer relating to T^4, conductive and convective heat transfers dominated the heat transfer in the FPVC system. The area around the cell had higher temperatures than any other part of the IMS board, there were no significant temperature differences measured on the IMS board when they were over 18mm away from the cells for all experimental conditions.

The temperature differences between the solar cell and the ambient air temperatures were similar for systems tested at different ambient air temperature conditions. The temperature difference between the solar cell and the trough base rear was significant compared to the distance between them, and possibly may be due to the high thermal resistance between the IMS board and the trough base. They were almost the same at similar solar radiation intensities for both natural and forced air flow conditions. When the solar radiation was 1000W/m^2, the temperature difference between the solar cell and the trough base rear was around 38°C, and approximately 8°C at 200W/m^2. Under forced convection, the solar cell temperature was significantly reduced compared to that for similar solar radiation

intensities and natural convective conditions. There was no significant temperature difference between the No.3 solar cell, when tested at similar solar radiation intensities and ambient air temperatures under air flow along the long axis of the FPVC system and with air flow across the cross section. In order to increase the solar to electrical conversion efficiency of the FPVC systems, in the future, the FPVC systems should be installed at the place with frequent wind flow.

In the simulated worst case scenario, when the FPVC system was tested at the simulated solar radiation intensity of 1000W/m^2, ambient air temperature of 50°C and natural convection only, the predicted solar cell efficiency in the FPVC system was 7.95%.

7.2 Recommendation for future work

The following recommendations are made for future research:

- The measured radiation output for the designed solar simulator was lower than that predicted. The measured output beam uniformity was within ±13% deviation on the test plane. This is due to the reflectivity of reflector 3 (section 4.2, figure 4.1) being significantly reduced at the solar incidence angle of 45°, compared to when reflecting solar radiation incident perpendicular to its surface, and thus, the reflectivity for the secondary reflector at solar incidence angles of 45° should be improved through a reliable coating method.
- The radiation output intensity and uniformity for the designed solar simulator could be optimised by using a Miro-Silver 4270 AG reflective material to replace the graduated coated reflector 3 (section 4.2, figure 4.1) to increase the solar simulator radiation output. Simultaneously, a variable transmittance filter would be installed at the aperture

of the solar simulator to modify the flux intensity coming from the Miro-Silver 4270 AG reflective material to achieve a uniform level.

- The measured collimation angles for the designed solar simulator were all 0° in the vertical directions and at maximum ±8° along the horizontal direction on a 600mm by 800mm test plane, this is due to the design of the solar simulator being unable to collimate the output energy in the horizontal plane. A three-dimensional optical mode should be developed in future solar simulator design.
- The Phase Change Material (PCM) RT27 integrated to the rear of the PV panel moderated the temperature rise experienced by the PV and increased solar to electrical conversion efficiency, however, the thermal conductivity of the RT27 was only 0.2 W/m·K, which may be restrict the heat transfer between the solar cell and PCM material. A PCM with higher thermal conductivity than the RT27 or enhanced heat transfer techniques should be investigated and coupled to the PV system to further improve the solar cell temperature rise in future work.
- The ACPPVC-55/PCM was tested in an indoor experimental environment with three different incident solar radiation intensities. The long term dynamic performance characterises of the ACPPVC-55/PCM should be investigated under outdoor conditions to obtain better understanding of the system durability and operational characteristics. This would be best accomplished by long term outdoor monitoring programme of performance of a building façade integrated ACPPVC-55/PCM system.
- An ACPPVC-55/PCM system coupled with BP Saturn laser grooved buried contact solar cells was studied. Thin film solar cells, III-V solar cells and other solar cells with different temperature and electrical conversion efficiency relationships should be used in the ACPPVC-55/PCM system for future experimental analysis. This would enable

which solar cells that are most suitable for the ACPPVC-55/PCM system to be determined and enhance the overall efficiency of the system.

- A time dependent two-dimensional heat transfer model with mixed conduction, convection and radiation components should be developed and validated for the ACPPVC-55/PCM system to completely understand the thermal performance of the system. The thermal performance results from the simulations could be used to both improve the design of the system and identify design limitations.
- The temperature difference between the solar cell and the trough base rear for the FPVC system was significant compared to the distance between them, and possibly may be due to the high thermal resistance between the IMS board and the trough base. A cheap thermal conductive material should be installed between the IMS board and the trough base of the FPVC system to reduce the thermal resistance and thus moderate the temperature rise of the solar cell in the FPVC system. Techniques to enhance the heat transfer should be developed and coupled to the FPVC system to further decrease the rise in solar cell temperature.

Appendix A

Solar simulators using a parabolic reflector provide good collimation. However, their output flux distribution is non-uniform along the width of the test plane, a graduated coated secondary reflector was used in the solar simulator to improve the solar simulator output uniformity (detailed discussion are presented in Chapter 4). In the following sections, other designs of solar simulator in which the design of the parabolic reflectors is optimised to obtain good collimation and flux output within ±2% deviation are described.

A cross sectional view of a solar simulator using parabolic reflector and the paths of rays generated by the light source are shown in figure A.1. The focal length of the reflector is 10cm and the light source is located at the focal point of the parabolic reflector. From light trace shown in figure A.1, the energy flux intensity of the output light on the test plane can be obtained and calculated by equation A.1.

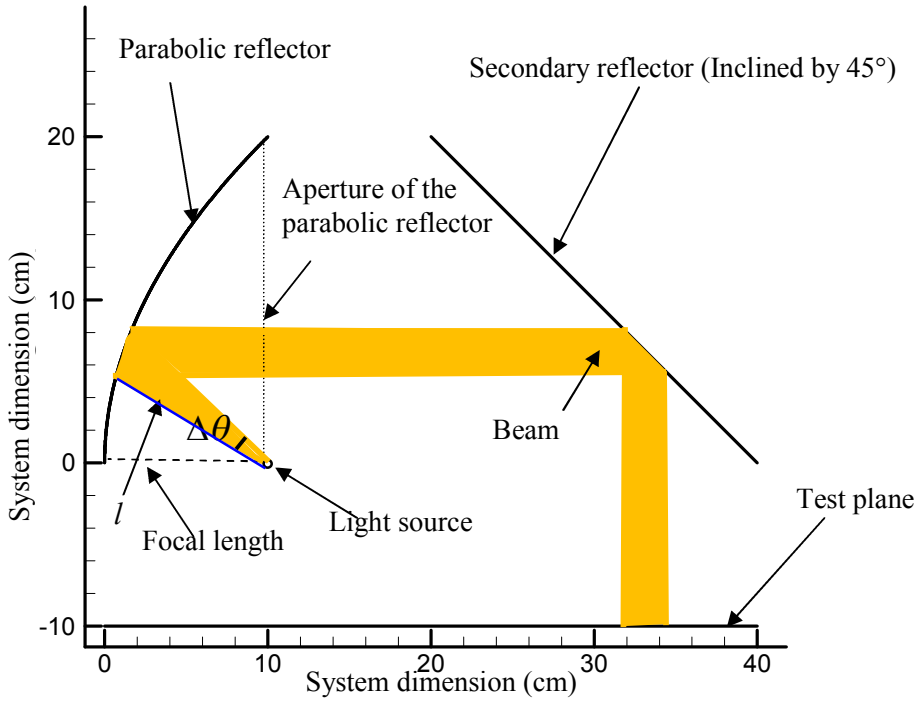

Figure A.1 A 2D side view of the solar simulator using parabolic reflector

$$I_{beam} = \frac{\frac{\Delta\theta}{360} I_{lamp}}{l \times \Delta\theta} = \frac{1}{l \cdot 360} I_{lamp} \qquad \text{(A.1)}$$

Where $\Delta\theta$ is a subtended angle, l is the distance between the focal point and the parabola and $l \times \Delta\theta$ is the parabolic arc length.

From figure A.1 and equation A.1, it can be seen that the energy flux intensity for the output beam of light depends on the distance between the light source and the parabolic reflector, subtended angle and the radiation intensity output of the lamp. For the same subtended angle, the irradiance of light from the light source is inversely proportional to the distance from the source. Therefore, if a same dimension of a section of the parabolic reflector twice as far away from the light source, it receives only half the flux intensity.

Thus to maintain flux intensity output within ±2% deviation and also maintain good collimation for a solar simulator using a parabolic reflector, the distances between components and the focal point (light source) of the parabolic reflector should be within a deviation of ±2%. A solar simulator using parabolic reflectors sections was designed as shown in figure A.2. The light source is located at the focal point for all the parabolic reflector sections and the distances between the various parabolic reflectors and the light source are within a deviation of ±2% of a reference focal length 10cm.

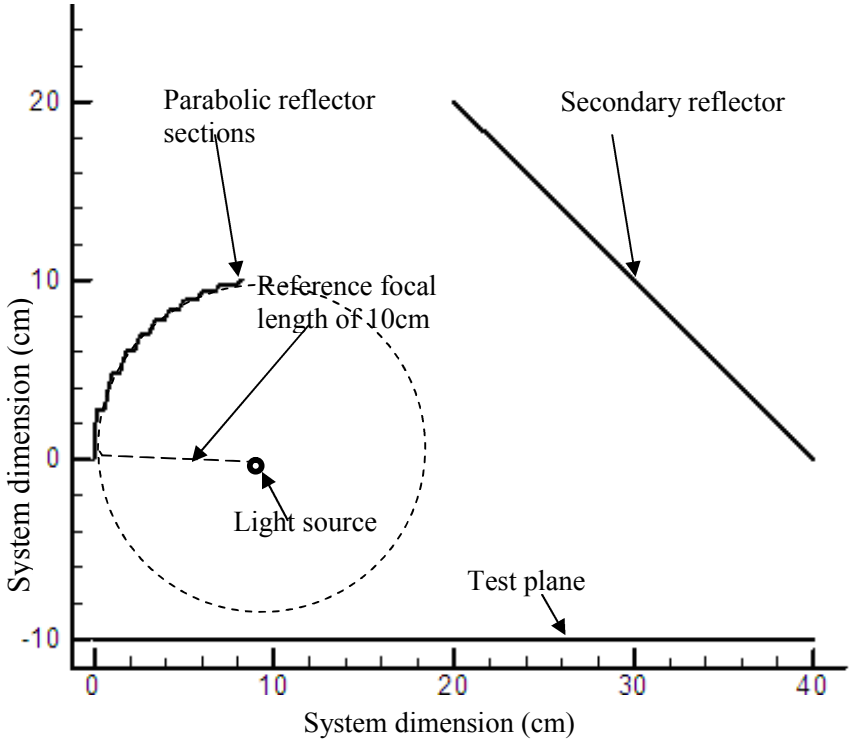

Figure A.2 A 2D side view of the optimised solar simulator using parabolic reflector sections

Ray trace techniques have been used to predict the optical performance of the solar simulator. All rays were assumed specular in the ray trace model, each ray carried the same amount of energy with the light output angle (θ) was considered from the horizontal. A ray trace diagram for the optimised solar simulator system for light output angels from 0° to 85° at 1° interval are shown in figure A.3. The output energy flux for the optimised solar simulator was predicted by tracing 360,000 rays in the simulation as shown in figure A.4. From figures A.3 and A. 4, it can be seen that the rays are uniformly distributed along the width of the test plane. The predicted output beam uniformity for the solar simulator using parabolic reflector sections is within ±2%.

A suitable design was developed to produce a highly collimated large illumination area solar simulator. The parabolic reflectors provide good collimation for the solar radiation

output, and the designed sectional parabolic reflectors improve the irradiation output uniformity.

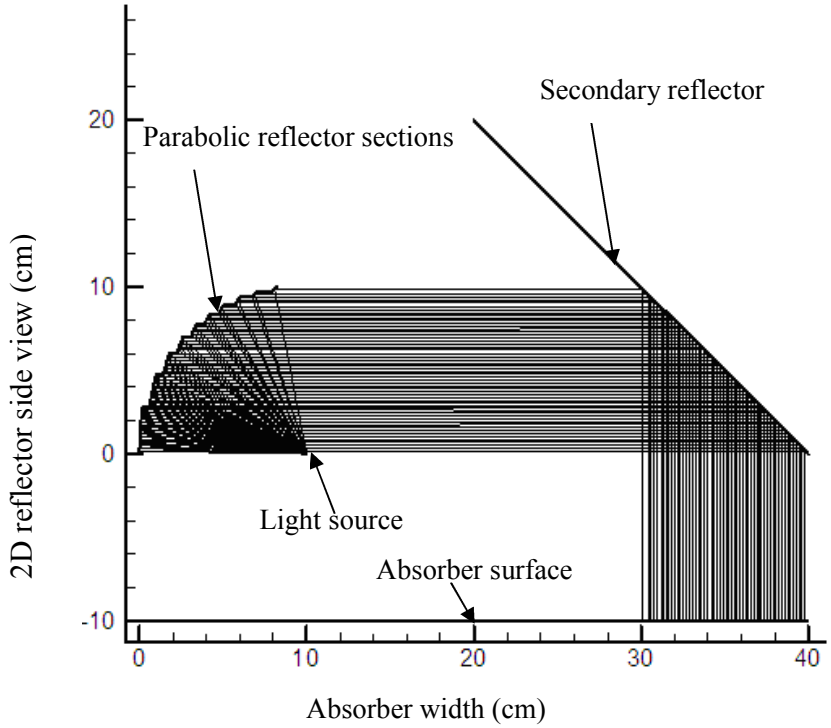

Figure A.3 A 2D cross section ray trace diagram of the optimised solar simulator, 86 rays from 0° to 85° are illustrated

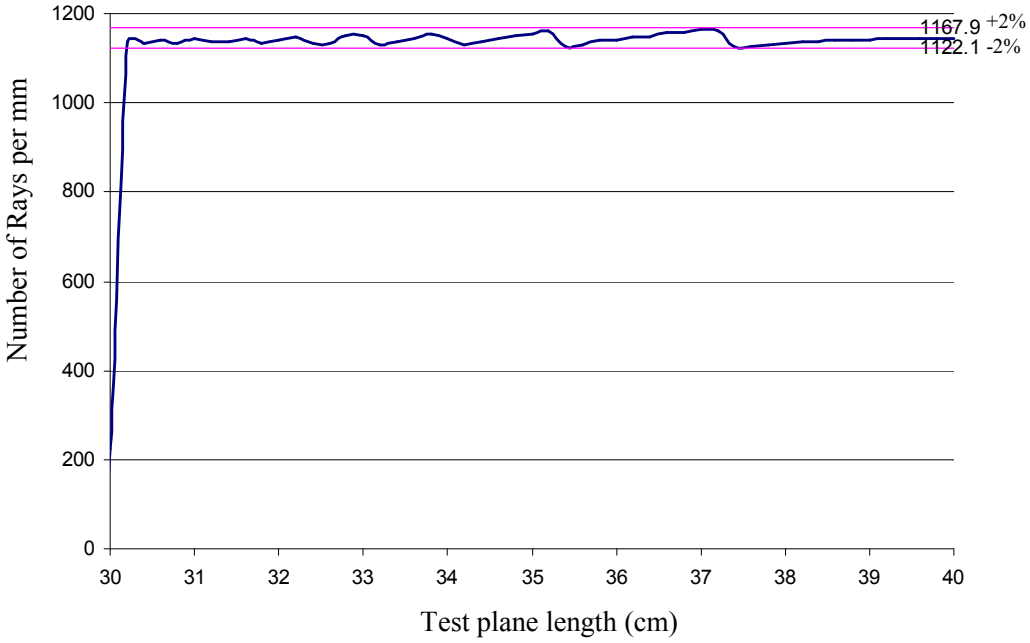

Figure A.4 Output beam uniformity for the optimised solar simulator

Appendix B

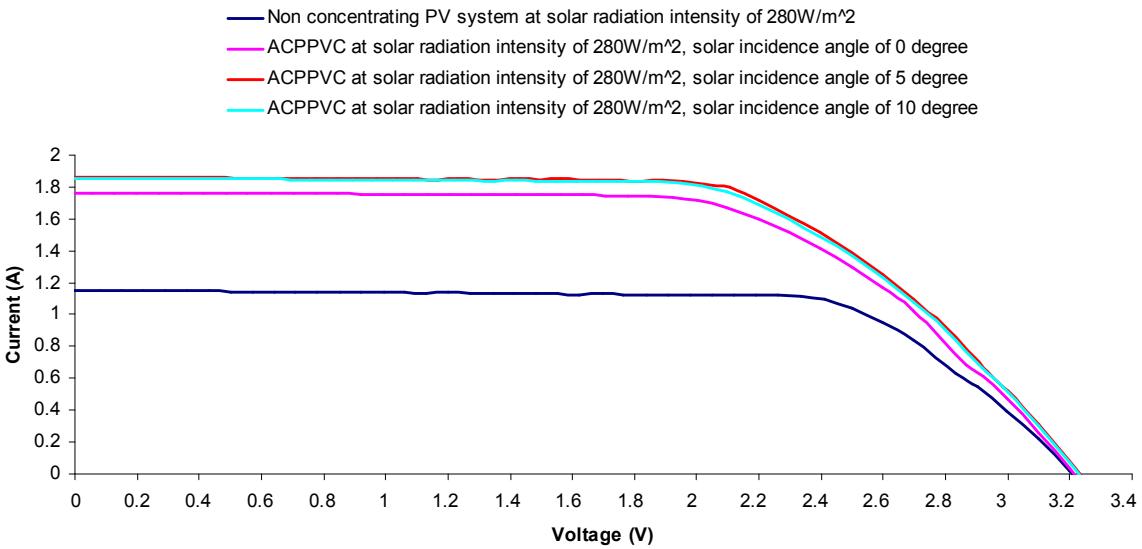

Figure B.1 Measured I-V characteristics of ACPPVC-55 system at solar radiation intensity of 280 W/m^2 and solar radiation incidence angles of 0°, 5° and 10°.

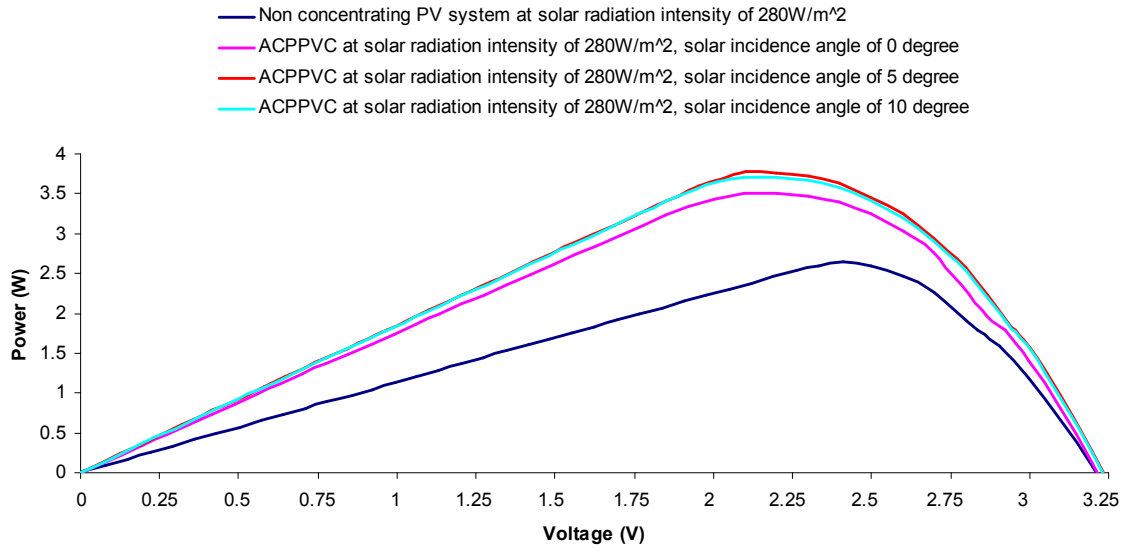

Figure B.2 Variation of instantaneous power with sweep voltage for non-concentrating PV system and the ACPPVC-55 system at incident solar radiation intensity of 280W/m^2

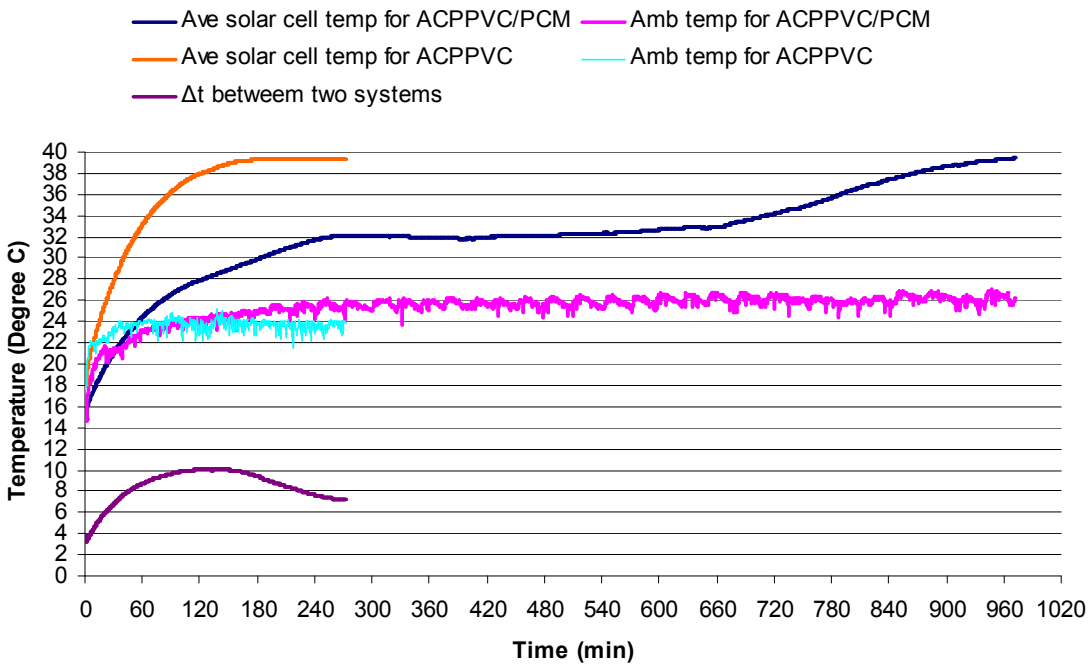

Figure B.3 The measured average solar cell temperature with time for the ACPPVC and ACPPVC/PCM system for incident solar radiation intensity of 280W/m^2 and solar radiation incidence angle of 5°

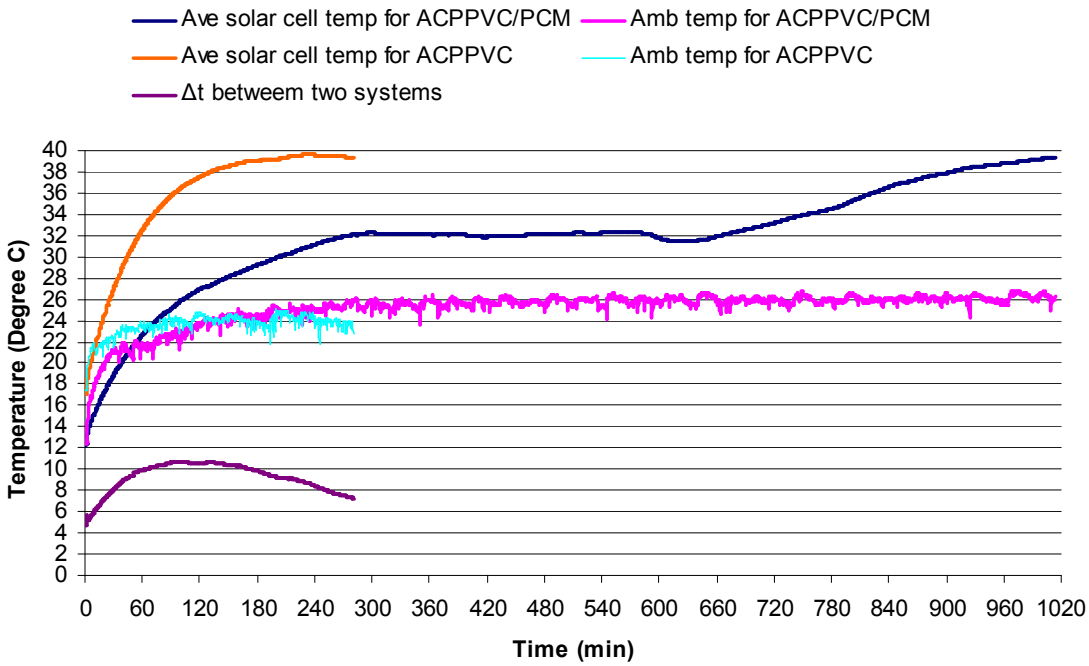

Figure B.4 The measured average solar cell temperature with time for the ACPPVC and ACPPVC/PCM system for incident solar radiation intensity of 280W/m^2 and solar radiation incidence angle of 10°

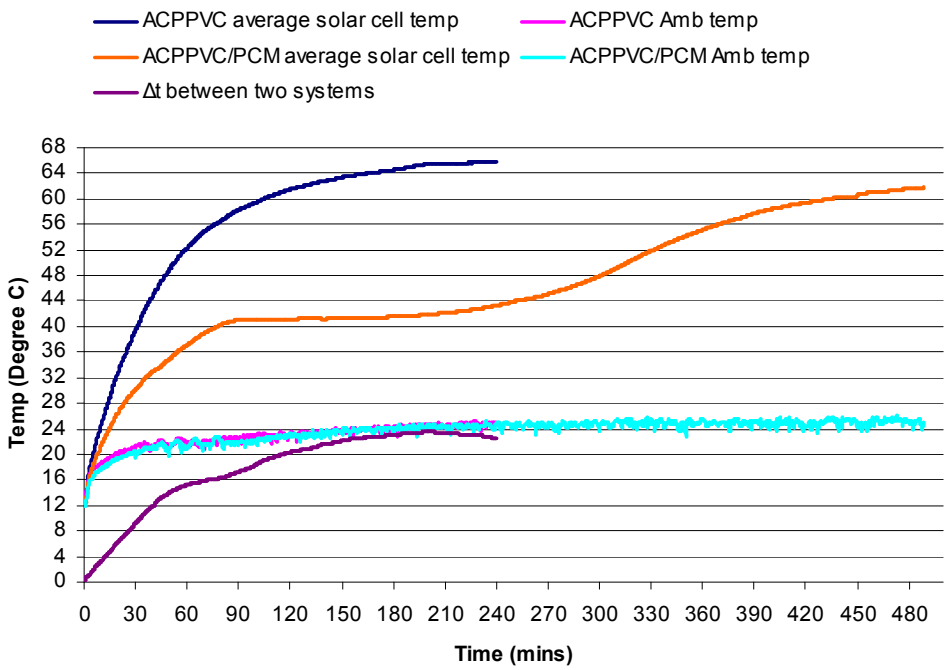

Figure B.5 Measured average solar cell temperatures with time for the ACPPVC and ACPPVC/PCM system with incident solar radiation 672W/m^2 and incidence angle of 5°

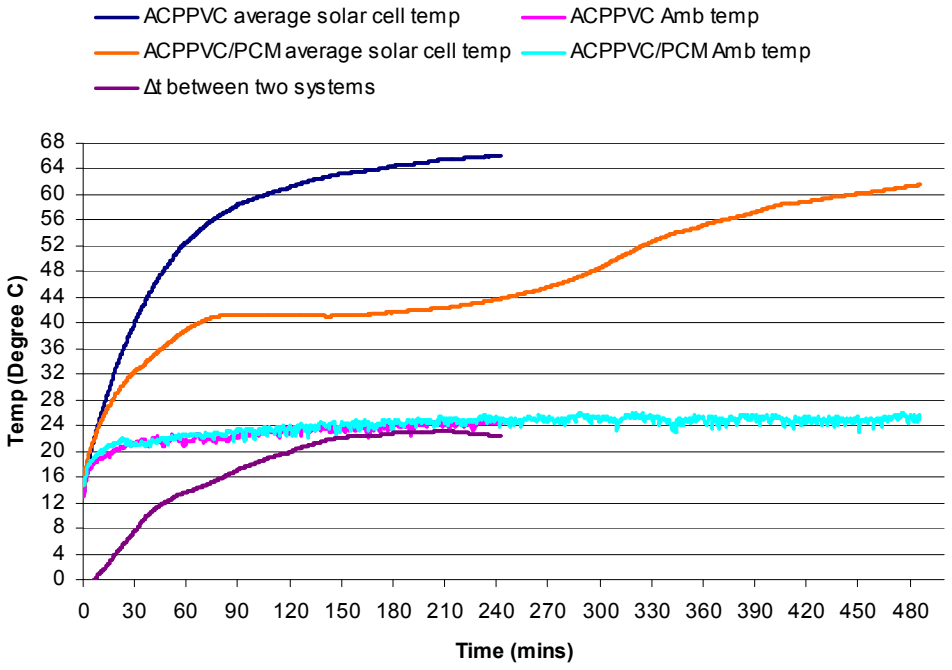

Figure B.6 Measured average solar cell temperatures with time for the ACPPVC and ACPPVC/PCM system with incident solar radiation 672W/m^2 and incidence angle of 10°

Reference

Abhat, A. (1981) Low temperature latent heat thermal energy storage: heat storage materials, Solar Energy, Vol.4, pp. 313–332.

Agarwal, R. K.. and Garg, H. P. (1994) Study of a photovoltaic-thermal system-thermosyphonic solar water heater combined with solar cells. Energy Conversion and Management, Vol.35, pp. 605-620.

Andreev, W. M., Grilikhes, V. A., Rumyanstev, V. D. (1997) Photovoltaic Conversion of Concentrated Sunlight. John Wiley & Sons Ltd. Chichester, West Sussex, UK.

Andreev, V. M., Grilikhes, V. A., Khvostikov, V. P., Khvostikova, O.A., Rumyantsev, V. D., Sadchikov, N. A. and Shvarts, M. Z. (2004) Concentrator PV modules and solar cells for TPV systems. Solar Energy Materials & Solar cells, Vol.84, pp 3-17.

Anon, (2005a) Planning and Installing Photovoltaic Systems: A guide for installers, architects and engineers by the German Solar Energy Society (DGS). James & James, London, U.K.

Anon (2005b) RS Data sheet 3M ™ DP-460 Epoxy Adhesive. RS Components Ltd. U.K.

Anon (2006a) Laser silver mirror film, Acrosolar Company, California, USA.

Anon (2006b) Miro-Sun, ALANOD Aluminium, Veredlung GmbH & Co. KG. Germany

Anon (2006c) Solar Cell, BP solar, Madrid, Spain.

Anon (2006d) Sylgard-184 Coating, Dow Corning Corporation. Midland. MI. U.S

Anon (2006e) RT27 phase change material, RubiTherm, Berlin, Germany

Anon (2007) Sn-Pb-Ag low melting point solder, RS Components Ltd, Northants, UK

Anon (2008a) Copper PV ribbons, Ulbrich Company, Hamburg, Germany.

Anon(2008b) RS Data sheet LOCTITE® 315™. RS Components Ltd. U.K.

Anon (2008c) Weather underground, http://www.wunderground.com/global/MI.html

Anon (2008d) International Electro-technical Commission, IEC Standard 60904-9 solar simulator requirements. http://www.iec.ch.

Anon (2008e) Data sheet SQP-HLA660, Superior Quartz Products, INC, USA

Al-Baali, A. A. (1986) Improving the power of a solar panel by cooling and light concentrating. Solar & Wind Technology, Vol.3, pp. 241-245.

Aste, N., Beccali, M. and Chiesa, G. (2002) Experimental evaluation of the performance of a proto-type hybrid solar Photovoltaic-thermal (PV/T) Air collector for the integration in sloped roof. Conference “EPIC 2002 AIVC”, Lyon, France, 23-26 October.

Ayoub, J. Dignard-bailey, I. and Filion, A. (2001) Photovoltaics for buildings: Opportunities for Canada. Catalogue No: M39-76/2001E, Government of Canada, NRCAN/CANMET Energy Technology Centre-Varennes.

Bakker, M., Elswijk, M. J., Zondag, H. A., Ottenbros, M. T. N., van Helden, W.G.J. (2004) Outdoor Performance of Uncovered PV/ Thermal Panels. Paris: 19th European PV Solar Energy Conference and Exhibition 7-11 June

Bansal, N. K., Mathur, J., Mathurb, S. and Jain M. (2005) Modeling of window-sized solar chimneys for ventilation. Building and Environment, Vol.40, pp.1302–1308

Baum, H. P. and Gordon, J. M. (1984) Technical Note: Geometric Characteristics of ideal non-imaging (CPC) solar collectors with cylindrical absorber. Solar Energy, Vol.33, No.5, pp.455-458

Bhargava, A. K., Garg, H. P. and Agarwal, R. K. (1991) Study of a hybrid solar system-solar air heater combined with solar cells. Energy Conversion and Management, Vol.31, pp. 471-479.

Bickler, D. (1967) The simulation of solar radiation. United States Patent 3334217.

Bloem, J. J. (2008) Evaluation of PV-integrated building application in a well-controlled outdoor test environment. Building and Environment, Vol.43, pp. 205-216.

Bohm, M., Scheer H. C. and Wagemann, H. G. (1985) Solar simulator measurement system for large area solar cells at standard test conditions. Energy conversation and Management, Vol.25, pp. 105-113.

Bouchair, A. (1994) Solar chimney for promoting cooling ventilation in southern Algeria. Building Services Engineering Research & Technology, Vol.15, pp. 81–93

Boyle, Godfrey (2004) Renewable energy, Oxford University Press, Oxford, U.K.

BP (2008) BP statistical review of world energy. www.bp.com/statisticalreview.

Brinkworth, B. J, Cross, B. M., Marshall, R.H. and Yang, H (1997) Thermal regulation of photovoltaic cladding. Solar Energy, Vol.61, pp. 169-178.

Brinkworth, B. J., Marshall, R. H. and Ibarahim, Z. (2000a) A Validated model of naturally ventilated PV cladding. Solar Energy Vol.69, pp. 67-81.

Brinkworth, B. J. (2000b) Estimation of flow and heat transfer for the design of PV cooling ducts. Solar Energy, Vol.69, pp. 413-420.

Brinkworth, B. J. and Sandberg, M. (2006a) Design procedure for cooling ducts to minimise efficiency loss due to temperature rise in PV arrays. Solar Energy, Vol.80, pp. 89-103.

Brinkworth, B. J. (2006b) Optimum depth for PV cooling ducts. Solar Energy, Vol.80, pp. 1131-1134.

Brogren, M., Nostell, P. and Karlsson, B. (2001) Optical efficiency of a PV- Thermal hybrid CPC module for high latitudes. Solar Energy, Vol.69, pp.173-185.

Brogren, M., Karlsson, B., Roos, A. and Wermer, A. (2004a) Analysis of the effects of outdoor and accelerated ageing on the optical properties of reflector materials for solar energy applications. Solar Energy Material and Solar Cells, Vol. 82, pp. 491-515.

Brogren, M. (2004b) Optical efficiency of a low concentrating solar energy systems with parabolic reflectors. PhD Thesis. Uppsala University, Sweden.

Cabeza, L. F., Mehling, H., Hiebler, S. and Ziegler, F. (2002) Heat transfer enhancement in water when used as PCM in thermal energy storage. Applied Thermal Engineering, Vol.22, pp. 1141-1151.

Cooperative Community Energy (2009) http://www.cooperativecommunityenergy.com/t_index.html

Coventry, J. S., Franklin, E. and Blakers, A. (2002a) Thermal and electrical performance of a concentrating PV/ Thermal Collector: results from the ANU CHAPS collector. In Proceeding of ANZSES Solar Energy Conference, Newcastle, Australia.

Coventry, J. S. (2002b) Simulation of a concentrating PV/Thermal collector using TRNSYS. In Proceeding of ANZSES Solar Energy Conference, Newcastle, Australia.

Coventry, J. S. (2005) Performance of a concentrating photovoltaic/ thermal solar collector. Solar Energy, Vol.78, pp. 211-222.

Cross, M.B. (1994) Development, testing and first installations of an integrated solar roof system. Photovoltaic Energy Conversion, Vol.1, pp. 1020-1023.

Duffie, J. A. and Beckman, W. A. (1991) Solar Engineering of Thermal Processes. Wiley & Sons Inc, Hoboken, New Jersey, USA.

Duffie, J. A. and Beckman, W. A. (2006) Solar Engineering of Thermal Processes 3rd Edition. Wiley & Sons Inc, Hoboken, New Jersey, USA.

Eames, P. C. and Norton, B. (1993) Validated, unified model for optics and heat transfer in line-axis concentrating solar energy collectors. Solar Energy, Vol. 50, pp. 339-355.

Ettouney, H., El-Dessouky, H. and Al-Ali, A. (2005) Heat Transfer during Phase Change of Paraffin Wax Stored in Spherical Shells. Solar Energy and Engineering, Vol. 127, pp. 357-368.

Feuermann, D. and Gordon, J. M. (2001) High concentration photovoltaic designs based on miniature parabolic dishes. Solar Energy, Vol.70, pp. 423-430.

Frier, D. and Cable, R. G. (1999) An Overview and Operation Optimisation of the Kramer Junction Solar Electric Generating System. ISES World Congress 1999, Jerusalem Vol.1, pp. 241–246.

Gan, G. H. and Riffat, S. B. (1998) A Numerical Study of Solar Chimney for Natural Ventilation of Buildings with Heat Recovery. Applied Thermal Engineering, Vol.18, pp. 1171-1187.

Gan, G. H. and Riffat, S. B. (2004) CFD modelling of air flow and thermal performance of an atrium integrated with photovoltaics. Building and Environment, Vol.39, pp. 735-748.

Garg, H. P., Shukla, A. R., Madhuri, I., Agnihotri, R. C. and Chakravertty, S. (1985) Development of a Simple Low-Cost Solar Simulator for Indoor Collector Testing. Applied Energy, Vol.21, pp. 43-54.

Garg, H. P. and Agarwal, R. K. and Bhargava A. K. (1991) The effect of plane booster reflectors on the performance of a solar air heater with solar cells suitable for a solar dryer. Energy Convers. Mgmt., Vol.32, pp.543-554.

Garg, H. P. and Agarwal, R. K. (1995) Some aspects of a PV/T collector/forced circulation flat plate solar water heater with solar cells. Energy Conversion and Management, Vol.36, pp. 87-99.

Garg, H. P. and Adhikari, R. S. (1997) Conventional hybrid photovoltaic/ thermal (PV/T) air heating collectors: steady-state simulation. Renewable Energy, Vol.11, pp. 363-385.

Garg, H. P. and Adhikari, R. S. (1998a) Transient simulation of conventional hybrid photovoltaic/thermal(PV/T) air heating collectors. International Journal of Energy Research, Vol.22, pp. 547-562.

Garg, H. P. and Adhikari, R. S. (1998b) Optical design calculations for CPC's. Energy-Int. Journal, Vol. 23, pp. 907-909.

Garg, H. P. and Adhikari, R. S. (1999a) System performance studies on a photovoltaics/ thermal (PV/T) air heating collector. Renewable Energy, Vol. 16, pp. 725-730.

Garg, H. P. and Adhikari, R. S. (1999b) Performance analysis of a hybrid photovoltaic/Thermal (PV/T) collector with integrated CPC troughs. International journal of energy research, Vol.23, pp. 1295-1304.

Gordon, J. (2001) Solar Energy – The State of the Art. James & James Ltd. London, U.K.

Green, M.A., Zhao, J., Wang, A. and Wenham, S.R.(1999) Very high efficiency silicon solar cells-science and technology. IEEE Transactions on Electron Devices, Vol.46, pp. 1940-1947.

Green, M.A. (2000) The future of crystalline silicon solar cells. Progress in Photovoltaics: Research and Applications**,** Vol.8, pp 127–139.

Green, M.A. (2002) Photovoltaic principles. Physica E., Vol.14, pp. 11-17.

Green, M. A., Emery, K., Hisikawa, Y. and Warta, W. (2008) Solar Cell Efficiency Tables (Version 31). Progress in Photovoltaics: Research and Applications, Vol.16, pp. 61-67.

Griffiths, P. W. and Eames, P. C. (2007) Performance of chilled ceiling panels using phase change material slurries as the heat transport medium. Applied Thermal Engineering, Vol.27, pp. 1756-1760.

Hendrie, S. D. (1980) Evaluation of combined Photovoltaic/ Thermal collectors. ISES International Congress and Silver Jubilee, Atlanta, GA.

Henry, C. H. (1980) Limiting efficiencies of ideal single and multiple energy gap terrestrial solar cells. Journal of Applied Physics, Vol.51, pp. 4494-4500.

Hinterberger, H. and Winston, R. (1966) Efficient light coupler for threshold Čerenkov counters. Rev. Sci. Indtr., Vol.37, pp. 1094-1095

Holman, J. P. (1997) Heat transfer 8th edition . London, U.K: McGraw-Hill.

Huang, M. (2002) The application of Computational Fluid Dynamics (CFD) to predict the thermal performance of phase change materials for the control of photovoltaic cell temperature in Buildings. PhD Thesis

Huang, M. J., Eames, P.C. and Norton, B. (2004) Thermal regulation of building-integrated photovoltaics using phase change materials. International Journal of Heat and Mass Transfer, Vol. 47, pp 2715-2733.

Huang, M. J., Eames, P.C. and Norton, B. (2006a) Phase change materials for limiting temperature rise in building integrated photovoltaics. Solar Energy, Vol. 80, pp 1121-1130.

Huang, M. J., Eames, P.C. and Hewitt, N.J. (2006b) The application of a validated numerical predict the energy conservation potential of using phase change materials in the fabric of a building. Solar Energy Materials & Solar Cells, Vol.90, pp 1951–1960.

Huang, M. J., Eames, P.C. and Norton, B. (2006c) Comparison of a small-scale 3D PCM thermal control model with a validated 2D PCM thermal control model. Solar Energy Materials and Solar Cells, Vol.90, pp. 1961-1972.

Ito, S., Matsui, H., Okada, K., Kusano, S., Kiamura, T., Wada, Y., and Yanagida, S. (2004) Calibration of solar simulator for evaluation of dye-sensitized solar cells. Solar Energy Materials & Cells, Vol.82, pp 421-429.

Jensen, S.Ø. (2001) Results from measurements on the PV-VENT systems at Lundebjerg. Solar Energy Centre Denmark, Danish Technological Institute. SEC-R-14. ISBN 87-7756-611-0.

Johnston, G., Lovegrove, K. and Luzzi, A. (2003) Optical performance of spherical reflecting elements for use with paraboloidal dish concentrators. Solar Energy, Vol.74 pp. 133-140.

Jotshi, C. K., Goswami, D. Y. and Tomlinson, J. J., (1992). Solar thermal energy storage in phase change materials. In: Proceedings of the Annual Conference of the American Solar Energy Society, pp175-179.

Kohraku, S. and Kurokawa, K. (2006) A fundamental experiment for discrete-wavelength LED solar simulator. Solar Energy Materials & Solar Cells. Vol. 90, pp 3364-3370.

Kuhn, P. and Hunt, A. (1991) A new solar simulator to study high temperature solid-state reactions with highly concentrated radiation. Solar Energy Materials Vol.24, pp.742-750.

Luque, A. and Hegedus, S. (2003) Handbook of Photovoltaic Science and Engineering. John Wiley & Sons, Chichester, West Sussex, UK

Mallick, T. K., Eames, P.C. and Norton, B. (2002) Asymmetric compound parabolic photovoltaic concentrators for building integration in the UK: An optical analysis. World Renewable Energy Congress-VII, 29th June-5th July. Köln, Germany.

Mallick, T. K. (2003) Optics and heat transfer for asymmetric compound parabolic photovoltaic concentrators for building integrated photovoltaics. PhD thesis. University of Ulster, Newtownabbey, N.I. U.K.

Mallick, T. K., Eames, P.C., Hyde, T. J. and Norton, B. (2004) The design and experimental characterization of an asymmetric compound parabolic photovoltaic concentrator for building façade integration in the UK. Solar Energy, Vol.77, pp. 319-327

Mallick, T. K., Eames, P.C. and Norton, B. (2006) Non-concentrating and asymmetric compound parabolic concentrating building façade integrated photovoltaics: An experimental comparison. Solar Energy, Vol.80, pp. 834-849.

Mallick, T. K., Eames, P.C. and Norton, B. (2007a) Using air flow to alleviate temperature elevation in solar cells within asymmetric compound parabolic concentrators. Solar Energy, Vol.81, pp. 173-184.

Mallick, T. K., Eames, P.C. and Norton, B. (2007b) Power losses in an asymmetric compound parabolic photovoltaic concentrator. Solar Energy Materials and Solar Cells, Vol. 91, pp. 1137-1146.

Mallick, T. K. and Eames, P. C. (2007c) Optical performance predictions for a high concentration point focus photovoltaics system. Proceeding of ICSC-4, El Escorial, Spain.

Mallick, T. K. and Eames, P. C. (2007d) Optical and thermal performance predictions for a high concentration point focus photovoltaic system. Proceeding of ISES 2007, Beijing, China.

Markvart, T. (1994) Solar Electricity, John Wiley & Sons Ltd. Chichester, West Sussex, UK.

Mason, N.B, Russell, R., Artigao, A., Fernandez, J.M. and Nast-Hartley, O. (2004) New generation BP solar saturn cell in production the BP7180 module. 19th Symposium PV solarenergie, Kloster Banz (Staffelstein).

Maycock, P. (2005) PV review: World Solar PV market continues explosive growth. ReFOCUS, Vol.6, pp. 18-22.

Miles, R. W., Hynes, K. M. and Forbes, I. (2005) Photovoltaic solar cells: An overview of state-of-the art cell development and environmental issues. Progress in Crystal Growth and Characterization of Materials, Vol.51, pp. 1-42

Mills, D. R. and Giutronich, J. E (1978) Asymmetrical non-imaging cylindrical solar concentrators. Solar energy, Vol.20, pp.45-55.

Mills, D. (2004) Advances in solar thermal electricity technology. Solar Energy, Vol.76, pp.19-31.

Miyazaki, T., Akisawa, A., Kashiwagi, T. (2006) The effects of solar chimneys on thermal load mitigation of office buildings under the Japanese climate. Renewable Energy, Vol.31, pp. 987-1010

Moshfegh, B and Sandberg, B. (1998) Flow and heat transfer in the air gap behind photovoltaic panels. Renewable and Sustainable Energy Reviews, Vol.2, pp. 287-301

Nabelek, B., Maly, M. and Jirka, Vl. (1991) Linear fresnel lenses, their design and use. Renewable Energy, Vol.1, pp 403-408.

Norton B. (1992) Solar energy thermal technology, Springer-Verlag London Limited. UK.

Othman, M.Y., Yatim, B., Sopian, K. and Bakar, M. N. (2005) Performance analysis of a double-pass photovoltaic/thermal (PV/T) solar collector with CPC and fins. Renewable Energy, Vol.30, pp. 2005-2017.

Oliver, M. and Jackson, T. (2001*)* Energy and economic evaluation of building-integrated photovoltaics. Energy, Vol.26, pp. 431–439

Pal, D. and Joshi, Y. K. (1999) Thermal control of horizontally mounted heat sources using phase change materials. Advances in Electronic Packaging , Vol. 2, pp. 1625-1630.

Peuser, F. A., Remmers, K. and Schnauss, M. (2002) Solar Thermal Systems, Solarpraxis AG, Germany.

Rabl, A. (1976a) Comparison of solar concentrators. Solar Energy, Vol.18, pp. 93-111.

Rabl, A. (1976b) Optical and thermal properties of compound parabolic concentrators. Solar Energy, Vol. 18, pp. 497-511.

Rabl, A. (1985) Active solar collectors and their applications. Oxford University Press, New York. USA.

Reber, G., Steiner, R., Oelhafen, P. and Romanyuk, A. (2005) Angular dependent solar gain for insulation glasses from experimental optical and thermal data. CISBAT Proceedings: Renewables in a changing climate innovation in building envelopes and environmental systems, Lausanne, Switzerland.

Ryu, K., Rhee, J. G., Park, K. M. and Kim, J. (2006) Concept and design of modular Fresnel Lenses for Concentration solar PV system. Solar Energy, Vol.80, pp. 1580-1587.

Salim, A. A. and Eugenio, N. N. (1990) A comprehensive report on the performance of the longest operating 350kW concentrator photovoltaic power system. Solar energy, Vol.29, pp 1-24.

Siegel, R. (1977) Solidification of Low Conductivity Material Containing Dispersed High Conductivity Particles. Heat Mass Transfer, Vol.20, pp. 1087-1089

Sopian, K., Yigit, K. S., Liu, H. T., Kakac, S. and Veiroglu, T. N. (1995) Performance analysis of photovoltaic thermal air heaters. Energy Conversion and Management, Vol.37, pp. 1657-1670.

Sørensen, H. and Munro, D. (2000) Hybrid PV/ Thermal Collectors. The proceeding of the 2nd World Solar Electric Building Conference: Sydney 8th-10th March.

Stritih, U (2004) An experimental study of enhanced heat transfer in rectangular PCM thermal storage. International Journal of Heat and Mass Transfer, Vol.47, pp 2841-2847

Tabatabaie-Raissi, A. and Antal Jr., M. J. (1986) Design and operation of a 30KWe/2KWth downward facing beam ARC image furnace. Solar Energy, Vol.36, pp. 419-429.

Tonui, J.K. and Tripanagnostopoulos,Y. (2007) Improved PV/T solar collectors with heat extraction by forced or natural air circulation. Renewable Energy, Vol.32, pp. 623-637.

Trieb, F., Langniß, O. and Klaiß, H. (1997) Solar electricity generation: a comparative view of technologies, costs and environmental impact. Solar Energy, Vol. 9. pp. 89-99.

Tripanagnostopoulos, Y., Nousia, Th., Soluiotis, M. and Yianoulis, P. (2002) Hybrid photovoltaic/ thermal solar systems. Solar Energy, Vol.72, pp. 217-234.

Ure, Z. (1998) Eutectic thermal energy storage concept. In proceeding of the Phase Change Materials and Chemical Reactions for Thermal Energy Storage First Workshop. Adana, Turkey.

Welford, W. T. and Winston, R. (1978) The Optics of Non-imaging Concentrators: Light and Solar Energy. Academic Press. INC. London, U.K.

Welford, W. T. and Winston, R. (1989) High Collection Non-imaging Optics. Academic Press. INC. London, U.K.

Whitfiled. G. R., Bentley, R. W., Weatherby, C. K., Hunt, A. C., Mohring, H. D., Klotz, F. H., Keuber, P. and Minano, J. C. (1999) The development and testing of small concentrating PV system. Solar Energy, Vol. 67, pp. 23-34.

Winston, R (1974) Principles of Solar Collectors of a Novel Design. Solar Energy, Vol.16, pp 89-95.

Winston, R., Miñano J. C. and Benítez, P. (2005) Nonimaging Optics. Elsevier Academic Press. London U.K.

Wong, P. W., Shimoda, Y., Nonaka, M., Inoue, M. and Mizuno, M. (2008) Semi-transparent PV: Thermal performance, power generation, daylight modelling and energy saving potential in a residential application. Renewable Energy, Vol.33, pp. 1024-1036.

Wu Y., Eames P. C. and Smyth M. (2007a) Optical analysis of Asymmetric Compound Parabolic Photovoltaic Concentrators (ACPPVC) suitable for building façade integration. ICSC-4. El Escorial, Spain.

Wu Y, Eames P C, Smyth M and Mallick T K (2007b) Optical analysis and thermal prediction of different Asymmetric Compound Parabolic Photovoltaic Concentrators (ACPPVC) systems for building integration. ISES SWC 2007, Beiging, China.

Yang, H. X., Marshall, R. H. and Brinkworth, B.J. (1996) Validated simulation for thermal regulation of photovoltaic wall structures. Proceeding of 25th IEEE PV specialists conference, Washington DC.

Yang, H. and Li, Y. (2007) Potential of building-integrated photovoltaic applications. International Journal of Low Carbon Technologies, Vol.2, pp. 250 261.

Zacharopoulos, A., Eames, P. C., Mclarnon, D. and Norton, B. (2000) Linear dielectric non-imaging concentrating covers for PV integrated building façades. Solar Energy, Vol.68, pp. 439-452.

Zondag, H. A. and van Helden, W. G. J. (2003) PV-Thermal Domestic Systems. Proceeding of Osaka: 3rd World Conference on Photovoltaic Energy Conversion.